# GRAPHENE - METAL TUNGSTATE NANOCOMPOSITES FOR CATALYTIC APPLICATIONS

**Thesis**

Submitted in partial fulfillment of the requirements for the degree of

**DOCTOR OF PHILOSOPHY**

**by**

**MOHAMED JAFFER SADIQ M**
**(Register No: 145044CY14F01)**

**DEPARTMENT OF CHEMISTRY**
**NATIONAL INSTITUTE OF TECHNOLOGY KARNATAKA**
**SURATHKAL, MANGALORE - 575025**

**NOVEMBER, 2017**

**DECLARATION**

*By the Ph.D. Research Scholar*

I hereby *declare* that the Research Thesis entitled **'Graphene - Metal Tungstate Nanocomposites for Catalytic Applications'** which is being submitted to the **National Institute of Technology Karnataka, Surathkal** in partial fulfilment of the requirements for the award of the Degree of **Doctor of Philosophy** in **Chemistry** is a *bonafide report of the research work carried out by me*. The material contained in this Research Thesis has not been submitted to any University or Institution for the award of any degree.

(Signature of the Research Scholar)

Name: Mohamed Jaffer Sadiq M
Reg. No: 145044CY14F01
Department: Chemistry

Place: NITK - Surathkal
Date:

# CERTIFICATE

This is to *certify* that the Research Thesis entitled **'Graphene - Metal Tungstate Nanocomposites for Catalytic Applications'** submitted by **Mr. Mohamed Jaffer Sadiq M** (Register Number: **145044CY14F01**) as the record of the research work carried out by him, is *accepted as the Research Thesis submission* in partial fulfilment of the requirements for the award of degree of **Doctor of Philosophy.**

Prof. D. Krishna Bhat
Research Guide and Chairman - DRPC

*I dedicate this Thesis to God,*

*My Parents, Sisters, Uncles, Cousins,*

*My Teachers, My beloved ones;*

*And to everyone who have given me knowledge, time and*

*experience.*

## ACKNOWLEDGEMENT

First and foremost, I would like to express my sincere gratitude to ***God;*** I thank God for all the wisdom and perseverance that he has been bestowing upon me during this research work, and indeed, throughout my life: “I can do all good only through him who gives me all strength”.

I wish to express my sincere and respectful gratitude to my research supervisor ***Prof. D. Krishna Bhat,*** Head, Department of Chemistry, National Institute of Technology Karnataka, Surathkal, for giving me an opportunity to carry out research under his able guidance and for providing me the required experimental facilities in the Department. I admire his friendly nature, constant supervision, ample patience, support and encouragement throughout this research work. I appreciate all his contributions of time and ideas rendered to make my research experience productive and stimulating. I remain ever grateful to my supervisor who has made this thesis possible.

I sincerely thank the members of RPAC, ***Dr. M.N. Satyanarayana,*** Department of Physics, National Institute of Technology Karnataka, Surathkal, and ***Dr. Darshak R. Trivedi,*** Department of Chemistry, National Institute of Technology Karnataka, Surathkal, for their valuable suggestions and fruitful discussions during this work.

I owe my gratitude toward the faculty members of the Department of Chemistry, National Institute of Technology Karnataka, Surathkal; ***Prof. A. Nityananda Shetty, Prof. A. Vasudeva Adhikari, Prof. A. Chitharanjan Hegde, Prof. B. Ramachandra Bhat, Dr. Arun M. Isloor, Dr. D. Udaya Kumar, Dr. Sib Sankar Mal, Dr. P.B. Beneesh, Dr. Debashree Chakraborty*** and ***Dr. Saikat Dutta*** for their suggestions and support. I am ever grateful to the Department of Chemistry, NITK for all the laboratory and technical support.

I am indebted to the nonteaching staff, Department of Chemistry NITK, ***Mrs. Shamila Nandini, Mrs. Sharmila, Mrs. Deepa, Mr. Prashanth, Mr. Pradeep Crasta,***

***Mr. Harish, Mr. Santhosh*** and ***Mr. Gopal*** for their help in official and laboratory works.

My special thanks to ***Dr. Sandhya Shenoy, Dr. J. Mathiyarasu, Dr. S. Mutyala, Dr. C. Suresh*** and ***Mr. Varadharajan Perumal*** for their kind cooperation and support during my research work.

I was fortunate to be blessed with a friendly, knowledgeable and cheerful group of fellow research scholars for making my stay at NITK during research a memorable one.

I gratefully acknowledge the cooperation and encouragement given by my teacher ***Prof. A. Samson Nesaraj,*** Department of Chemistry, Karunya University, Coimbatore, and ***Dr. V. Gunasekaran***, Department of Materials Science, Central University of Tamilnadu, Thiruvarur, who encouraged me to take up research as my career.

I also express my heartfelt thanks to ***Mr. H. Mohamed Ibrahim, Mrs. M. Ameen Bivi, Mr. A. Mohamed Bilal, Mrs. M. Shajitha, Mr. M. Mohamed Yousuff, Mrs. M. Rasitha, Mr. M. Mohamed Ukkas, Mr. M. Mohamed Mahroos, Ms. M. Aaffiya,*** and ***Mr. M. Syed Wahid*** for their unselfish and altruistic support, motivations, love and encouragements.

Finally, I must acknowledge the good wishes, encouragement and wholehearted support from God, my research supervisor, my parents and family members. I wish to thank all those who sincerely extended their cooperation, encouragement, support, love and affection.

**MOHAMED JAFFER SADIQ M**

## ABSTRACT

The research thesis entitled **'Graphene - Metal Tungstate Nanocomposites for Catalytic Applications**' deals with the synthesis, characterization and studies on catalytic properties of some graphene - metal tungstate nanocomposites. The work describes successful synthesis of five different kinds of novel graphene-metal tungstate based nanocomposites namely, NRGO/$ZnWO_4$/$Fe_3O_4$, NRGO/$NiWO_4$/ZnO, NRGO/$CoWO_4$/$Fe_2O_3$, NRGO/$FeWO_4$/$Fe_3O_4$ and NRGO/$BaWO_4$/g-$C_3N_4$ using facile microwave irradiation method. All the synthesized nanocomposites were carefully characterized for their elemental composition, structural, morphological and optical properties by employing appropriate techniques such as, XRD, SEM, FESEM, TEM, HRTEM, BET, XPS, DRS, Raman, FTIR, UV-Vis and PL spectroscopies. Thereafter, each nanocomposite was investigated for its catalytic efficiency towards, (i) The photodegradation of methylene blue dye under the visible light irradiation, (ii) The reduction of 4-Nitrophenol to 4-Aminophenol by sodium borohydride in aqueous media and (iii) The electrocatalytic hydrogen evolution reaction in alkaline media. The synthesized nanocomposites exhibit high catalytic activity due to the synergistic effects of the components of the nanocomposite materials. The reusability of the catalysts in all the above processes is also good. Therefore, the observed results suggest that these novel graphene - transition metal tungstate based ternary nanocomposites are potential candidates as multifunctional catalysts in the field of clean energy and environmental applications.



***Keywords:*** *Graphene, Metal Tungstates, Microwave Irradiation, Photocatalysts, Reduction, Electrocatalysts*.

**TABLE OF CONTENTS** **PAGE NO**

**CHAPTER 1: INTRODUCTION**

**CHAPTER 2: SYNTHESIS OF NOVEL NRGO/$ZnWO_4$/$Fe_3O_4$ NANOCOMPOSITE AS AN EFFICIENT CATALYTIC MATERIAL FOR ENERGY AND ENVIRONMENTAL APPLICATIONS**

## ABBREVIATIONS

| | | |
|---|---|---|
| 4-AP | - | 4-Aminophenol |
| 4-NP | - | 4-Nitrophenol |
| BET | - | Brunauer-Emmett-Teller |
| BQ | - | Benzoquinone |
| CB | - | Conduction Band |
| CV | - | Cyclic Voltammetry |
| CVD | - | Chemical Vapor Deposition |
| DRS | - | Diffuse Reflectance Spectroscopy |
| EDX | - | Energy Dispersive X-ray |
| FESEM | - | Field Emission Scanning Electron Microscopy |
| FTIR | - | Fourier Transmission Infra-Red |
| GCE | - | Glassy Carbon Electrode |
| g-$C_3N_4$ | - | Graphitic Carbon Nitride |
| GO | - | Graphene Oxide |
| HER | - | Hydrogen Evolution Reaction |
| HRTEM | - | High Resolution Transmission Electron Microscopy |
| LSV | - | Linear Sweep Voltammetry |
| MB | - | Methylene Blue |
| NRGO | - | Nitrogen Doped Reduced Graphene Oxide |
| PL | - | Photo-Luminescence |
| RGO | - | Reduced Graphene Oxide |
| SEM | - | Scanning Electron Microscopy |
| TBA | - | Ternary Butyl Alcohol |
| TEM | - | Transmission Electron Microscopy |
| TOC | - | Total Organic Carbon |
| UV-Vis | - | Ultraviolet-Visible |
| VB | - | Valence Band |
| XPS | - | X-ray Photoelectron Spectroscopy |
| XRD | - | X-Ray Diffraction |

# CHAPTER – 1

## INTRODUCTION

*This chapter gives a brief introduction to the basic aspects of the study undertaken. It also gives a brief overview of the relevant works in the literature which focus upon graphene, metal tungstate, metal tungstate-based nanocomposites, graphene-based nanocomposites, their synthesis methods and catalytic applications. Scope and objectives of the present research work have been given at the end.*

## 1.1 CARBON SOURCES

Carbon is one of the most important materials in catalytic science and technology due to its adsorption capacities and as a support for various heterogeneous catalysts. It also plays different roles in the preparation and performance of catalysts. The presence of carbonaceous materials in a semiconductor composite significantly improves the catalytic performance of the composite. (Bruno and Philippe 2012, Philippe and Bruno 2015). Graphene oxide (GO), graphene, N-doped reduced graphene oxide (NRGO) and graphitic carbon nitride (g-$C_3N_4$) belong to this interesting class of carbonaceous materials.

### 1.1.1 Graphene Overview

Graphene is a two-dimensional single-layer carbon sheet that has attracted great interest recently in various fields of science and engineering because of its unique electrical, optical, thermal, and mechanical properties (Allen et al. 2009). Although a lot of methods have been developed for the preparation of graphene sheets the most widely used technique is chemical reduction of GO by Hummers' method (Hummers and Offeman 1958). According to this method, graphene is prepared by exfoliating GO, obtained by oxidation of natural graphite powder with strong chemical oxidants, such as $HNO_3$, $KMnO_4$ and $H_2SO_4$. In recent years, graphene based nanocomposites have attracted attention towards the heterogeneous catalysis such as photocatalytic dye degradation processes, electrocatalytic hydrogen evolution reaction (HER), cross-coupling reactions, propylene epoxidation, hydrogenation reactions, reduction of 4-Nitrophenol (4-NP) to 4-Aminophenol (4-AP), oxidation of alcohols due to their excellent sensitivity, durability and stability (Chang and Wu 2013). Several research groups are working on graphene-based nanocomposite materials like GO-polymer, GO-metal, GO-semiconductor, GO-metal oxide and GO-

magnetic material composites for various engineering applications due to its high surface area and high chemical stability (Stankovich et al. 2006). Further, graphene has also been used profusely as an active supporting component in the preparation of nanocomposite materials for adsorption, separation, degradation of organic dyes, the reduction of 4-NP to 4-AP and electrocatalytic HER (Chowdhury and Balasubramanian 2014).

### 1.1.2 NRGO Overview

By doping with heteroatoms (nitrogen, sulphur, boron), the physiochemical properties of nanostructured carbon nanotubes and graphene can be improved. Among the heteroatoms nitrogen is preferred because it can enhance the electrochemical reduction of oxygen which increases charge transportation capacity. N-doped graphene also possess large surface area, high thermal and electrical conductivity, tunable electronic properties, and increased number of active catalytic sites. This can be used as a supporting matrix for semiconductor catalyst to enhance its catalytic activity in degradation of dyes, electrocatalysts of HER and reduction of 4-NP to 4-AP. The photo-induced charge separation, transfer and collection is improved due to the strengthened interfacial interaction and the formation of p-n heterojunction between semiconductor and N-doped graphene (Zhang et al. 2014, Chang and Baek 2016, Li et al. 2016).

### 1.1.3 Graphitic Carbon Nitride Overview

g-$C_3N_4$ has a polymeric structure based on heptazine units. It is chemically inert and insoluble in acidic, neutral or basic solutions. Because of the presence of carbon and nitrogen, g-$C_3N_4$ has surface properties suitable for catalysis and includes basic surface functionalities, electron-rich properties, H-bonding motifs etc. It has high thermal stability (stable upto 600 °C in air) and hydrothermal stability. g-$C_3N_4$ is used as a catalyst for various reactions such as $CO_2$ activation, transesterification, oxygen reduction, electrocatalytic hydrogen production, reduction of 4-NP to 4-AP and photodegradation of dyes (Dong et al. 2011, Dai et al. 2013, Zhu et al. 2014). Because of the unique electronic structure, g-$C_3N_4$ can be coupled with various functional materials to enhance the catalytic performance. According to catalytic mechanism and

processes, six primary systems of g-$C_3N_4$ based nanocomposites are identified: g-$C_3N_4$ based metal-free heterojunction, g-$C_3N_4$/single metal oxide (metal sulfide) heterojunction, g-$C_3N_4$/composite oxide, g-$C_3N_4$/halide heterojunction, g-$C_3N_4$/noble metal heterostructures, and g-$C_3N_4$ based complex system (Zhao et al. 2015).

## 1.2 METAL TUNGSTATE OVERVIEW

Metal tungstates with the formula of $AWO_4$ type compounds where A is a divalent transition metal ion have attracted a lot of scientific interest in recent times because of their interesting structural properties (Suresh et al. 2011, Xiang and Yu 2013). It can be used in various applications such as scintillators, photoanodes, ceramics, laser hosts, optical fibres, sensors, photoluminescence, magnetic, multiferroic, electrical transport, photocatalysts, electrocatalysts, reduction catalysts, oxidation of benzyl chlorides, bromides and alcohols with hydrogen peroxide (Xie et al. 2002, Wang et al. 2006, Cavalli et al. 2008, Kumar et al. 2010, Shi et al. 2010). The major natural tungsten ores are formed by the minerals scheelite and wolframite with its end members ferberite and hubnerite. Depending on the ionic radius of the cation ($A^{2+}$ sites) tungstates can crystallize in either the scheelite or the wolframite structure. Scheelite structures with the tungsten in tetrahedral coordination are formed with large bivalent cations (ionic radius $\geq$ 0.99 Å) like Ca, Ba, Pb and Sr. Alternatively, tungstates with smaller bivalent cations (ionic radius $\leq$ 0.77Å) like Fe, Cu, Mn, Co, Ni, Mg and Zn, crystallize in wolframite structure with the tungsten in octahedral coordination (Ryu et al. 2005, Sakthivel et al. 2012, Renkun et al. 2013, Zawawi et al. 2013, Sakthivel et al. 2014). So far, a variety of methods have been used to synthesize metal tungstates including hydrothermal synthesis, ultrasonic irradiation, high temperature solid-state synthesis, flux methods, reaction of oxides with $WO_3$ vapor, mechanochemical activation, Czochralski technique, sol-gel technique, aqueous solution growth polymerized complex method, hydrothermal combined with annealing treatment, template method, self-propagating combustion method, microwave irradiation and co-precipitation (An et al. 2002, Liao et al. 2002, Geng et al. 2006, Kalinko and Kuzmin 2011, Kumar and Karuppuchamy 2016, Gohari and Yangieh 2017).

## 1.3 CATALYSIS

The increase in the rate of a chemical reaction with the addition of certain substances, without itself getting consumed, is called catalysis. The term catalysis was coined by Berzelius in 1835. The substance is called as catalyst and they can be protonic acids, multifunctional solids, transition metals etc. Catalyst reacts with reactant to form an intermediate with activation energy lower than that required for the reaction without using catalysts (Zhou et. al. 2004). Types of catalysis such as organocatalysis, electrocatalysis, nanocatalysis, enzymes and biocatalysis, hydrogenation catalysis and photocatalysis (Viswanathan 2009) have drawn widespread attention due to their potential applications in environmental remediation and renewable resource production, such as water purification and hydrogen production.

### 1.3.1 Photocatalysis

The toxic organic and inorganic wastes from industries are the major contaminants in the environment and pose a serious problem in the current scenario (Herrmann 1999). Dyes such as methylene blue (MB), rhodamine B (RhB) are the major organic compounds used in various industries, such as textile industries, dyeing, printing, and cosmetics (Garg et al. 2004). These dye effluents are discharged from various industries into the nearby water source without further treatment (Cooper 1993). Most of the dyes are toxic in nature and their disposal into the environment causes serious health hazards and it also poses a threat to our ecosystem. Therefore, it is necessary to remove the dye pollutants from industrial wastewater to reduce water pollution (Robinson et al. 2001). Photocatalysis is an excellent method for the degradation of highly toxic hazardous pollutants present in waste water (Herrmann 1999). Although it is a less expensive process compared to other advanced oxidation processes, the overall cost can be further reduced by optimizing the operating environment. Hence, photocatalysis can be practically implemented along with the combination of heterogeneous catalysts and made more cost effective. Semiconductor photocatalytic materials are a green tool for the decomposition of organic pollutants into non-hazardous compounds under light irradiation (Chen et al.

2010). To date, the practical applications of photocatalysts are restricted by two important factors: the fast recombination of photogenerated electron-hole pairs and the limited visible-light response. Thus, there have been intense efforts to develop new highly efficient visible light photocatalysts.

### 1.3.2 Mechanism of Photocatalysis

Photocatalysis generally involves the process of photosensitization, where a photochemical reaction occurs in one chemical species due to the absorption of photonic energy by another species called photosensitizer, which, in most cases, refers to a semiconductor. The mechanism of photocatalysis is illustrated in Figure 1.1. When photons with energies larger than the band gap energy ($\Delta E$) of the photocatalyst are absorbed, the electrons in the valence band (VB) of the semiconductor photocatalyst are excited into the conduction band (CB), leaving behind an equal number of holes in the VB (equation 1.1). Apart from the recombination that may occur in the bulk or on the surface of the catalyst, the photo-generated electron-hole pairs will separate from each other and migrate to catalytically active sites at the semiconductor/liquid interface and then react with any adsorbed species. The holes, with high oxidative potential, will either oxidize the organic species directly (equation 1.2), or form very active hydroxyl radicals ($^{\cdot}OH$) by decomposition of water (equation 1.3) or react with hydroxyl ions ($OH^-$) in water (equation 1.4). The electrons in the CB on the catalyst surface, on the other hand, can reduce adsorbed oxygen into superoxide anions (equation 1.5) or peroxides (equation 1.6), which may subsequently form hydroxyl radicals ($^{\cdot}OH$) (equation 1.7). The hydroxyl radical is a highly powerful, non-selective oxidant ($E° = +3.06$ V) which causes partial or complete decomposition of many organic compounds (equation 1.8), and hence is an important species that mineralizes organics in the photocatalytic reactions (Tang and Huren 1995, Galindo and Jacques 2001, Khodja et al. 2001, Daneshvar et al. 2004, Wan et al. 2005).

The process of photocatalytic degradation can also be represented by a series of equations. The photoexcitation of semiconductor catalyst (SC) by UV light irradiation, followed by the formation of electron-hole pairs can be expressed below:

$SC + h\nu \rightarrow SC\ (e^- + h^+)$ ---------- (1.1)

The photogenerated holes and electrons are strong oxidizing and reducing agents, which will cause a series of subsequent oxidative and reductive reactions, respectively, as illustrated by

Photooxidation reactions

$h^+ + dye + dye^{\cdot+} \rightarrow$ degradation of the dye ---------- (1.2)

$h^+ + H_2O \rightarrow H^+ + {}^{\cdot}OH$ ---------- (1.3)

$h^+ + OH^- \rightarrow {}^{\cdot}OH$ ---------- (1.4)

Photoreduction reactions

$e^- + O_2 \rightarrow O_2^{\cdot-}$ ---------- (1.5)

$2e^- + O_2 + 2H^+ \rightarrow H_2O_2$ ---------- (1.6)

$e^- + H_2O_2 \rightarrow OH^- + {}^{\cdot}OH$ ---------- (1.7)

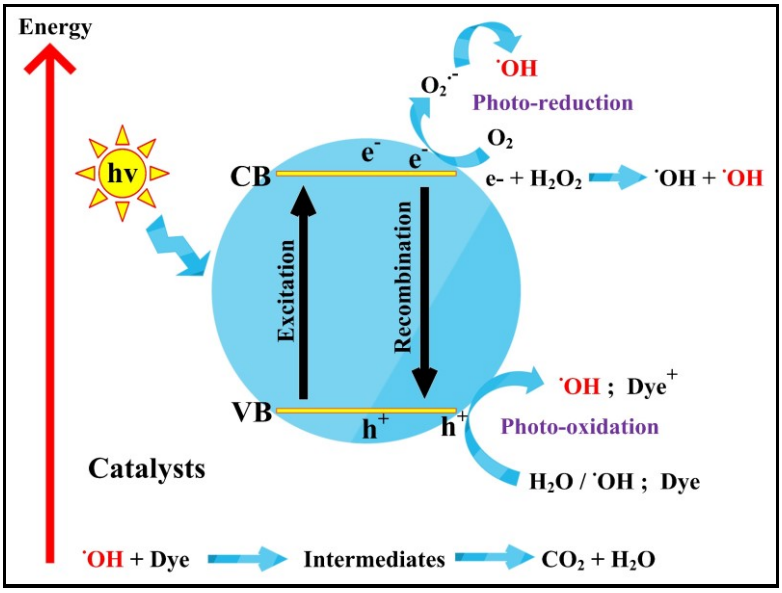


**Figure 1.1** A schematic diagram illustrating the principle of photocatalysis (Ahmed et al. 2010).

The primary degradation of dye is caused by the hydroxyl radicals generated through the previous processes, as represented by equation (1.8).

$$^{\cdot}OH + \text{dye} \rightarrow \text{intermediate} \rightarrow CO_2 + H_2O \quad \text{----------} \quad (1.8)$$

It is worth noting that the presence of adsorbed oxygen molecules prevents the recombination of the photogenerated electron-hole pairs. In a typical photocatalytic reaction, if the reduction of adsorbed oxygen does not take place simultaneously with the oxidation of organic dyes, there is a large chance that the electrons will accumulate on the catalyst surface, leading to an increased recombination rate of the electrons and holes. Hence it is very important to prevent electron accumulation by introducing oxygen molecules into the reaction mixture to achieve an efficient photocatalytic reaction.

### 1.3.3 4-NP Reduction

Among the various organic pollutants, 4-NP is listed as toxic by the United States Environmental Protection Agency (Ju and Parales 2010). Hence, the discharge of 4-NP from industries into the nearby water system without any treatment leads to serious environmental problems (Bhattacharjee and Ahmaruzzaman 2015). Therefore, the removal of 4-NP from the wastewater is very much important from the environmental point of view. Many processes such as adsorption, microbial degradation, photocatalytic degradation, Fenton method and electrochemical treatment have been developed (Chang and Chen 2009). 4-NP is also a precursor for the synthesis of 4-AP. 4-AP is an important intermediate in the synthesis of various analgesic and antipyretic drugs such as paracetamol, acetanilide and phenacetin (Vaidya et al. 2003). It has enormous applications in the synthesis of various dyes, as a photographic-developer and corrosion inhibitor. So, a great deal of efforts has been made on the reduction of 4-NP to 4-AP. Among them, the sodium borohydride ($NaBH_4$) reduction of 4-NP to 4-AP by semiconductor nanoparticles (which act as a catalyst) is particularly attractive because this reaction can be performed in aqueous solution under mild condition. However, for the sake of saving energy, safe operation, and avoiding the use of organic solvents, the development of more appropriate

processes for the reduction of 4-NP to 4-AP in aqueous solutions under mild condition is still in demand (Chiou et al. 2013).

### 1.3.4 Mechanism of 4-NP Reduction

The mechanism of 4-NP reduction is schematically shown in Figure 1.2. It is believed that the 4-NP molecules would transform into p-nitrophenolate ions in alkali atmosphere and adsorb on the surface of catalyst.

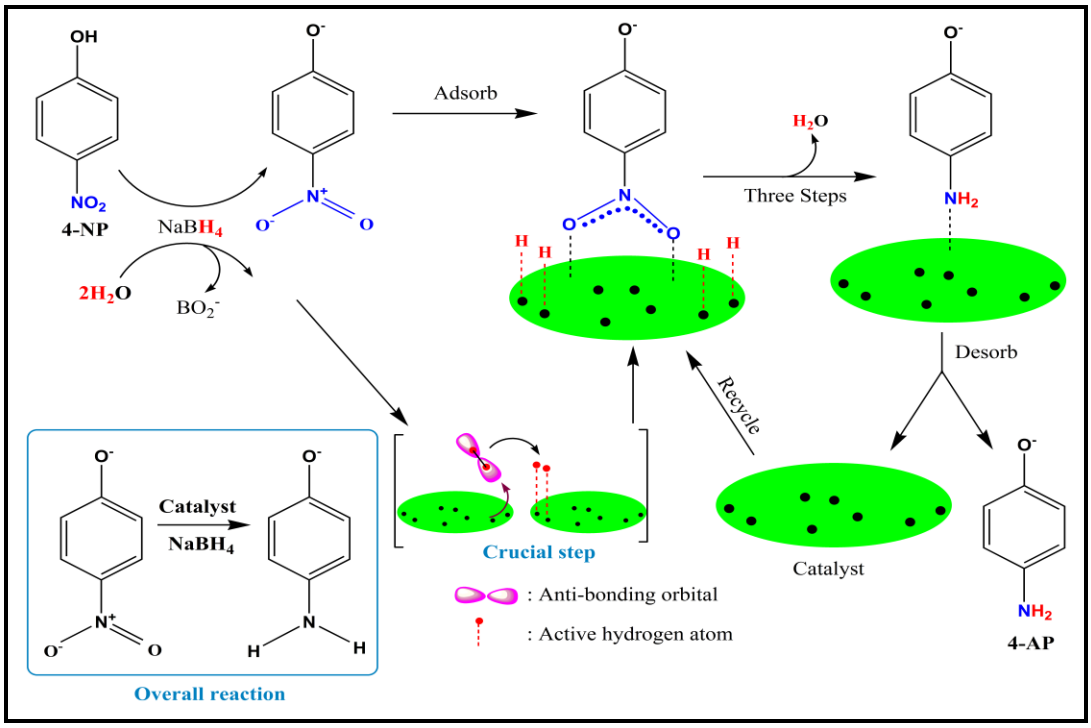


**Figure 1.2**The proposed mechanism for reduction of 4-NP by $NaBH_4$over the catalysts.

The strong nucleophile $BH_4^-$ would give electrons to catalyst, and hydrogen is formed from the hydride and the protons ($H^+$, provided by $H_2O$) (Du et al. 2012, El-Bahy 2013). The freshly formed $H_2$ molecule binds to the surface of catalyst and its anti-bonding molecular orbital accepts the electron pairs from the catalyst. Thus, the bond order of $H_2$ declines and active hydrogen atoms are formed on the surface of catalyst. The active hydrogen atoms will then attack the nitro groups of 4-NP and ultimately reduce them into amino groups via following three steps.

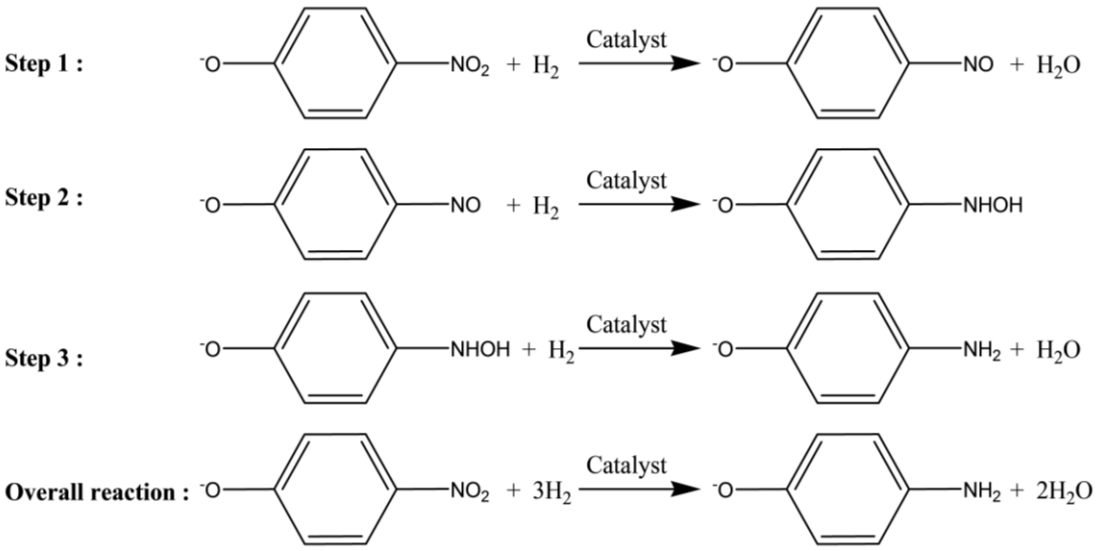


The mechanism also indicates that two factors may influence the sample's catalytic activity for the reduction of 4-NP: (1) adsorption of the p-nitrophenolate ion on the surface of catalyst and generation of surface active hydrogen atoms; (2) the rate of interfacial charge transfer in heterojunction. The reduction of 4-NP mainly happens on the surface of catalyst. Since the larger specific surface area can provide more active sites for borohydride ions, generated active hydrogen atoms and 4-NP adsorption, it is easy to understand that catalysts with the largest specific surface area will exhibit the best catalytic activity (Yu et al. 2007, Zhang et al. 2010).

### 1.3.5 Electrocatalysis

Hydrogen has been perceived as a valid alternative to fossil fuels in many applications because of its advantage of being a clean fuel, considering that its use emits almost nothing other than water. Additionally, it can be produced using any energy source, with renewable energy being most attractive, making it one of the solutions to sustainable energy supply in the so-called new "hydrogen economy" (Bokris et al. 1981).

Notwithstanding the increasing interest in hydrogen as an energy carrier, its main uses continue to be in petroleum refining, ammonia production, metal refining, and electronics fabrication, with an average worldwide consumption of about 40 million tons (Sato et al. 2003). This large-scale hydrogen consumption consequently requires large-scale hydrogen production. Presently, the technologies that dominate

hydrogen production include reforming of natural gas, gasification of coal and petroleum coke as well as gasification and reforming of heavy oil (Momirlan 2002). Hydrogen fuel obtained by water electrolysis is free of the contaminants which are found in hydrogen gas obtained from reformed hydrocarbons that can poison traditional fuel cell electrocatalysts, reducing their efficiency and lifetime (Sato et al. 2003).

### 1.3.6 Mechanism of Electrocatalysis

HER ($2H^+ + 2e^- \rightleftharpoons H_2$) is a multi-step electrochemical process taking place on the surface of an electrode that generates gaseous hydrogen. Generally accepted reaction mechanism of the electrocatalytic evolution of $H_2$ on the surface of the catalystselectrode is schematically shown in the Figure 1.3. In alkaline media, the HER pathway could be through the Volmer-Tafel (equation 1.9 and 1.11) process or Volmer-Heyrovsky (equation 1.9 and 1.10) pathways (Conway and Tilak 2002).

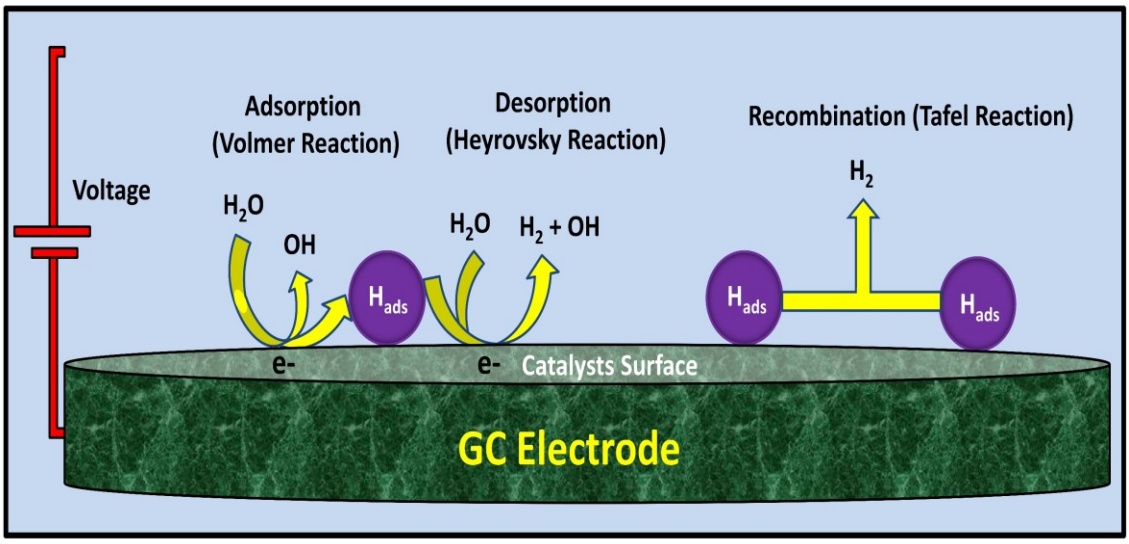


**Figure 1.3** The schematic representation of HER mechanism.

Electrochemical hydrogen adsorption (Volmer reaction) (equation 1.9)

$$H_2O + M + e^- \rightleftharpoons M - H_{ads} + OH^- \qquad \text{----------} \qquad (1.9)$$

followed by

Electrochemical desorption (Heyrovsky reaction) (equation 1.10)

$$M - H_{ads} + H_2O + e^- \rightleftharpoons M + OH^- + H_2 \uparrow \qquad \text{----------} \qquad (1.10)$$

or

Chemical desorption (Tafel reaction) (equation 1.11)

$$2\,M - H_{ads} \rightleftharpoons 2M + H_2 \uparrow \quad \text{----------} \quad (1.11)$$

where $H_{ads}$ designates a hydrogen atom chemically adsorbed on an active site of the electrode surface (M).

Both pathways involve the adsorption of $H_2O$ molecule, electrochemical reduction of adsorbed $H_2O$ into adsorbed $OH^-$ and H atom, desorption of $OH^-$ to refresh the surface and formation of H adsorbed intermediate for $H_2$ generation. Therefore, it is established that HER mechanism with Tafel slope values in the range of 66 mV per decade corresponds to Volmer-Heyrovsky and that in the neighbourhood of 118 mV per decade follows Volmer-Tafel and finally if the values are above 200 mV per decade the process is known to be following the Tafel mechanism (Markovic and Ross 2002, Norskov et al. 2005).

## 1.4 A REVIEW OF LITERATURE

A survey of literature, carried out to know the latest advancements in the field of graphene based nanocomposites is given below. Various synthetic techniques employed for the synthesis of components of the composite such as graphene, NRGO, g-$C_3N_4$ and metal tungstates in the recent past has been discussed below, followed by a brief account on their applications in photocatalysis, reduction of 4-NP and HER.

### 1.4.1 Graphene

The first reported synthesis of graphene is by mechanical cleavage of graphite with Scotch tape. Afterwards, a wide range of synthesis methods have been reported. These techniques can be divided into 'bottom-up' and 'top-down' methods. In the bottom-up methods, graphene is synthesized from atoms or molecules via chemical reactions. Some typical examples are epitaxial growth on single-crystal and chemical vapor deposition (CVD) on metal foil surfaces. High-quality graphene with a well-defined molecular structure is usually prepared by top-down methods such as chemical exfoliation of graphite, thermal exfoliation and electrostatic deposition.

Although a lot of methods have been developed for the preparation of graphene sheets, the most suitable and efficient approach is the solution-based chemical reduction of exfoliated RGO by Hummers' method (Hummers and Offeman 1958). The resulting RGO product is usually purified by centrifugation, washing and dialysis to remove some aggregates and various inorganic impurities such as residual ions and acids. Moreover, the functional GO can be reduced to graphene with partial restoration of the $sp^2$ hybridized network by thermal, chemical, electrochemical, photothermal, photocatalytic, sonochemical and microwave reduction methods. The presence of oxygen functionalities in GO allows interactions with the cations and provides reactive sites for the nucleation and growth of nanoparticles, which results in the rapid growth of various graphene-based composites.

Chen et al. (2009) have reported the oxidation of expanded graphite using concentrated $H_2SO_4$and $KMnO_4$ to form high quality graphene oxide in water. The method was claimed to be a simple and inexpensive route for the production of large quantity of graphene sheets.

Gao et al. (2009) have devised a complete reduction process of GO through chemical conversion by sodium borohydride and sulfuric acid treatment, followed by thermal annealing. Only small amounts of impurities were present in the final product (less than 0.5 wt.% of sulfur and nitrogen, compared to about 3 wt.% with other chemical reductions). This method is particularly effective in the restoration of the π-conjugated structure and leads to highly soluble and conductive graphene materials.

Marcano et al. (2010) have reported an improved method for the preparation of GO. They found that excluding $NaNO_3$, increasing the amount of $KMnO_4$, and performing the reaction in a 9:1 mixture of $H_2SO_4/H_3PO_4$ improves the efficiency of the oxidation process. This improved method provided a greater amount of hydrophilic oxidized graphene material as compared to Hummers' method. In contrast to Hummers' method, the new method did not generate toxic gases and the temperature control was easy. A comparison of the methods is schematically shown in the Figure 1.4.

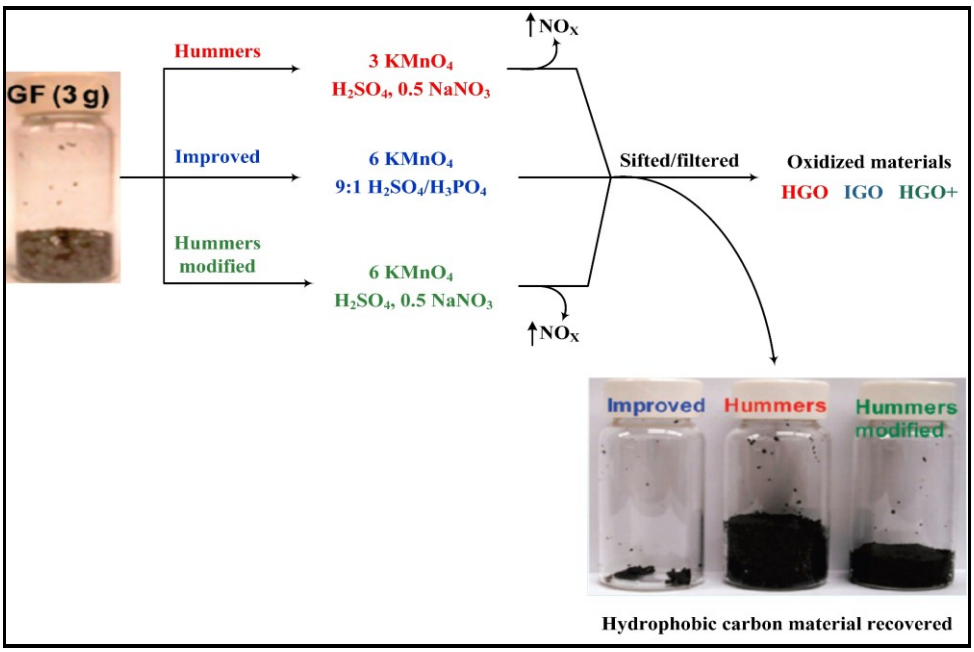


**Figure 1.4** Schematic representation of Hummers', Improved Hummers', and modified Hummers' Methods.

Jacob et al. (2015) reported CVD method for synthesis of high quality graphene sheets using isopropyl alcohol as the carbon precursor and decomposed on a nickel foil catalyst using a Meker burner. Ni foil was submerged in acetic acid to etch the native oxide from its surface. Then, the Ni foil was placed inside a quartz tube and the system was tightly sealed to ensure that oxygen and water vapor from the air do not enter during growth. The reaction conditions were maintained to obtain graphene coated nickel foil.

Dinesh et al. (2016) fabricated graphene nanoplatelets from expandable graphite by rapid microwave exfoliation. Expandable graphite was irradiated in microwave in full power for 3 minutes, soaked in mixture of nitric acid and sulphuric acid at volume ratio of 1:1 for 24 hours and re-irradiated to obtain graphene nanoplatelets.

### 1.4.2 NRGO

Sheng et al. (2011) proposed a facile, catalyst-free thermal annealing approach for large-scale synthesis of NRGO using low-cost industrial material melamine as the nitrogen source. This approach can completely avoid the contamination of transition

metal catalysts, and thus the intrinsic catalytic performance of pure N-doped graphene can be investigated. This catalyst-free approach opens up the possibility for the synthesis of N-doped graphene in gram-scale for electronic devices and as cathodic materials for fuel cells and biosensors.

Zhang et al. (2014) proposed a solid microwave-mediated method for scalable production of nitrogen-doped graphene sheets using low-cost industrial material melamine as functionalizing agent and nitrogen source. The strong interaction of microwaves with graphene oxide has been fully utilized to generate in situ heating that induces the decomposition of melamine and nitrogen doping of graphene.

Liu et al. (2016) synthesized N-doped graphene in hexamethylenetetramine flame from graphite oxide powder within a few seconds. The hexamethylenetetramine not only acts as the fuel for flame, but also as the nitrogen source and reducing agent. The exfoliation, reduction and nitrogen doping are achieved simultaneously in the nitrogen-rich flame plasma. The method features high efficiency, cost-effective and facile operation, and shed a light for the synthesis of nitrogen doped carbons in gram-scale towards energy storage applications. The N-doped graphene was evaluated as good electrode material for supercapacitor applications.

### 1.4.3 Graphitic Carbon Nitride

Dong et al. (2011) synthesized polymeric g-$C_3N_4$ layered materials with high surface areas efficiently from an oxygen-containing precursor by directly treating urea in air between 450 °C - 600 °C, without the assistance of a template. The g-$C_3N_4$ materials are demonstrated to exhibit much higher visible light photocatalytic activity than that of carbon doped $TiO_2$ and g-$C_3N_4$prepared from dicyanamide. The efficient synthesis method for g-$C_3N_4$ combined with efficient photocatalytic activity is of significant interest for environmental pollutants degradation and solar energy conversion in large scale applications.

Roberto et al. (2011) synthesized g-$C_3N_4$ starting from melamine and uric acid. Uric acid was chosen because it thermally decomposes, and reacts with melamine by condensation at temperatures in the range of 400 °C - 600 °C. The reagents were

mixed with alumina and subsequently the samples were treated in an oven under nitrogen flux. Alumina favored the deposition of the graphitic carbon nitrides layers on the exposed surface. This method can be assimilated to an in-situ CVD.

Dai et al. (2013) prepared g-$C_3N_4$ sub-microspheres via a facile microwave synthesis through polymerization reaction between cyanuric chloride and sodium azide using acetonitrile as solvent. The results show that g-$C_3N_4$ are insoluble to conventional solvents except dimethyl sulfoxide, and it exhibits a good chemical stability, thermal stability (< 650 °C), particle size with 0.076 μm - 0.137 μm diameter, surface area of 89.1 $m^2$/g and a band gap of 2.41 eV. Additionally, g-$C_3N_4$ prepared by microwave method also displays higher thermal stability, smaller particle radius, larger surface area, lower band gap and stronger emission intensity than traditional solvothermal method.

Dong et al. (2013) developed a facile in situ method to construct g-$C_3N_4$/g-$C_3N_4$ metal-free isotype heterojunction with molecular composite precursors with the aim to greatly promote the charge separation. Considering the fact that g-$C_3N_4$ samples prepared from urea and thiourea separately have different band structure, the molecular composite precursors of urea and thiourea were treated simultaneously under the same thermal conditions, in-situ creating a novel layered g-$C_3N_4$/g-$C_3N_4$ metal-free heterojunction (g-g CN heterojunction). For the removal of NO in air, the g-g CN heterojunction exhibited significantly enhanced visible light photocatalytic activity over g-$C_3N_4$ alone and physical mixture of g-$C_3N_4$ samples.

### 1.4.4 Metal Tungstates

Phani et al. (2000) have synthesized $ZnWO_4$ by solid state process from an equivalent molar mixture of ZnO and $WO_3$ at two different temperatures one at 900 $^oC$ and other at 1000 $^oC$. The result showed the uniform crystal formation of $ZnWO_4$ nanocrystals at 1000 $^oC$ for 24 hours.

Chen et al. (2003) have synthesized nanocrystalline $ZnWO_4$ with different morphologies and sizes at reaction temperature of 180 $^oC$ and pH ranging from 5.0 to

11.0 by using simple hydrothermal route. It was observed that the length of $ZnWO_4$ nanorod increased with the increase in pH of the reaction mixture.

Kloprogge et al. (2004) have reported the microwave-assisted synthesis of a variety of metal tungstates, $MWO_4$ (M = Ca, Pb, Fe, Mn, Zn) at two different temperatures 100 ºC and 150 ºC within a time frame from 30 minutes to 2 hours. The result shows the formation of equi-dimensional and needle-like crystals. The increase in synthesis time and temperature resulted in the disappearance of needles and the growth of the equi-dimensional crystals.

Cavalcante et al. (2008) have synthesized the $BaWO_4$ powders with different morphologies via a simple soft solution processing based on precipitation technique at different pH (range 7-13). The increase in the pH value, caused the two ends of the $BaWO_4$ crystallites with more and more branches and changing morphology such as, from double-taper-like into scissors like, fasciculus-like and flower-like structures.

Somchai et al. (2008) synthesized $MnWO_4$ with nanoplates in flower-like clusters from the mists of the solutions containing $MnCl_2 \cdot 4H_2O$ and $Na_2WO_4 \cdot 2H_2O$ at different pH values by 300 W -900 W cyclic microwave radiation. The synthesized material had bulk electrical conductivity, relatively low melting point and novel magnetic property. It exhibited photoluminescence in 409 nm - 420 nm range.

Wu et al. (2008) prepared nanocrystalline $Bi_2WO_6$ photocatalyst with nanosheet morphology by a microwave-solvothermal process using $Bi(NO_3)_3 \cdot 5H_2O$ and $(NH_4)_{10}W_{12}O_{41} \cdot 5H_2O$ as the starting materials. Ethylene glycol was used as the surfactant and the pH was adjusted by using ammonia solution. The microwave-solvothermal processes had many advantages: shorter reaction time, higher surface area and more oxygen vacancies for the preparation of $Bi_2WO_6$ samples. Nanocrystalline $Bi_2WO_6$ samples obtained by microwave-solvothermal process showed higher photocatalytic activity than that of the sample obtained by conventional hydrothermal process for the decomposition of RhB under visible light irradiation.

Shen et al. (2011) synthesized single-crystal $BaWO_4$ nanoparticles under microwave irradiation using $NaWO_4 \cdot 2H_2O$ and $BaCl_2$ in 10 mL $H_2O$. Nearly monodisperse $BaWO_4$ nanoparticles were successfully prepared without using surfactants. The photoluminescence properties were studied and the products showed a strong photoluminescence peak in 432 nm - 436 nm range with the excitation at 365 nm.

Garadkar et al. (2013) prepared $ZnWO_4$ nanoparticles by a simple microwave assisted technique using the solutions of zinc nitrate in ethylene glycol and aqueous solution of $Na_2WO_4$. The pH was adjusted to 10 by using ammonia. The obtained nanoparticles were used for the degradation of aqueous MB and RhB to test the photocatalytic activity under UV irradiation and showed an enhanced activity.

Li et al. (2013) synthesized $CaWO_4$ nanoparticles by microwave-assisted method at a temperature of 120 °C. $CaCl_2$, $Na_2WO_4 \cdot 2H_2O$, and poly ethylene glycol (PEG1000) were used as the starting materials and $CaWO_4$ nanocrystals were prepared by microwave-assisted method in the absence of any organic additives. The photoluminescence property was studied and showed a good relationship with the crystallinity.

Dhilip and Karuppuchamy (2014) synthesized $CuWO_4$nanopowder by microwave assisted synthesis using $H_2WO_4$ and $CuCl_2 \cdot 2H_2O$ as precursors. Prepared Cu-$WO_3$ sample have high conductivity and good stability when compare to $CuWO_4$nanopowder. The synthesized nanostructured $CuWO_4$ is promising for the supercapacitor applications.

Farsi and Zahra (2014) prepared nanostructured calcium tungstate from aqueous solution via co-precipitation method. $CaCl_2 \cdot 6H_2O$ and $Na_2WO_4 \cdot 2H_2O$ were used as the precursors. The pH of the solution was adjusted to 7 using sodium hydroxide and nitric acid. This nanostructured calcium tungstate was used as a supporting material for platinum, a well-known electrocatalyst for oxygen reduction. Preparation of the Pt/$CaWO_4$-graphite catalyst was carried out by electrodeposition of Pt onto the surface of $CaWO_4$/graphite electrode. It was found that the Pt/$CaWO_4$-

graphite has higher electrocatalytic activity for oxygen reduction in comparison with Pt/graphite catalyst.

Pourmortazavi et al. (2014) prepared copper tungstate nanoparticles by a chemical precipitation reaction in aqueous solution involving direct addition of copper ion solution to the solution of tungstate reagent. Hydrated salts of sodium tungstate and copper nitrate were used as the precursor. Optimization of the synthesis procedure was done using Taguchi robust design as a statistical method. Copper tungstate has wide range of applications as scintillation detectors, photoanodes, laser host, electrode material for photoelectrolysis, optical fibres, solar assisted water splitting etc.

Khaksar et al. (2015) prepared nanoparticles of $MnWO_4$ via an impregnation method using $Mn(NO_3)_2 \cdot 4H_2O$ and $WO_3$ as a source of manganese and tungsten, respectively. $MnWO_4$ is a cheap, environmentally friendly material and could be prepared as nano-sized particles with large surface area, and thus many of their active sites are accessible to the reactants. Therefore, these nanoparticles showed severe catalytic performances for the degradation of MB in the presence of tert-butyl hydrogen peroxide as the oxidant at room temperature in water.

Sun et al. (2015) synthesized $CaWO_4$ nanostructures (nanospheres, nanorods and nanoplates) by a hydrothermal process. The magnetic measurement of these $CaWO_4$ nanostructures indicated that $CaWO_4$ nanostructures possesses obvious room-temperature ferromagnetism, suggesting the potential of $CaWO_4$ nanostructures in various practical applications as laser host materials in quantum electronics and scintillators in medical devices. The nanostructures were synthesized by a facile hydrothermal process using $Ca(CH_3COO)_2 \cdot H_2O$ and $Na_2WO_4 \cdot 2H_2O$ as precursors.

Hu et al. (2016) prepared $CuWO_4$ nanoflake array films by using a solid phase reaction method in which the $WO_3$ nanoflakes were employed as sacrificial templates and $Cu(NO_3)_2$ in acetic acid as copper source. The $CuWO_4$ nanoflake films showed a superior photoelectrochemical activity compared to other $CuWO_4$ photoanodes reported earlier for oxygen evolution reaction. Thus, nanostructured $CuWO_4$ is a promising photoanode for solar water splitting.

Mostafa and Ali (2016) synthesized $CuWO_4$ nanoparticles via a large-scale and facile sonochemical method with the aid of copper (II) nitrate and sodium tungstate dihydrate in aqueous solution. The polymeric surfactant, polyvinyl pyrrolidone is used to get better morphology nanoparticles. The nanocrystalline $CuWO_4$ as a photocatalyst showed maximum degradation of methyl orange upon the irradiation of UV light.

Khademolhosein and Zarkar (2016) prepared $BaWO_4$ nanoparticles by sonochemical route based on the reaction between barium salt and $Na_2WO_4 \cdot 2H_2O$ in water. This method is free from any surfactant and organic solvents. The photocatalytic degradation efficiency of the prepared nanoparticles was investigated using MO solution with ultraviolet light irradiation.

### 1.4.5 Graphene Based Nanocomposites for Photocatalysis

Huang et al. (2013) have reported formation of α-$SnWO_4$/RGO by hydrothermal method at 200 °C using GO, $SnCl_2 \cdot 2H_2O$ and $(NH_4)_5H_5[H_2(WO_4)_6] \cdot H_2O$ in aqueous solution.

Haldorai et al. (2014) have prepared ZnO/RGO composites by an in-situ method using supercritical $CO_2$. The formed ZnO were tightly coated on RGO surface. It is believed that supercritical $CO_2$ helped to debundle RGO nanosheets and densely dispersed ZnO on RGO prevented restacking of the nanosheets.

Ullah et al. (2014) have synthesized PbS-graphene/$TiO_2$ photocatalyst by sol-gel method and studied photocatalytic degradation on MB under visible light irradiation. The result showed higher photocatalytic activity of PbS-graphene/$TiO_2$ composite than PbS-graphene. This was attributed to the coupling of PbS semiconductor with $TiO_2$ which provides a maximum interfacial contact with graphene surface.

Meng et al. (2014) have reported the flower-like ZnO/RGO/Ag micro/nano composites by a one-step microwave technique using graphene oxide, $AgNO_3$ and $Zn(CH_3COO)_2$ as raw materials without adding any external toxic reagent. The composite shows an enhanced and faster ultraviolet and simulated daylight

photocatalytic property, i.e. 92.73 % and 70.43 % degradation of methyl orange in 20 minutes as compared to the values of 70.91 % and 60.82 %, 55.48 % and 50.61 % by bare ZnO and RGO/ZnO, respectively. The enhanced photocatalytic property is attributed to an efficient charge transfer process from ZnO to both Ag and RGO. This method was found to be beneficial for synthesizing efficient ZnO-based ternary photocatalysts with a combination of metal and RGO.

Cheng et al. (2016) have successfully synthesized a ternary P25-graphene-$Fe_3O_4$ magnetic nanocomposite by decorating P25 and $Fe_3O_4$ nanoparticles on the RGO through a facile solvothermal reaction and its ability to photodegrade organic dyes in aqueous solutions was investigated. The as-synthesized sample exhibits high photocatalytic activity toward RhB dye and can be easily recycled by normal magnet due to the existence of $Fe_3O_4$ nanoparticles. Furthermore, owing to the presence of RGO, the photodissolution behavior of $Fe_3O_4$ nanoparticles occurring in the $TiO_2$-$Fe_3O_4$ binary nanocomposites was suppressed effectively, which increased the durability of such a recollectable photocatalyst.

Brindha and Sivakumar (2017) employed hydrothermal method for the synthesis of nitrogen and sulfur co-doped $TiO_2$/RGO composite. Photocatalytic activity of the nanocomposites in the decolorization and mineralization of congo red, MB and reactive orange was studied. More than 80 % mineralization was completed in less than 120 minutes. Four successive cycles showed no considerable phase change.

### 1.4.6 Graphene Based Nanocomposites for Reduction of 4-NP to 4-AP

Mao et al. (2012) have reported preparation of GO sheets decorated by Ag nanoparticles, using a liquid-liquid two phase method at the room temperature. Furthermore, Ag/GO were found to serve as effective catalysts to activate the reduction of 4-NP in the presence of $NaBH_4$ in only 30 minutes.

Sun et al. (2013) have reported a facile and green method to synthesize a new type of catalyst by coating Pd nanoparticles on RGO-carbon nanotube nanocomposite by hydrothermal treatment method. It exhibited excellent and stable catalytic activity

for the reduction of 4-NP to 4-AP using $NaBH_4$ as a catalyst. The reduction was completed in only 20 seconds at room temperature, even when the Pd content of the catalyst was 1.12 wt.%. This method did not require rigorous conditions or toxic agents and thus was a rapid, efficient, and green approach for the fabrication of highly active catalysts.

Tian et al. (2015) have developed an environmentally friendly, one-pot strategy toward preparation of Ni nanoparticles decorated RGO hybrids, through the use of ethylene glycol as both solvent and reducing agent under solvothermal conditions. Furthermore, taking the advantage of the synergetic effects between supported Ni nanoparticles and RGO sheets, Ni-RGO hybrids exhibited a better catalytic activity than pure Ni nanoparticles for the reduction of 4-NP to 4-AP with $NaBH_4$, with kinetic reaction rate being over 2.5 times that of pure Ni nanoparticles.

Nasrollahzadeh et al. (2016) have reported synthesis of Ag/RGO/$TiO_2$ nanocomposite through simple, cost efficient, surfactant free and green method using Euphorbia helioscopia L. leaf extract as a stabilizing and reducing agent. The Euphorbia helioscopia L. leaf extract was used for the reduction of $Ag^+$ ions and GO to Ag nanoparticles and RGO, respectively. The Ag/RGO/$TiO_2$ nanocomposite was highly active for the reduction of 4-NP, congo red and MB in aqueous media at an ambient temperature. The Ag/RGO/$TiO_2$ nanocomposite was easily separated and recovered from the reaction mixture by centrifugation and reused for several cycles without any significant loss of catalytic activity.

### 1.4.7 Graphene Based Nanocomposites for HER

Yang et al. (2013) reported $WS_2$ and $WS_2$/RGO nanosheets fabricated by hydrothermal synthesis using tungsten chloride, thioacetamide, and GO as starting materials. The $WS_2$ nanosheets are efficiently templated on the RGO layer. The $WS_2$/RGO hybrid nanosheets show much better electrocatalytic activity for the HER than $WS_2$ nanosheets alone.

Zheng et al. (2014) reported a novel solvent-evaporation-assisted intercalation method to fabricate the hybrid of alternating $MoS_2$ sheets and RGO layers, in which

the nanosize of the $MoS_2$ nanosheets can be effectively controlled by leveraging the confinement effect within the two-dimensional graphene layers. Significantly, the resulting $MoS_2$/RGO composite shows excellent catalytic activity for HER characterized by higher current densities and lower onset potentials than the conventional pre-exfoliated RGO supported $MoS_2$ nanosheets.

Lingpu et al. (2015) reported promising catalytic activity of $MoSe_2$ in the HER and synthesized it on a new reduced graphene oxide/polyimide (RGO/PI) substrate by a simple electrochemical method. The $MoSe_2$ nanoparticles had excellent photo-responsive properties; the potential difference reached 0.45 V with the photo-responsive time just 0.6 seconds. It has a greater cathode current at more positive potential compared to other $MoSe_2$ and $MoS_2$, and the efficiency of $H_2$ evolution is strongly influenced by illumination which suggested that $MoSe_2$ composite film had good photoelectrocatalysis properties for hydrogen evolution. Besides, for both dark and illumination $MoSe_2$ films exhibited extremely high stability in acidic solution as the HER catalytic activity shows no degradation after 100 cycles for two hours. All results indicated that $MoSe_2$-RGO/PI composite film had potential to be a better catalyst for HER.

Lianbo et al. (2015) reported cobalt oxide porous (CoP) nanoparticles uniformly deposited on RGO sheets prepared through a facile two-step approach and the composite was investigated as an electrocatalyst for the HER. They found that the CoP/RGO composite shows an enhanced catalytic activity with a smaller Tafel slope (104.8 mV per decade), a much larger exchange current density ($4.0 \times 10^{-5}$ A $cm^{-2}$) and lower estimated HER activation energy (41.4 kJ $mol^{-1}$) than pure CoP. Besides, the CoP/RGO composite exhibits good stability in acidic solution and it's HER catalytic activity shows no obvious degradation after 500 cycles.

Subramanya et al. (2015) reported the facile preparation of highly porous Co-Ni-graphene composite electrodes by electrodeposition for electrocatalytic applications. The incorporation of graphene into the Co-Ni matrix enhanced the catalyst's activity for the HER in an alkaline solution.

Subramanya et al. (2015) developed efficient electrode for hydrogen production by embedding graphene in the Fe-Ni matrix via room temperature electrodeposition. Addition of graphene to electrolyte bath resulted in porous 3D projections of nano-sized spheres of Fe-Ni on the surface of graphene, which effectively increased the electrochemically active surface area. The addition of graphene favored the deposition of metallic nickel, which accelerated the rate determining proton discharge reaction.

Kasinath et al. (2016) reported excellent electrocatalytic performance of RGO based $Mo_2C$ composites in water splitting. It showed high catalytic current density of ~125 mA $cm^{-2}$ (at 400 mV vs. RHE) and high stability of the RGO based composite in long run HER (> 15 hours chronopotentiametry studies and > 1200 LSV cycles) in acidic medium. The role of graphene in the composite was critical for its electrocatalytic efficiency and very high catalytic activity was possible with low onset potential (59 mV) following Volmer-Heyrovsky reaction mechanism.

Long et al. (2016) developed CoP/RGO layered composites as bifunctional catalysts for overall water splitting, via a GO-templated metal organic framework growth and subsequent pyrolysis and phosphating process. The resultant CoP/RGO-400 nanocomposite exhibits superior HER catalytic performance in acid solution. Moreover, it was able to behave as an electrocatalyst for both the HER and OER, in alkaline solution with great efficiency and durability. Significantly, CoP/RGO-400 can be directly employed as a catalyst for both electrodes to afford efficient $H_2$ and $O_2$ generation in a single electrolyzer, making it a promising overall water splitting catalyst.

### 1.4.8 Recent Research Trends in Graphene Based Nanocomposites as Catalysts

A brief survey of latest advancements in the field of graphene based nanocomposites for catalytic applications is provided here. The information is given in the format, Catalysts; Type of Study; Synthesis Method; Observations; Reference.

$CuFe_2O_4$/GO; Photocatalysis;Hydrothermal method; Source: Visible-light irradiation (450 W Xenon lamp, cut-off filter, $\lambda \geqslant 420$ nm), Model Pollutants: AO7,

Achievements: Completely degraded within 60 minutes and Stability: Does not show obvious loss after five recycles (Chen et al. 2016).

Molecular imprinted polymer-$TiO_2$/graphene; Photocatalysis; Solvothermal synthesis method; Source: Visible light irradiation (300 W Xenon lamp with a 400 nm cut-off filter), Model Pollutant: Bisphenol A, Achievements: Optimization such as pH of 6.0, catalyst concentration of 1.0 g/L, Bisphenol A concentration of 4 mg/L and degradation efficiency of 67.6 % in 180 minutes (Lai et al. 2016).

Bismuth vanadium oxide-graphene sheets; Photocatalysis; Solvothermal method; Source: Visible light irradiation (350 W Xenon lamp with a 420 nm cut-off filter), Model Pollutant: (i) NO, Achievements: 60 % degradation in 90 minutes, (ii)RhB, Achievements: 94 % degradation in 90 minutes (Ou et al. 2016).

Graphene-like hexagonal boron nitride/$Ag_3PO_4$; Photocatalysis; Simple deposition-precipitation process; Source: Visible-light irradiation (500 W Xenon arc lamp with a 420 nm optical filter), Model Pollutants: MB, Achievements: Completely degraded within 50 minutes and stability upto 5 cycles (Zhu et al. 2016).

Graphene-$Bi_8La_{10}O_{27}$-Zeolite; Photocatalysis; Microwave assisted synthesis; Source: Visible light irradiation (8 W, $\lambda > 420$ nm), Model Pollutant: (i) RhB, Achievements: Rate constant (k), $5.71 \times 10^{-2}$ $min^{-1}$, (ii) MB, Achievements: Rate constant (k), $4.74 \times 10^{-2}$ $min^{-1}$, (iii) Texbrite, Achievements: Rate constant (k), $6.94 \times 10^{-2}$ $min^{-1}$ and Stability: Excellent stability even after 4 successive cycles (Areerob et al. 2017).

Ni@$Ni(OH)_2$-Pd-RGO interfaces; HER; Hydrothermal synthesis; Overpotential: 76 mV at 10 $mA/cm^2$, Tafel slope: 70 mV/dec and Stability: Excellent stability (1000 cycles) for the HER in alkaline environment (Deng et al. 2017).

Pd/Au@g-$C_3N_4$-N; Reduction of 4-NP to 4-AP; Facile one-pot deposition reduction method; Achievements: Complete conversion within 4.5 minutes, Optimization: Pd/Au@g-$C_3N_4$-N (1:1) with the highest catalytic activity and Rate constant, k: 0.7907 $min^{-1}$ (Fang et al. 2017).

W-Mo-O/RGO; HER; Simple one step hydrothermal method; Achievements: Showed excellent electrocatalytic activity for HER (W-Mo-O/RGO), Onset potential: 50 mV, Tafel slope: 46 mV/dec and Stability: Good durability up to 2000 cycles in acidic medium (Imran et al. 2017).

$Ag_2S$/RGO; Reduction of 4-NP to 4-AP; Facile hydrothermal sulfurization method; Achievements: Reduction completed in 5 minutes and Rate constant, k: $Ag_2S$/RGO (0.55 $min^{-1}$) which was almost 13-fold higher than that of Ag/RGO (0.041 $min^{-1}$) (Lang and Yu 2017).

RGO-Ni-Au; Reduction of 4-NP to 4-AP; In-situ co-reduction and surfactant-free method; Achievements: Complete conversion in only 4.5 minutes, Optimization: RGO-Ni-Au-6h with the highest catalytic activity, Rate constant, k: 11.03 x $10^{-3}$ $s^{-1}$, Catalytic activity parameter: 36.77 $s^{-1}g^{-1}$ and Stability: Recycled over 6 times without obvious performance decay or even morphology change (Li et al. 2017).

AuPd NCs/RGO; HER; Simple one-pot aqueous method; Onset potential: $E_{onset}$ for AuPd NCs/RGO (-33 mV) was close to Pt/C (-28 mV), Overpotential: 55 mV was required for AuPd NCs/RGO at the fixed current density of 10 mA/$cm^2$, which is comparable to Pt/C (41 mV), Tafel slope: 40 mV/dec for AuPd NCs/RGO and 31 mV/dec for Pt/C and Stability: AuPd NCs/RGO only show a slight decrease in current density after 5000 cycles, which shows excellent stability (Lin et al. 2017).

$CoS_2$/$MoS_2$/RGO; HER; One-pot hydrothermal method; Onset overpotential: 80 mV (vs. RHE), Tafel slope: 56 mV/dec, Exchange current density: 11.4 A/$cm^2$ and Stability: Good durability up to 4000 cycles (Liu et al. 2017).

(0D/3D) $MoS_2$/P-rGO; HER; Hydrothermal method; Overpotential: only ~150 mV vs. RHE, Tafel slope: ~56 mV/dec and Stability: No deactivation observed even after 1000 cycles (Liu et al. 2017).

Tungsten carbide/Co@Nitrogen doped CNTs; HER; Thermal annealing method; Low Onset potential: ~18 mV, Overpotential, $\eta_{10}$: 98 mV at 10 mA/$cm^2$, Tafel slope: 52 mV/dec, Exchange current density ($j_o$): 0.103 mA/$cm^2$, Stability: About 97 % of the catalytic current was maintained after 45000 seconds (12.5 hours)

testing, and a very small enhancement of ~15 mV was found at $\eta_{10}$ after 2000 cycles and shows good stability (Ma et al. 2017).

Ag/RGO/$Fe_3O_4$; Reduction of 4-NP to 4-AP; Biosynthesis method using Lotus garcinii leaf extract; Achievements: Reduction reaction was completed in 180 seconds at room temperature (Maham et al. 2017).

1T-$MoS_2$/RGO; Reduction of 4-NP to 4-AP; Novel self-assemble method at low temperature; Achievements: Reduction completed in less than 4 minutes, Rate constant, k: 0.72718 $min^{-1}$ and Stability: Reused for 3 consecutive catalytic cycles (Meng et al. 2017).

$Cu_2O$-$TiO_2$/g-$C_3N_4$; Photocatalysis; Hydrothermal method; Source: Visible-light irradiation (300 W Xenon lamp equipped with a 420 nm cut-off filter), Model Pollutants: Dyes in the presence of $H_2O_2$, (i) RhB, Achievements: Fully discolored within 3 minutes, (ii) MB, Achievements: Fully discolored within 10 minutes and (iii) Methyl orange, Achievements: Fully discolored within 15 minutes (Min et al. 2017).

3D $WS_2$/graphene/Ni binder-free electrode; HER; Thermal decomposition method; Overpotential: 87 mV at 10 $mA/cm^2$, Current density: 119.1 $mA/cm^2$, Overpotential: 250 mV and Stability: Decreases from 119.1 to 110.1 $mA/cm^2$ even after 3000 cycles (Qi et al. 2017).

Ag@MWCNTs-polymer composite; Reduction of 4-NP to 4-AP; Simple ultrasonic-treated method; Achievements: Reduction completed in 5 minutes, Rate constant, k: $7.88 \times 10^{-3}$ $s^{-1}$, Catalytic activity parameter: 11.64 $s^{-1}g^{-1}$ and Stability: Reused for 5 consecutive catalytic cycles (Saad et al. 2017).

NiO/graphene; Photocatalysis; Sublimation method; Model Pollutant: MO dye, (i) Source: UV (OSRAM HTC 400 W, $\lambda$ = 315-400 nm), Achievements: 90.3 % degradation after 75 minutes (ii) Source: Visible light (300 W Xenon lamp with a 420 nm cut-off filter, $\lambda >$ 420 nm), Achievements: 78 % degradation after 180 minutes (Soofivand and Masoud 2017).

RGO-$TiO_2$-CdS; Photocatalysis; Hydrothermal method; Source: Visible-light (300 W Xenon lamp with a 400 nm cut-off filter), (i) Model Pollutant: p-chlorophenol, Achievements: 65.3 % degradation in 60 minutes and (ii) Model Pollutant: MB, Achievements: 90.3 % degradation in 60 minutes (Tian et al. 2017).

Pd-gum arabic/RGO; Reduction of 4-NP to 4-AP; Facile approach for in-situ synthesis; Achievements: Reduction completed in 5 minutes, Rate constant, k: 0.1199 $min^{-1}$ and Stability: 10 consecutive catalytic cycles without any apparent loss of its activity (Vilian et al. 2017).

NiSe-RGO-PI/CNT film; HER; Green electrodeposition method; Low overpotential: 270 mV, Tafel slope: 61 mV/decand Stability: 500 cycles (Wang et al. 2017).

MoP-RGO; HER; Solvothermal followed by high temperature treatment method; Optimization: MoP-RGO nanocomposite obtained at 900 °C exhibits excellent electrocatalytic activity for HER, Overpotentials: 117 mV and 150 mV at a current density of 10 $mA/cm^2$ in acid and alkaline medium and Stability: No deactivation observed even after 5000 cycles (Wu et al. 2017).

NiFe-NGT composites; HER; Thermal annealing method; Optimization: NiFe-NGT-800 composites exhibit excellent catalytic activity for HER, Low Onset potential: 70.5 mV, Small Tafel slope: 63.4 mV per decade, Overpotential, η: 150 mV and Stability: Slight decrease from 18 to 10 $mA/cm^2$ after 3000 cycles in acidic solution (Wu et al. 2017).

$MoS_2$/RGO; HER; Facile hydrothermal method; Achievements: $MoS_2$/RGO hybrid nanostructures exhibited 3D leaf-like morphology, excellent electrocatalytic activities of HER, Low overpotential: 105 mV, Tafel slope: 51 mV/dec, Exchange current density ($j_o$): $3.28 \times 10^{-5}$ $A/cm^2$ and Stability: 2000 cycles (Xiaobing et al. 2017).

$Ag_3PO_4$/graphene; Photocatalysis;Hydrothermal method; Source: Visible light (Tungsten halogen lamp with 500 W output power, with cut-off filter < 420 nm), Model Pollutant: Organic dyes, Indigo dye heterocyclic dye, Azo dye and

Anthraquinone dye (10 mg/L), Achievements: ~100 % degradation within 7 hours (Xu et al. 2017).

Nitrogen-doped graphene quantum dots-BiOI/$MnNb_2O_6$; Photocatalysis; Hydrothermal method; Source: Visible light irradiation (250 W Xenon lamp with cut-off filter < 420 nm), Model Pollutant: Antibiotics, (i) Tetracycline, Achievements: 87.2 % degradation within 60 minutes, (ii) Oxytetracyline, Achievements: 72.1 % degradation within 120 minutes, (iii) Ciprofloxacin, Achievements: 57.4 % degradation within 120 minutes and (iv) Doxycycline, Achievements: 64.7 % degradation within 120 minutes (Yan et al. 2017).

Co@carbon nitride; Reduction of 4-NP to 4-AP; Simple direct carbonization method; Achievements: Complete conversion in 40 seconds, Optimization: Co@N-C 700 with the highest catalytic activity and Stability: Successfully reducing 100 % 4-NP to 4-AP even after 6 cycles (Yusran et al. 2017).

Porous Bi@Cs; Reduction of 4-NP to 4-AP; Hydrothermal method; Achievements: Reduction completed in 140 seconds, Rate constant, k: 0.02429 $s^{-1}$/0.1 mg and 242.9 $s^{-1}$ $g^{-1}$, which is higher than previously reported values for Ag-C (3.38 $s^{-1}$ $g^{-1}$) and Au-$Fe_3O_4$ (27.6 $s^{-1}$ $g^{-1}$) (Zhou et al. 2017).

Reduced graphene-$BiFeO_3$; Photocatalysis; Hydrothermal method; Source: 300 W UV-visible lamp (OSRAM, Germany, $\lambda$ > 400 nm), Model Pollutant: $NH_3$, Achievements: 91.20 % degradation of $NH_3$ solution (50 mg/L) at pH 11 and high stability after 7 reaction cycles (Zou et al. 2017).

Co/carbon nitride; Reduction of 4-NP to 4-AP; Facile thermal treatment method; Achievements: Completely reduced 20 mg/L of p-nitrophenol within 7.5 minutes (Zubair et al. 2017).

## 1.5 PROBLEM IDENTIFICATION

Besides established synthesis methods, finding a simple and cost-effective route to synthesize nanocrystalline $AWO_4$ is still a challenge. Microwave irradiation has been applied for fast synthesis of inorganic solids and organic synthetic reactions

(Gedye et al. 1986). As it causes internal heating of the material even at lower temperature and shorter duration, it is a more efficient method than conventional one. It is an inexpensive, facile and fast method for the preparation of nanocrystalline sample with a unique property. Several studies on the microwave-assisted synthesis have revealed that the kinetics of the organic and inorganic chemical reactions can be accelerated significantly by microwave radiations. In view of this, microwave irradiation assisted technique has been employed to synthesize selected divalent metal tungstates that crystallize either with the scheelite or wolframite structure ($AWO_4$, A = Fe, Co, Ni, Zn, Ba). Only very few studies are available about $AWO_4$ for catalytic applications.

Photocatalysis has been proven as a promising technique for purification and treatment of various kinds of pollutants (Herrmann 1999). However, the high recombination rates of photoinduced electron-hole pairs and low quantum efficiency have hindered the practical application of $AWO_4$. There are several methods to improve the photocatalytic activity of $AWO_4$ such as doping with carbon, metal ions, coupling with other semiconductors and so on (Li et al. 2017).

In the past several years, carbon materials such as graphene, nitrogen doped graphene, g-$C_3N_4$ has drawn much attention due to its remarkable properties such as large surface area and high carrier mobility (Allen et al. 2009). Therefore, it can serve as an ideal support material for semiconductor catalysts, which would show improved photocatalytic activity for the following two reasons. Firstly, a hybrid of graphene-semiconductor would show enhanced adsorption activity. Secondly, graphene can help to reduce the recombination rate of photogenerated electron-hole pairs. Compared to single-phased catalysts, the advantages of heterostructures include not only the extended light responsive range, but also the enhanced photogenerated charge carrier separation abilities (Li et al. 2009, Liu et al. 2014). To obtain the desirable heterostructured catalysts, another important aspect of coupled semiconductor system is to extend the photo response of large band gap semiconductor to visible region by coupling it with a short band gap semiconductor i.e., matching of energy levels between the two components so as to promote charge carrier separation. In other words, the CB minimum of the narrow band gap

semiconductor should be higher than that of the other semiconductor component with larger band gap (Wang et al. 2015).

Catalysis has revolutionized the field of manufacturing of chemicals. One such manufacturing process is reduction of organic molecules by catalytic hydrogenation. Nitrophenols are considered to be amongst the most prevalent organic pollutants in waste water generated from agricultural and industrial sources (Pradhan et al. 2001, Ghosh et al. 2004). In recent times, based on the requirements such as greener route and safer operation, environmentally friendly catalytic conversion routes have been developed for the conversion of 4-NP to 4-AP in aqueous medium under mild conditions. One such route by which 4-AP is obtained involves direct hydrogenation of 4-NP using $NaBH_4$, which is a mild agent and the reaction can be conducted in an aqueous medium (Rode et al. 1999, Yang et al. 2014, Woo et al. 2015).

Tremendous research has been conducted on development of electrocatalysts for application in fuel cells (Guo et al. 2006, Debe 2012). Although Pt can be used as electro-catalyst, it has various disadvantages which limit its application (Sun et al. 2011, Huang et al. 2012). For instance, Pt is a precious metal and it has limited availability. Its high cost narrowed the interest of using it as a catalyst. In addition, during electrocatalysis, Pt may disrupt the reaction due to poisoning of intermediate compounds (Shao et al. 2008, Ge et al. 2014). Therefore, the development of ecofriendly materials to overcome these problems is of great importance and a challenge in current scenario.

## 1.6 SCOPE AND OBJECTIVES OF THE WORK

### 1.6.1 Scope

The development of newer eco-friendly methods of destroying organic pollutants from air and wastewater streams has become an imperative task for the world. Also, the energy demand is growing tremendously fast, because of the rapid increase in the population as well as the increase in the per capita energy consumption. The technology of semiconductor based photocatalytic degradation, reduction of organic pollutants and electrocatalytic production of HER can be considered as one of the most important approaches to solve both the environment

pollution and world energy crisis. The benefits, which arise from the application of semiconductor nanomaterials for remediation would be: more rapid or cost-effective cleanup of wastes and its environmental friendly features.

Recently many research groups are working on the nanocomposite materials particularly graphene based composite materials for energy and environmental applications. However, limited information is available on the graphene based metal tungstate nanocomposite materials. Furthermore, multiple catalytic activities of nanocomposite materials towards photochemical reactions, reduction and electrochemical processes have not been investigated. Also, there is a need to develop a process to treat the non-biodegradable compounds present in industrial wastewater which are not treated by conventional treatment processes effectively and also to produce hydrogen energy from water electrolysis using electrocatalytic methods. In order to improve the economy of the process, it is also required to increase the efficiency of the catalyst and hence there is a great need for development of high performance catalysts. Accordingly, this thesis work has been carried out with the following objectives:

### 1.6.2 Objectives

- To synthesize graphene - transition metal tungstate nanocomposites.
- To characterize the synthesized graphene based transition metal tungstate nanocomposites.
- To investigate catalytic property of the prepared nanocomposites towards, the photodegradation of dyes under visible light irradiation, reduction of 4-NP to 4-AP in aqueous media and electrolytic HER in alkaline media.

## 1.7 THESIS WORK

The present thesis reports the successful synthesis of five different kinds of novel graphene-metal tungstate based nanocomposites namely, NRGO/$ZnWO_4$/$Fe_3O_4$, NRGO/$NiWO_4$/ZnO, NRGO/$CoWO_4$/$Fe_2O_3$, NRGO/$FeWO_4$/$Fe_3O_4$, and NRGO/$BaWO_4$/g-$C_3N_4$ using facile microwave irradiation method. All the synthesized nanocomposites were carefully characterized for their elemental

composition, structural, morphological and optical properties by employing appropriate techniques such as X-Ray Diffraction (XRD), Scanning Electron Microscopy (SEM), Field Emission Scanning Electron Microscopy (FESEM), Transmission Electron Microscopy (TEM), High Resolution Transmission Electron Microscopy (HRTEM), Brunauer-Emmett-Teller (BET) Method,Raman Spectroscopy, Fourier Transmission Infra-Red (FTIR) Spectroscopy, Ultra Violet - Visible (UV-Vis) Spectroscopy, X-ray Photoelectron Spectroscopy (XPS), Photo-Luminescence (PL) Spectroscopy and Diffuse Reflectance Spectroscopy (DRS). Thereafter, each nanocomposite was investigated for its catalytic efficiency towards, (i) The photodegradation of MB dye under the visible light irradiation, (ii) The reduction of 4-NP to 4-AP in the presence of $NaBH_4$ in aqueous media and (iii) The electrolytic HER in alkaline media.

The contents presented in the thesis have been broadly divided into seven chapters with several sections in each chapter and the outline of this thesis work is shown in Figure 1.5.

**Chapter 1** gives a brief introduction to the basic aspects of the study undertaken. It also gives a brief overview of the relevant works in the literature which focus upon graphene, metal tungstate, metal tungstate-based nanocomposites, graphene-based nanocomposites, their synthesis methods and catalytic applications. Scope and objectives of the present research work have been given at the end.

**Chapter 2** presents and discusses the synthesis of novel NRGO/$ZnWO_4$/$Fe_3O_4$ nanocomposite as an efficient catalytic material for energy and environmental applications.

**Chapter 3** deals with the microwave synthesis of NRGO/$NiWO_4$/ZnO ternary nanocomposite as an efficient catalyst for photodegradation of MB, reduction of 4-NP and electrolytic HER.

**Chapter 4** provides details of synthesis, characterization and catalytic applications of novel NRGO/$CoWO_4$/$Fe_2O_3$ nanocomposite.

**Chapter 5** describes the synthesis, characterization and studies on catalytic performance of NRGO/$FeWO_4$/$Fe_3O_4$ ternary nanocomposite in environmental and energy applications.

**Chapter 6** gives a descriptive report on the synthesis, characterization and multifunctional catalytic performance of novel NRGO/$BaWO_4$/g-$C_3N_4$ nanocomposite.

**Chapter 7** outlines the summary of the work presented in the thesis along with important conclusions drawn from the study. The results of experimental investigation presented in the thesis are also compared with reported literatures. Scope for further research has also been included in this chapter.

References used have been listed at the end.

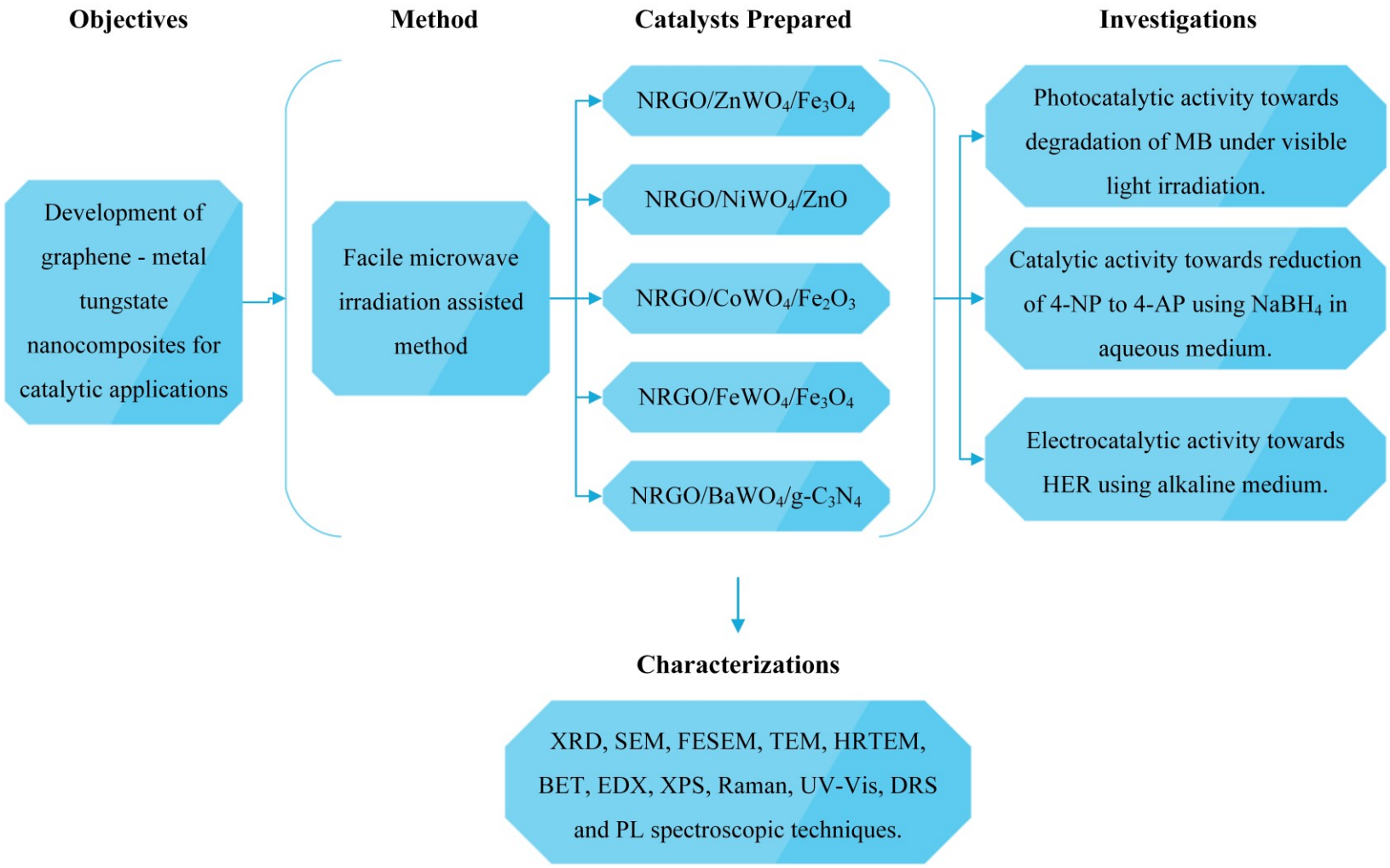


**Figure 1.5** The outline of this thesis work.

# CHAPTER - 2

## SYNTHESIS OF NOVEL NRGO/$ZnWO_4$/$Fe_3O_4$ NANOCOMPOSITE AS AN EFFICIENT CATALYTIC MATERIAL FOR ENERGY AND ENVIRONMENTAL APPLICATIONS

***Chapter 2*** *presents and discusses the synthesis of novel NRGO/$ZnWO_4$/$Fe_3O_4$ nanocomposite as an efficient catalytic material for energy and environmental applications.*

## 2.1 INTRODUCTION

The toxic organic and inorganic wastes from industries are the major contaminants of the environment and poses a serious problem in the current scenario (Kuo 1992, Patel et al. 2014). Photocatalysis is an excellent method for the degradation of highly toxic hazardous pollutants present in waste water (Suslick 1989, Zhang et al. 2007). Although it is a less expensive process compared to other advanced oxidation processes, the overall cost can be further reduced by optimizing the operating environment. Hence, photocatalysis can be practically implemented along with the combination of heterogeneous catalyst and made more cost effective (Pera-Titus et al. 2004, Madhavan et al. 2010). Semiconductor photocatalytic materials are a green tool for the decomposition of organic pollutants into non-hazardous compounds under light irradiation. It is well known that $TiO_2$ is an excellent photocatalytic material due to its high activity and stability, but it is only active under UV light irradiation because of its wide band gap. Therefore, there is a need to develop novel visible light based photocatalytic materials.

In recent years, graphene based nanocomposites have attracted attention towards photocatalytic process due to their excellent sensitivity, durability and stability. Several research groups are working on graphene-based nanocomposite materials like GO-polymer, GO-metal, GO-semiconductor, GO-metal oxide and GO-magnetic material composites for various engineering applications due to its high surface area and high chemical stability (Allen et al. 2009). Further, graphene has also been used profusely as an active supporting component in the preparation of nanocomposite materials for adsorption, separation and degradation of organic dyes from the industrial waste water (Li et al. 2008, Sun et al. 2011). The incorporation of electron-rich nitrogen atoms into the graphene materials promotes the interaction between neighboring carbons and electrons, providing a superior heteroatom-doped catalyst. NRGO increases the transfer rate of electron from the conduction band of the

semiconductor whereas, the doping of nitrogen into semiconductors creates an additional donor level above the valence band of semiconductors thereby reducing the energy requirement for the excitation of electron from VB to CB of semiconductor materials. The semiconductor materials supported on nitrogen doped graphene show significant enhancement in their catalytic performance (Li et al. 2009).

Moreover, to improve the photocatalytic activity of materials, many research groups are focusing on the combination of metal oxides and tungstates to transfer the photoinduced electrons. The combination of graphene and metal tungstates/oxides are believed to increase the photoelectron transfer rate and enhance photocatalytic activity. Several reports are available in which the transition metal oxides and carbon-based metal oxide nanocomposites are used as a catalyst material for water purification (Pal et al. 2007, Guo et al. 2011, Pradhan et al. 2011, Xiang and Yu 2013). Generally, metal tungstates ($BaWO_4$, $NiWO_4$, $Bi_2WO_6$, $ZnWO_4$) are important class of inorganic materials which can be used in many applications in various fields like photoanodes, luminescent materials, gas-sensing, optical fibers, ceramics and photocatalysts (Cavalli et al. 2008, Shi et al. 2010, He et al. 2011). There are several methods to synthesize metal tungstates such as sol-gel, hydrothermal synthesis, solid state methods, ultrasonic irradiation, microwave irradiation and co-precipitation (Yang et al. 2008, Yu and Jimmy 2009, Kalinko and Kuzmin 2011).

Additionally, the catalytic activity for the reduction of 4-NP on metal oxide-graphene in the presence of $NaBH_4$ has been mostly studied in the manufacture of 4-AP, which is a well-known intermediate in the synthesis of antipyretic and analgesic drugs (Vaidya et al. 2003, Meng et al. 2015). 4-AP is widely used as an anticorrosion-lubricant, corrosion inhibitor, hair-dyeing agent and photographic developer (Rode et al. 1999, Woo et al. 2015).

Further, electrocatalysts are crucial assets in electrolysis and developing a cost effective and efficient electrocatalyst materials is one of the most giant demanding situations in the research development of polymer electrolyte membrane fuel cells (Debe 2012). The most effective environmental friendly method of $H_2$ production is known to be via electrolysis of water and has been named as HER (Zeng and Zhang

2010). Always Pt-based catalysts are regarded as the best electrocatalysts, despite the fact that the excessive cost and availability limit numerous utilities of Pt-based electrocatalysts in electrolysis involving HER (Shao et al. 2008, Ge et al. 2014). For that reason, several studies are dedicated to developing non-precious metal/metal oxide/metal complexes based electrocatalytic materials at low cost and exceedingly energetic electrode material for HER (Wang et al. 2012).

However, there are only a few reports on graphene based ternary nanocomposites as catalysts with high activity towards photodegradation of dyes, reduction of aromatic nitro compounds and electrolytic HER (Subramanya et al. 2015, Sun et al. 2015, Woo et al. 2015). In view of this, the synthesis of novel NRGO/$ZnWO_4$/$Fe_3O_4$ nanocomposites by microwave irradiation method and characterization of the as prepared samples by XRD, SEM, FESEM, TEM, HRTEM, XPS, EDX, Raman, PL and UV-Vis spectroscopic techniques is reported here. The prepared nanocomposites have been studied as catalysts for photodegradation of MB dye under visible light irradiation, conversion of 4-NP to 4-AP in the presence of $NaBH_4$ and electrolytic HER in alkaline medium.

## 2.2 EXPERIMENTAL

### 2.2.1 Materials and Methods

All the reagents and chemicals were obtained from Sigma-Aldrich and were utilized without additional purification. Natural graphite, Iron acetate and Nafion was procured from Sigma Aldrich and zinc acetate, Sodium tungstate, potassium permanganate, ammonia, sulfuric acid, hydrogen peroxide, hydrochloric acid and ethanol were purchased from Merck Chemical Ltd. All experimental solutions were prepared using deionized water (18 MΩ cm).

### 2.2.2 Synthesis of GO

GO was synthesized from graphite flake by using modified Hummers method (Hummers and Offeman 1958). Typically, 1.0 g of graphite flakes were mixed with 100 mL of conc. $H_2SO_4$ in a 400 mL beaker and stirred in an ice bath. Under vigorous stirring, 6.0 g of $KMnO_4$ was added slowly with the temperature of the reaction

mixture being maintained below 20 °C. Then, the reaction mixture was continuously stirred for another 12 hours at room temperature, followed by addition of 100 mL DI water. The temperature of the reaction mixture was increased slowly to 98 °C and maintained for 2 hours and then cooled to room temperature. When the temperature of the reaction mixture was dropped to 75 °C, 50 mL of DI water was added followed by 5 mL of $H_2O_2$. Further, the reaction mixture was cooled down to room temperature. The obtained GO solution was washed, centrifuged with 5 times of 10 % HCl and DI water several times. Finally, the sample was freeze-dried to get GO powder.

### 2.2.3 Synthesis of $ZnWO_4$

$ZnWO_4$ was prepared by the microwave irradiation method. In a typical synthesis, 0.05 M of zinc acetate was dissolved in 50 mL of DI water to form a solution. Then 50 mL of 0.05 M sodium tungstate solution was added slowly to the above solution under stirring for about 2 hours. Then, the mixture was treated with microwave irradiation at 350 W for 10 minutes and then the mixture was cooled to room temperature naturally. The white precipitate was collected and centrifuged with DI water and 10 % ethanol several times. Finally, the sample was dried in a vacuum oven at 80 °C for 12 hours.

### 2.2.4 Synthesis of $Fe_3O_4$

$Fe_3O_4$ was prepared by the microwave irradiation method. Typically, 0.01 M of iron acetate was dissolved in 50 mL of ethanol and water mixture and added 10 mL of ammonia solution under stirring for about 30 minutes. After that the reaction mixture was treated with microwave irradiation at 350 W for 10 minutes. The black precipitate was collected and centrifuged with DI water and 10 % ethanol several times. Finally, the sample was dried in a vacuum oven at 80 $^oC$ for 12 hours.

### 2.2.5 Synthesis of RGO/$ZnWO_4$ Nanocomposites

x-RGO/$ZnWO_4$ (x = 1, 2, 3 and 4 wt.% GO) nanocomposite was synthesized by a one-step microwave irradiation method. Briefly, 0.05 M of zinc acetate solution (50 mL) was slowly added to the dispersed GO solution obtained from the procedure above. Then 0.05 M sodium tungstate solution (50 mL) was slowly added to the

mixture under constant stirring for about 2 hours. Using ammonia, the pH of the solution was maintained at 9. Later, the mixture was treated with microwave irradiation at 350 W for 10 minutes and was allowed to cool down to room temperature naturally. The blackish precipitate obtained was centrifuged with DI water and 10 % ethanol several times. Finally, the sample was dried in a vacuum oven at 80 °C for 12 hours.

### 2.2.6 Synthesis of RGO/$Fe_3O_4$ Nanocomposites

RGO/$Fe_3O_4$ nanocomposite was synthesized by a one-step microwave irradiation method. Briefly, 0.01 M of iron acetate solution (50 mL) was slowly added to the calculated amount of dispersed GO solution obtained from the procedure above. Then 10 mL of ammonia solution was added under constant stirring for about 2 hours. Later, the mixture was treated with microwave irradiation at 350 W for 10 minutes and was allowed to cool down to room temperature naturally. The blackish precipitate was collected and centrifuged with DI water and 10 % ethanol several times. Finally, the sample was dried in a vacuum oven at 80 °C for 12 hours.

### 2.2.7 Synthesis of RGO/$ZnWO_4$/$Fe_3O_4$ Nanocomposites

RGO/$ZnWO_4$/$Fe_3O_4$(y) (y = 0.005 M, 0.01 M and 0.02 M of precursor solution) nanocomposites were also synthesized by one-step microwave irradiation method. In a typical experiment, to an optimized amount of RGO/$ZnWO_4$ nanocomposite solution, 50 mL of (0.005 M, 0.01 M and 0.02 M) iron acetate in ethanol and water mixture was added. To this 10 mL of ammonia was added and the reaction mixture was stirred for about 30 minutes before subjecting it to 350 W microwave radiation for 10 minutes. The obtained precipitate was washed with water and ethanol and dried in vacuum oven at 80 °C for 12 hours.

### 2.2.8 Synthesis of NRGO/$ZnWO_4$/$Fe_3O_4$ Nanocomposites

NRGO/$ZnWO_4$/$Fe_3O_4$ ternary nanocomposites were synthesized by a one-step microwave irradiation method similar to the one explained above for the synthesis of RGO/$ZnWO_4$/$Fe_3O_4$ nanocomposites but with a change that desired amount of GO solution was mixed with 1% urea first and then followed by other steps. Schematic

illustration of the synthesis procedure for NRGO/$ZnWO_4$/$Fe_3O_4$ nanocomposite as shown in Figure 2.1.

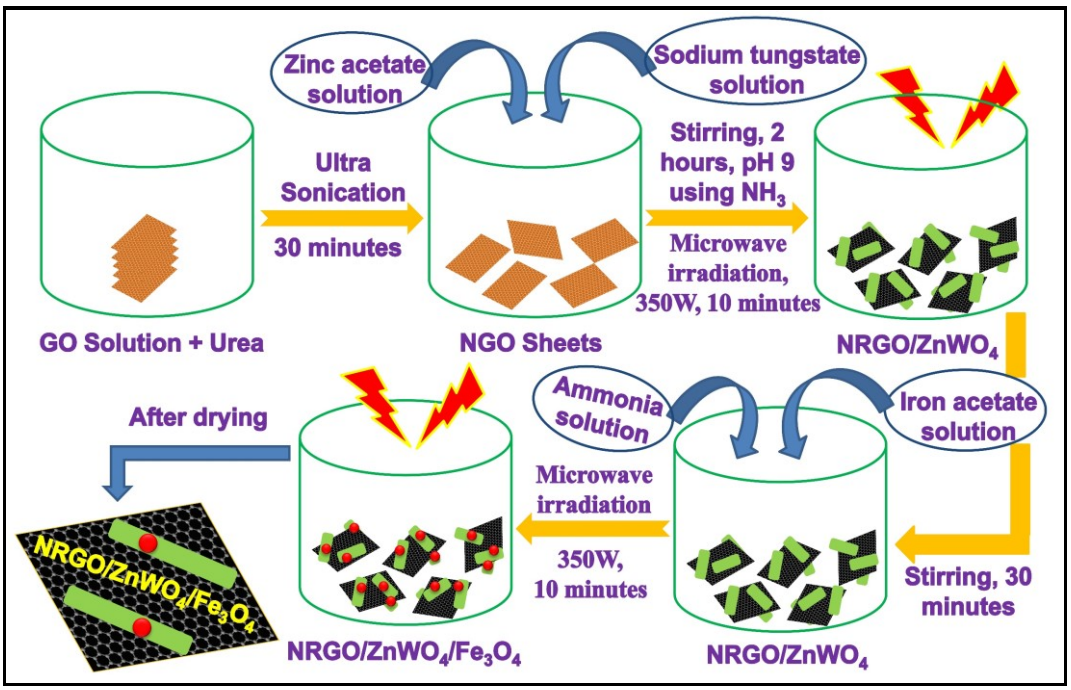


**Figure 2.1** Schematic illustration of the synthesis procedure for NRGO/$ZnWO_4$/$Fe_3O_4$ nanocomposite.

### 2.2.9 Characterization

The structural characterization of the synthesized nanocomposites was performed using X-ray diffractometer (Rigaku, Japan) using nickel filtered Cu $K_\alpha$ radiation at a scan rate of 1° per minute in the range of 5°-70°. The surface morphology was observed using SEM, (JEOL), FESEM, (Zeiss Ultra 55), TEM (Tecnai G20), HRTEM (Tecnai). Raman spectra were measured by laser Raman microscope (Renishaw Invia) with a 532 nm excitation laser from He-Ne source. The surface elemental analysis of the as-synthesized samples was performed by EDX (Zeiss Ultra 55) and XPS (Multilab 2000 Thermo scientific, UK) using Mg $K_\alpha$ X-ray with 200 W power as excitation source and 10 eV energy pass for data collection. Room temperature PL spectrum was measured with 380 nm excitation wavelength source (LS-55, Perkin Elmer Instruments). The absorbance spectra were measured on a UV-Vis spectrophotometer (Analytik Jena). The TOC concentration was measured using TOC analyzer (TOC-V CSN, Shimadzu, Japan).

### 2.2.10 Determination of Photocatalytic Activity

Determination of photocatalytic activity of MB dye was carried out using photoreactor under ambient atmospheric condition. The photoreactor was equipped with a 250 W Hg lamp fitted with a 400 nm cut-off filter, as a source for visible light irradiation. In these experiments, 200 mL of MB dye solution (10 mg/L) and photocatalyst (20 mg) was added into a 500 mL Pyrex glass beaker and stirred for about 30 minutes in dark to reach the adsorption-desorption equilibrium of the photocatalyst. Then the solution is exposed to the visible light irradiation. During photocatalytic studies, at regular time intervals, 4 mL of the reacted MB solution was taken out, centrifuged and the supernatant solution was used to measure the concentration of the MB solution through UV-Vis spectroscopic analysis at a wavelength of 664 nm. The percentage of degradation of dye was calculated as per equation (2.1).

$$\text{Percentage degradation of dye} = [(C_o - C) / C_o] \times 100 \quad \text{----------} \quad (2.1)$$

where, $C_o$ is the initial concentration and C is the concentration at a given interval time of the MB dye solution, respectively. Further, all the data presented are averages of three independent measurements.

The extent of mineralization of the dye was calculated by using TOC analysis. The TOC content was analyzed before start ($TOC_o$) and after the photocatalytic reaction for a specific interval of time ($TOC_t$). The percentage mineralization of the dye was calculated by using equation (2.2).

$$\text{Percentage Mineralization of the dye} = [(TOC_o - TOC_t) / TOC_o] \times 100 \quad \text{--------} \quad (2.2)$$

where, $TOC_o$ is the initial concentration and $TOC_t$ is the concentration at a given interval time, of the dye solution respectively. All the experiments were carried out following the same procedure for photocatalytic degradation mentioned above.

### 2.2.11 Catalytic Reduction of 4-NP to 4-AP

2.7 mL of 0.1 mM of 4-NP was mixed with 0.3 mL of 0.1 M $NaBH_4$ solution under constant magnetic stirring followed by addition of 0.1 mg of catalyst. The

reduction reaction of 4-NP was investigated using UV-Vis absorption spectroscopy in the range of 250 nm to 500 nm. The recovery of the catalyst was done as follows. Once the reaction was completed, the catalyst was separated by ultra-centrifugation. The catalyst was then thoroughly washed with 10 % ethanol solution followed by vacuum drying at 60 °C for 6 hours. The catalyst was then reused for subsequent cycles to study its stability and reusability.

### 2.2.12 Electrochemical Measurements

Typically, 2 mg of nanocomposite was mixed with 5 µL Nafion solution (5 wt.%) and the mixture was dispersed in 995 µL of the solution containing 497.5 µL of ethanol and 497.5 µL of DI water by sonicating for 20 minutes to reach the homogeneous ink status. Then 5 µL of the prepared ink (containing 10 µg of nanocomposite) was drop cast onto the surface of the glassy carbon electrode (GCE, 3 mm in diameter) and dried at room temperature to yield a catalyst loading of 0.1425 mg/cm$^2$.

The electrocatalytic activity of the nanocomposite towards HER was measured by standard three-electrode setup (IVIUM, Germany) using linear sweep voltammetry (LSV) technique with a scan rate of 5 mV/s in 0.1 M KOH. Saturated calomel electrode, Pt wire and GCE were employed as the reference, counter and working electrodes respectively. Chronopotentiometry was carried out at a constant current density of -10 mA/cm$^2$ to know the efficiency of the nanocomposite in HER. The electrolyte solution was purged with $N_2$ for 30 minutes to remove the oxygen completely before the HER experiment.

## 2.3 RESULTS AND DISCUSSION

### 2.3.1 Structural, Morphological and Elemental Studies of Graphite, GO, RGO and NRGO

The structural, morphological and elemental composition features of the graphite flakes, GO, RGO and NRGO sheets were determined from XRD, SEM and EDX spectroscopy techniques.

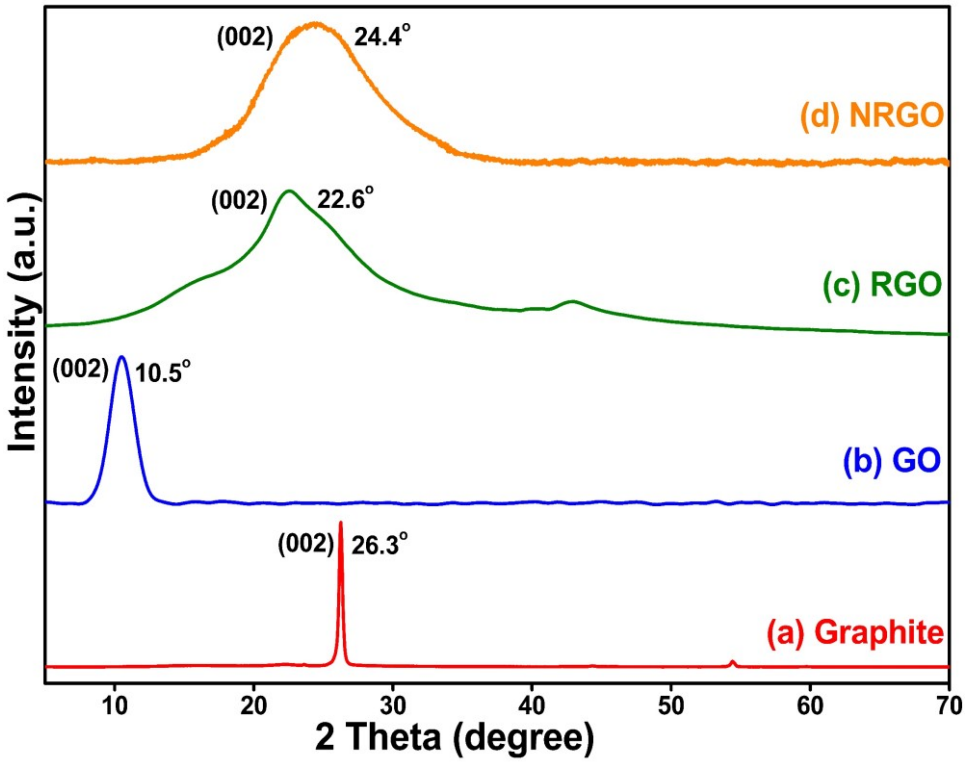


**Figure 2.2** XRD patterns of (a) Graphite, (b) GO, (c) RGO and (d) NRGO.

The XRD patterns of graphite, GO, RGO and NRGO are shown in Figure 2.2. The XRD pattern of graphite shows a sharp peak corresponding to the reflection from the (002) plane at 2θ=26.3° with a d-spacing of 0.339 nm. Whereas, GO exhibits a slightly broader peak at 10.5° with a d-spacing of 0.842 nm matching with the reflection from the (002) plane. These patterns are very similar to those reported previously for graphite and GO (Khandelwal et al. 2015). The XRD pattern of RGO is quite different from graphite and GO, and shows a slightly broader peak at 22.6° which corresponds to the reflection from the (002) plane with a d-spacing of 0.365 nm, suggesting the reduction of GO (Fu et al. 2016). Although the doping of nitrogen in NRGO is in a small amount, differences between RGO and NRGO can be clarified easily. In contrast to the XRD pattern of RGO, NRGO shows a relatively broader peak at 24.4° again corresponding to the reflection from the (002) plane with a d-spacing of 0.355 nm. The slight increase in the reflection angle for (002) plane in NRGO compared to that of RGO may be ascribed to the entry of nitrogen atoms into the crystal lattice of graphite causing the increased distance between the graphite layers (Szabo et al. 2006).

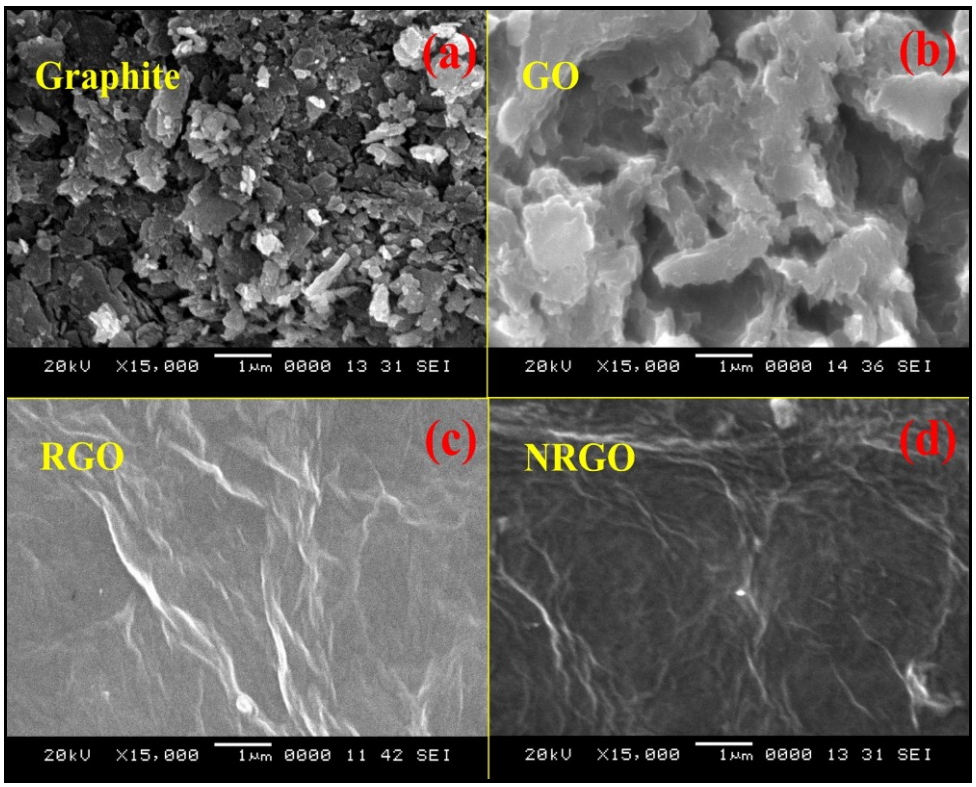


**Figure 2.3** SEM images of (a) Graphite, (b) GO, (c) RGO and (d) NRGO.

SEM image of the graphite flakes, GO, RGO and NRGO sheets are shown in Figure 2.3 Figure 2.3a shows the SEM image of the natural graphite flakes in which the sizes of the graphite particles are shown in the micrometer range. Figure 2.3b shows the GO, which clearly reflect the morphologies of graphite flakes before and after exfoliation. The graphite flakes presented a typical multilayer structure, whereas their stacking graphitic sheets were separated from one another after oxidation with the modified Hummer's method. However, after microwave reduction, it is highly notable in Figure 2.3c that the RGO, which consists of thin, crumpled sheets that are closely associated with each other. It is observed from SEM image of Figure 2.3d that the NRGO obtained in this work reveals more crumpled nanosheets, which is ascribed to the structural distortion caused by the doped nitrogen atoms. These morphological results also suggest that the oxidation, reduction and doping processes have not caused much damage to the graphitic structure of graphene.

The EDX spectra in Figure 2.4 show the presence of carbon, oxygen and nitrogen in the GO, RGO and NRGO sheets. EDX spectra of GO show the presence

of a large amount of oxygen due to the presence of oxygen containing functional groups in GO (Figure 2.4a). However, after the reduction of GO, the amount of oxygen containing functional groups present in RGO gets reduced and the observed oxygen peak is mainly due to the presence of carbon dioxide (Figure 2.4b). The EDX spectra in Figure 2.4c show the presence of C, N, and O. The N peak confirms the successful doping of N on the RGO sheets. Figure 2.4d shows the weight percentage of C, O and N in all the materials.

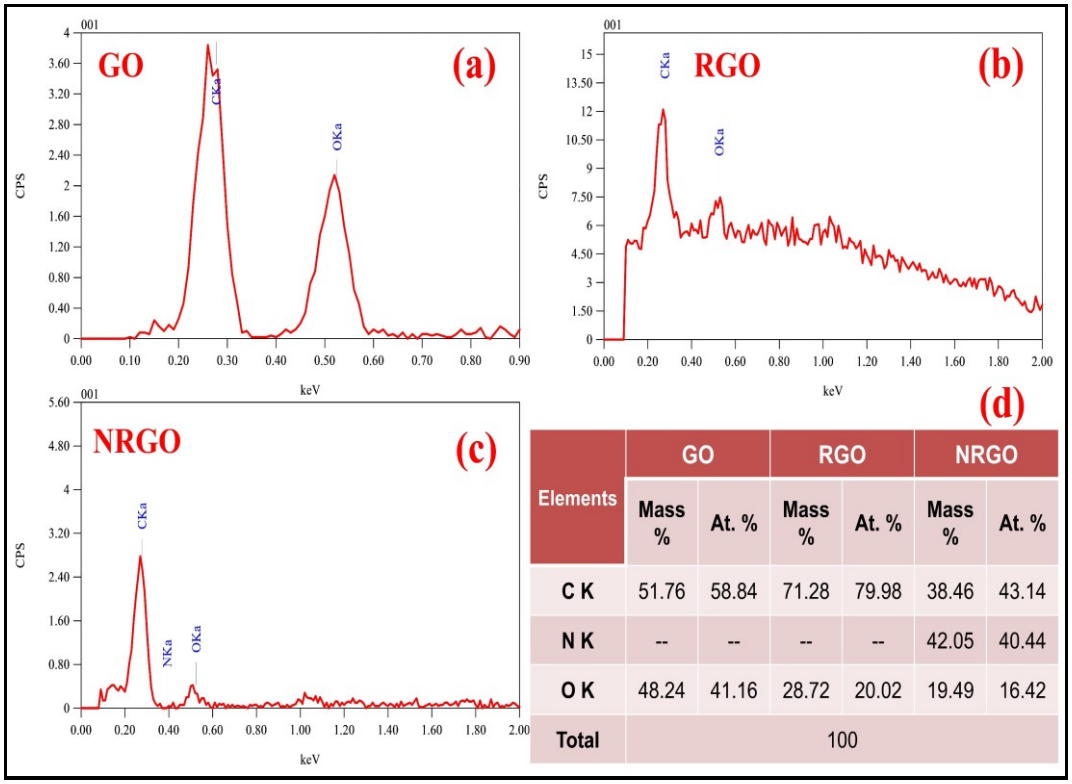


| Elements | GO | | RGO | | NRGO | |
|---|---|---|---|---|---|---|
| | Mass % | At. % | Mass % | At. % | Mass % | At. % |
| C K | 51.76 | 58.84 | 71.28 | 79.98 | 38.46 | 43.14 |
| N K | -- | -- | -- | -- | 42.05 | 40.44 |
| O K | 48.24 | 41.16 | 28.72 | 20.02 | 19.49 | 16.42 |
| Total | 100 | | | | | |

**Figure 2.4** EDX patterns (a-c) and elemental composition (d) of the GO, RGO and NRGO.

### 2.3.2 XRD Studies

Figure 2.5 shows the XRD patterns of the as-prepared RGO, $ZnWO_4$, $Fe_3O_4$, RGO/$ZnWO_4$/$Fe_3O_4$ and NRGO/$ZnWO_4$/$Fe_3O_4$. The diffraction peaks at 22.6° and 42.6° were ascribed to (002) and (100) planes of RGO sheets. The diffraction peaks at 15.3°, 18.7°, 23.6°, 24.3°, 30.4°, 36.3°, 38.2°, 41.0°, 44.4°, 45.5°, 48.6°, 50.1°, 51.5°, 53.9°, 61.7°, 64.9° and 68.1° were ascribed to the (010), (100), (011), (110), (111), (021), (200), (121), (112), (211), (022), (220), (130), (122), (113), (311) and (041)

crystal planes of $ZnWO_4$ and well conforms to JCPDS file no. 15-0774. Similarly, the diffraction peaks at 30.3°, 35.6°, 43.4°, 53.7°, 57.3° and 62.9° can be indexed to the (220), (311), (400), (422), (511) and (440) crystal planes of $Fe_3O_4$ and are in good agreement with JCPDS file no. 19-0629. No obvious carbon diffraction peak for RGO/NRGO was detected in the XRD patterns of RGO/$ZnWO_4$/$Fe_3O_4$ and NRGO/$ZnWO_4$/$Fe_3O_4$ nanocomposite, which may be due to the small amount of RGO/NRGO in the composite samples (Liu et al. 2004, Qiu et al. 2014).

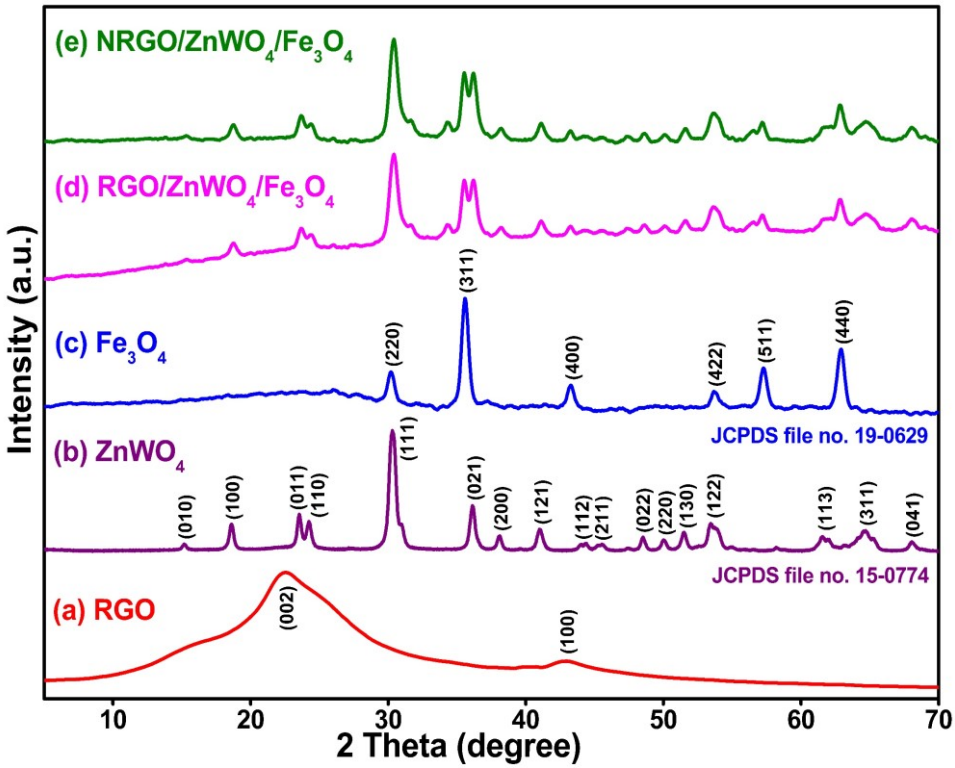


**Figure 2.5** XRD patterns of (a) RGO, (b) $ZnWO_4$, (c) $Fe_3O_4$, (d) RGO/$ZnWO_4$/$Fe_3O_4$ and (e) NRGO/$ZnWO_4$/$Fe_3O_4$ nanocomposites.

### 2.3.3 Raman Studies

The obtained Raman spectra of the as-prepared NRGO/$ZnWO_4$/$Fe_3O_4$ composite samples are shown in Figure 2.6. As can be observed from the figure, two peaks at 1348.3 $cm^{-1}$ and 1602.2 $cm^{-1}$ correspond to the characteristic Raman mode of the plane vibrations of $sp^3$ defects in carbon (D band) and $sp^2$ bonded carbons (G band) of NRGO sheets. Above mentioned results confirmed that the NRGO/$ZnWO_4$/$Fe_3O_4$ nanocomposites are successfully anchored to the NRGO sheets

and such results are also available in the literature (Xu et al. 2014). Further, D to G band peak intensity ratio, $I_D/I_G$ is generally used to confirm the degree of defects of carbon nanomaterial. As shown in Figure 2.6, the calculated intensity ratio of RGO, RGO/$ZnWO_4$/$Fe_3O_4$ and NRGO/$ZnWO_4$/$Fe_3O_4$ ($I_D/I_G$ = 1.10, 1.03 and 1.01) is higher than that of GO ($I_D/I_G$ = 0.98), indicating the introduction of defects during the reduction of GO into RGO/NRGO sheets. The lower $I_D/I_G$ of NRGO/$ZnWO_4$/$Fe_3O_4$ than that of RGO may be due to the adherence and interaction of $ZnWO_4$ and $Fe_3O_4$ nanoparticles on the NRGO sheets. Moreover, the broad D band and G band with weak intensity may be ascribed to the low content of NRGO and relatively higher concentration and interaction of $ZnWO_4$ and $Fe_3O_4$ nanoparticles on the NRGO sheets (Wang et al. 2015).

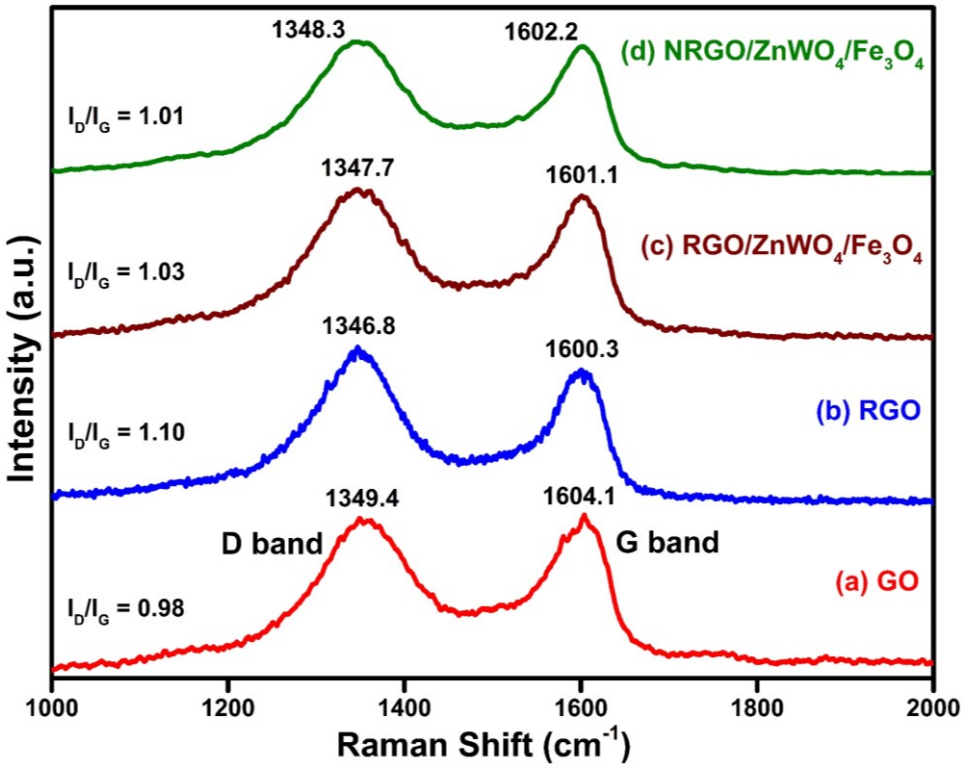


**Figure 2.6** Raman spectra of (a) GO, (b) RGO, (c) RGO/$ZnWO_4$/$Fe_3O_4$ and (d) NRGO/$ZnWO_4$/$Fe_3O_4$ nanocomposites.

### 2.3.4 Morphology Studies

The structure and morphological features of synthesized RGO/$ZnWO_4$/$Fe_3O_4$ and NRGO/$ZnWO_4$/$Fe_3O_4$ nanocomposite materials were investigated by microscopic

techniques. Figure 2.7a and b show the SEM images of the rod shaped particles of $ZnWO_4$ and spherical like $Fe_3O_4$ particles. Figure 2.7c and d show the FESEM image of the RGO/$ZnWO_4$/$Fe_3O_4$ and NRGO/$ZnWO_4$/$Fe_3O_4$ nanocomposites wherein $ZnWO_4$ nanorods and $Fe_3O_4$nanospheres are anchored on the surface of the RGO/NRGO nanosheets.

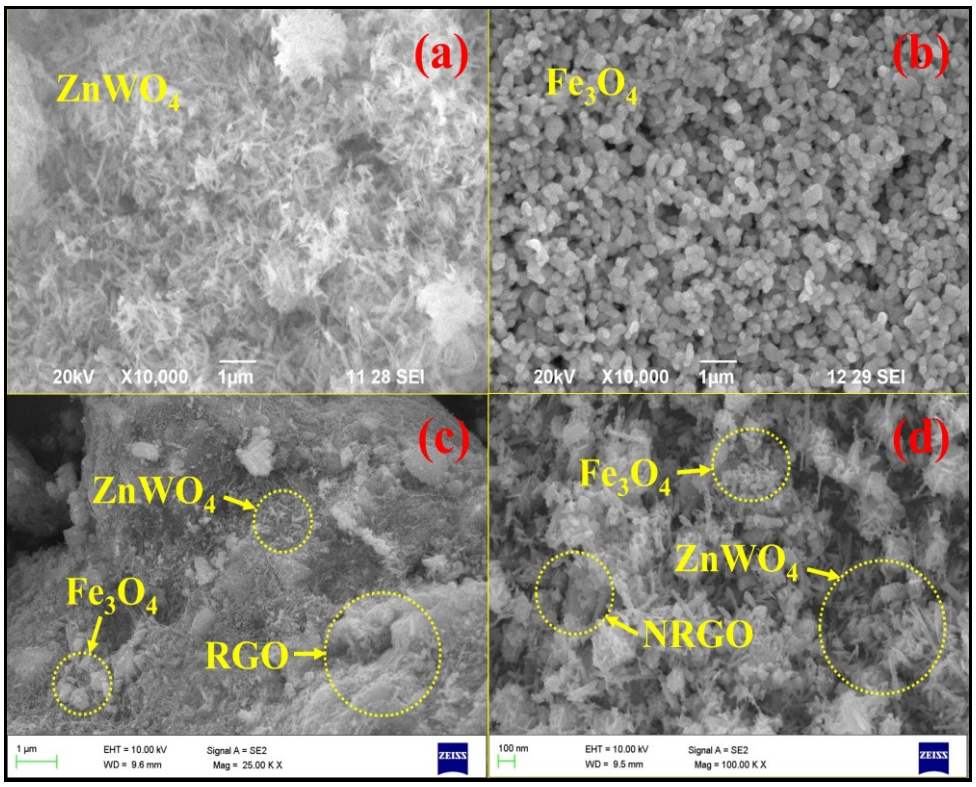


**Figure 2.7** SEM images of (a) $ZnWO_4$ and (b) $Fe_3O_4$. FESEM images of (c) RGO/$ZnWO_4$/$Fe_3O_4$ and (d) NRGO/$ZnWO_4$/$Fe_3O_4$.

To get further information on morphology of the synthesized materials, TEM and HRTEM measurements were carried out. Figure 2.8a and b show the TEM image indicating the two-dimensional wrinkled sheet like morphology of RGO as well as NRGO. TEM image of the synthesized $ZnWO_4$ is shown in Figure 2.8c, which clearly reveals the nanorod-like structures. As can be observed from Figure 2.8d and e, the rod-like $ZnWO_4$ and spherical $Fe_3O_4$ nanoparticles adhere on the surface of the NRGO/RGO nanosheets.

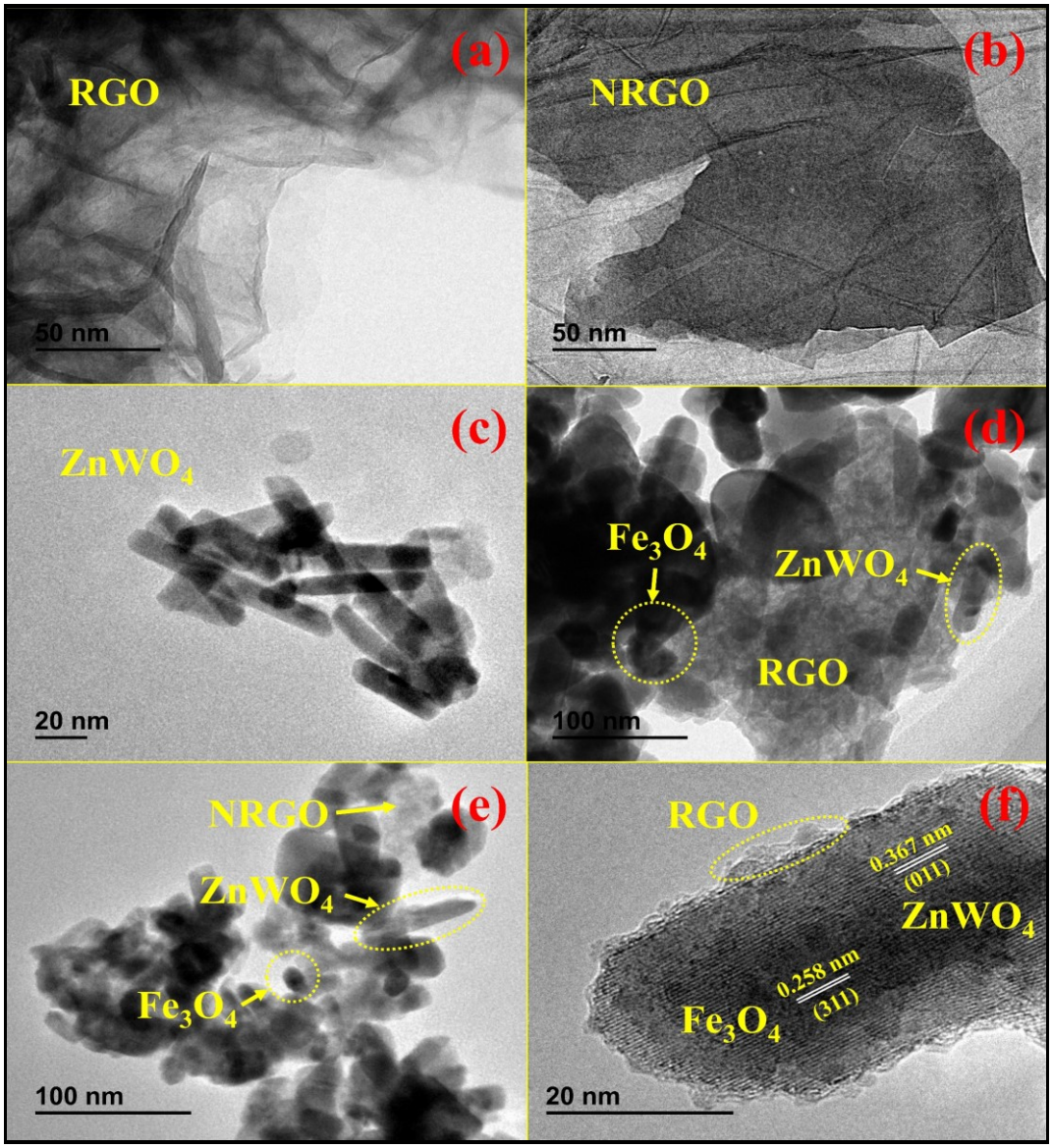


**Figure 2.8** TEM images of (a) RGO, (b) NRGO, (c) $ZnWO_4$, (d) RGO/$ZnWO_4$/$Fe_3O_4$, (e) NRGO/$ZnWO_4$/$Fe_3O_4$ and (d) HRTEM image of NRGO/$ZnWO_4$/$Fe_3O_4$.

Figure 2.8f shows the HRTEM image of RGO/$ZnWO_4$/$Fe_3O_4$ wherein, the interface between $ZnWO_4$ and $Fe_3O_4$ nanomaterials on the surface of the RGO nanosheets can be seen. The lattice fringes of about 0.367 nm correspond to the (011) plane of $ZnWO_4$ and 0.258 nm corresponded to the (311) plane of $Fe_3O_4$. Thus, it is evident that the interface is formed by the $Fe_3O_4$ (311) plane and the $ZnWO_4$ (011) plane on the surface of the RGO sheets. The EDX spectrum shown in Figure 2.9

indicated N, C, Zn, W, Fe and O as the elements present in the NRGO/$ZnWO_4$/$Fe_3O_4$ nanocomposite further compliments the characterization and formation of the ternary composite.

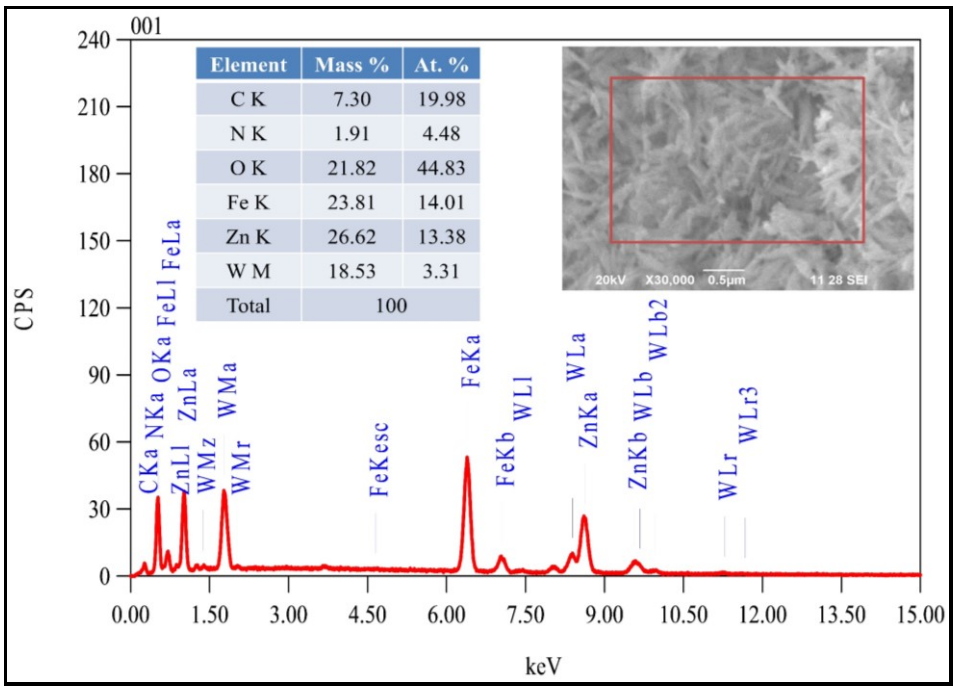


**Figure 2.9** EDX spectrum of NRGO/$ZnWO_4$/$Fe_3O_4$.

### 2.3.5 XPS Studies

Figure 2.10, shows the detailed information on the chemical states of ions present in the as-prepared samples through XPS analysis. C 1s peak (284.8 eV) was used as a reference for calibrating the binding energy values in the XPS analysis. Figure 2.10a, shows the general survey XPS spectra of the as-prepared NRGO/$ZnWO_4$/$Fe_3O_4$ nanocomposites, the surface of which contains C, N, Zn, W, Fe and O. Figure 2.10b, shows the high-resolution C 1s spectra, which could be deconvoluted into four peaks of different binding energies, 284.9 eV, 286.8 eV, 289.0 eV and 291.2 eV. These peaks correspond to the C-C/C=C in the aromatic ring of $sp^2$, C-N, C=O and π-π* interaction bonds, respectively (Zhu et al. 2016). Figure 2.10c, shows the high-resolution N 1sspectra which could be deconvoluted into four peaks at 397.8 eV (pyridinic-N), 399.0 eV (pyrrolic-N), 401.3 eV (graphitic-N) and 403.3 eV (pyridine-N-oxide), respectively (Wang et al. 2015).

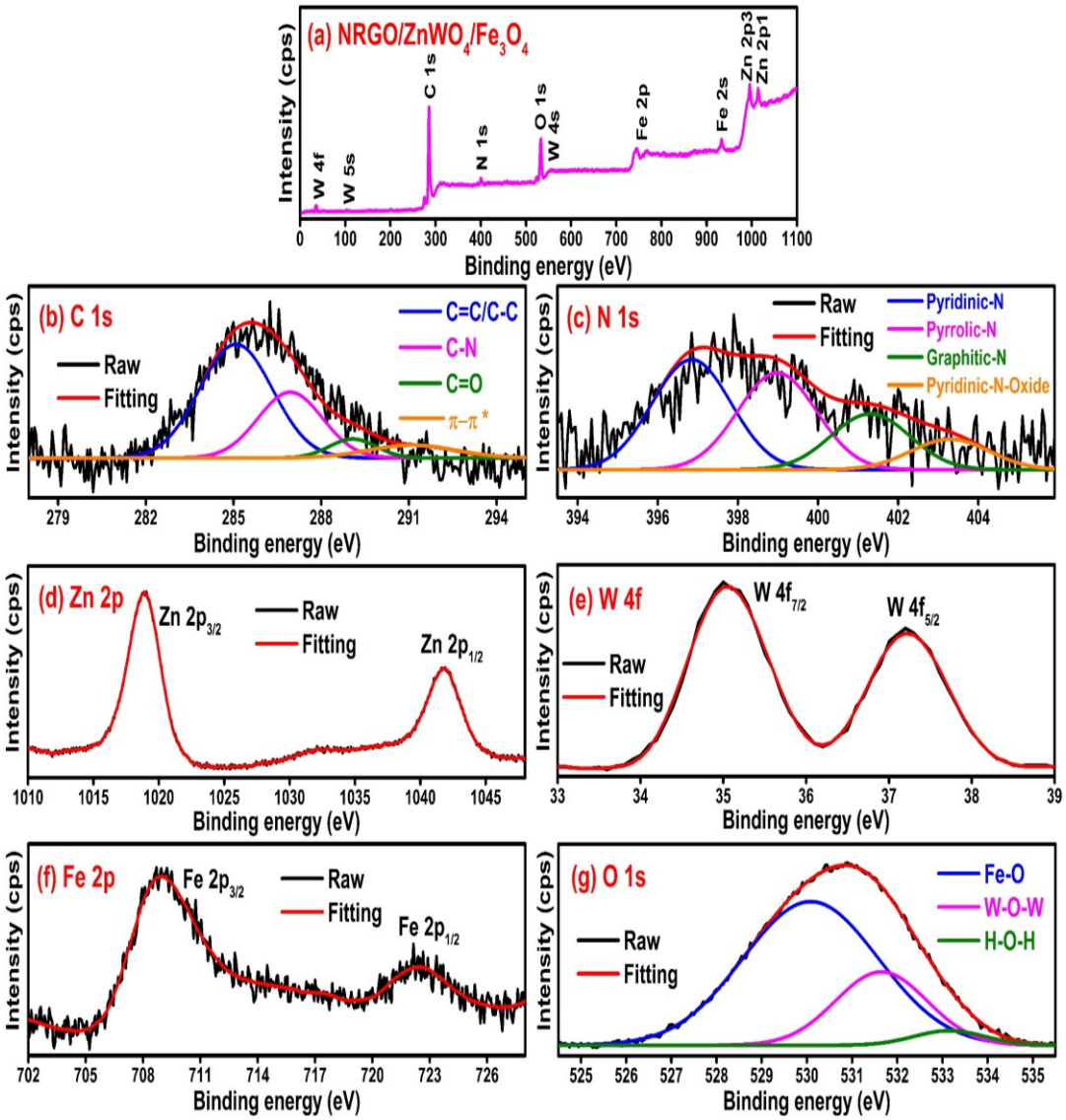


**Figure 2.10** XPS spectra of as-prepared samples (a) survey of NRGO/$ZnWO_4$/$Fe_3O_4$. High-resolution XPS spectra of (b) C 1s, (c) N 1s, (d) Zn 2p, (e) W 4f, (f) Fe 2p and (g) O 1s.

Figure 2.10d, shows the high- resolution Zn 2p region, with two broad peaks at 1018.9 eV and 1041.8 eV which are indexed to Zn $2p_{3/2}$ and Zn $2p_{1/2}$ state, respectively (Li et al. 2013). Figure 2.10e, shows the high-resolution W 4f spectra which could be deconvoluted into two different peaks at 35.1 eV and 37.2 eV being allotted to W $4f_{7/2}$ and W $4f_{5/2}$, respectively. These results are also in conformity with that of $ZnWO_4$ values reported previously (Li et al. 2013). Figure 2.10f, shows high resolution Fe 2p region with two photoelectron peaks at 708.9 eV and 722.5 eV. They

correspond to Fe $2p_{3/2}$ and Fe $2p_{1/2}$, states of iron respectively. Figure 2.10g, shows the high resolution O1s spectra which could be deconvoluted into three peaks of binding energy values, 530.1 eV, 531.6 eV and 533.2 eV corresponding to Fe-O, W-O-W and H-O-H bonds respectively (Nguyen et al. 2005). These results ascertain that a composite of $Fe_3O_4$, $ZnWO_4$ and NRGO sheets has been formed successfully (Yang et al. 2005).

### 2.3.6 Optical Absorbance Analysis

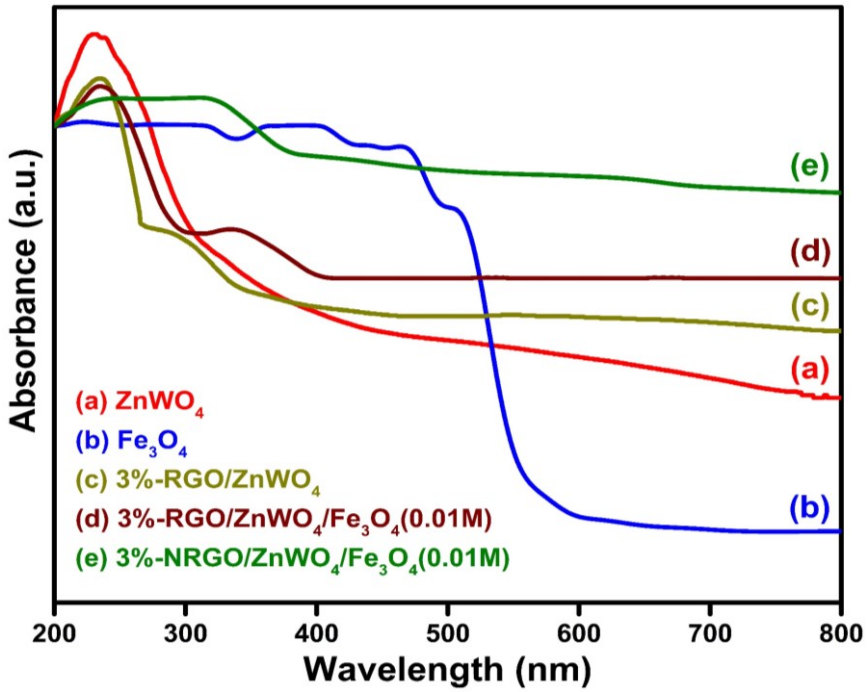


**Figure 2.11** UV-Vis spectra of (a) $ZnWO_4$, (b) $Fe_3O_4$, (c) RGO/$ZnWO_4$, (d) RGO/$ZnWO_4$/$Fe_3O_4$ and (e) NRGO/$ZnWO_4$/$Fe_3O_4$.

Figure 2.11, shows the absorption spectrum of NRGO/$ZnWO_4$/$Fe_3O_4$, RGO/$ZnWO_4$/$Fe_3O_4$, RGO/$ZnWO_4$ pure $ZnWO_4$ and pure $Fe_3O_4$. The band gap is the most important factor with regard to the photocatalytic activity of the materials. To calculate the band gap of the materials, the Tauc relation (Tauc et al. 1966) as given in equation (2.3) was used.

$$\alpha h\upsilon = K (h\upsilon - E_g)^{n/2} \quad \text{----------} \quad (2.3)$$

where, α is the absorption coefficient, hυ is the energy of photon, K is a constant, $E_g$ is the band gap of semiconductor. Among these parameters, n is determined by the type of transition process that occur in a semiconductor (n = 1 for a direct transition and n = 4 for an indirect transition). Direct band gap is considered in general for semiconductor photocatalysis processes (Hojamberdiev et al. 2010, Garadkar et al. 2013, Das et al. 2016).

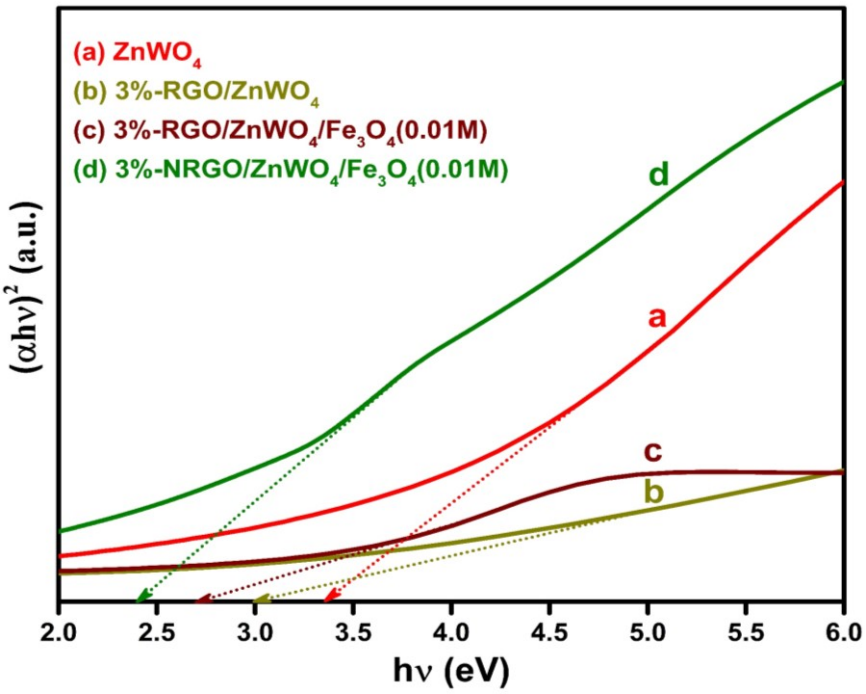


**Figure 2.12** Band gap plots for (a) $ZnWO_4$, (b) $RGO/ZnWO_4$, (c) $RGO/ZnWO_4/Fe_3O_4$ and (d) $NRGO/ZnWO_4/Fe_3O_4$.

Accordingly, the band gap energy ($E_g$) for pure $ZnWO_4$, $RGO/ZnWO_4$, $Fe_3O_4$, $RGO/ZnWO_4/Fe_3O_4$ and $NRGO/ZnWO_4/Fe_3O_4$ nanocomposites were estimated from a plot of $(\alpha h\upsilon)^2$ versus energy (hυ), as shown in Figure 2.12 and 2.13. As can be seen from the figure, a strong absorption edge at 313 nm is observed for pure $ZnWO_4$ which is equivalent to a band gap of 3.35 eV. The same for $RGO/ZnWO_4$ nanocomposite is estimated to be at 353 nm which is equivalent to a band gap of 3.0 eV. Similarly, the calculated band gap for the ternary $RGO/ZnWO_4/Fe_3O_4$ and $NRGO/ZnWO_4/Fe_3O_4$ nanocomposite is 2.71 eV and 2.40 eV. The band gap narrowed from 3.35 eV to 2.40 eV for $NRGO/ZnWO_4/Fe_3O_4$ nanocomposite, indicating the

interaction between these three components. It is therefore evident that NRGO/$ZnWO_4$/$Fe_3O_4$ nanocomposite facilitates strong absorption in the visible region of the spectrum and the phenomena can be attributed to the synergetic effects of $ZnWO_4$, $Fe_3O_4$ and NRGO nanosheets (Wang et al. 2012, Jo and Selvam 2015). The results clearly suggest that the novel ternary composite can perform efficiently as photocatalyst under visible light.

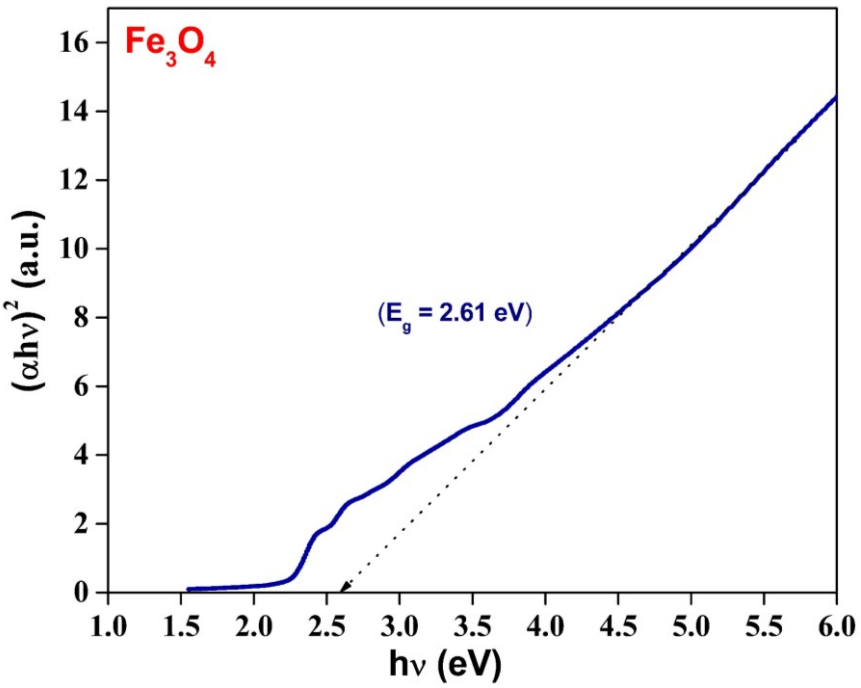


**Figure 2.13** Band gap plot for pure $Fe_3O_4$.

### 2.3.7 Photoluminescence Analysis

It is well known that a PL spectrum is a very useful tool to study the dynamics of separation and recombination of photogenerated electron-hole pairs. This is mainly due to the fact that the PL emission signal arises from the recombination of excited electrons and holes. It is also well established that the electron-hole pair separation improves the photocatalytic performance of materials. The photo induced electron hole pair transfer mechanism in the NRGO sheets, $ZnWO_4$ and $Fe_3O_4$ nanomaterials are determined by the photoluminescence emission intensity analysis. The PL spectra of NRGO/$ZnWO_4$/$Fe_3O_4$, RGO/$ZnWO_4$/$Fe_3O_4$, RGO/$ZnWO_4$ and pure $ZnWO_4$

nanocomposites are measured using an excitation wavelength of 380 nm (Figure 2.14).

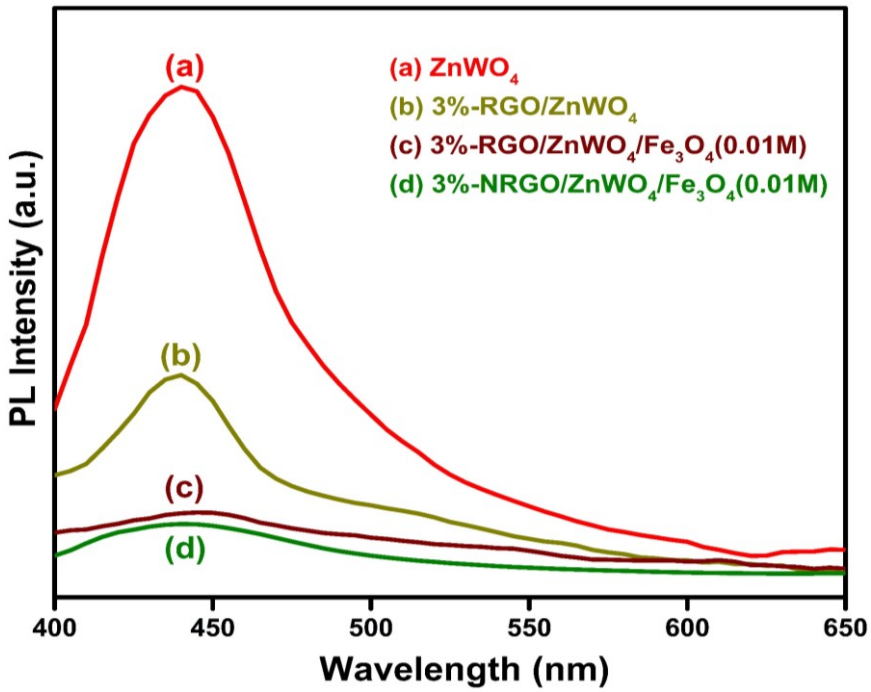


**Figure 2.14** PL spectra of (a) $ZnWO_4$, (b) RGO/$ZnWO_4$ (c) RGO/$ZnWO_4$/$Fe_3O_4$ and (d) NRGO/$ZnWO_4$/$Fe_3O_4$.

The PL spectrum of $ZnWO_4$ shows a high intensity broad peak at 441 nm which can be corresponded to the recombination of photogenerated electron hole pairs. The weak intensity of RGO/$ZnWO_4$ nanocomposite may be due to the transfer of photoinduced electrons from the trapped states of $ZnWO_4$ to RGO nanosheets (Williams and Kamat 2009). As can be seen from the figure, the PL intensity of the NRGO/$ZnWO_4$/$Fe_3O_4$ nanocomposite is very weak indicating that the fluorescence of this nanocomposite is quenched in a more powerful manner than that of RGO/$ZnWO_4$/$Fe_3O_4$ and RGO/$ZnWO_4$ nanocomposite proving the synergistic effect induced by zinc tungstate and iron oxide component via NRGO interlayer in the nanocomposite towards the separation of electron hole pairs. This observation suggests that the combination of $ZnWO_4$ and $Fe_3O_4$ on NRGO nanosheets can enhance the prevention of the photoinduced electron hole pair recombination (Wang et al. 2015).

### 2.3.8 Photocatalytic Activity

The photocatalytic activity of the as-prepared materials was estimated for the degradation of MB under visible light irradiation. The adsorption of the MB solution was carried out for 30 minutes in dark to reach the adsorption-desorption equilibrium with the photocatalyst before exposing it to the visible light. In a blank test, wherein the MB solution was taken without any photocatalyst in the reactor, there was no appreciable degradation. This result suggests that the photolysis of MB is negligible. RGO composition in the RGO/$ZnWO_4$ nanocomposites was optimized based on the degradation of MB results.

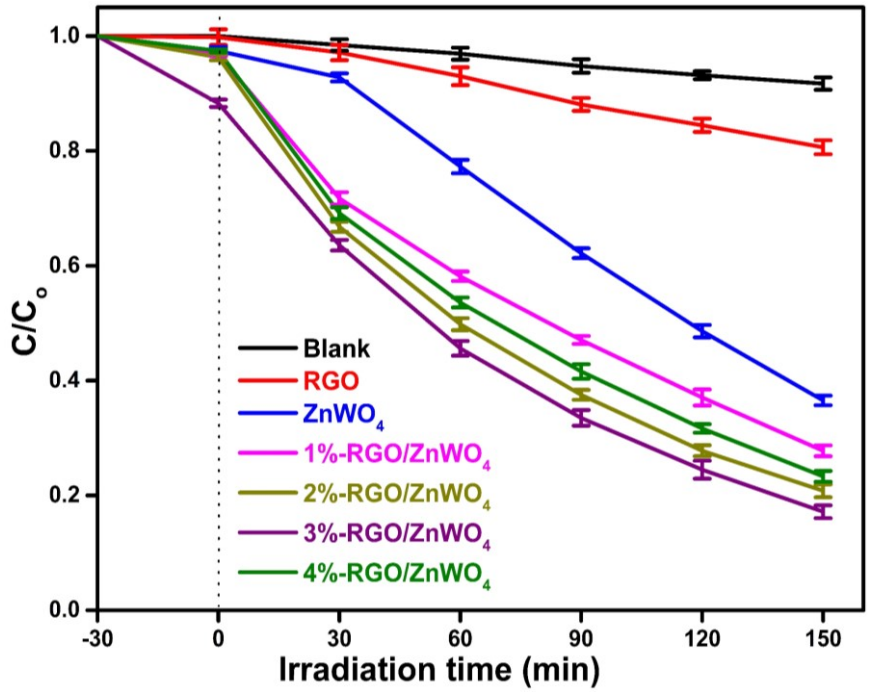


**Figure 2.15** Degradation of MB by RGO/$ZnWO_4$ under visible light irradiation.

Figure 2.15, shows the photocatalytic degradation of RGO/$ZnWO_4$ nanocomposites with varying amounts of RGO. It is observed that the photocatalytic degradation efficiency of the nanocomposites increased with increase in RGO content up to 3 % which registered 85 % conversion within 150 minutes whereas the same for pure $ZnWO_4$ under same conditions was only 60 %. However further increase in the RGO content decreased the catalytic efficiency of the nanocomposite and this behavior may be due to the fact that the superfluous RGO hinders the photon

absorption by the semiconductor and hence in turn reduces the efficiency. As 3 wt.% RGO/$ZnWO_4$ nanocomposite showed the best activity, the same was taken as the optimized base material for further variation in the $Fe_3O_4$ content.

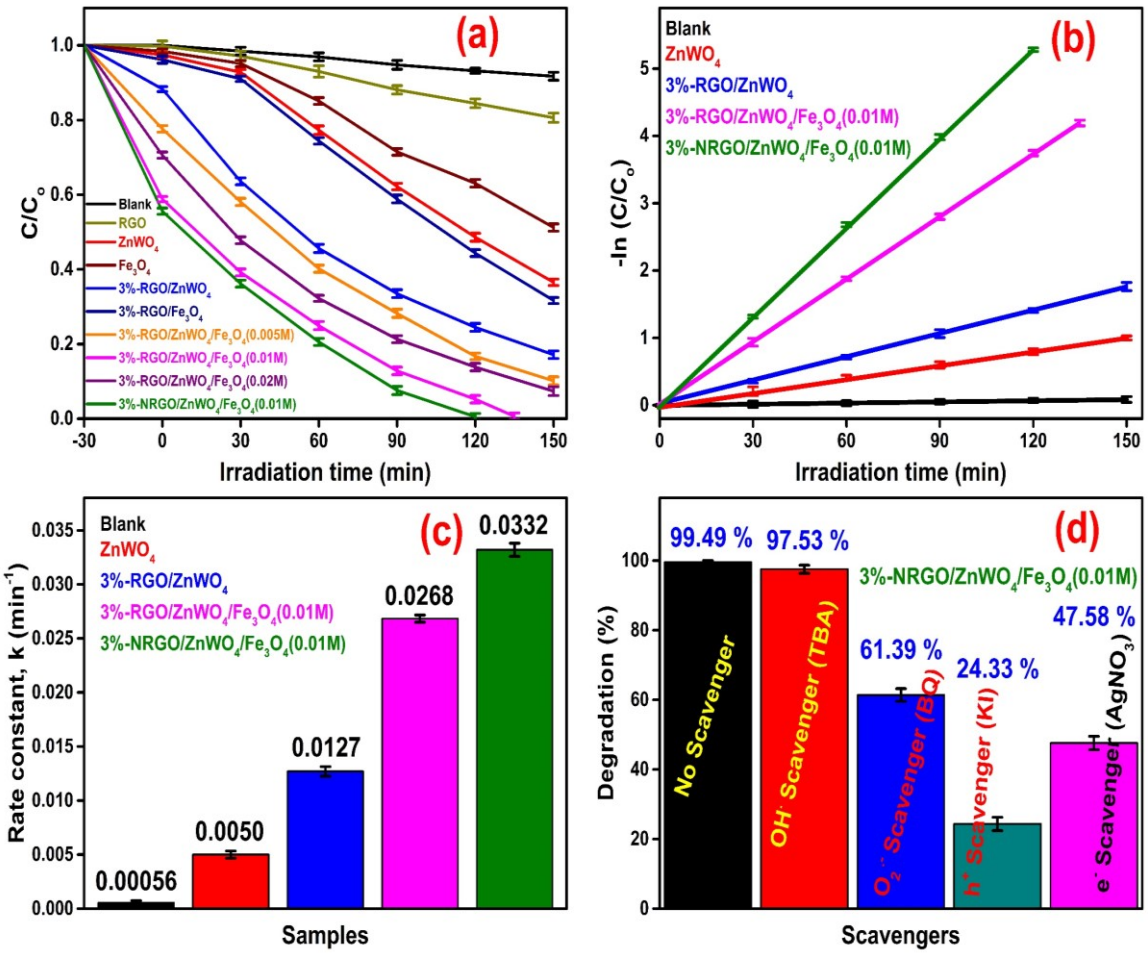


**Figure 2.16** (a)Degradation plot, (b) First order kinetics plot, (c) Rate constants plot for the photodegradation of MB over various catalysts and (d) Effect of different scavengers on the photodegradation of MB by 3%-NRGO/$ZnWO_4$/$Fe_3O_4$ (0.01 M) nanocomposites under visible light irradiation.

Figure 2.16a, shows the photocatalytic degradation of MB by 3 wt.% RGO-$ZnWO_4$ with 0.005 M, 0.01 M and 0.02 M $Fe_3O_4$nanospheres content. The photocatalytic activity of the nanocomposites increased with the increase in $Fe_3O_4$ content. The nanocomposite with 0.01 M $Fe_3O_4$ content showed maximum efficiency and degraded the dye almost completely within 135 minutes. However, further increase in $Fe_3O_4$ nanoparticles content in the nanocomposite decreased the

photocatalytic degradation rate of MB dye which may be ascribed to the hindrance of $Fe_3O_4$ nanoparticles clusters on the ternary nanocomposites to effective charge transfer on RGO sheets. The result confirms that the ternary 3 wt.% RGO/$ZnWO_4$/$Fe_3O_4$ (0.01 M) nanocomposite is very efficient as photocatalyst under visible light irradiation.

To see the effect of nitrogen doping on RGO in the catalytic activity of the composite, 3 wt.% NRGO/$ZnWO_4$/$Fe_3O_4$ (0.01 M) nanocomposite was prepared and tested for its photocatalytic activity (Figure 2.16a). The results showed that the Nitrogen doped RGO/$ZnWO_4$/$Fe_3O_4$semiconductor nanocomposite exhibits better catalytic performance and the degradation was over within 120 minutes. Thus, 3%-NRGO/$ZnWO_4$/$Fe_3O_4$ (0.01 M) was only used for all further studies.

The kinetics of photocatalytic degradation of MB dye by the prepared nanocomposites conforming to the pseudo first order rate equation as given in equation (2.4) is shown in Figure 2.16b.

$$\ln (C/C_o) = -kt \qquad \text{----------} \qquad (2.4)$$

where, $C_o$ is the initial concentration, C is the concentration at irradiation time 't' and 'k' is the first order rate constant. The 'k' values were measured from slope of the straight lines.

The comparison of the rate constants for different nanocomposites is shown in a bar diagram (Figure 2.16c). As can be seen from the diagram, the best composite 3% NRGO/$ZnWO_4$/$Fe_3O_4$ (0.01 M) shows 6.64 times, 2.61 times and 1.24 times more efficiency than the pure $ZnWO_4$, 3%-RGO/$ZnWO_4$ and 3%-RGO/$ZnWO_4$/$Fe_3O_4$ (0.01 M) respectively. The rate constant results suggest that the ternary 3%-NRGO/$ZnWO_4$/$Fe_3O_4$ (0.01 M) nanocomposite is very efficient as photocatalyst under visible light irradiation.

To determine the degree of mineralization of MB, during its photodegradation catalyzed by 3%-NRGO/$ZnWO_4$/$Fe_3O_4$ (0.01M) nanocomposite, TOC analysis was performed (Cui et al. 2013). Figure 2.17 shows the TOC values for the MB solution at different intervals of time. The TOC value increased to 84.37 % under visible light

irradiation for 120 minutes of visible light irradiation. Thus, it is very evident that, the 3%-NRGO/$ZnWO_4$/$Fe_3O_4$ (0.01M) nanocomposite has high catalytic efficiency towards photodegradation of MB molecules and that organic carbon is mostly converted to $CO_2$ during the process.

The reusability of ternary nanocomposites is of great need for practical applications. To evaluate the reusability of the 3 wt.% NRGO/$ZnWO_4$/$Fe_3O_4$ (0.01 M) nanocomposite, the photocatalytic activity of MB under visible light irradiation was tested for 5 consecutive cycles and the same is shown in Figure 2.18. It is observed that there is only minimum loss of photocatalytic degradation efficiency during the test and the MB dye was almost completely degraded within 150 minutes even in the $5^{th}$ cycle. This indicates that the 3 wt.% NRGO/$ZnWO_4$/$Fe_3O_4$ (0.01 M) composite possesses sufficient stability for photocatalytic degradation reactions and that the novel NRGO/$ZnWO_4$/$Fe_3O_4$ nanocomposite can be used as an environmental friendly photocatalyst for water treatment.

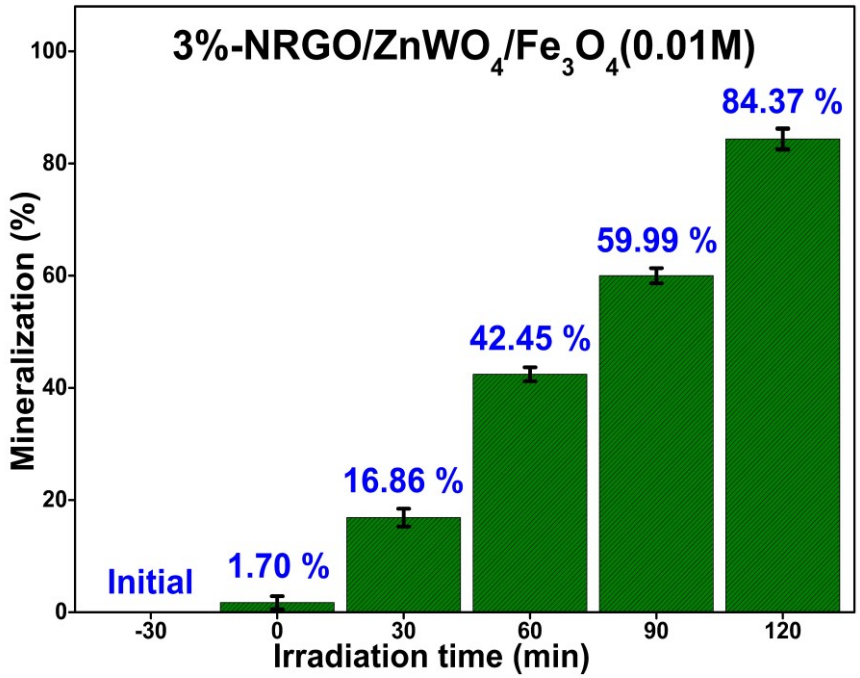


**Figure 2.17** Mineralization values for degradation of MB at different intervals of time.

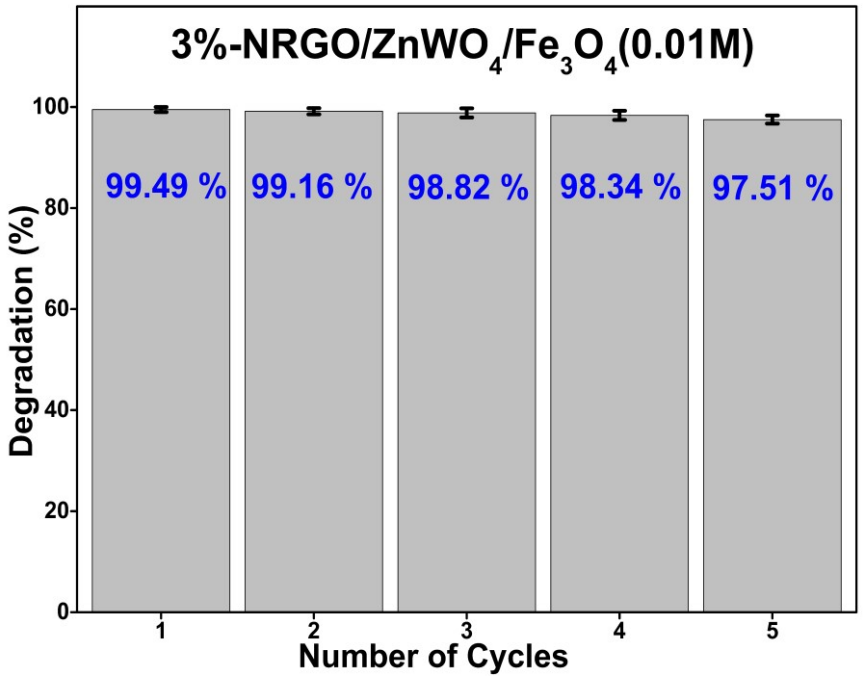


**Figure 2.18** Recyclability of 3%-NRGO/$ZnWO_4$/$Fe_3O_4$ (0.01 M) catalyst for the photodegradation of MB under visible irradiation.

### 2.3.9 Mechanism of the Photocatalytic Activity

In order to figure out the mechanism of photodegradation of MB dye, experiments were carried out using radical scavengers (Figure 2.16d). The control experiments were done to analyze the role of superoxide radicals ($O_2^{\cdot -}$), hydroxyl radicals ($\cdot OH$), photogenerated electrons ($e^-$) and photogenerated holes ($h^+$) in the photocatalysis process by using benzoquinone (BQ), ternary butyl alcohol (TBA), silver nitrate and potassium iodide for $O_2^{\cdot -}$, $\cdot OH$, $e^-$ and $h^+$ respectively. Addition of TBA caused slight decrease in the photodegradation efficiency due to the removal of hydroxyl radicals, indicating that they play a minor role in the mechanism. BQ, $AgNO_3$ and KI caused decrease in the efficiency in the increasing order suggesting that holes play a major role in the overall degradation pathway.

The enhanced photocatalytic activity of NRGO/$ZnWO_4$/$Fe_3O_4$ composites is mainly related to the superior photo absorption in the visible region and the efficient generation, separation and transfer of the photoinduced electron-hole pairs, which strongly depends on the overall band structure of the composites. Thus, the VB edge positions and the CB edge positions of $ZnWO_4$ and $Fe_3O_4$ were estimated according

to the Mulliken electronegativity theory (Pearson 1988, Li et al. 2013) following equations (2.5) and (2.6).

$$E_{VB} = \chi - E^e + 0.5\ E_g \quad \text{----------} \quad (2.5)$$

$$E_{CB} = E_{VB} - E_g \quad \text{----------} \quad (2.6)$$

where $E_{VB}$ is the VB edge potential, $E_{CB}$ is the CB edge potential, $E_g$ is the band gap energy of the semiconductor, $\chi$ is the electronegativity of the semiconductor; the geometric mean of the electronegativity of the constituent atoms and $E^e$ is the energy of free electrons on the hydrogen scale (-4.5 eV). According to the $\chi$ and $E_g$ values, $E_{VB}$ and $E_{CB}$ of $ZnWO_4$ and $Fe_3O_4$ were separately calculated as listed in Table 2.1.

**Table 2.1** Band gap parameters of $ZnWO_4$ and $Fe_3O_4$.

| **Samples** | **$\chi$ (eV)** | **$E_g$ (eV)** | **$E_{VB}$ (eV)** | **$E_{CB}$ (eV)** |
|---|---|---|---|---|
| $ZnWO_4$ | 6.313 | 3.35 | 3.488 | 0.138 |
| $Fe_3O_4$ | 5.783 | 2.61 | 2.588 | -0.022 |

On the basis of the above results, the photodegradation mechanism for highly efficient electron-hole pair charge separation of the NRGO/$ZnWO_4$/$Fe_3O_4$ nanocomposites is proposed as shown in Figure 2.19. Clearly, $Fe_3O_4$ can be easily excited to form electron-hole pairs under visible light irradiation. In the case of $ZnWO_4$, excitation by visible light irradiation is not possible due to its wide energy gap. When $Fe_3O_4$ is introduced, the electrons in CB edge of $Fe_3O_4$ would easily get transferred to the CB of $ZnWO_4$ via NRGO interlayer, leaving holes at the VB of $Fe_3O_4$. Thus, the photoinduced electrons and holes can be efficiently separated overturning the possibility of the recombination of electron-hole pairs. The separated holes will directly react with MB or react with water to generate hydroxyl radicals. The separated electrons would subsequently react with water and oxygen to generate hydroxyl and superoxide radicals. The radicals would subsequently oxidize the MB due to their high oxidative capacity to harmless degraded products.

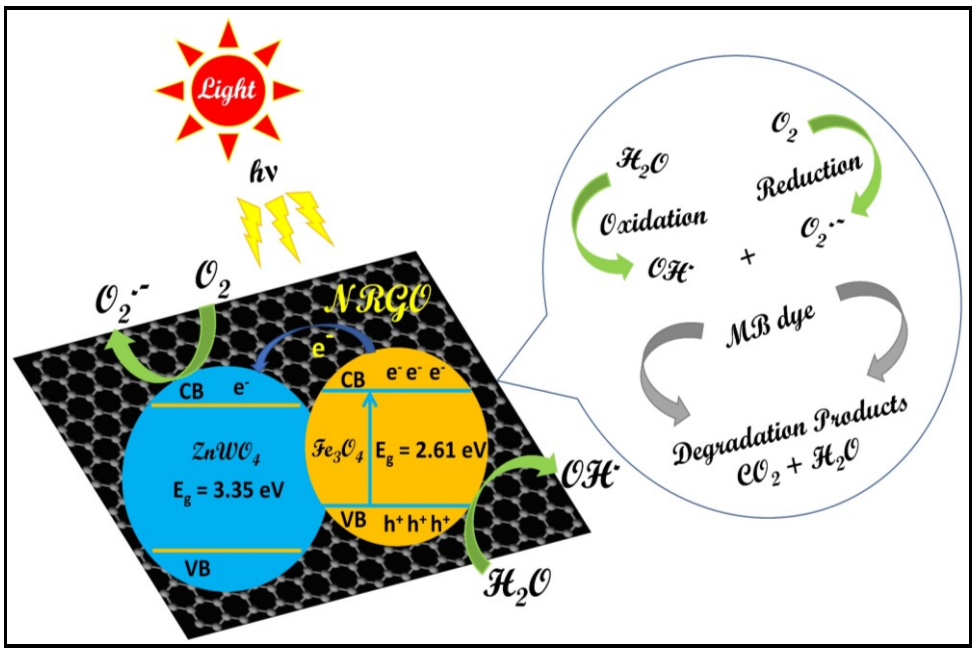


**Figure 2.19** Schematic diagram for photodegradation of MB over NRGO/$ZnWO_4$/$Fe_3O_4$ nanocomposites under visible light irradiation.

The improvement in the photocatalytic performance of the NRGO/$ZnWO_4$/$Fe_3O_4$ nanocomposite is mainly due to the high efficiency in the separation of photogenerated charge facilitated by the combination of $ZnWO_4$ and $Fe_3O_4$ via NRGO interlayer.

### 2.3.10 Catalytic Reduction of 4-NP to 4-AP

The catalytic activity of the as prepared 3%-NRGO/$ZnWO_4$/$Fe_3O_4$(0.01 M) nanocomposite in reduction of 4-NP to 4-AP by $NaBH_4$ is estimated in an aqueous medium. The reduction reaction does not proceed in the absence of the catalyst. This is indicated by the undeterred absorption peak at 400 nm. However, when 3%-NRGO/$ZnWO_4$/$Fe_3O_4$ (0.01 M) nanocomposite was added into the 4-NP solution, the absorption of 4-NP found at 400 nm peak decreased immediately and new absorption peak of 4-AP at 300 nm was obtained. The intensity of this new peak increased with time as shown in Figure 2.20. The catalytic reduction of 4-NP into 4-AP was over within just 30 seconds. The completeness of the reaction is indicated by the reduction of the absorbance of the solution at 400 nm to zero and also by the change in color of the solution from bright yellow to colorless (inset in Figure 2.20) (Zheng et al. 2013).

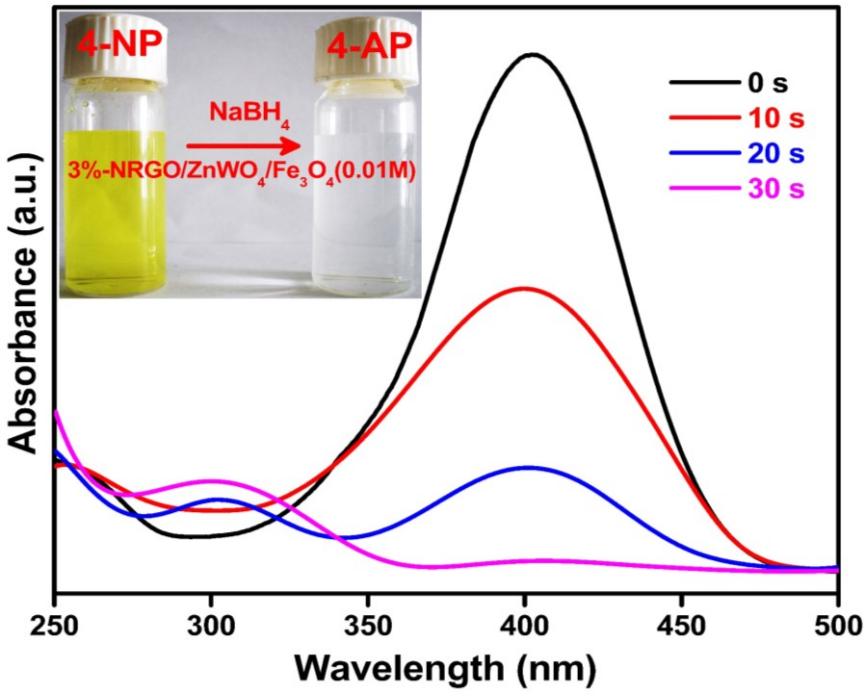


**Figure 2.20** UV-Vis absorption spectra for the reduction of 4-NP to 4-AP by $NaBH_4$ in the presence of 3%-NRGO/$ZnWO_4$/$Fe_3O_4$(0.01 M) nanocomposite.

For comparison, the catalytic activities of the individual components of the composite in terms of pseudo first order rate constants have also been determined under identical condition (Table 2.2). As can be seen from the Table, the catalytic efficiency of the 3%-NRGO/$ZnWO_4$/$Fe_3O_4$(0.01 M) nanocomposite is more than that of the other component materials.

The reaction rate constants conforming to the pseudo first order kinetics with respect to 4-NP concentration have been determined. The reaction kinetics can be described as $-\ln(C/C_o) = kt$, where k is the rate constant at a given temperature and t is the reaction time. $C_o$ and C are the 4-NP concentration at the beginning and at time t, respectively. The plot of $-\ln(C/C_o)$ vs. time shows a straight line with a positive slope (Figure 2.21) from which the rate constant 'k' values are determined. The kinetic rate constant 'k' values are given in Table 2.2. It is interesting to note the differences in the efficiencies of various catalysts. Individually, the activity of iron oxide is more than two times that of zinc tungstate. This may be due to higher catalytically active sites on iron oxide. But with RGO, activity of zinc tungstate is more than three times that of RGO/$Fe_3O_4$. This may be due to the ease of electron transportation that is

possible with RGO/$ZnWO_4$ combination compared to that of RGO/$Fe_3O_4$. When iron oxide is combined with RGO/$ZnWO_4$, the activity of the resulted nanocomposite is more than that of RGO/$ZnWO_4$. When NRGO is introduced in place of RGO in RGO/$ZnWO_4$/$Fe_3O_4$, the catalytic activity of the resulting nanocomposite is much better than that of RGO/$ZnWO_4$/$Fe_3O_4$. Further, it is worth noting that the observed activity of the catalyst described here is much higher compared to that of reported catalysts (Jiang et al. 2011, Li et al. 2012, Wu et al. 2014, Yang et al. 2014).

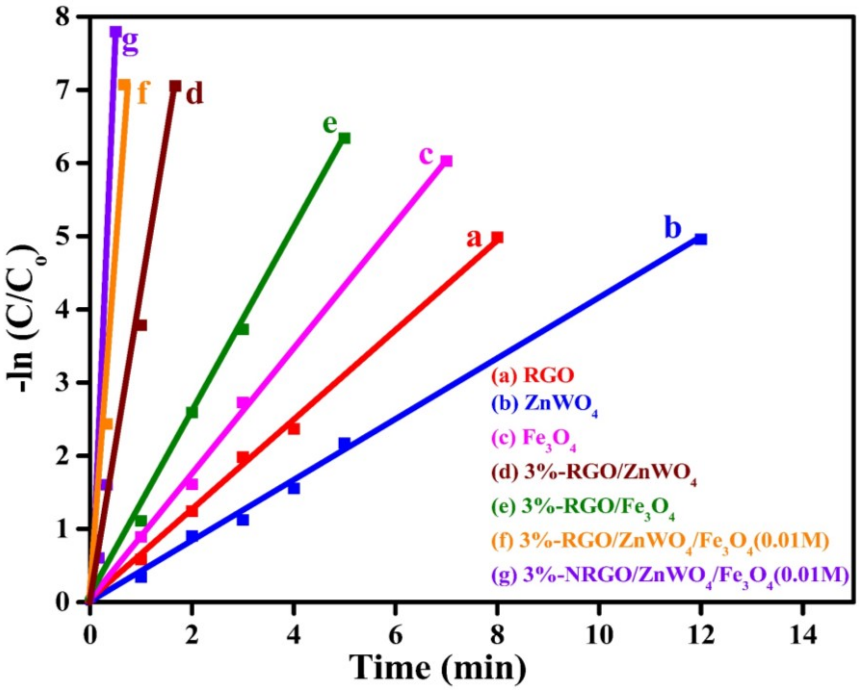


**Figure 2.21** Plots of -ln($C/C_o$) against time for reduction of 4-NP to 4-AP over various catalysts.

The stability and reusability of the 3%-NRGO/$ZnWO_4$/$Fe_3O_4$(0.01 M) nanocomposites was examined by carrying out the reduction reaction with the same catalyst after recovery from the previous reaction mixture. The results from 10 such successive reactions are shown in Figure 2.22. The reused catalyst exhibited excellent activity even after 10 successive cycles, with nearly 100 % conversion within a time period of 48 seconds.

The possible mechanism for reduction of 4-NP to 4-AP by $NaBH_4$ in the presence of 3%-NRGO/$ZnWO_4$/$Fe_3O_4$(0.01M) nanocomposite catalyst may be

explained as follows. The 4-NP molecule being slightly acidic can be adsorbed on to the catalyst surface to a better extent because of the fact that the NRGO provides a slightly negatively charged surface.

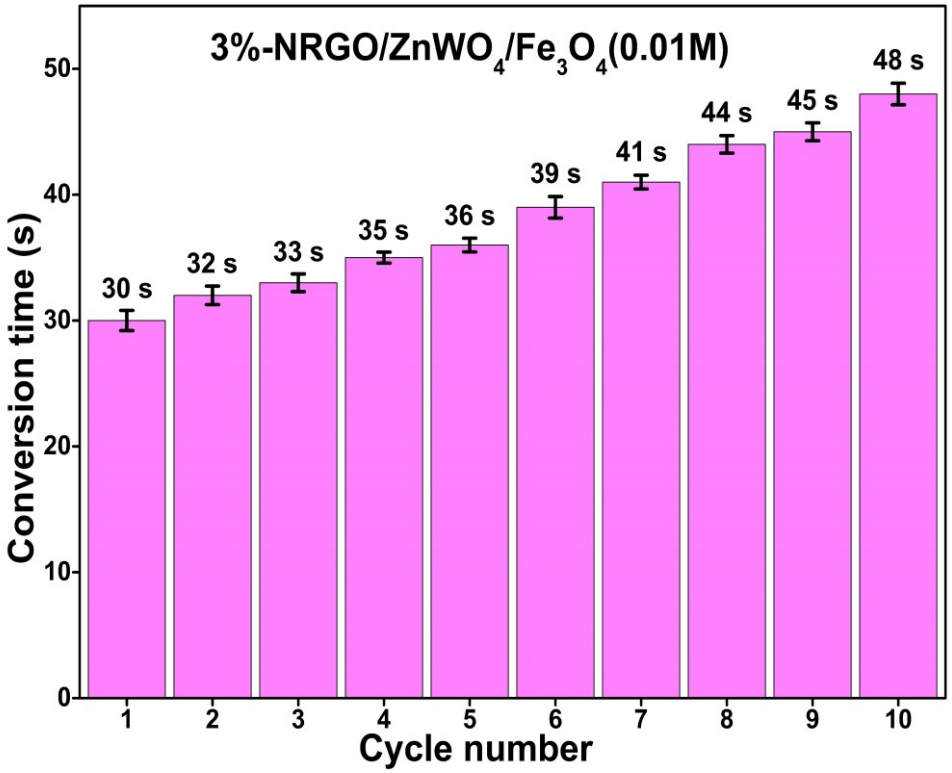


**Figure 2.22** Catalytic stability of 3%-NRGO/$ZnWO_4$/$Fe_3O_4$(0.01M) nanocomposites with successive 10 cycles of the same reduction condition.

Further, the presence of $ZnWO_4$ nanoparticles on the NRGO surface provides not only better active sites for adsorption but also facilitates effective interaction between the substrate, reducing agent and catalyst matrix. This property is further enhanced by the presence of $Fe_3O_4$ nanoparticles in the nanocomposite catalyst. This is also supported by the enhancement in the rate of reduction reaction observed (Figure 2.21) when $Fe_3O_4$ is added to the NRGO/$ZnWO_4$ nanocomposite. Also, the ease of electron transfer over NRGO matrix makes it an ideal mediator for reduction process and enables the acceptance of electrons by 4-NP molecules and its conversion to 4-AP. Over all, the combination of NRGO, $ZnWO_4$, $Fe_3O_4$ in the NRGO/$ZnWO_4$/$Fe_3O_4$ nanocomposite provides favorable synergetic effects to the rapid and complete catalytic reduction of 4-NP to 4-AP by $NaBH_4$. Further, the

NRGO/$ZnWO_4$/$Fe_3O_4$ nanocomposite also exhibits excellent reusability and stability for reduction processes.

**Table 2.2** The rate constant values for different types of catalysts.

| **Types of catalysts** | **k ($s^{-1}$)** | **References** |
|---|---|---|
| RGO | 0.00995 | Present work |
| $ZnWO_4$ | 0.00483 | Present work |
| $Fe_3O_4$ | 0.01395 | Present work |
| 3%-RGO/$ZnWO_4$ | 0.05081 | Present work |
| 3%-RGO/$Fe_3O_4$ | 0.02083 | Present work |
| 3%-RGO/$ZnWO_4$/$Fe_3O_4$(0.01 M) | 0.12420 | Present work |
| 3%-NRGO/$ZnWO_4$/$Fe_3O_4$(0.01 M) | 0.13344 | Present work |
| Ni/graphene | 0.0007 | Wu et al. (2014) |
| Au@Ag/ZIF-8 | 0.0003 | Jiang et al. (2011) |
| Au/graphene | 0.00317 | Li et al. (2012) |
| Ni/MC-750 | 0.00626 | Yang et al. (2014) |

### 2.3.11 Electrocatalytic Studies of HER

The electrocatalytic activity of RGO, $ZnWO_4$, 3%-RGO/$ZnWO_4$, 3%-RGO/$Fe_3O_4$, 3%-RGO/$ZnWO_4$/$Fe_3O_4$ (0.01 M) and 3%-NRGO/$ZnWO_4$/$Fe_3O_4$ (0.01 M) nanocomposites were studied in alkaline medium via LSV technique (Figure 2.23a). LSVs were measured from 0.1 V to -0.4 V vs RHE at scan rate of 5 mV/s using 0.1 M KOH solutions. In contrast, 3%-NRGO/$ZnWO_4$/$Fe_3O_4$ (0.01 M) exhibits small onset potential of -113 mV, which is much smaller than that for 3%-RGO/$ZnWO_4$, 3%-RGO/$Fe_3O_4$ and 3%-RGO/$ZnWO_4$/$Fe_3O_4$ (0.01M), which have the values, -208 mV, -182 mV and -135 mV, at current density of 10 mA $cm^{-2}$,

respectively. Normally, Pt/C shows excellent electrocatalytic activity for HER with an overpotential close to zero (Chen et al. 2013).

Figure 2.23b shows the kinetic behavior of the RGO, $ZnWO_4$, 3%-RGO/$ZnWO_4$, 3%-RGO/$Fe_3O_4$, 3%-RGO/$ZnWO_4$/$Fe_3O_4$ (0.01 M) and 3%-NRGO/$ZnWO_4$/$Fe_3O_4$ (0.01 M) nanocomposites in terms of Tafel slopes. The established HER mechanism in alkaline medium is as given in equations 2.7, 2.8 and 2.9 (Bhardwaj and Balasubramaniam 2008).

(i) Volmer reaction mechanism (via electrochemical hydrogen adsorption)

$$H_2O + A + e^- \rightleftharpoons A - H^+ + OH^- \quad \text{----------} \quad (2.7)$$

Tafel slope = 120 mV $dec^{-1}$

(ii) Heyrovsky reaction mechanism (via electrochemical desorption)

$$A - H^+ + H_2O + e^- \rightleftharpoons A + OH^- + H_2 \uparrow \quad \text{----------} \quad (2.8)$$

Tafel slope = 40 mV $dec^{-1}$

(iii) Tafel reaction mechanism (via Chemical desorption)

$$2\,A - H^+ \rightleftharpoons 2A + H_2 \uparrow \quad \text{----------} \quad (2.9)$$

Tafel slope = 30 mV $dec^{-1}$

where $H^+$ is an electrochemically adsorbed hydrogen on an active site of the electrode surface (A).

The linear region of the Tafel plots were fitted with the Tafel equation (Wang et al. 2014) ($\eta = b \log (j) + a$, where b is the Tafel slop, j is the current density, $\eta$ is the overpotential and a is the constant). The yielding of Tafel slopes are at 230 mV $dec^{-1}$, 120 mV $dec^{-1}$, 103 mV $dec^{-1}$, 84 mV $dec^{-1}$and 75 mV $dec^{-1}$ for $ZnWO_4$, 3%-RGO/$ZnWO_4$, 3%-RGO/$Fe_3O_4$, 3%-RGO/$ZnWO_4$/$Fe_3O_4$ (0.01M) and 3%-NRGO/$ZnWO_4$/$Fe_3O_4$(0.01M) nanocomposite, respectively. The overpotential are at -320.48 mV, -304.14 mV, -249.21 mV and -218.55 mV for 3%-RGO/$ZnWO_4$, 3%-RGO/$Fe_3O_4$, 3%-RGO/$ZnWO_4$/$Fe_3O_4$ (0.01 M) and 3%-NRGO/$ZnWO_4$/$Fe_3O_4$ (0.01 M) nanocomposite, respectively.

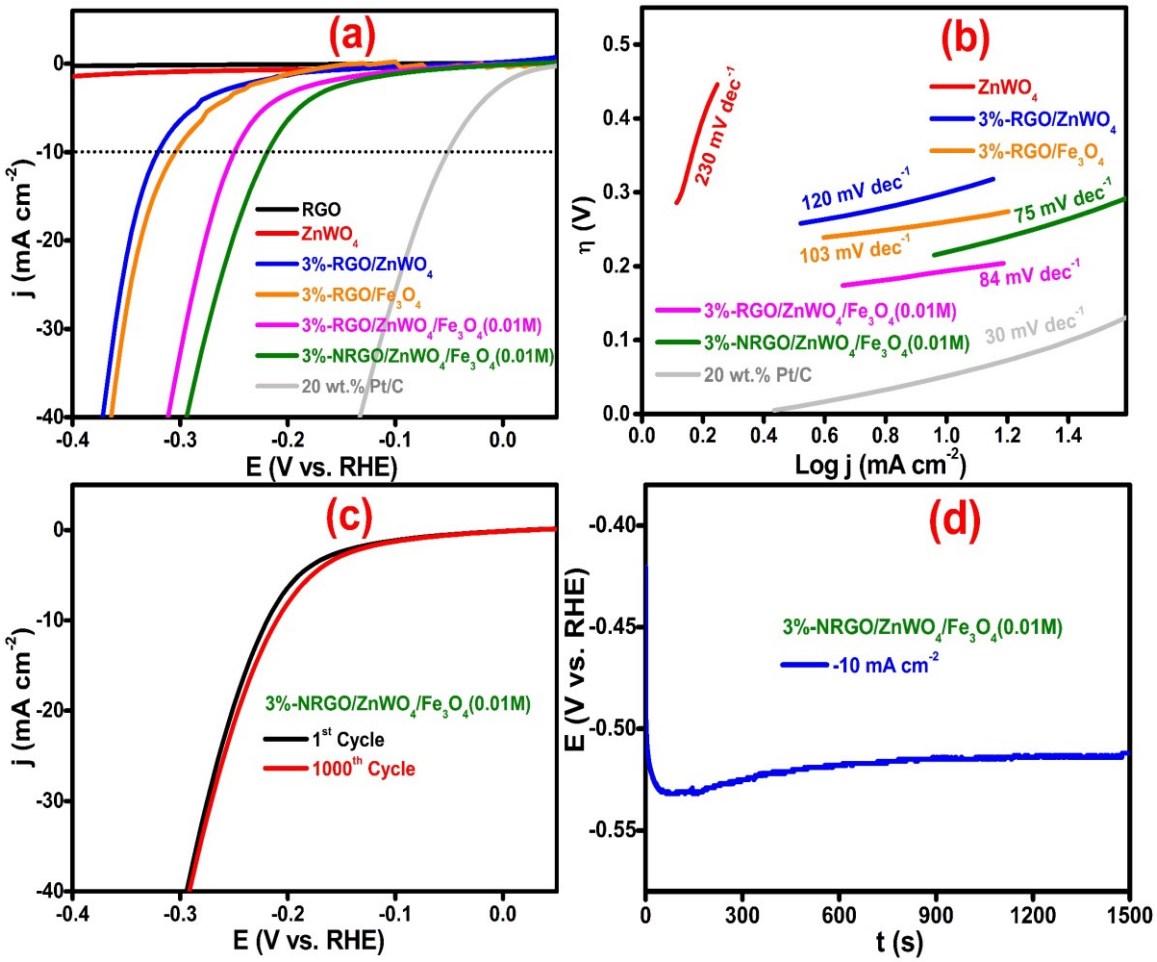


**Figure 2.23** (a) LSV and (b) Tafel slope curve for different electrode materials. (c) Stability curve of 3%-NRGO/$ZnWO_4$/$Fe_3O_4$ (0.01 M) nanocomposite and (d) Chrono-potentiometry curves at -10 mA $cm^{-2}$ recorded using 3%-NRGO/$ZnWO_4$/$Fe_3O_4$ (0.01 M) nanocomposites.

These results indicate a small Tafel slope with low overpotential for 3%-NRGO/$ZnWO_4$/$Fe_3O_4$ (0.01 M) electrode compared to other materials signaling much higher electrocatalytic activity of the ternary composite. The observation of small Tafel slope of 75 mV $dec^{-1}$ confirms that the HER here follows the Volmer-Heyrovsky mechanism. However, the activity is lesser than that of the Pt based materials but it is a satisfactory value for a Pt-free catalyst. The measured values of important electrocatalytic parameters for the nanocomposites are listed in Table 2.3. The results indicate that the ternary catalyst is superior in its performance compared to other catalysts.

The stability of the 3%-NRGO/$ZnWO_4$/$Fe_3O_4$ (0.01 M) nanocomposite is studied via cyclic voltammetry (CV) measurements of 1000 cycles in 0.1 M KOH (Figure 2.23c). From the figure, it is evident that, before and after stability test, there is only very small current loss. This indicates that the 3%-NRGO/$ZnWO_4$/$Fe_3O_4$ (0.01 M) catalysts has good electrochemical stability for HER in 0.1 M KOH solution even after 1000 cycles.

**Table 2.3** Comparison of HER electrocatalysis parameter values.

| **Catalysts** | **Onset potential (mV)** | **Over potential (mV)** | **Tafel Slope (mV dec$^{-1}$)** |
|---|---|---|---|
| | **Current density (-10 mA cm$^{-2}$)** | | |
| $ZnWO_4$ | -- | -- | 230 |
| 3%-RGO/$ZnWO_4$ | - 208 | -320.48 | 120 |
| 3%-RGO/$Fe_3O_4$ | - 182 | -304.14 | 103 |
| 3%-RGO/$ZnWO_4$/$Fe_3O_4$(0.01 M) | - 135 | -249.21 | 84 |
| 3%-NRGO/$ZnWO_4$/$Fe_3O_4$(0.01 M) | - 113 | -218.55 | 75 |

Further, the commercial application of the electrocatalyst was studied by chronopotentiometry technique at a constant current density, applied through sufficient period of time. Figure 2.23d shows the chronopotentiometry plots for the 3%-NRGO/$ZnWO_4$/$Fe_3O_4$ (0.01 M) nanocomposites at current density of -10 mA cm$^{-2}$ for a duration of 1500 seconds. The observed result shows that the initially high potential later slowly decreases and then reaches a stabilized state of HER. This phenomenon is attributed to the development of $H_2$ bubbles on the electrode surfaces. Overall, the results demonstrate that the 3%-NRGO/$ZnWO_4$/$Fe_3O_4$ (0.01 M) nanocomposite is indeed a highly efficient cathode material for electrolytic HER in alkaline medium.

## 2.4 CONCLUSIONS

In summary, a simple microwave irradiation method for the synthesis of novel noble metal free ternary NRGO/$ZnWO_4$/$Fe_3O_4$ nanocomposites is reported. The

structural, surface morphological and optical properties of the as-synthesized NRGO/$ZnWO_4$/$Fe_3O_4$ nanocomposites are studied by XRD, SEM, FESEM, TEM, HRTEM, XPS, EDX, Raman, PL and UV-Vis spectroscopic techniques. The visible light photocatalytic activities of the as-prepared nanocomposites are evaluated using MB solution as substrate. It is observed that 3 wt.% NRGO/$ZnWO_4$/$Fe_3O_4$ (0.01 M) is the optimum concentration for efficient catalysis of MB decomposition. The decomposition process is completed in 120 minutes. The enhanced photocatalytic activity of the nanocomposite may be due to the synergistic effects from its components. The nanocomposite showed high activity and high stability, even after 5 cycles of photocatalytic processes. Also, the resulting nanocomposite possess outstanding catalytic activity in the reduction of 4-NP to 4-AP in the presence of $NaBH_4$ which is completed in 30 seconds. The catalyst showed good stability, recyclability (10 cycles) and high catalytic performance due to its synergistic chemical adsorption and electron transfer effects. Additionally, the electrocatalytic activity of HER in 0.1M KOH solution is investigated. It showed a lesser onset potential and overpotential of -113 mV and -218.55 mV at a current density of -10 mA $cm^{-2}$. The observed Tafel slope of 75 mV $dec^{-1}$ suggests that the Volmer-Heyrovsky mechanism is operating in the HER process. Further, the nanocomposite exhibited good durability and high activity for HER even after 1000 cycles.

# CHAPTER - 3

# MICROWAVE SYNTHESIS OF NRGO/$NiWO_4$/ZnO TERNARY NANOCOMPOSITE AS AN EFFICIENT CATALYST FOR PHOTODEGRADATION OF MB, REDUCTION OF 4-NP AND ELECTROLYTIC HER

***Chapter 3*** *deals with the microwave synthesis of NRGO/$NiWO_4$/ZnO ternary nanocomposite as an efficient catalyst for photodegradation of MB, reduction of 4-NP and electrolytic HER.*

## 3.1 INTRODUCTION

In last few decades, water pollution due to industrial effluents has become a huge menace to the environment (Chen et al. 2016). Waste water released from various industries containing toxic chemicals has posed a threat to aquatic as well as human life. In such a situation development of new strategies for environmental remediation is the need of the day. Photocatalysis has emerged as a savior in this respect. Nanoparticles like ZnO, NiO, $TiO_2$, $Fe_3O_4$, $Co_3O_4$ and their composites have shown a great promise as photocatalysts due to their excellent physical and chemical properties (Bhatt and Bhat 2012, Selvakumar and Bhat 2012, Ahmad et al. 2013). Likewise, metal tungstates have also attracted attention due to their band gap tunability when coupled with other semiconductors (Hisatomi et al. 2014, Pirhashemi and Yangjeh 2017). RGO is a single-atom thick sheet formed by $sp^2$-bonded carbon atoms packed into a 2D hexagonal lattice. It has desirable properties like large surface area; better chemical and mechanical strength; good optical, electrical and thermal properties (Subramanya and Bhat 2015).

In order to achieve excellent catalytic performance in nanocomposites, two important factors have to be considered: faster electron transfer and better charge separation. A combination of semiconductors with suitable band gaps can promote charge carrier separation (Banerjee et al. 2014). There are many reports on the incorporation of carbon nanostructures such as graphene and carbon nanotubes as components of photocatalyst composites to enhance the activity (Zhang et al. 2011, Xiang et al. 2015, Farhadian et al. 2016, Jafari et al. 2016, Keihan et al. 2016). The incorporation of nitrogen atoms which are rich in electrons, into RGO promotes the interaction between neighboring carbons atoms and electrons. NRGO increases the transfer rate of electron from the CB of the semiconductor and also creates an additional donor level above the VB of semiconductors thereby reducing the energy requirement for the excitation of electron from VB to CB of semiconductor materials (Wang et al.

2015). The ternary composites have better charge carrier separation and a fast electron transfer system compared to the pristine semiconductor materials. However, excellent catalytic performance with high stability and low cost are still rare (Chang and Wu 2013).

In view of the aforementioned facts a novel NRGO/$NiWO_4$/ZnO ternary nanocomposite has been efficiently synthesized via a facile, cost effective microwave irradiation technique. The as-synthesized nanocomposite was characterized by diffraction, microscopic, spectroscopic techniques to study the elemental composition, morphology and optical properties. The catalytic efficiency of the nanocomposite was studied towards photodegradation of MB dye in aqueous solution, hydrogenation of 4-NP to 4-AP using $NaBH_4$ and HER via electrolysis of water in alkaline medium. The ternary composite shows excellent photocatalytic activity, stability and reusability compared to the pristine materials. This multifunctional catalyst shows a huge promise in environmental remediation and industrial application.

## 3.2 EXPERIMENTAL

### 3.2.1 Preparation of $NiWO_4$ and ZnO Nanomaterials

To synthesize $NiWO_4$, 0.01 M of nickel acetate solution and 0.01 M of sodium tungstate solution were stirred for 1 hour. The mixture was irradiated with microwave for 10 minutes at 350 W. The obtained precipitate was cooled, centrifuged and washed with water and ethanol. It was finally dried at 80 °C for 12 hours. For synthesis of ZnO the same procedure was employed, but by using zinc acetate and sodium hydroxide solution in 1:2 ratio.

### 3.2.2 Preparation of the NRGO/$NiWO_4$/ZnO Ternary Nanocomposites

GO was prepared by modified Hummers method as given in section 2.2.2. (A)-NRGO/$NiWO_4$/(B)-ZnO ternary nanocomposites (A = 0.5, 1, 2.5 and 5 wt. % GO; B = 0 M, 0.005 M, 0.01 M and 0.02 M of zinc precursor solution) were synthesized via microwave irradiation method. In a typical synthesis, 0.01 M of nickel acetate solution and 0.01 M of sodium tungstate solution was slowly added to the dispersed GO solution under consistent stirring for approximately 2 hours. During this calculated amount of

zinc acetate and sodium hydroxide was also added. The pH of the solution was maintained at 9 using ammonia. Later, 1 % urea was added to the above mixture. The resulting solution was irradiated with microwave (350 W) for 10 minutes and the obtained precipitate was allowed to cool naturally. The precipitate was centrifuged and washed several times with water and ethanol and then finally dried at 80 °C for 12 hours. Control sample containing RGO was synthesized in the absence of urea.

### 3.2.3 Characterization and Catalytic Studies

The characterization of the synthesized samples was carried out as given in section 2.2.9. In addition to that nitrogen adsorption and desorption experiments were performed at 77 K on a Micromeritics ASAP 2020 system. Prior to analysis, the samples were degassed at 200 °C in vacuum for 24 hours. The specific surface area was calculated by the BET method based on adsorption data in the relative pressure ($P/P^o$) range of 0.05 to 0.3. The pore size distribution was calculated using the Barrett-Joyner-Halenda (BJH) model applied to the desorption branch. The catalytic studies were performed as described in section 2.2.10 - 2.2.12.

## 3.3 RESULTS AND DISCUSSION

### 3.3.1 XRD Studies

Figure 3.1 shows the XRD patterns of the as-synthesized GO, $NiWO_4$, ZnO and 2.5%-NRGO/$NiWO_4$/ZnO (0.01M). The diffraction peak at 10.5° corresponds to (002) planes of GO sheets. ZnO diffraction peaks at 31.6°, 34.2°, 36.1°, 47.4°, 56.4°, 62.7°, 66.2°, 67.8° and 68.9° can be indexed to the (100), (002), (101), (102), (110), (103), (200), (112) and (201) as indicated in JCPDS file no. 36-1451 (Bhat 2008). $NiWO_4$ diffraction peaks at 19.2°, 24.1°, 24.8°, 30.9°, 31.5°, 36.7°, 38.7°, 41.6°, 44.9°, 49.1°, 50.6°, 52.0°, 54.2°, 65.2° and 68.6° is ascribed to the (100), (011), (110), (111), (020), (002), (200), (102), (112), (022), (220), (130), (202), (132) and (041) planes according to JCPDS file no. 15-0755. Peaks corresponding to NRGO were not found in the diffraction pattern of ternary composite. This may be due to the small quantity and exfoliated nature of NRGO in the composite (Sudhakar et al. 2014).

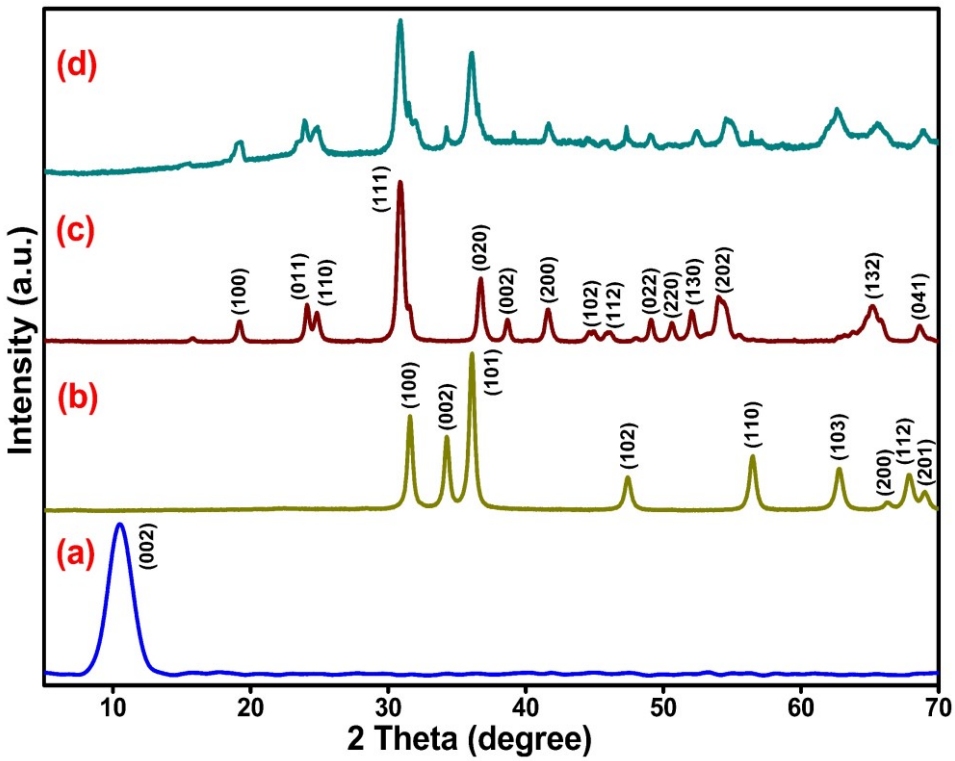


**Figure 3.1** XRD spectrum of (a) GO, (b) $NiWO_4$, (c) ZnO and (d) 2.5%-NRGO/$NiWO_4$/ZnO (0.01M).

### 3.3.2 Raman Studies

Raman spectrum of GO (Figure 3.2a) reveals two distinct modes: G mode at 1599 $cm^{-1}$ and D mode at 1355 $cm^{-1}$. The intensity ratios of D to G band ($I_D/I_G$) is a measure of relative concentration of $sp^3$ hybridized defects to $sp^2$ hybridized GO domains (Subramanya and Bhat 2014). We see that after microwave irradiation the $I_D/I_G$ ratio increases from 0.87 for GO to 1.09 for the composite indicating the formation of more defects in NRGO (Figure 3.2b) during the reduction. Slight variation in the Raman frequency, appearance of a prominent 2D band at 2639 $cm^{-1}$ in Figure 3.2b may be attributed to the formation of NRGO from GO. Figure 3.2c shows the Raman spectrum of 2.5%-NRGO/$NiWO_4$/ZnO (0.01M) ternary nanocomposite. Raman bands at 785 $cm^{-1}$, 901 $cm^{-1}$ and 1038 $cm^{-1}$ correspond to Raman active modes of $NiWO_4$. Bands at 115 $cm^{-1}$, 337 $cm^{-1}$, 410 $cm^{-1}$, 431 $cm^{-1}$, 535 $cm^{-1}$, 860 $cm^{-1}$, 1098 $cm^{-1}$, 1750 $cm^{-1}$, 2275 $cm^{-1}$ and 2813 $cm^{-1}$ correspond to the Raman active modes of ZnO. Peaks at 1379 $cm^{-1}$ (D mode); 1609 $cm^{-1}$ (G mode) with $I_D/I_G$ ratio 1.10 and 2D band at 2639 $cm^{-1}$ with $I_{2D}/I_G$ ratio as 1.06 correspond to presence of double layered NRGO with defects in the ternary

composite. The change in the value of Raman frequencies of D and G band and increased value of $I_D/I_G$ ratio in the composite may be due to the interaction between the NRGO sheets and the semiconductor particles (Graf et al. 2007).

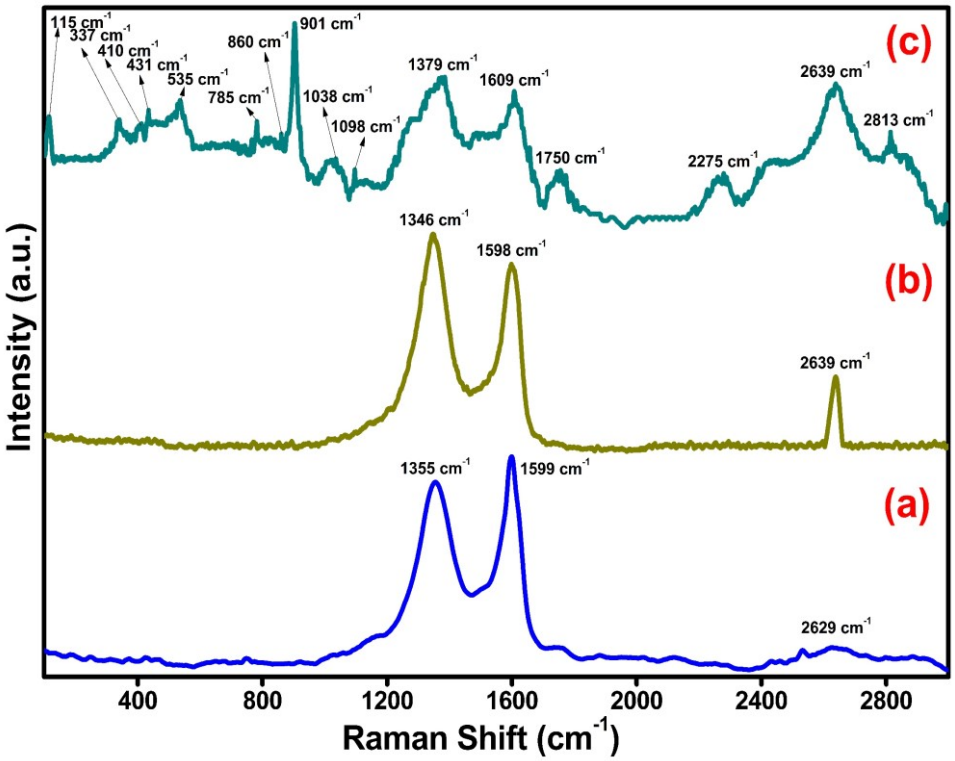


**Figure 3.2** Raman spectra of (a) GO, (b) NRGO and (c) 2.5%-NRGO/$NiWO_4$/ZnO (0.01M).

### 3.3.3 BET Surface Area Analysis

The nitrogen adsorption-desorption isotherms were used to obtain information about the BET specific surface area and pore size distribution in the nanocomposites (Subramanya and Bhat 2014). As observed in Figure 3.3, the isotherm exhibits a characteristic type-IV pattern with a significant hysteresis in the $P/P_o$ range 0.6-1.0, implying the existence of abundant mesopores in the synthesized nanocomposites. The slightly wide capillary condensation step is a consequence of the relatively broad pore size distribution, as shown in Figure 3.3.

BET analysis showed that the specific surface area of $NiWO_4$, 2.5%-NRGO/$NiWO_4$ and 2.5%-NRGO/$NiWO_4$/ZnO (0.01 M) are 25.25 $m^2/g$, 34.64 $m^2/g$ and 38.83 $m^2/g$, respectively. From these results, it is evident that the higher surface area of

2.5%-NRGO/$NiWO_4$ and 2.5%-NRGO/$NiWO_4$/ZnO (0.01 M) nanocomposites than that of pure $NiWO_4$, is due to the contribution from NRGO and ZnO components. The pore size distribution calculated by the BJH method indicates that the nanocomposite has a hierarchical pore structure, the sizes of which peak at 3.34 nm and 5.61 nm. The presence of such mesopores is believed to increase the total surface area which in turn would enhance the catalytic activity of the ternary nanocomposites.

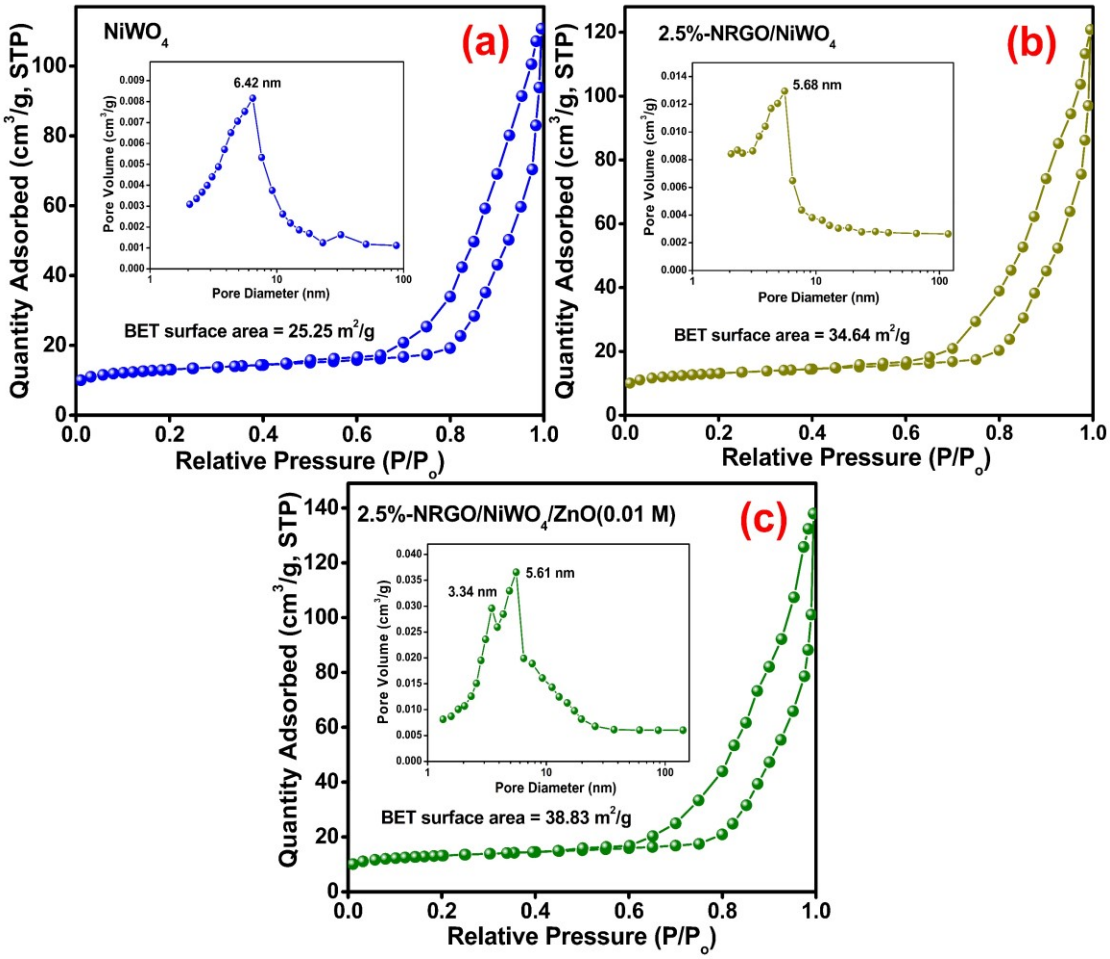


**Figure 3.3** BET surface area analysis: Adsorption-desorption isotherms.

### 3.3.4 Morphology Studies

The morphology of the samples was studied using electron microscopy. The FESEM images of the $NiWO_4$ and ZnO (Figure 3.4a-b) suggest that the particles have approximately spherical shape. Similarly (Figure 3.5a) reveals that the 2.5%-NRGO/$NiWO_4$/ZnO (0.01 M) ternary nanocomposite consists of ZnO and $NiWO_4$ nanoparticles well anchored on the surface of the NRGO sheets. This observation is

further supported by the TEM image (Figure 3.5b). EDX spectra of the encircled areas are shown in Figure 3.5c-d. The average size of the nanoparticles was found to be 13.4 nm for $NiWO_4$ and 22.7 nm for ZnO (Figure 3.6). HRTEM image in Figure 3.7a shows the interface between $NiWO_4$, ZnO and NRGO in 2.5%-NRGO/$NiWO_4$/ZnO (0.01 M) ternary nanocomposite. The obtained lattice fringes of 0.15 nm correspond to the (111) plane of $NiWO_4$ and that of 0.283 nm correspond to the (100) plane of ZnO. The EDX spectrum (Figure 3.7b) revealed N, C, O, Ni, Zn and W as the elements present in the composite. The elemental mapping shown in Figure 3.7c-h indicates the uniform distribution of the particles in the composite.

### 3.3.5 XPS Studies

The XPS survey spectrum of 2.5%-NRGO/$NiWO_4$/ZnO (0.01 M) nanocomposites is shown in Figure 3.8 and detailed elemental compositions are summarized in Table 3.1.

The binding energy positions in the XPS spectrum were calibrated with C 1s at 284.8 eV. Figure 3.9a shows the C 1s spectra which can be deconvoluted into five peaks at 284.5 eV (C-C/C=C), 285.5 eV (C-N), 286.1 eV (C-O), 287.2 eV (C=O) and 290.2 eV (O-C=O), respectively (Zhang et al. 2016). Figure 3.9b reveals the N 1s spectra which can be deconvoluted into four peaks at 398.4 eV (pyridinic-N), 399.4 eV (pyrrolic-N), 400.8 eV (graphitic-N) and 402.4 eV (pyridine-N-oxide), respectively (Li et al. 2009, Zhang et al. 2016). Figure 3.9c depicts Ni 2p spectra deconvoluted into six peaks located at 855.9 eV, 857.7 eV (satellite), 861.6 eV which belongs to Ni $2p_{3/2}$ and 873.6 eV, 875.4 eV (satellite), 879.5 eV which belongs to the Ni $2p_{1/2}$, respectively (Chen et al. 2016). Figure 3.9d shows the W 4f spectra deconvoluted into four peaks corresponding to W $4f_{7/2}$ (34.8 eV and its satellite 35.4 eV) and W $4f_{5/2}$ (36.9 eV and its satellite 37.5 eV), respectively. Figure 3.9e shows the Zn 2p spectra deconvoluted into four peaks placed at 1018.1 eV, 1019.6 eV (satellite) which belongs to Zn $2p_{3/2}$ and 1041.1 eV, 1042.5 eV (satellite) belongs to the Zn $2p_{1/2}$, respectively (Xu et al. 2016). Figure 3.9f reveals O 1s spectra deconvoluted into three peaks at 530.2 eV, 532.2 eV and 533.1 eV related to ZnO, $NiWO_4$ and H-O-H bonds, respectively.

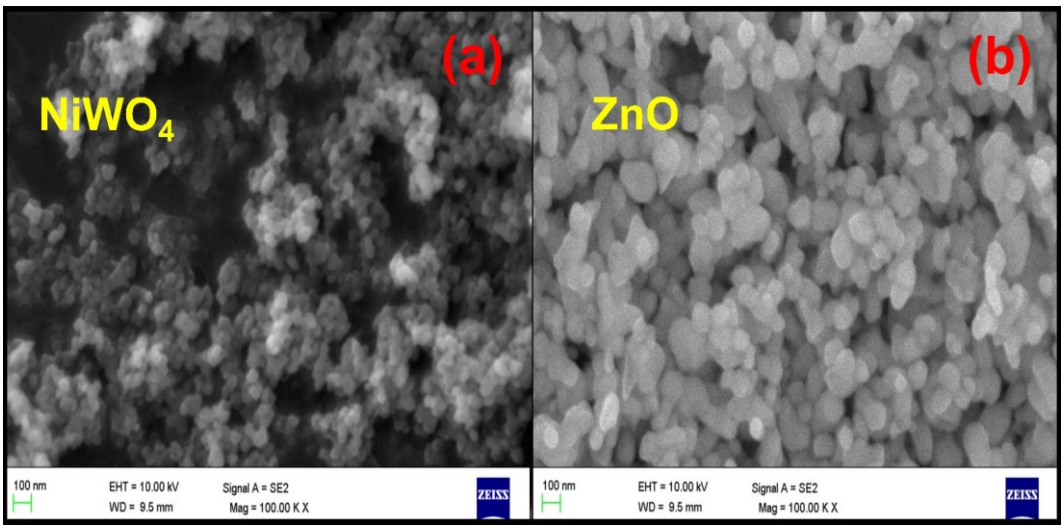


**Figure 3.4** FESEM TEM image of (a) $NiWO_4$ and (b) ZnO nanoparticles.

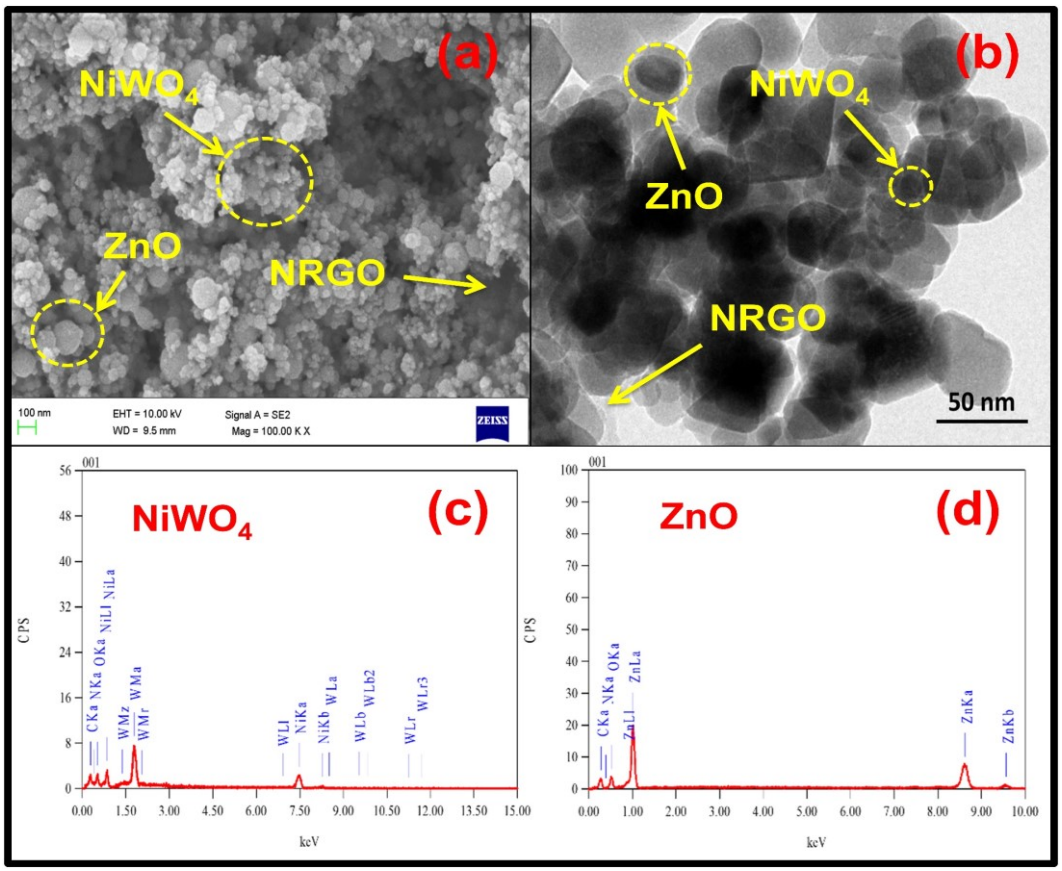


**Figure 3.5** (a) FESEM, (b) TEM image of 2.5%-NRGO/$NiWO_4$/ZnO (0.01 M) ternary nanocomposite, EDX spectrum of (c) $NiWO_4$ and (d) ZnO nanoparticles present in the ternary composite.

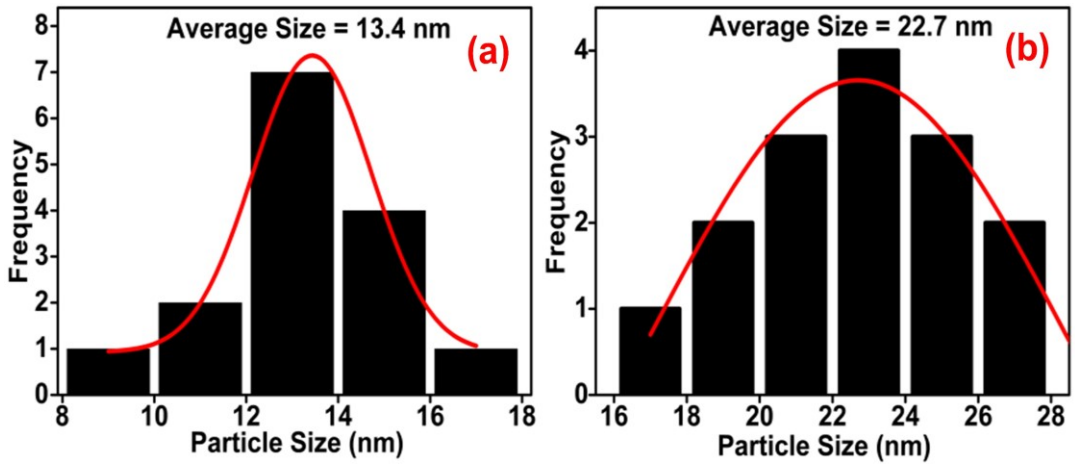


**Figure 3.6** Average particle size of $NiWO_4$ and ZnO obtained from TEM analysis.

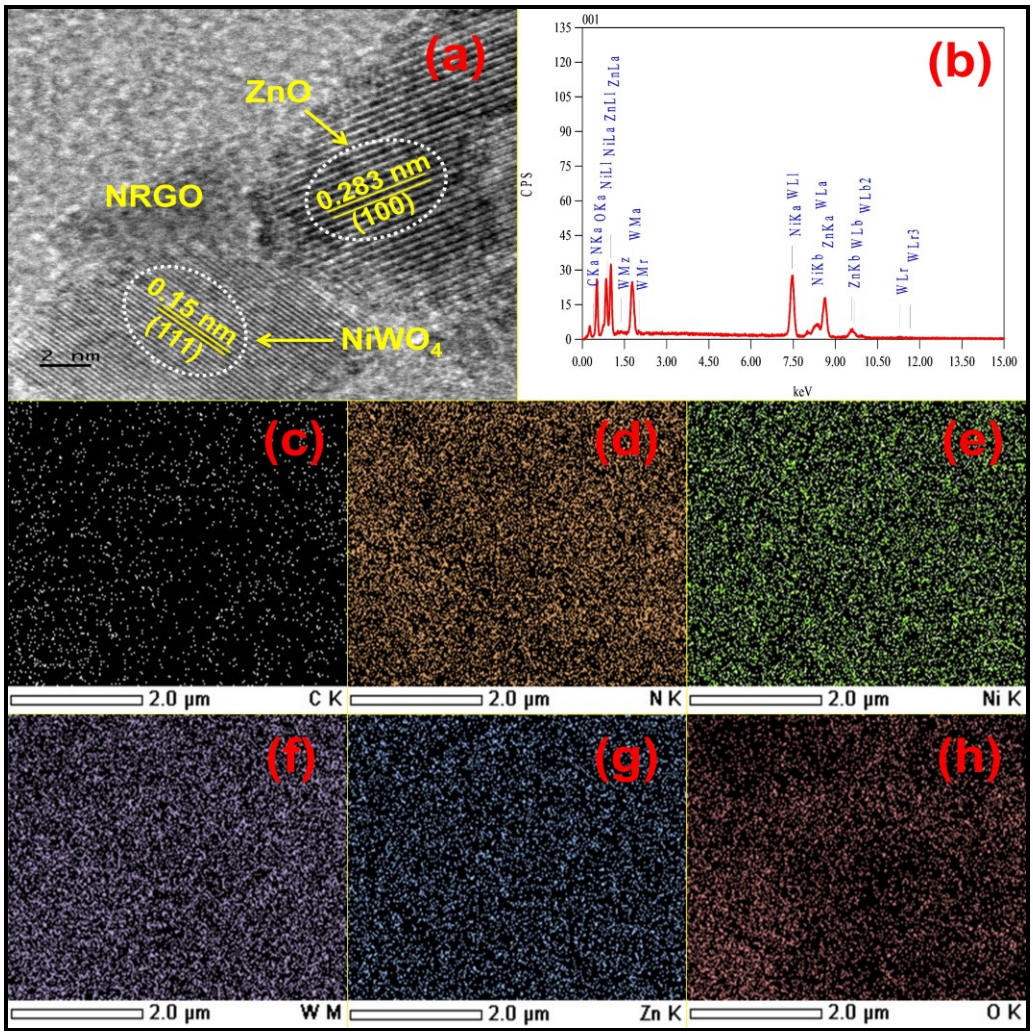


**Figure 3.7** (a) HRTEM image, (b) EDX spectrum, elemental mapping of (c) C, (d) N, (e) Ni, (f) W, (g) Zn and (h) O of 2.5%-NRGO/$NiWO_4$/ZnO (0.01 M) ternary nanocomposite.

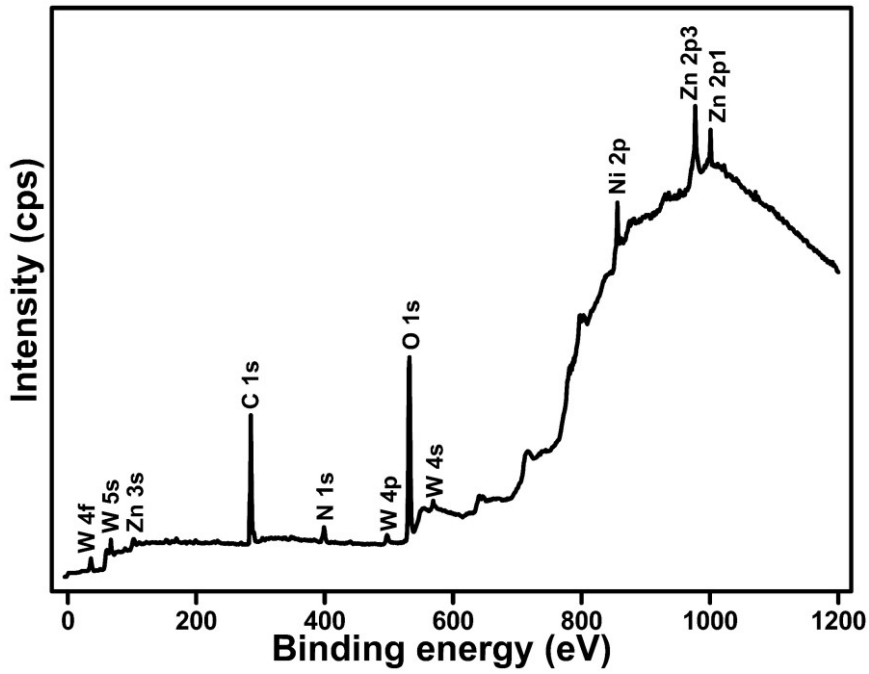


**Figure 3.8** XPS survey spectrum of 2.5%-NRGO/$NiWO_4$/ZnO (0.01 M) ternary nanocomposite.

**Table 3.1** Surface elemental composition with relative intensities of C 1s, N 1s, Ni 2p, W 4f, Zn 2p, O 1s peaks of 2.5%-NRGO/$NiWO_4$/ZnO (0.01 M) nanocomposite from XPS.

| **XPS** | **Total Content** | | | | | |
|---|---|---|---|---|---|---|
| **Elements** | **C** | **N** | **Ni** | **W** | **Zn** | **O** |
| **At %** | 18.37 % | 3.05 % | 11.24 % | 6.78 % | 27.52 % | 33.04 % |
| **C 1s** | **C-C** | **C-N** | **C-O** | **C=O** | **O-C=O** | |
| | 70.15 % | 14.34 % | 8.51 % | 5.06 % | 1.94 % | |
| **N 1s** | **Pyridinic-N** | **Pyrrolic-N** | **Graphitic-N** | **Pyridinic-N-Oxide** | | |
| | 32.09 % | 43.57 % | 13.41 % | 10.93 % | | |
| **Ni 2p** | **Ni $2p_{3/2}$** | | **Sat.** | **Ni $2p_{1/2}$** | | |
| | 34.32 % | 25.83 % | 11.20 % | 11.51 % | 7.56 % | |
| **W 4f** | **W $4f_{7/2}$** | | | **W $4f_{5/2}$** | | |
| | 37.53 % | 20.36 % | | 23.15 % | 18.96 % | |
| **Zn 2p** | **Zn $2p_{3/2}$** | | | **Zn $2p_{1/2}$** | | |
| | 35.86 % | 31.09 % | | 18.27 % | 14.78 % | |
| **O 1s** | **Zn-O** | | **W-O-W** | **H-O-H** | | |
| | 51.52 % | | 38.94 % | 9.54 % | | |

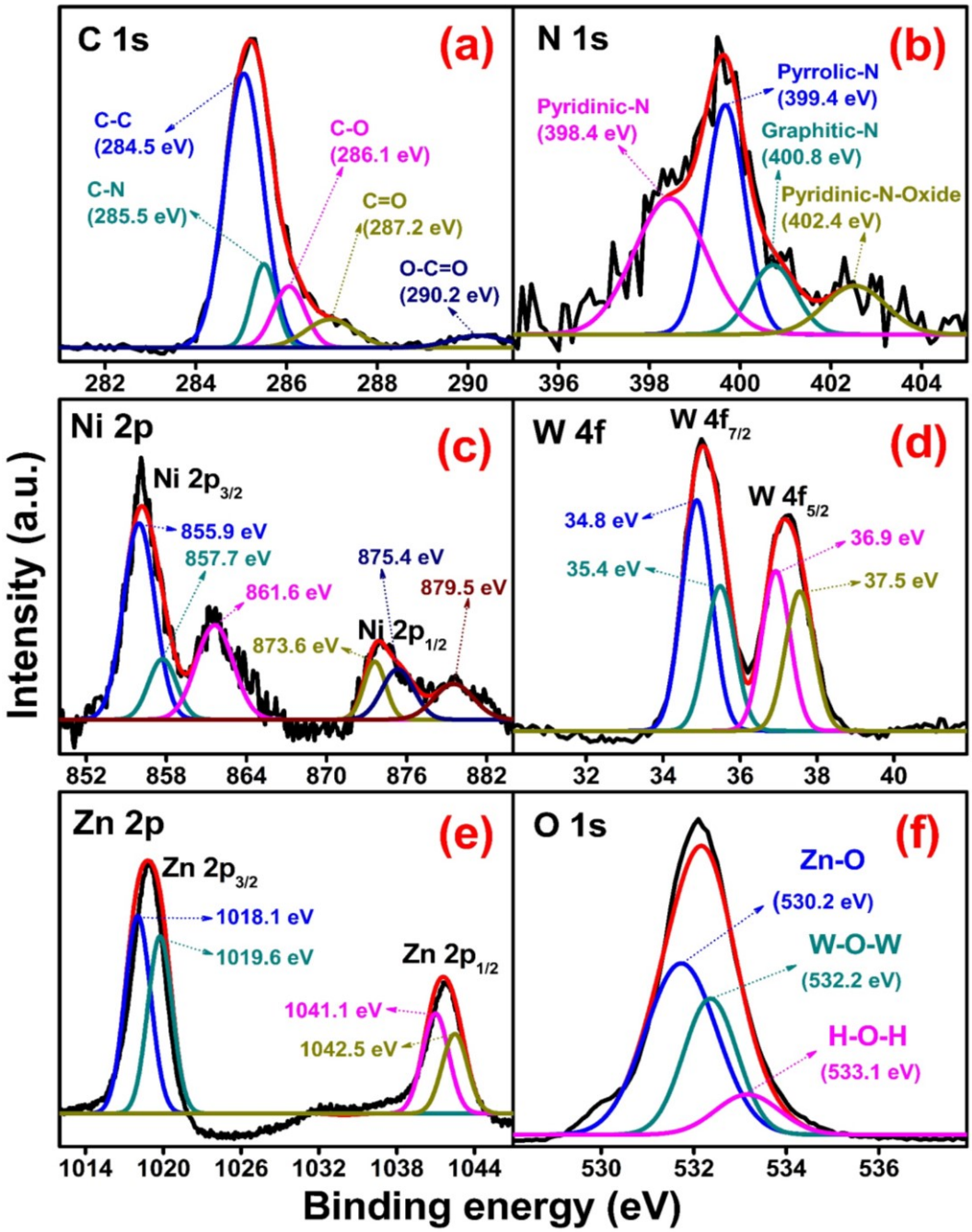


**Figure 3.9** High-resolution XPS spectra of 2.5%-NRGO/$NiWO_4$/ZnO (0.01 M) (a) C 1s, (b) N 1s, (c) Ni 2p, (d) W 4f, (e) Zn 2p and (f) O 1s.

### 3.3.6 Optical Absorbance Analysis

The optical properties of the as-synthesized nanocomposites are studied by DRS. The absorption of 2.5%-NRGO/ZnO and 2.5%-NRGO/$NiWO_4$ (Figure 3.10a) is high in comparison to pure ZnO and $NiWO_4$. The optical energy band gap (Figure

3.10b) of the nanocomposites was measured using the Tauc relation (equation 2.3) as in the previous chapter. The obtained band gap energy values of ZnO, $NiWO_4$, 2.5%-NRGO/ZnO, 2.5%-NRGO/$NiWO_4$ and 2.5%-NRGO/$NiWO_4$/ZnO (0.01 M) are 3.0 eV, 3.10 eV, 2.82 eV, 2.42 eV and 2.27 eV, respectively. From the results, it is evident that there is an appreciable reduction in the band gap energy of the ternary nanocomposite in comparison with other components. This may be attributed to the synergic effect of the composite components, ZnO and NRGO leading to appreciable interaction among the components causing formation of new molecular orbitals of lower energy.

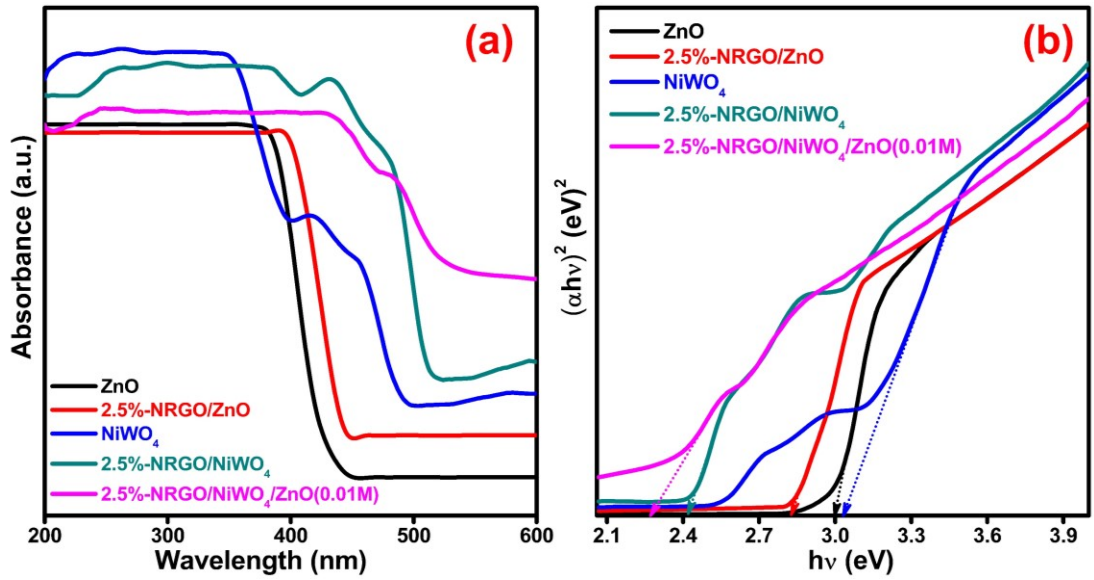


**Figure 3.10** (a) UV-Vis spectra and (b) band gap plots of ZnO, $NiWO_4$, 2.5%-NRGO/ZnO, 2.5%-NRGO/$NiWO_4$ and 2.5%-NRGO/$NiWO_4$/ZnO (0.01 M).

Using the DRS results, the band edge positions of the nanocomposites were calculated theoretically using Mulliken electronegativity theory following the empirical equations 2.5 and 2.6 from chapter 2. The calculated band edge potentials of the CB and VB of ZnO and $NiWO_4$ are given in Table 3.2.

**Table 3.2** Band gap parameters of $NiWO_4$ and ZnO

| Samples | χ (eV) | $E_g$ (eV) | $E_{VB}$ (eV) | $E_{CB}$ (eV) |
|---|---|---|---|---|
| **$NiWO_4$** | 6.301 | 3.1 | 3.351 | 0.251 |
| **ZnO** | 5.792 | 3.0 | 2.792 | -0.208 |

### 3.3.7 Photoluminescence Analysis

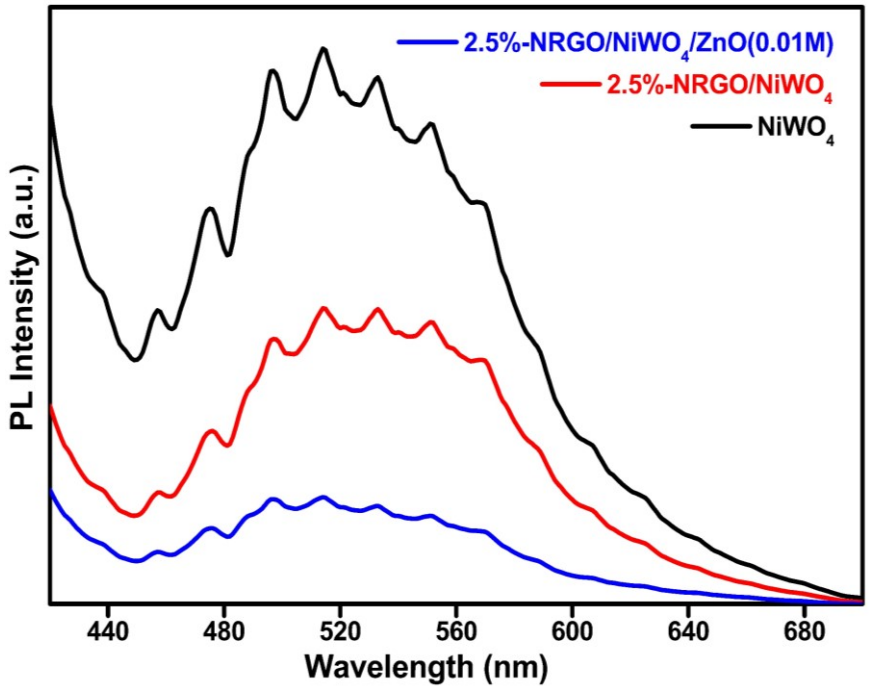


**Figure 3.11** PL spectra of $NiWO_4$, 2.5%-NRGO/$NiWO_4$ and 2.5%-NRGO/$NiWO_4$/ZnO (0.01 M) ternary nanocomposite.

An efficient photocatalyst should have very less recombination rate of photogenerated electron hole pair. The recombination of photogenerated electron-holes and charge separation in the ternary nanocomposite were investigated through PL emission spectrum as shown in Figure 3.11. An intense PL peak corresponds to faster recombination rate of photo generated electron-hole pairs (Wang et al. 2015). All the synthesized materials exhibited a broad emission peak in the visible region starting from 420 nm to 700 nm with the excitation wavelength of about 400 nm. Pure $NiWO_4$ showed an intense broad peak around 520 nm indicating rapid recombination of charge carriers. Introduction of NRGO led to slight decrease in PL intensity. The higher conductivity of the NRGO sheet matrix facilitates smooth electron transport and hence results in the increased separation of electron hole pairs (Ma et al. 2015). Further, when ZnO is introduced, the PL spectrum of 2.5%-NRGO/$NiWO_4$/ZnO (0.01 M) nanocomposite exhibits very less intensity. This can be ascribed to the contribution of ZnO towards further separation of electron hole pairs. In the ternary composite, electrons are excited from VB to CB of ZnO and then immediately transported to the

CB of $NiWO_4$ due to favorable energy level difference. From CB of $NiWO_4$ electrons would get transported through NRGO network due to the high conductivity of NRGO. Thus, the entire process results in an efficient and enhanced separation of electron hole pairs and leads to appreciable decrease in the PL intensity in 2.5%-NRGO/$NiWO_4$/ZnO (0.01 M) nanocomposite (Meng et al. 2014, Ma et al. 2015, Wang et al. 2015).

### 3.3.8 Photocatalytic Activity

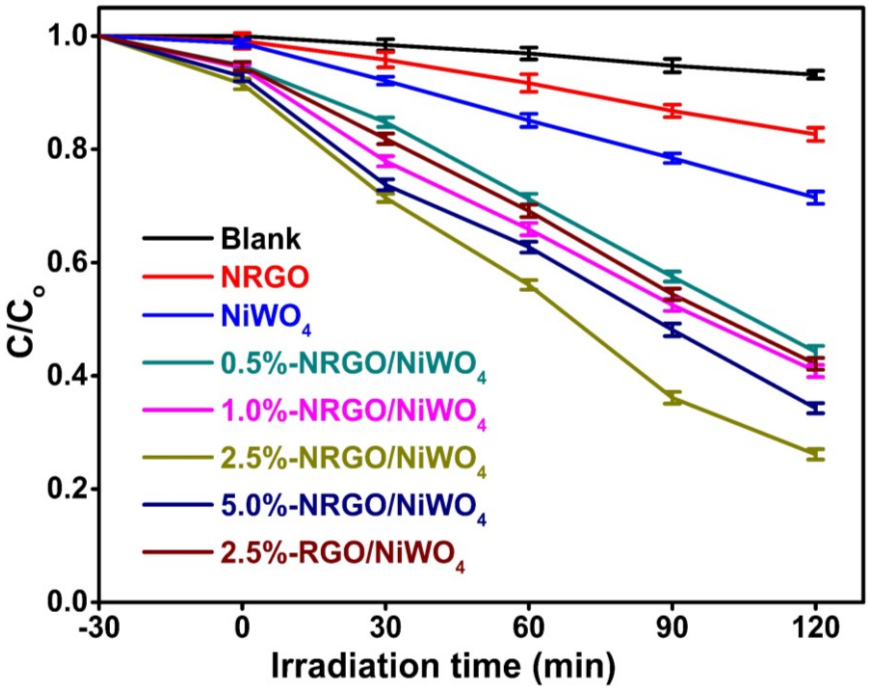


**Figure 3.12** Degradation rates of MB under visible light photocatalysis by NRGO/$NiWO_4$ composites.

The efficiency of the as-synthesized nanocomposite as a photocatalyst was studied using MB as substrate in aqueous media under visible light irradiation. The blank test was performed without adding nanocomposite to MB solution. There was no noticeable degradation which indicated that the photolysis is insignificant for the blank MB solution. The NRGO composition in the nanocomposite was optimized based on the photodegradation efficiency. The photocatalytic efficiency of catalyst with varying NRGO content (Figure 3.12) indicates that with increase in NRGO content the efficiency increases up to 2.5 % NRGO and decreases there onwards. This decrease in efficiency may be due to NRGO sheets covering the surface of semiconductor which in

turn hinders the absorption of photon by the semiconductor. Such observations are well documented in the literature (Zhang et al. 2011, Dai et al. 2013, Xiang et al. 2015). Hence NRGO content was kept constant at 2.5 % and ZnO content was varied for further experiments.

The photocatalytic degradation efficiency with varied ZnO content (Figure 3.13a) showed increase in efficiency with increase in ZnO content up to 0.01 M ZnO. 2.5%-NRGO/$NiWO_4$/ZnO (0.01 M) ternary composite showed maximum efficiency by degrading MB dye within 120 minutes. For sake of comparison even RGO composites were considered. RGO composites showed lesser efficiency than NRGO composites.

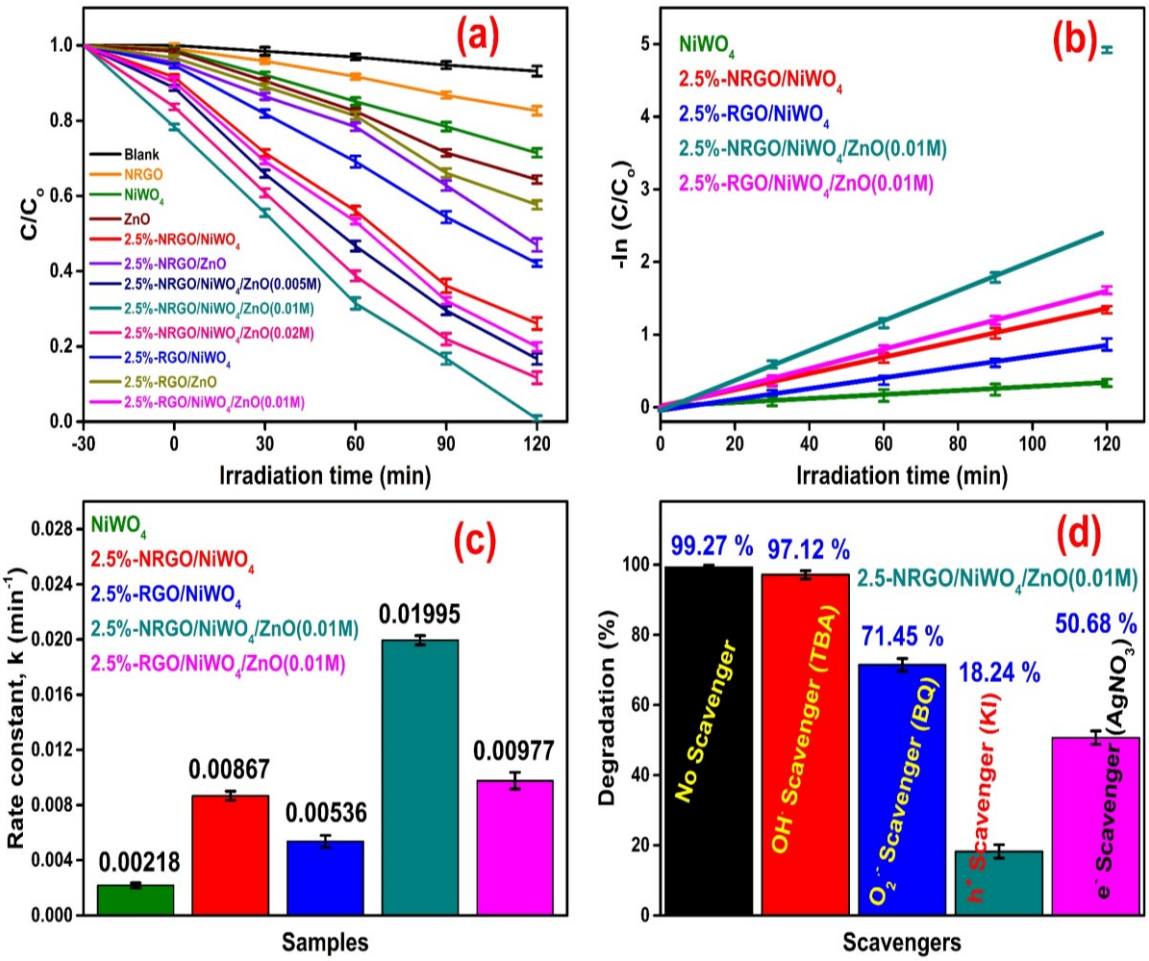


**Figure 3.13** (a) Degradation rate, (b) first order kinetics plot, (c) rate constants plot for the photodegradation of MB over various catalysts and (d) effects of different scavengers on the photodegradation of MB using NRGO/$NiWO_4$/ZnO ternary composites under visible light irradiation.

The as-prepared nanocomposite showed first order kinetics for photocatalytic degradation of MB solution as given in equation (2.4) in the previous chapter. The rate constant (k) values were calculated from the slope of the straight line (Figure 3.13b). Figure 3.13c shows the rate constant values of different nanocomposites. The first order rate constants of ternary composite show 9 and 2.5 times more photocatalytic efficiency than that for pure $NiWO_4$ and 2.5%-NRGO/$NiWO_4$, respectively.

To determine the degree of mineralization of MB, during its photodegradation catalyzed by 2.5%-NRGO/$NiWO_4$/ZnO (0.01 M) nanocomposite, TOC analysis was performed (Cui et al. 2013). Figure 3.14a shows the plot of absorbance vs. wavelength for MB at different time intervals. As can be observed from the plot, the absorbance at 664 nm decreased with time and reached 99.27 % during scan at 120 minutes under visible light irradiation. Figure 3.14b shows the TOC values for the MB solution at different intervals of time. The TOC value decreased to 88.28 % under visible light irradiation for 120 minutes of visible light irradiation. Thus, it is very evident that, the 2.5%-NRGO/$NiWO_4$/ZnO (0.01 M) nanocomposite has high catalytic efficiency towards photodegradation of MB molecules and that organic carbon is mostly converted to $CO_2$ during the process.

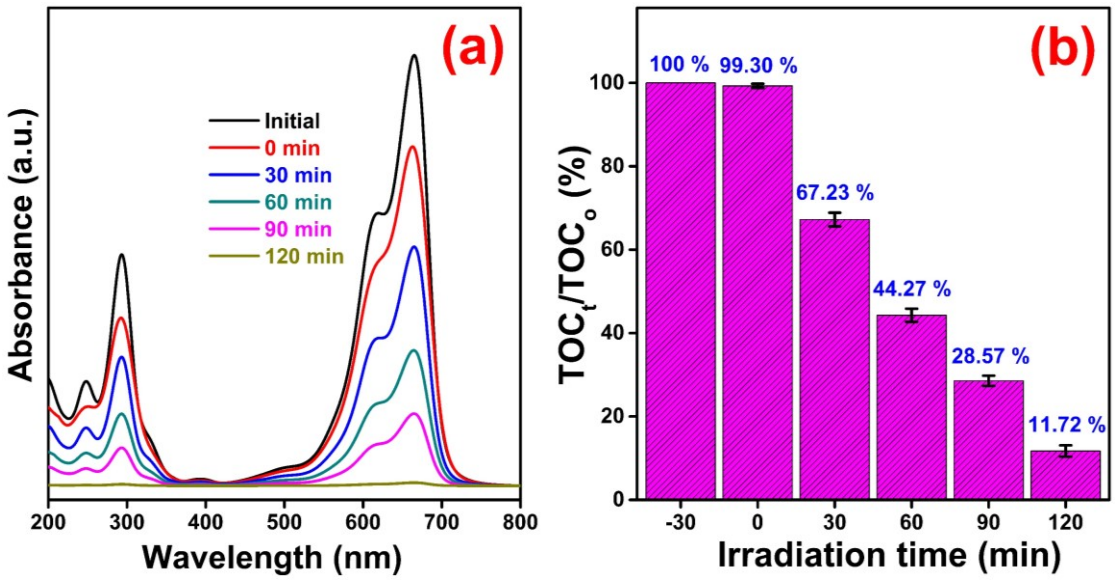


**Figure 3.14** (a) Absorbance versus wavelength and (b) TOC values for the MB solution at different intervals of time.

Further, the recyclability of the ternary nanocomposite has also been investigated. It is observed that even after 5 consecutive cycles (Figure 3.15) the efficiency of the photocatalytic activity of nanocomposite showed only a small reduction from 99.27 % to 96.72 %, which is negligible. The results therefore ascertain that the ternary composite also has sufficient stability for use in environmental applications.

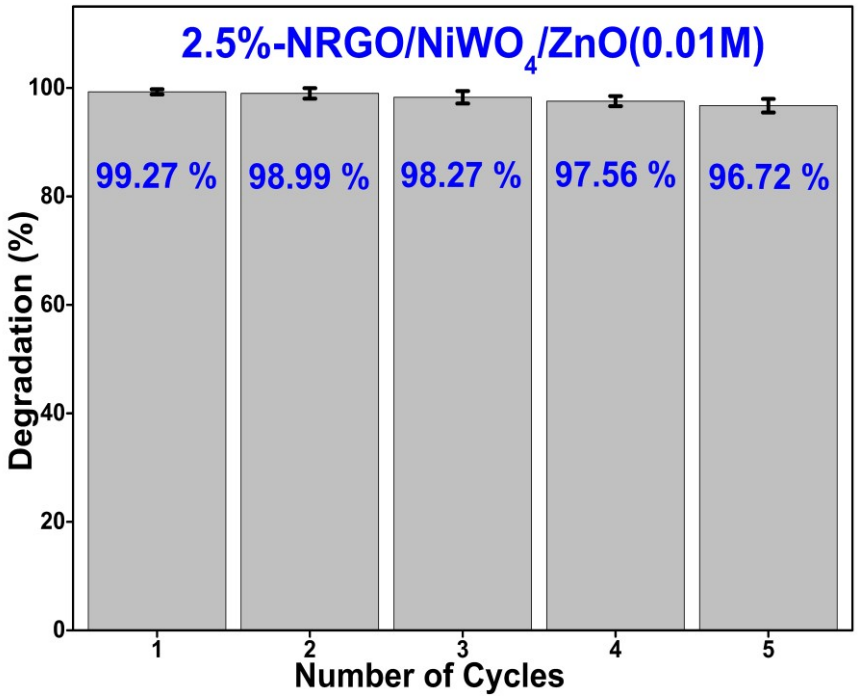


**Figure 3.15** Reusability test of MB using NRGO-$NiWO_4$-ZnO nanocomposites.

### 3.3.9 Mechanism of the Photocatalytic Activity

To determine the active species involved in photodegradation and to find out the mechanism, trapping experiments (Figure 3.13d) were carried using scavenging agents such as, BQ (a quencher of $O_2^{\cdot-}$), KI (a quencher of $h^+$), $AgNO_3$ (a quencher of $e^-$) and TBA (a quencher of $OH^{\cdot}$). Addition of TBA caused only a small decrease in efficiency (97.12 %) which meant hydroxyl radical was not the active species. But addition of KI, $AgNO_3$ and BQ caused dramatic decrease in the efficiency 18.24 %, 50.68 % and 71.45 % respectively. Based on these results the following mechanism is proposed.

$$ZnO + h\upsilon \rightarrow ZnO\ (e^-_{CB} + h^+_{VB}) \quad \text{----------} \quad (3.1)$$

$ZnO\ (e^-_{CB}) + NiWO_4 \rightarrow ZnO + NiWO_4\ (e^-_{CB})$ ---------- (3.2)

$NiWO_4\ (e^-_{CB}) + O_2 \rightarrow NiWO_4 + O_2^{\cdot -}$ ---------- (3.3)

$ZnO\ (h^+_{VB}) + MB \rightarrow CO_2 + H_2O$ + Inorganic species ---------- (3.4)

where $e^-_{CB}$ is the electron in the conduction band and $h^+_{VB}$ is the hole in the valence band, respectively.

A schematic diagram showing mechanism of photodegradation is given in Figure 3.16. When ternary nanocomposite is irradiated with light, the electrons from the VB of ZnO get excited to the CB (Xu et al. 2016). These electrons migrate to the CB of $NiWO_4$ and from there, the electrons get transferred through NRGO matrix towards reaction site. This reduces the recombination rate of electron and holes. Then the electron combines with oxygen to form superoxide radical anion. The holes formed in the process degrade MB into products such as $CO_2$, $H_2O$ and other harmless species.

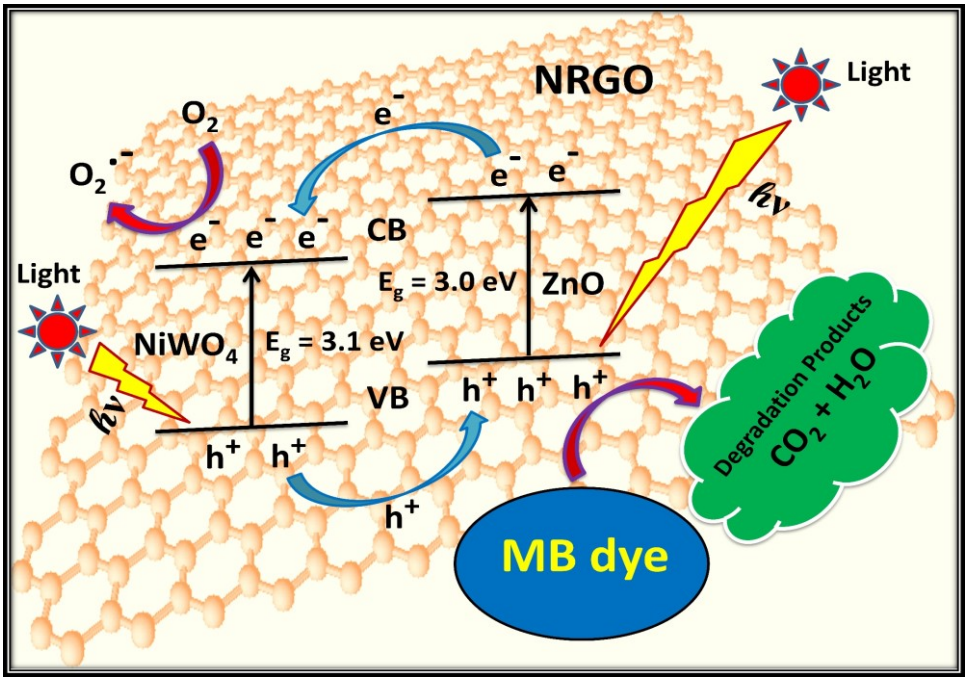


**Figure 3.16** Schematic diagram of photodegradation of MB over NRGO/$NiWO_4$/ZnO ternary nanocomposite under visible light irradiation.

### 3.3.10 Reduction Studies

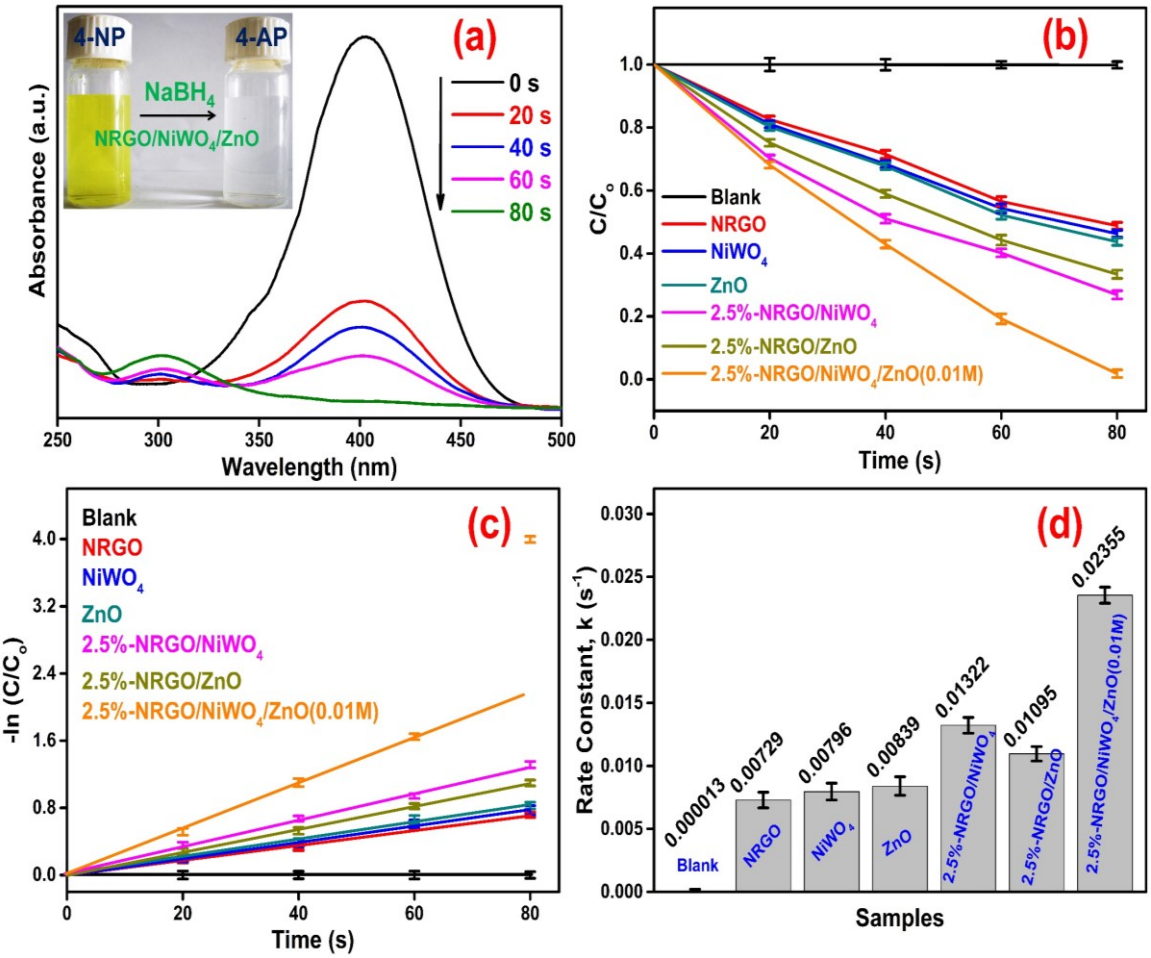


**Figure 3.17** (a) UV-Vis absorption spectra for the reduction of 4-NP to 4-AP by $NaBH_4$ in the presence of NRGO/$NiWO_4$/ZnO nanocomposite, (b) relative concentration plot of 4-NP to 4-AP, (c) kinetics plots and (d) rate constants of conversion of 4-NP to 4-AP using different catalysts.

The catalytic activity of the as-synthesized nanocomposites was evaluated for the reduction of 4-NP by $NaBH_4$ in an aqueous solution. Blank test was carried out in the absence of catalyst which showed negligible reduction of 4-NP. Addition of ternary nanocomposites into the 4-NP solution decreased the intensity of absorption peak of 4-NP found at 400 nm immediately and a new absorption peak corresponding to 4-AP at 300 nm was obtained (Figure 3.17a). The catalytic reduction of 4-NP to 4-AP was completed in 80 seconds. This is better compared to the previously reported literature where in the conversion took 100 seconds (Zheng et al. 2013). For comparison, the

catalytic activity of the individual components of the nanocomposite materials was analyzed and they showed lower catalytic activity than 2.5%-NRGO/$NiWO_4$/ZnO (0.01 M) nanocomposites. The reaction kinetics was studied as in the case of photodegradation of MB dye (Figure 3.17b-d). 2.5%-NRGO/$NiWO_4$/ZnO (0.01 M) nanocomposite showed maximum rate constant 1.78 times higher than 2.5%-NRGO/$NiWO_4$, 2.15 times higher than 2.5%-NRGO/ZnO, 2.81 times than that of ZnO, 2.96 times that of $NiWO_4$ and 3.23 times that of NRGO. Further the stability and reusability of the 2.5%-NRGO/$NiWO_4$/ZnO (0.01 M) ternary nanocomposites was analyzed. The catalyst was recovered and further used. The reused catalyst exhibited excellent catalytic activity even after 10 successive cycles, with nearly 100 % conversion within a time period of 108 seconds (Figure 3.18).

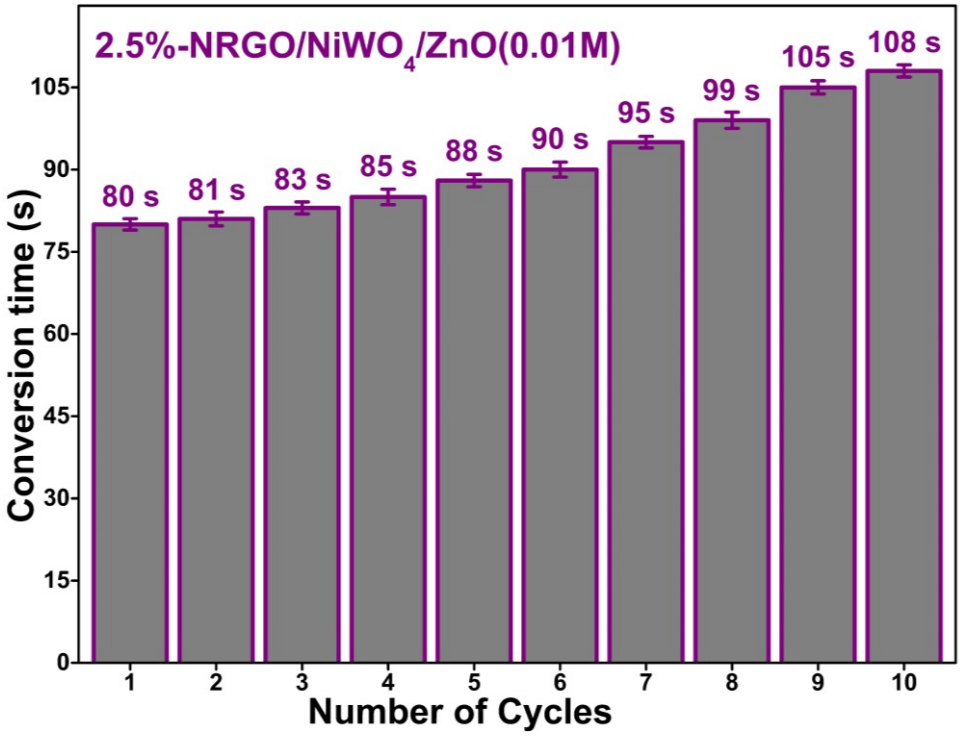


**Figure 3.18** Reusability test for 2.5%-NRGO/$NiWO_4$/ZnO (0.01 M) in the reduction of 4-NP to 4-AP.

### 3.3.11 Electrocatalytic HER Studies

The electrocatalytic performance of the 2.5%-NRGO/$NiWO_4$/ZnO (0.01 M) nanocomposite investigated in 0.1 M KOH solution using a standard three-electrode

system. For the sake of comparison, component materials and 20 wt.% Pt/C were also tested under the same conditions. The polarization curves for the HER on various electrodes are shown in Figure 3.19a. 2.5%-NRGO/$NiWO_4$/ZnO (0.01M) nanocomposites demonstrated a remarkably high activity with an onset potential 101 mV vs RHE and a HER current density of -10 mA $cm^{-2}$ at an overpotential of 257 mV. On the other hand, 2.5%-NRGO/$NiWO_4$ and 2.5%-NRGO/ZnO had an onset potential of 154 mV and 168 mV and current density of -10 mA $cm^{-2}$ at an overpotential of 371 mV and 406 mV, respectively.

The linear regions of the Tafel plots (Figure 3.19b) were fitted to the Tafel equation ($\eta = a + b \log (j)$, where j is the current density and b is the Tafel slope (Tilak and Chen 1993) yielding 93 mV $dec^{-1}$, 134 mV $dec^{-1}$, 150 mV $dec^{-1}$, 196 mV $dec^{-1}$, 210 mV $dec^{-1}$ and 230 mV $dec^{-1}$ for 2.5%-NRGO/$NiWO_4$/ZnO (0.01 M), 2.5%-NRGO/$NiWO_4$, 2.5%-NRGO/ZnO, NRGO, $NiWO_4$ and ZnO, respectively. This indicates that the 2.5%-NRGO/$NiWO_4$/ZnO (0.01M) nanocomposites electrode has much higher activity than the component materials electrode. Although its activity is still lower than the 20 wt.% Pt/C electrode, it may be considered significant because of the fact that it is a Pt-free catalyst. Thus, the experimentally observed Tafel slope of 93 mV $dec^{-1}$ indicated that the Heyrovsky mechanism is operating in the HER process for 2.5%-NRGO/$NiWO_4$/ZnO (0.01M) nanocomposite (Bhardwaj and Balasubramaniam 2008).

Stability test for the 2.5%-NRGO/$NiWO_4$/ZnO (0.01 M) catalyst was also carried out via CV measurements of 1000 cycles in 0.1 M KOH. As can be observed from Figure 3.19c, the current loss even after 1000 cycles is negligible. Thus, the test confirms that the 2.5%-NRGO/$NiWO_4$/ZnO (0.01 M) catalyst has good electrochemical stability for HER in 0.1 M KOH solution.

Further, the commercial application of the electrocatalyst was studied by chronopotentiometry technique at a constant current density of-10 mA/$cm^2$ applied for a duration of 2000 seconds (Figure 3.19d). The observed result shows that the initially high potential decreases slowly and then reaches to a stabilized state of HER. This phenomenon is attributed to the development of $H_2$ bubbles on the electrode surfaces.

Overall, the results demonstrate that the 2.5%-NRGO/$NiWO_4$/ZnO (0.01 M) nanocomposite is indeed a highly efficient electrocatalyst for HER in alkaline medium.

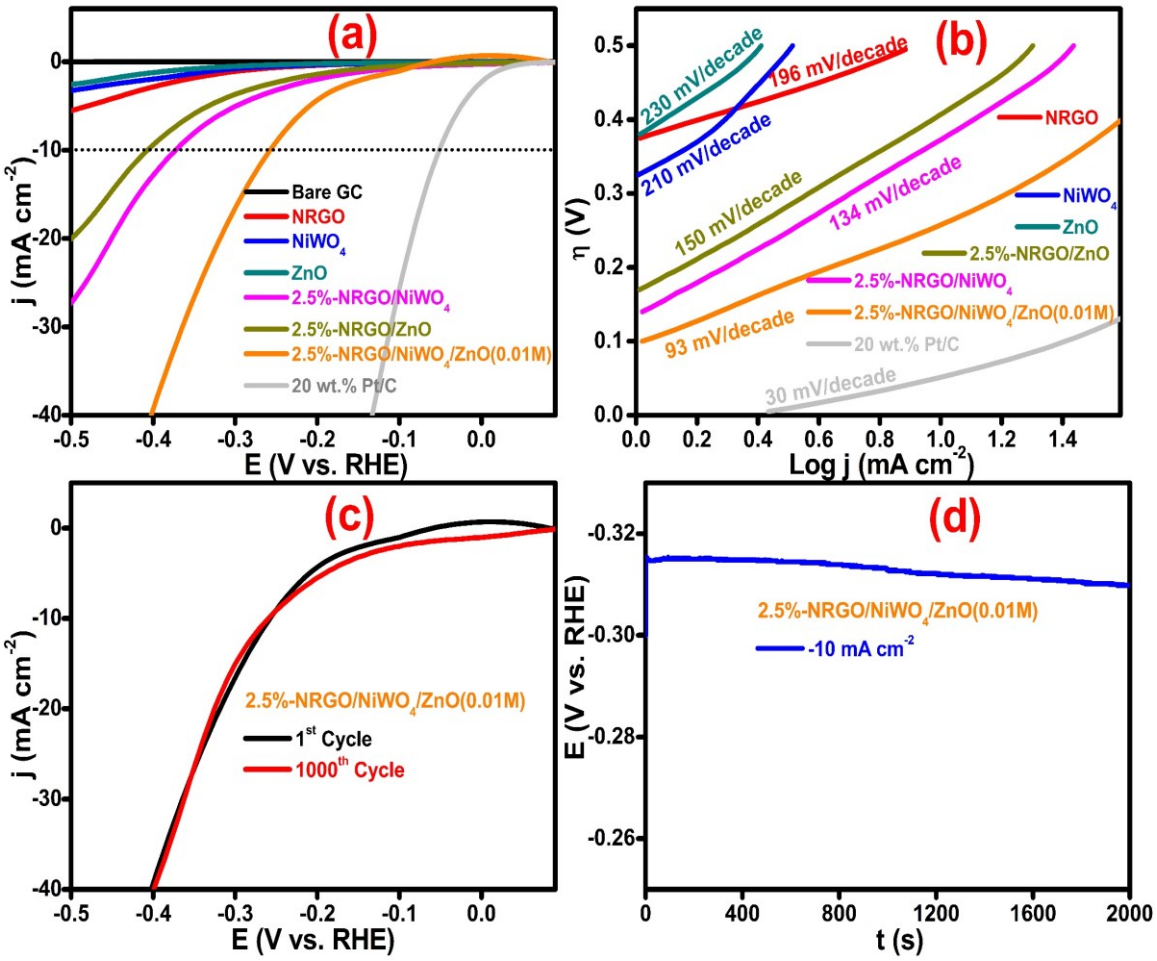


**Figure 3.19** (a) LSV and (b) Tafel curves for different electrode materials. (c) Stability curve of 2.5%-NRGO/$NiWO_4$/ZnO (0.01 M) nanocomposite and (d) Chrono-potentiometry curves at -10 mA cm$^{-2}$ recorded using 2.5%-NRGO/$NiWO_4$/ZnO (0.01 M) nanocomposites.

## 3.4 CONCLUSIONS

In summary, a successful microwave synthesis of NRGO/$NiWO_4$/ZnO ternary nanocomposites is reported. The phase structure, elemental composition, surface morphology and optical properties of the as-synthesized nanocomposites are studied by various techniques. The visible light photocatalytic activities of the composites towards the degradation of MB dye are studied. Optimized concentration of efficient catalyst is

found to be 2.5%-NRGO/$NiWO_4$/ZnO (0.01 M). The photodegradation efficiency of 2.5%-NRGO/$NiWO_4$/ZnO (0.01 M) is approximately 9 times higher than $NiWO_4$ and it showed high stability even after 5 cycles. The trapping experiments suggest that the photogenerated holes are the active species involved in the photocatalytic reactions. On the basis of the experimental results, the possible photodegradation mechanism is proposed. The composite also showed excellent catalytic activity in the reduction of 4-NP to 4-AP in the presence of $NaBH_4$. The reaction completed in 80 seconds. Additionally, it exhibited outstanding HER activity and stability requiring a low onset potential of 101 mV delivering a current density of -10 mA $cm^{-2}$ at a low overpotential of 257 mV. The Tafel slope of the HER was 93 mV $dec^{-1}$, indicating that the kinetics of the reaction follows Heyrovsky mechanism.

# CHAPTER - 4

## SYNTHESIS, CHARACTERIZATION AND CATALYTIC APPLICATIONS OF NOVEL NRGO/$CoWO_4$/$Fe_2O_3$ NANOCOMPOSITE

***Chapter 4*** *provides details of synthesis, characterization and catalytic applications of novel NRGO/$CoWO_4$/$Fe_2O_3$ nanocomposite.*

## 4.1 INTRODUCTION

Semiconductors and their nanocomposites are used in a variety of applications such as sensors, drug delivery, energy storage and as catalysts for several commercially significant reactions due to their catalytic nature (Mills and Le Hunte 1997, Bhatt et al. 2011, Kochuveedu et al. 2013, Hisatomi et al. 2014, Dutta et al. 2015). If a composite material is useful in more than one industrial or commercial applications, then such a material would be of great interest and importance to the scientific community. They can also have an enormous influence on the economy and the environment. Until now, the practical applications of many catalysts are restricted due to some inherent difficulties such as the fast recombination rate of photogenerated electron-hole pairs, limited visible light responses, poor adsorptive performance, low efficiency, non-reusability and high cost (Paola et al. 2012, Zhang et al. 2012). In order to overcome these drawbacks, it is necessary to develop nanocomposite materials using simple techniques which can be used for environmental applications.

$CoWO_4$ is considered as one of the most important class of metal tungstates with Wolframite structure, which has been used in the field of luminescence, energy conversion, energy storage, optical fibers, ceramics and photocatalysis (Xu et al. 2014, Alborzi and Abedini 2016). However, the practical application of $CoWO_4$ in catalysis is hindered due to high recombination rate and charge transfer. Hence, RGO is incorporated into semiconductors to assist the electron transfer and charge separation. The incorporation of electron-rich nitrogen atoms into RGO oxide materials promotes the interaction between neighboring carbons and electrons, providing a superior heteroatom-doped catalyst (Li et al. 2009). The semiconductor materials supported on NRGO show significant enhancement in their catalytic performance (Liu et al. 2014).

Semiconductor materials like ZnO, NiO, $Fe_2O_3$, $Fe_3O_4$ are used in catalytic studies for their excellent stability and large surface area for absorption capability (Paola et al. 2012). Recently, $Fe_2O_3$ based semiconductor nanoparticles were found to have excellent catalytic property due to their unique recombination rates and charge

carrier separation which led to the improvement in catalytic efficiency. Therefore, it is believed that $Fe_2O_3$ could be a good candidate for coupling with $CoWO_4$ and NRGO to form NRGO/$CoWO_4$/$Fe_2O_3$ composite with high catalytic activity. Also, there are no reports available on synthesis of NRGO/$CoWO_4$/$Fe_2O_3$ ternary nanocomposites using microwave irradiation method and their catalytic studies.

In view of this, the synthesis of NRGO/$CoWO_4$/$Fe_2O_3$ ternary nanocomposites by microwave irradiation method is reported here. The synthesized materials were thoroughly characterized. The catalytic activity of the ternary nanocomposites was tested for photodegradation of MB under the visible light source and examined for reduction of 4-NP to 4-AP using $NaBH_4$ reactions and also further electrocatalytic behavior of HER studies using alkaline medium.

## 4.2 EXPERIMENTAL

### 4.2.1 Synthesis of GO

GO was synthesized by using the modified Hummers method. In brief, 5 g of natural graphite flasks and 2.5 g of $NaNO_3$ was added in 150 mL of concentrated sulfuric acid under constant stirring in a beaker immersed in an ice water bath. Then, 15 g of $KMnO_4$ was added slowly and the mixture was stirred at the 30 °C for 2 hours. Later, 230 mL of distilled water was added and the mixture was further stirred for 30 min at 95 °C. Finally, 420 mL of distilled water and 10 mL of $H_2O_2$ were subsequently added to terminate the reactions. The color of the solution turned from dark brown to yellow. The obtained GO was separated by centrifugation, and washed.

### 4.2.2 Synthesis of $CoWO_4$

0.05 M of cobalt acetate was dissolved in 50 mL of DI water to which 50 mL of 0.05 M of sodium tungstate solution was slowly added under constant stirring for about 2 hours. The resulting mixture was treated with microwave irradiation at 350 W for 10 minutes and then allowed to cool to room temperature. The formed precipitate of $CoWO_4$ was collected and washed with 10 % ethanol several times and finally dried.

### 4.2.3 Synthesis of $Fe_2O_3$

0.005 M of ferric nitrate was dissolved in 50 mL of DI water. Then, 0.4 g of urea was added under constant stirring. Later, the reaction mixture was treated with

microwave irradiation at 350 W for 10 minutes. $Fe_2O_3$ precipitate formed was collected and washed several times with 10 % ethanol and later dried.

### 4.2.4 Synthesis of NRGO

NRGO was synthesized by a one-step microwave irradiation method. Urea was used as doping agent for nitrogen. In a typical synthesis, a calculated amount of GO was dispersed in the ethylene glycol solution (50 mL) under ultrasonic treatment for about 30 minutes. 1.0 g of urea was then added under constant stirring. The pH of the solution was maintained at 9.0 using required amount of ammonia solution. After 2 hours, the mixture was treated with microwave irradiation at 350 W for 10 minutes and then the mixture was allowed to cool to room temperature. The formed NRGO was washed several times with DI water and 10 % ethanol and then finally dried.

### 4.2.5 Synthesis of NRGO/$CoWO_4$/$Fe_2O_3$

(a)NRGO/$CoWO_4$/$Fe_2O_3$(b) nanocomposites were synthesized by a one-step microwave irradiation method (a = 0.5, 1, 2.5 and 5 wt.% of GO and b = 0.005 M, 0.01 M and 0.02 M of ferric nitrate). A calculated amount (a) of GO was dispersed in the ethylene glycol solution under ultrasonic treatment for about 30 minutes and 50 mL of 0.05 M of cobalt acetate solution was added to the above solution. Then 50 mL of 0.05 M of sodium tungstate solution was slowly added to the reaction mixture and 1.0 g of urea was added under constant stirring while maintaining the pH at 9.0 using ammonia. To this mixture, designated amount of ferric nitrate dissolved in 50 mL of DI water was added. Later, 0.4 g of urea was added under constant stirring. This was irradiated with microwave at 350 W for 10 minutes. The obtained product of NRGO/$CoWO_4$/$Fe_2O_3$ composite was washed with 10 % ethanol and dried. The schematic representation of the synthesis of NRGO/$CoWO_4$/$Fe_2O_3$ ternary nanocomposites is shown in Figure 4.1.

### 4.2.6 Characterization and Catalytic Studies

The characterization of the synthesized samples was carried out as given in section 2.2.9 and section 3.2.3. The catalytic studies were performed as described in section 2.2.10 - 2.2.12.

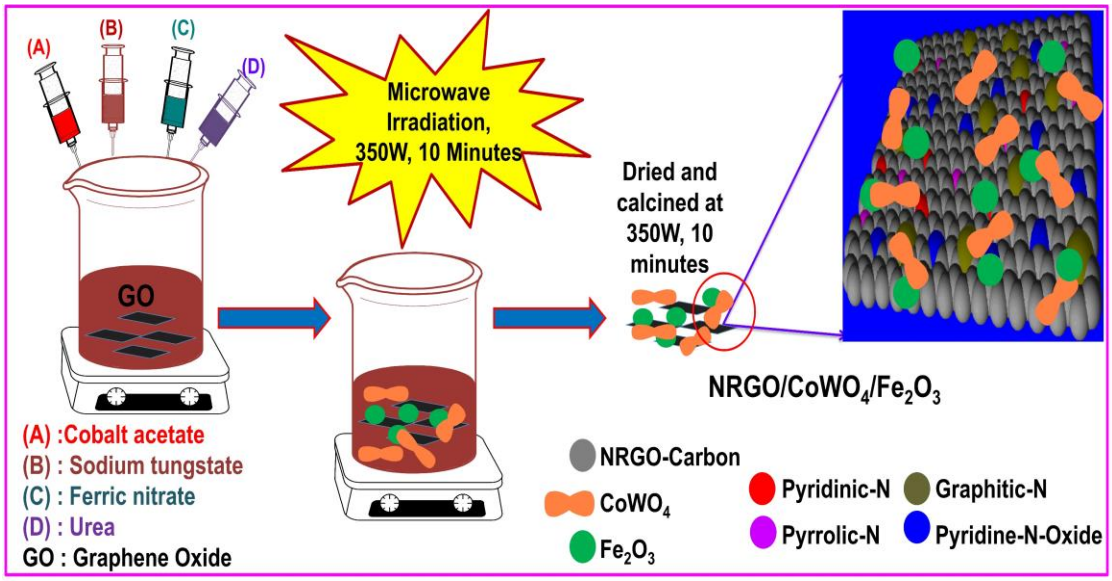


**Figure 4.1** Schematic representation of synthesis of NRGO/$CoWO_4$/$Fe_2O_3$ ternary nanocomposites.

## 4.3 RESULTS AND DISCUSSION

### 4.3.1 XRD Studies

Figure 4.2 shows the XRD patterns of the as-synthesized GO, RGO, NRGO, $CoWO_4$, $Fe_2O_3$ and NRGO/$CoWO_4$/$Fe_2O_3$. The XRD pattern of graphite shows a sharp peak corresponding to the reflection from the (002) plane at $2\theta$=26.3° with a d-spacing of 0.339 nm. Whereas, GO exhibits a slightly broader peak at 10.5° with a d-spacing of 0.842 nm matching with the reflection from the (002) plane. These patterns are very similar to those reported previously for graphite and GO (Khandelwal et al. 2015). The XRD pattern of RGO is quite different from graphite and GO, and shows a slightly broader peak at 22.6° which corresponds to the reflection from the (002) plane with a d-spacing of 0.365 nm, suggesting the reduction of GO (Fu et al. 2016). Although the concentration of nitrogen in NRGO is low, differences between RGO and NRGO can be clarified easily. In contrast to the XRD pattern of RGO, NRGO shows a relatively broader peak at 24.4° again corresponding to the reflection from the (002) plane with a d-spacing of 0.355 nm. The slight increase in the reflection angle for (002) plane in NRGO compared to that of RGO may be ascribed to the entry of nitrogen atoms into the crystal lattice of graphite causing an increased distance between the graphite layers (Szabo et al. 2006).

$CoWO_4$ and $Fe_2O_3$ diffraction patterns well matched with JCPDS file numbers 15-0867 and 33-0664, respectively. Also, XRD traces of the NRGO/$CoWO_4$/$Fe_2O_3$ ternary nanocomposite had all peaks of $CoWO_4$ and $Fe_2O_3$ confirming their existence in the nanocomposite and hence confirming the formation of the ternary nanocomposite. However, carbon diffraction peak for NRGO could not be clearly identified in NRGO/$CoWO_4$/$Fe_2O_3$ ternary nanocomposite, which may be due to overlapping with peaks from other components apart from small quantity, weak intensity and exfoliated nature of NRGO in the composite (Li et al. 2009).

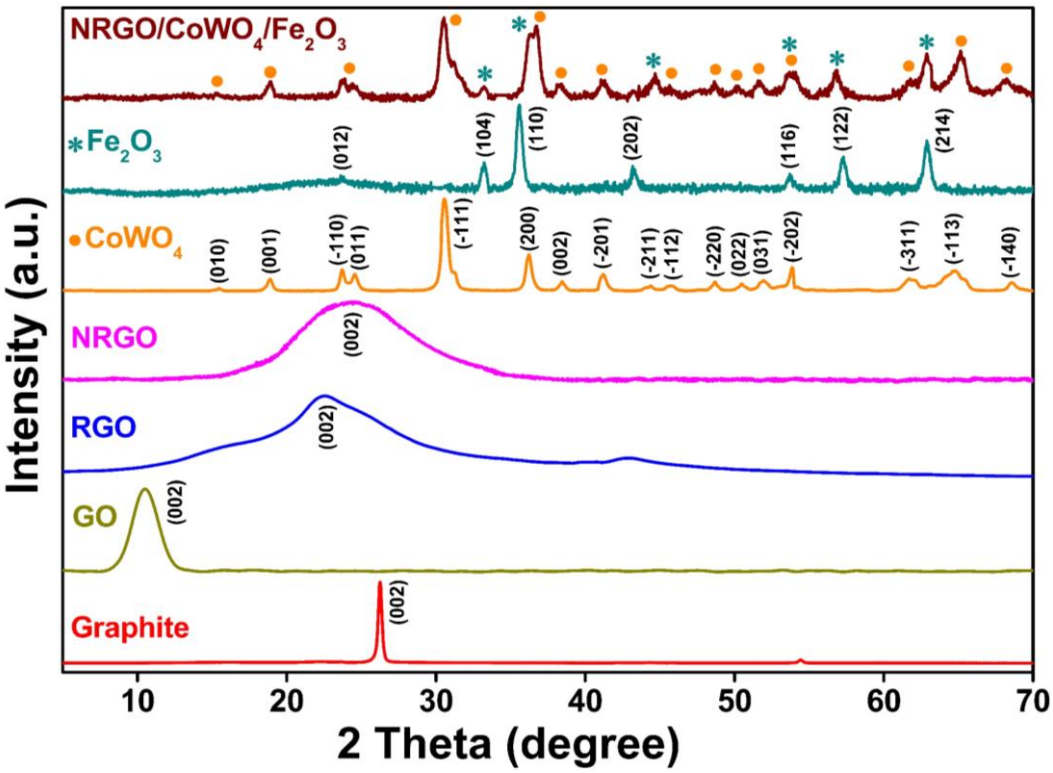


**Figure 4.2** XRD spectra of GO, RGO, NRGO, $CoWO_4$, $Fe_2O_3$ and NRGO/$CoWO_4$/$Fe_2O_3$.

### 4.3.2 Raman Studies

Raman spectroscopy is widely employed to study the ordered/disordered crystal structures of carbon-based materials (Ferrari and Basko 2013). In Figure 4.3, the Raman spectrum of GO reveals two important functions, the G mode at 1599 $cm^{-1}$ springing up from the emission region of zone-center optical phonons and D mode at 1355 $cm^{-1}$ arising from the doubly resonant disorder-precipitated mode. $I_D/I_G$ is the intensity ratio

of the D and G bands and it is a measure of the relative concentration of neighborhood defects (particularly the $sp^3$ hybridized defects) as compared to the $sp^2$ hybridized GO domain ones. It can be noted that, before the microwave irradiation, the $I_D/I_G$ ratio was 0.87 for GO. After the microwave irradiation treatment, the $I_D/I_G$ ratio increases to 1.09, indicating more defect formation, which may be due to the reduction and conversion of GO to NRGO and exfoliation of graphitic domains.

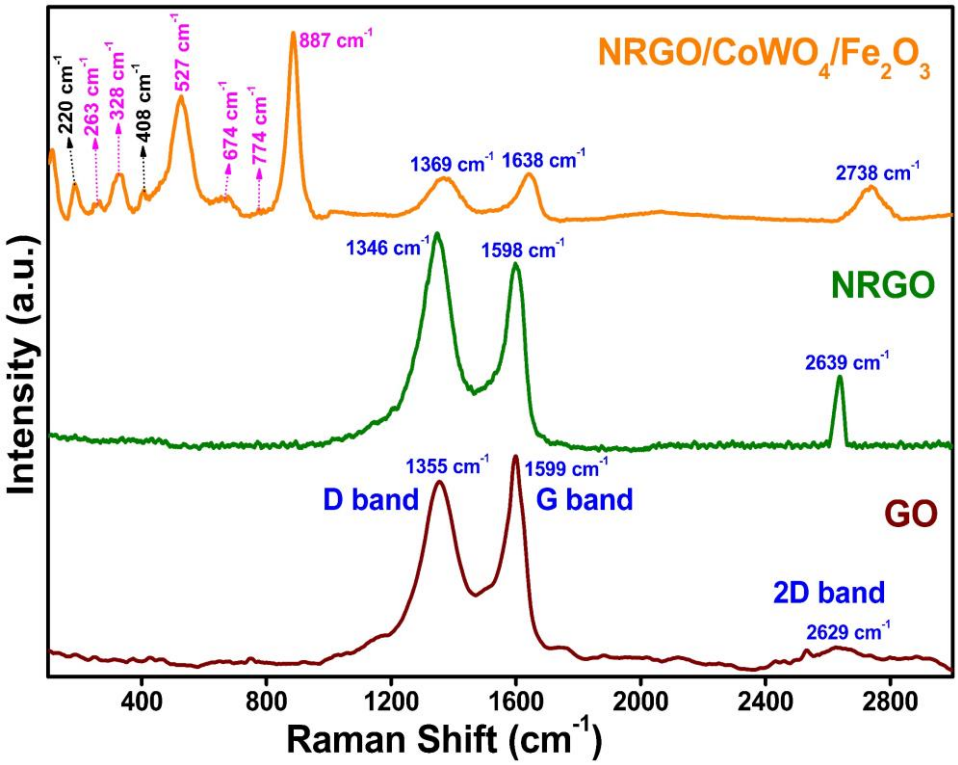


**Figure 4.3** Raman spectra of GO, NRGO and NRGO/$CoWO_4$/$Fe_2O_3$.

The bands observed at 263 $cm^{-1}$, 328 $cm^{-1}$, 527 $cm^{-1}$, 674 $cm^{-1}$, 774 $cm^{-1}$ and 887 $cm^{-1}$ are ascribed to the six Raman active modes of $CoWO_4$, respectively (Xu et al. 2014). Raman band at 220 $cm^{-1}$ and 408 $cm^{-1}$ are ascribed to the two Raman active modes of $Fe_2O_3$ (Wei et al. 2008). Raman peaks of 1369 $cm^{-1}$ (D band) to 1638 $cm^{-1}$ (G band), with an $I_D/I_G$ ratio 0.92 and the 2D band at 2738 $cm^{-1}$ with $I_{2D}/I_G$ ratio of 0.74, respectively are ascribed to NRGO. The $I_D/I_G$ ratios of pure NRGO and NRGO/$CoWO_4$/$Fe_2O_3$ nanocomposite are, 1.0899 and 0.9189 respectively. These values are slightly greater than that of GO (0.8748). This may be due to the increase in the defects formed during the course of reduction of GO to NRGO nanosheets.

The number of NRGO layers can be determined by the ratio $I_{2D}/I_G$, where $I_{2D}$ is intensity of 2D band and $I_G$ is intensity of G band. The ratio $I_{2D}/I_G$ of >2, 1 to 2, and <1 corresponds to single, double and multi-layers of NRGO sheets, respectively (Subramanya and Bhat 2015). In the present work $I_{2D}/I_G$ is found to be 0.6634 and 0.7427 for NRGO and NRGO/$CoWO_4$/$Fe_2O_3$ nanocomposite, respectively. This suggests that the NRGO sheets are mostly of multilayered nature.

### 4.3.3 XPS Studies

The chemical states of the essential elements of the NRGO/$CoWO_4$/$Fe_2O_3$ ternary nanocomposites were investigated via XPS analysis. The XPS survey spectrum and high-resolution spectrum of NRGO/$CoWO_4$/$Fe_2O_3$ ternary nanocomposites are as shown in Figure 4.4 and Figure 4.5, respectively.

The binding energy states in the XPS spectrum have been calibrated with C 1s region at 284.8 eV. The high-resolution C 1s spectrum, is deconvoluted into six peaks at 284.54 eV (C=C), 286.04 eV (C-N), 286.93 eV (C-O-C), 288.58 eV (C=O), 289.97 eV (O-C=O) and 291.58 eV ($\pi$-$\pi$* interaction), respectively (Liu et al. 2014). The high-resolution N 1s spectrum, is deconvoluted into four peaks at 398.77 eV (pyridinic-N), 400.14 eV (pyrrolic-N), 401.18 eV (graphitic-N) and 402.71 eV (pyridine-N-Oxide), respectively (Liu et al. 2014). The high-resolution Co 2p spectrum, is deconvoluted into ten peaks located at 780.31 eV, 796.79 eV of $Co^{3+}$ and 781.58 eV, 798.49 eV of $Co^{2+}$, which correspond to Co $2p_{3/2}$ and Co $2p_{1/2}$, respectively. The satellite peaks of $Co^{3+}$ are at 787.26 eV, 793.68 eV, 803.78 eV and that of $Co^{2+}$ are at 784.10 eV, 790.37 eV, 801.99 eV, respectively (Xu et al. 2014). The high-resolution W 4f spectrum, which can be deconvoluted into four peaks at 34.92 eV and 37.03 eV, belong to W $4f_{7/2}$ and W $4f_{5/2}$. And its satellite peaks are at 35.38eV and 37.43 eV, respectively (Xu et al. 2014). The high-resolution Fe2p spectrum are similarly deconvoluted into five peaks placed at 708.3 eV, 721.45 eV of $Fe^{2+}$ and 710.67 eV, 724.18 eV of $Fe^{3+}$ belong to the Fe $2p_{3/2}$ and Fe $2p_{1/2}$ states respectively. Its satellite peak is observed at 715.43 eV. The high-resolution O 1s spectrum is further deconvoluted into three peaks at 530.66 eV, 532.32 eV and 533.331 eV. These are related to $Fe_2O_3$, $CoWO_4$ and H-O-H bonds, respectively (Xu et al. 2014). XPS also provides evidence for doping of N into RGO.

Figure 4.6 shows survey and high resolution XPS spectra for NRGO. The presence of N could be clearly detected in the XPS spectra of NRGO, and the high-revolution N *1s* XPS spectra could be fitted into four types of N doping, such as, pyridinic N (398.3 eV), pyrrolic N (399.6 eV), graphite N (400.7 eV) and pyridinic N Oxide (402.5 eV) (Wang et al. 2015). The detailed composition values for C, N, Co, W, Fe and O determined through XPS is given in Table 4.1. All the above results confirm the successful formation of NRGO/$CoWO_4$/$Fe_2O_3$ nanocomposite.

**Table 4.1** Surface elemental composition and C, N, Co, W, Fe, O elemental contents with relative intensities of C 1s, N 1s, Co 2p, W 4f, Fe 2p, O 1s peaks of the NRGO/$CoWO_4$/$Fe_2O_3$ from XPS.

| **XPS** | **Total Contents** | | | | | | | | | |
|---|---|---|---|---|---|---|---|---|---|---|
| **Elements** | **C** | | **N** | | **Co** | **W** | | **Fe** | | **O** |
| **At %** | 15.60 % | | 1.07 % | | 5.67 % | 8.0 % | | 33.08 % | | 36.58 % |
| **C 1s** | **C=C** | | **C-N** | | **C-O-C** | **C=O** | | **O-C=O** | | **π-π*** |
| | 67.30 % | | 23.0 % | | 3.12 % | 2.54 % | | 2.37 % | | 1.67 % |
| **N 1s** | **Pyridinic-N** | | **Pyrrolic-N** | | | **Graphitic-N** | | **Pyridinic-N-Oxide** | | |
| | 49.64 % | | 25.35 % | | | 16.74 % | | 8.27 % | | |
| **Co2p** | **Co $2p_{3/2}$** | | **Sat.** | | **Sat.** | | **Co $2p_{1/2}$** | | **Sat.** | |
| | **3+** | **2+** | **2+** | **3+** | **2+** | **3+** | **3+** | **2+** | **2+** | **3+** |
| | 21.92 % | 21.37 % | 13.18 % | 11.71 % | 5.54 % | 5.84 % | 7.8 % | 4.07 % | 4.95 % | 3.54 % |
| **W 4f** | **W $4f_{7/2}$** | | | | | **W $4f_{5/2}$** | | | | |
| | 37.71 % | | 16.24 % | | | 25.33% | | 20.72% | | |
| **Fe 2p** | **Fe $2p_{3/2}$** | | | **Sat.** | **Fe $2p_{1/2}$** | | | | | |
| | **2+** | | **3+** | **3+** | **2+** | **3+** | | | | |
| | 35.82 % | | 32.47 % | 10.70 % | 12.78 % | 8.23 % | | | | |
| **O 1s** | **Fe-O** | | | **W-O-W** | | **H-O-H** | | | | |
| | 52.33 % | | | 37.72 % | | 9.95 % | | | | |

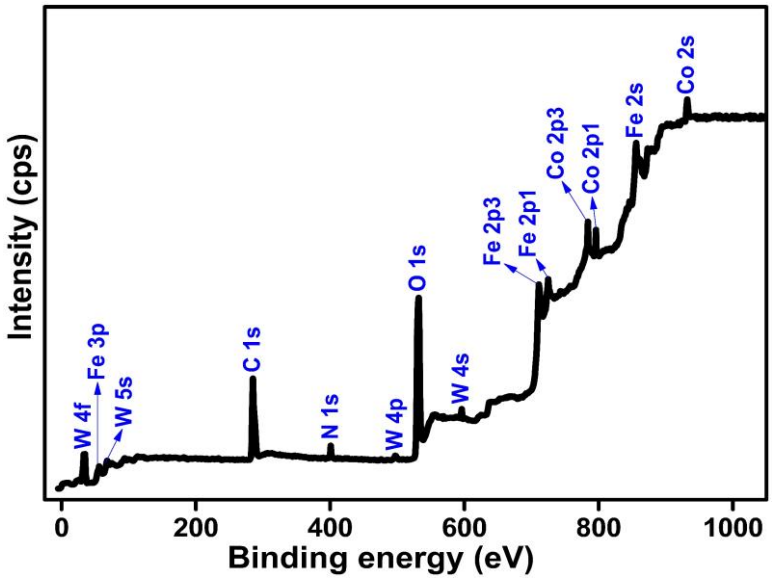


**Figure 4.4** XPS survey spectrum of NRGO/$CoWO_4$/$Fe_2O_3$.

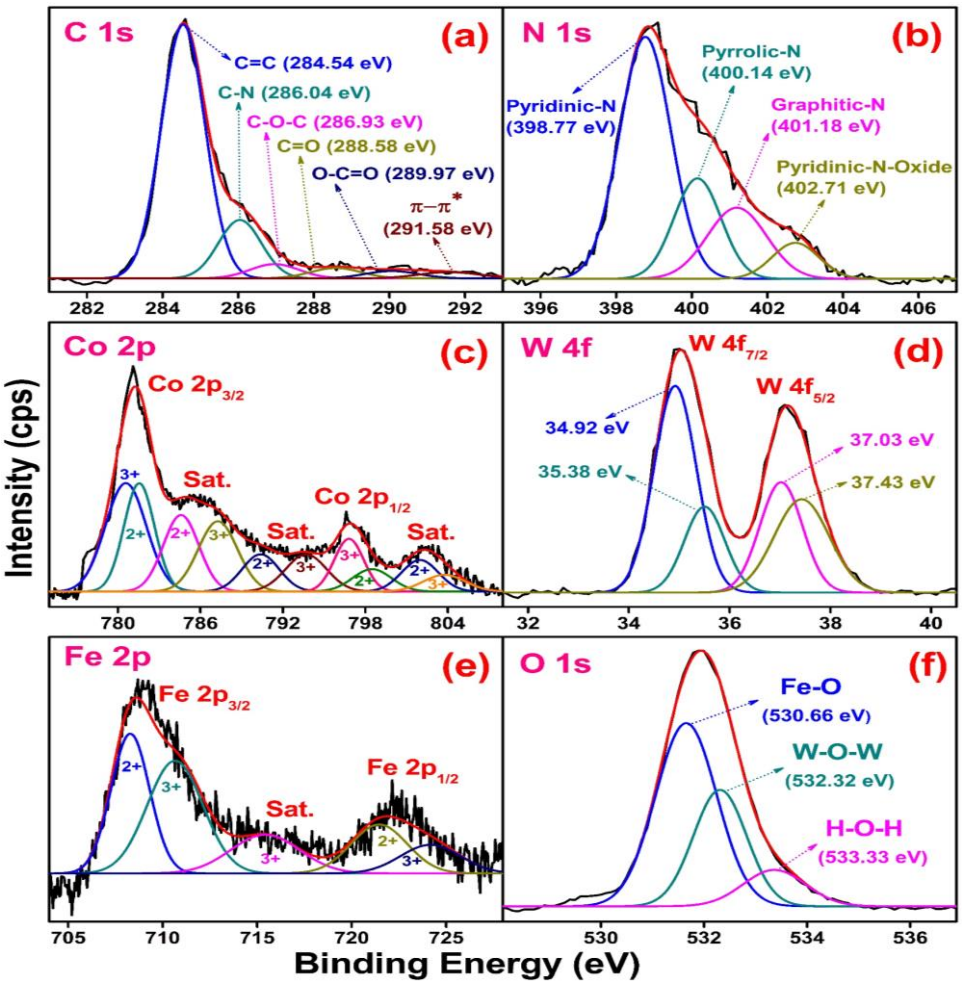


**Figure 4.5** XPS spectra of NRGO/$CoWO_4$/$Fe_2O_3$ in the high-resolution region of C 1s, N 1s, Co 2p, W 4f, Fe 2p and O 1s.

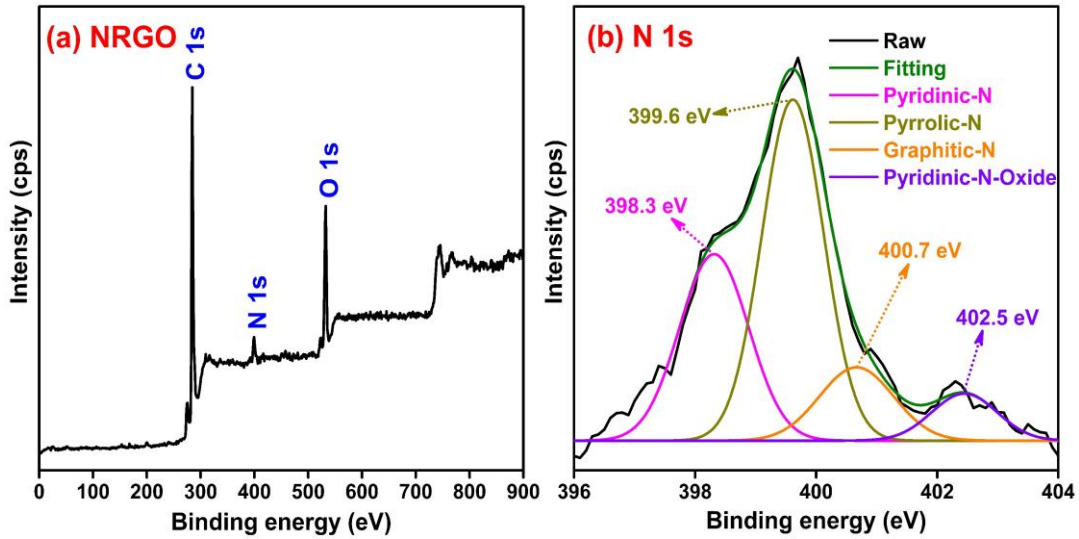


**Figure 4.6** XPS spectrum (a) survey and high-resolution spectra (b) N 1s of NRGO.

### 4.3.4 Surface Morphological Studies

The total surface area of $CoWO_4$, $CoWO_4/Fe_2O_3$ and $NRGO/CoWO_4/Fe_2O_3$ was determined from BET method. BET total surface area of $CoWO_4$, $CoWO_4/Fe_2O_3$ and $NRGO/CoWO_4/Fe_2O_3$ was 16.21 $m^2g^{-1}$, 22.25 $m^2g^{-1}$ and 31.38 $m^2g^{-1}$, respectively. From these values, it is evident that introduction of NRGO nanosheets in the $NRGO/CoWO_4/Fe_2O_3$ nanocomposites increased the surface area compared to that of $CoWO_4$ and $CoWO_4/Fe_2O_3$. The increased surface area can contribute to the enhancement in the catalytic activity of the $NRGO/CoWO_4/Fe_2O_3$ nanocomposites along with reduction in their reaction time.

The structural morphology of the as-synthesized nanocomposites was analyzed by electron microscopy (Figure 4.7). Figure 4.7a shows the TEM image of the wrinkled sheet-like nature of NRGO. Figure 4.7b reveals small rod-like shapes of $CoWO_4$ with a wrinkled NRGO sheet. Figure 4.7c shows $NRGO/CoWO_4/Fe_2O_3$ ternary nanocomposites containing 2D wrinkled sheet-like morphology of NRGO nanosheets, with approximately rod-like $CoWO_4$ and oval like $Fe_2O_3$ nanoparticles. Figure 4.7d shows the HRTEM image of $NRGO/CoWO_4/Fe_2O_3$ wherein, the formation of heterojunction interface between $CoWO_4$ and $Fe_2O_3$ on the edges of the NRGO nanosheets is seen. The obtained lattice fringe of 0.467 nm matched with the (001) plane of $CoWO_4$ and 0.268 nm corresponded to the (104) plane of $Fe_2O_3$. Therefore, it

is far more evident that the interface is fashioned with the $Fe_2O_3$ (104) plane and the $CoWO_4$ (001) planes and are stacking on the NRGO sheets. The average particle size distribution of the nanoparticles was found to be 19.02 nm for $CoWO_4$ and 7.74 nm for $Fe_2O_3$ (Figure 4.8). Further, uniform distributions of elements, N, C, O, Co, Fe and W are shown in the elemental color mapping image, Figure 4.9.

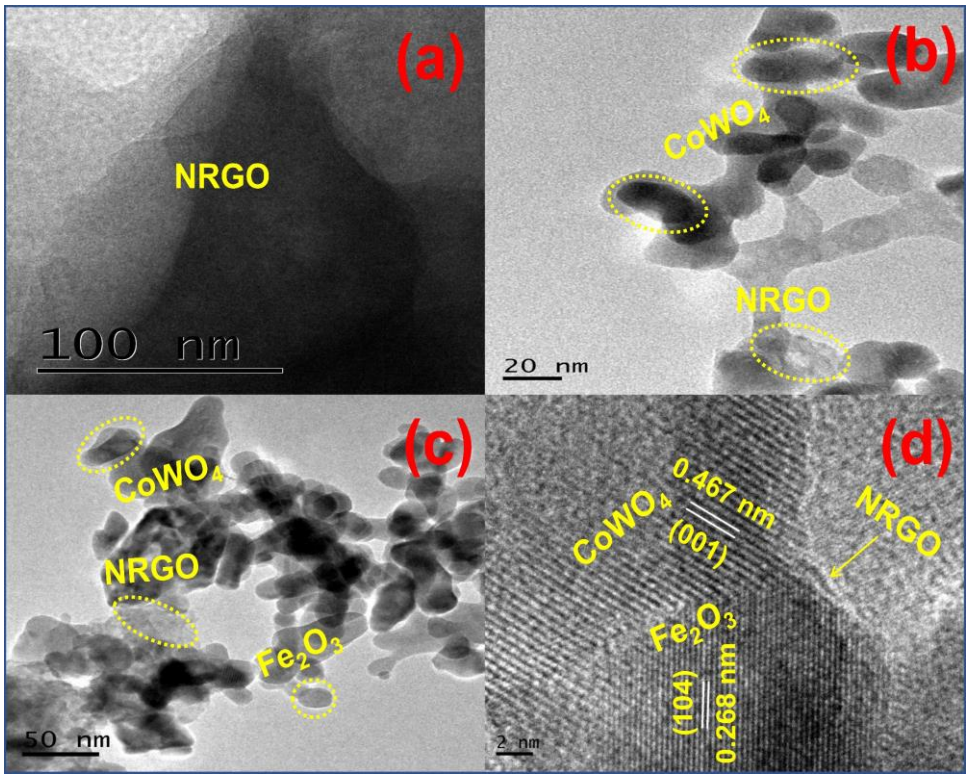


**Figure 4.7** TEM images of (a) NRGO, (b) NRGO/$CoWO_4$, (c) NRGO/$CoWO_4$/$Fe_2O_3$ and (d) HRTEM image of NRGO/$CoWO_4$/$Fe_2O_3$.

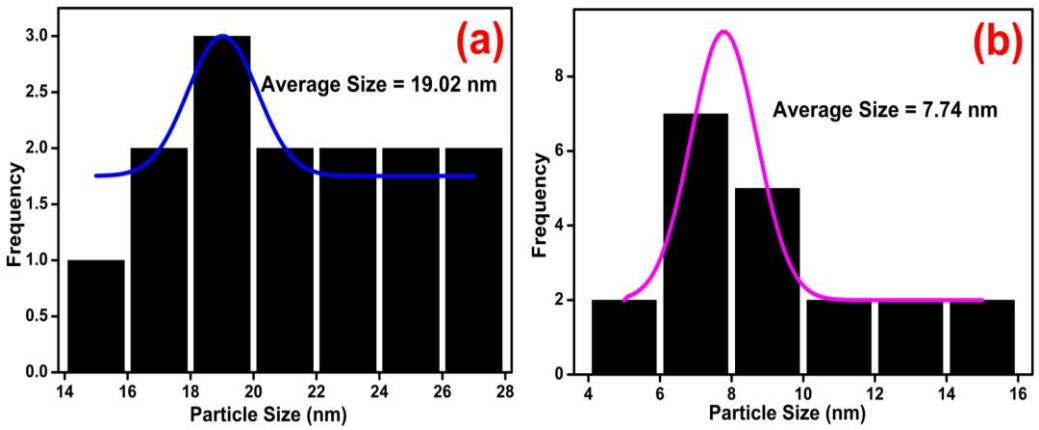


**Figure 4.8** The average particle size distribution of the (a) $CoWO_4$ and (b) $Fe_2O_3$ on NRGO/$CoWO_4$/$Fe_2O_3$ from TEM.

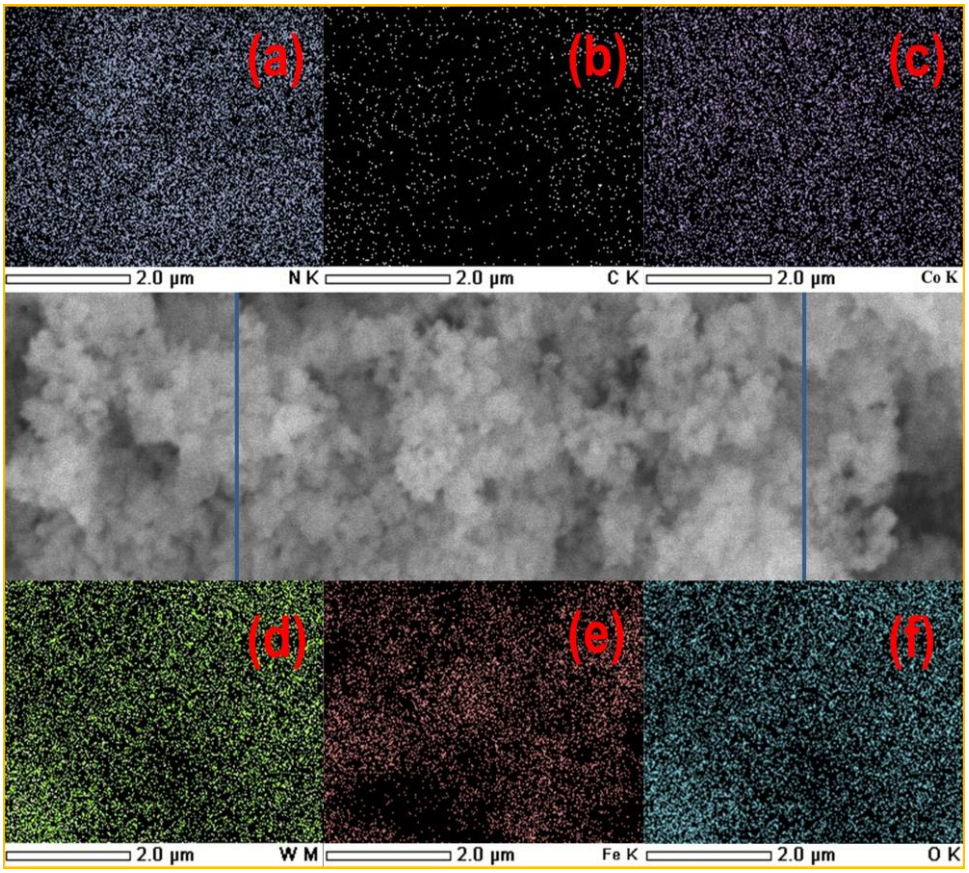


**Figure 4.9** Elemental mapping of NRGO/$CoWO_4$/$Fe_2O_3$ (a) N, (b) C, (c) Co, (d) W, (e) Fe and (f) O.

### 4.3.5 Optical Absorbance Analysis

The optical characteristics of the as-synthesized nanocomposites were examined by using the UV-Vis DRS. The absorbances of all the samples are in the visible region (Figure 4.10a). When $Fe_2O_3$ nanoparticles are added to NRGO/$CoWO_4$ the range and the extent to which the composite absorbs in the visible region increases compared to the component materials. This, in turn makes the ternary composite more efficient in photocatalytic degradation of organic pollutants. The band gaps of the materials are shown in Figure 4.11.

The band gap energy was estimated employing Tauc approach (equation 2.3) from plots of $(\alpha h\upsilon)^2$ versus photon energy ($h\upsilon$) for $CoWO_4$, NRGO/$CoWO_4$, $Fe_2O_3$, $CoWO_4$/$Fe_2O_3$ and NRGO/$CoWO_4$/$Fe_2O_3$ nanocomposites (Tauc et al. 1966). The calculated direct band gap energies (n=1) are 2.52 eV, 2.18 eV, 2.04 eV, 1.90 eV and

1.74 eV for $CoWO_4$, NRGO/$CoWO_4$, $Fe_2O_3$, $CoWO_4/Fe_2O_3$ and NRGO/$CoWO_4/Fe_2O_3$ nanocomposite, respectively. The decrease in the band gap energy of NRGO/$CoWO_4/Fe_2O_3$ nanocomposite facilitates the material to possess excellent visible light photocatalytic activity compared to other materials.

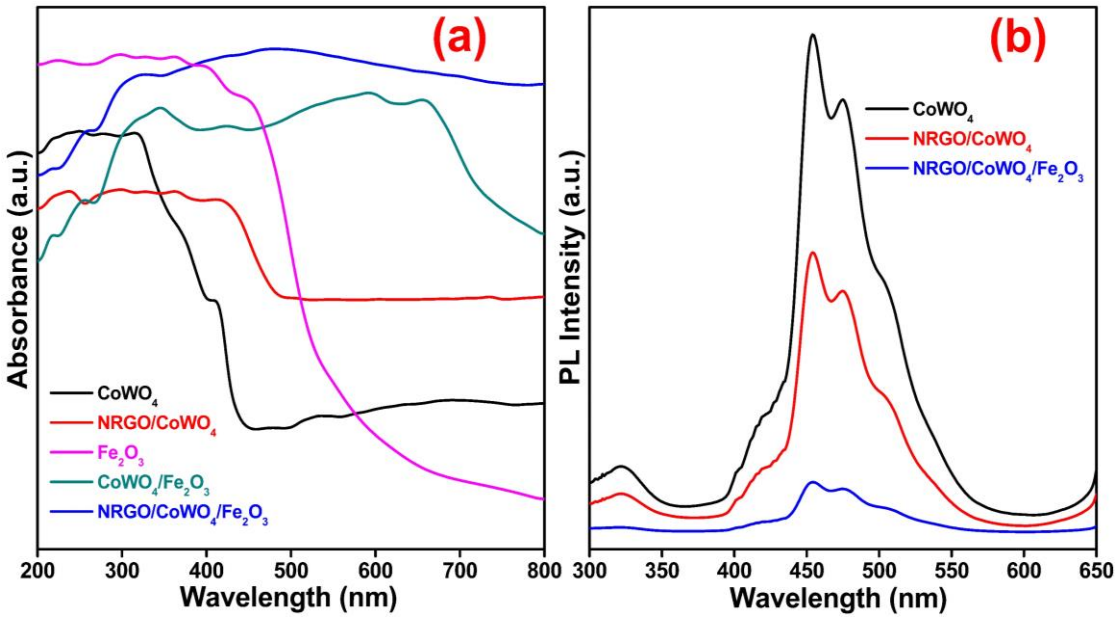


**Figure 4.10** (a) UV-Vis spectra of $CoWO_4$, NRGO/$CoWO_4$, $CoWO_4/Fe_2O_3$ and NRGO/$CoWO_4/Fe_2O_3$ and (b) PL spectra of $CoWO_4$, NRGO/$CoWO_4$ and NRGO/$CoWO_4/Fe_2O_3$.

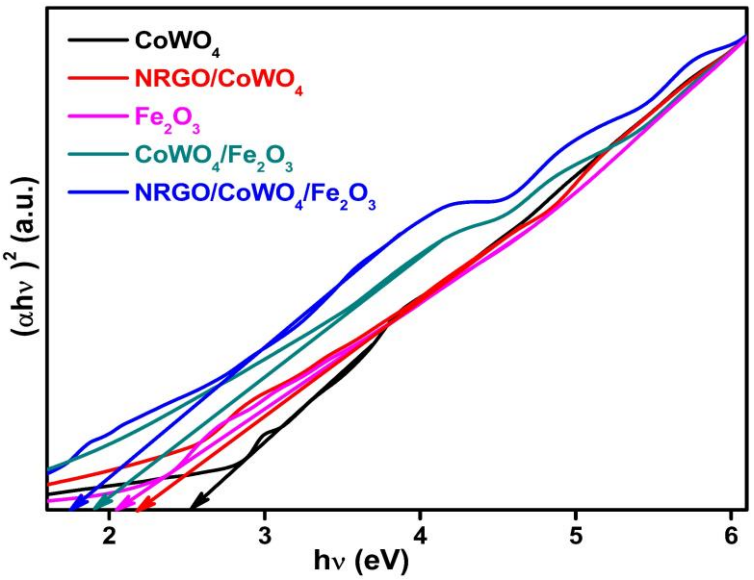


**Figure 4.11** Band gap plots of $CoWO_4$, NRGO/$CoWO_4$, $Fe_2O_3$, $CoWO_4/Fe_2O_3$ and NRGO/$CoWO_4/Fe_2O_3$.

Based on the above results, the band edge positions of the nanocomposites were calculated theoretically using the Mulliken electronegativity theory as narrated in section 2.3.9 of chapter 2. The calculated band edge potential values of CB and VB for $CoWO_4$ and $Fe_2O_3$ are listed in Table 4.2. The band gap energy of the bare $CoWO_4$ is determined to be 2.52 eV. The calculated band edge of $E_{CB}$ and $E_{VB}$ are 0.517 eV and 3.037 eV, respectively. For $Fe_2O_3$, the band edge values of $E_{CB}$ (0.366 eV) and $E_{VB}$ (2.406 eV) are slightly lesser than that of $CoWO_4$. This type of energy band gap alignment corresponds to type-II junction architecture and results in efficient charge separation and hence enhanced photocatalytic activity.

**Table 4.2** Band gaps of $CoWO_4$ and $Fe_2O_3$.

| **Samples** | **χ (eV)** | **$E_g$ (eV)** | **$E_{VB}$ (eV)** | **$E_{CB}$ (eV)** |
|---|---|---|---|---|
| **$CoWO_4$** | 6.277 | 2.52 | 3.037 | 0.517 |
| **$Fe_2O_3$** | 5.8862 | 2.04 | 2.406 | 0.366 |

### 4.3.6 Photoluminescence Analysis

The photocatalytic activities of ternary nanocomposites are assumed to be due to better separation of photogenerated electrons and holes. The charge carrier separation and recombination of photogenerated electron-holes in the ternary nanocomposite were investigated through PL emission spectrum. The PL spectra of the $CoWO_4$, NRGO/$CoWO_4$ and NRGO/$CoWO_4$/$Fe_2O_3$ are shown in Figure 4.10b. If the recombination rate is lesser, then the PL intensity would be lesser. All the samples exhibited a broad emission peak in the visible region starting from 300 nm to 650 nm with an excitation wavelength of about 280 nm. The pure $CoWO_4$ has an intense peak around 453 nm corresponding to the recombination of photo generated electron-holes (Gohari and Yangieh 2017). With introduction of NRGO the intensity of PL slightly decreased due to the increase in trapping states at the surface defect of NRGO/$CoWO_4$ nanocomposite. Further introduction of $Fe_2O_3$ made the PL intensity very weak due to the synergistic effect of both $CoWO_4$ and $Fe_2O_3$ with the NRGO interlayer in reducing the recombination of electron hole pairs.

### 4.3.7 Photocatalytic Activity

The photocatalytic activity of NRGO/$CoWO_4$/$Fe_2O_3$ ternary nanocomposite was assessed by the photocatalytic dye degradation of MB using the visible light source. In order to optimize the composition of NRGO and $Fe_2O_3$ in the nanocomposite, initially we prepared and analyzed the activities of NRGO/$CoWO_4$ composites with NRGO amount varying from 0.5 % to 5 %. The nanocomposite with 2.5 % NRGO showed highest activity and hence the nanocomposite with 2.5 % NRGO was used for the preparation of ternary composites with varying concentrations of $Fe_2O_3$ precursor, ferric nitrate solution (0.005 M to 0.02 M).

The nanocomposite with composition 2.5 % NRGO and $Fe_2O_3$ content of 0.01 M (in terms of ferric nitrate solution strength) showed maximum photocatalytic activity in the degradation of MB dye. Hence the nanocomposite with this composition was considered as the optimized sample and used for further studies. Figure 4.12a shows the results in the form of $C/C_o$ versus time plot. Blank test (control) was performed without the addition of nanocomposite and there was no noticeable degradation indicating that the photolysis of MB was negligible. The photocatalytic dye degradation efficiency of MB solutions in the presence of NRGO, $CoWO_4$, NRGO/$CoWO_4$, $CoWO_4$/$Fe_2O_3$ and NRGO/$CoWO_4$/$Fe_2O_3$ were about 17.35 %, 22.68 %, 59.40 %, 72.26 % and 99.05 % under visible light irradiation in time duration of 120 minutes. The obtained results show that the NRGO/$CoWO_4$/$Fe_2O_3$ ternary nanocomposites have excellent photocatalytic degradation efficiency than that of pure NRGO, $CoWO_4$, NRGO/$CoWO_4$ and $CoWO_4$/$Fe_2O_3$ and that the photocatalytic degradation efficiency of the $CoWO_4$ is significantly enhanced by NRGO and $Fe_2O_3$.

The as-prepared ternary nanocomposites exhibited first order kinetics for the photocatalytic degradation of MB dye (Kumar et al. 2016) conforming to equation (2.4). Figure 4.12b gives the rate constant 'k' values calculated from the slope of the straight lines obtained when equation (2.4) is plotted. As can be seen from the values that the rate constant for NRGO/$CoWO_4$/$Fe_2O_3$ is relatively high, in comparison to the other samples such as pure NRGO, $CoWO_4$, NRGO/$CoWO_4$ and $CoWO_4$/$Fe_2O_3$.

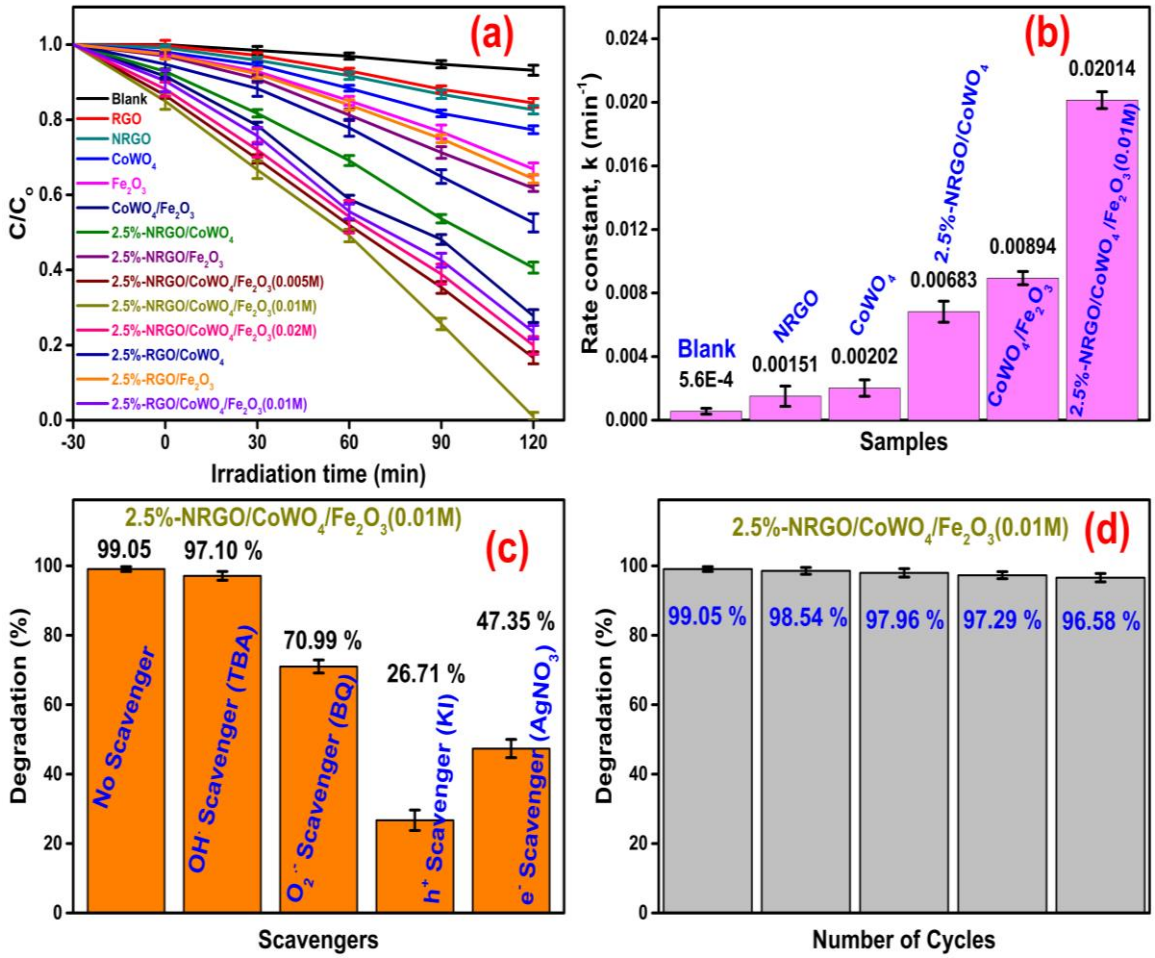


**Figure 4.12** (a) Degradation plots of MB over various catalysts under visible light irradiation, (b) First order rate constants for photodegradation of MB over various catalysts under visible light irradiation, (c) Plot depicting effects of different scavengers on degradation efficiency by NRGO/$CoWO_4$/$Fe_2O_3$ under visible light irradiation and (d) Reusability test plots.

In order to verify that the removal of MB is a process of photocatalytic degradation leading to complete mineralization of the dye, we have determined the TOC of the reaction medium during the photo catalysis process (Cui et al. 2013). Using the TOC values, percentage mineralization of the dye was calculated employing the equation (2.2) as given earlier. The mineralization test results are shown in the form of a bar diagram in Figure 4.13. As can be observed from the figure, it is evident that the mineralization value increased to 86.12 % in 120 minutes or TOC content decreased to 13.88 % indicating that the organic carbon is mostly converted to $CO_2$ during the

process. In view of this, it can be concluded that the nanocomposite is an eco-friendly photocatalyst.

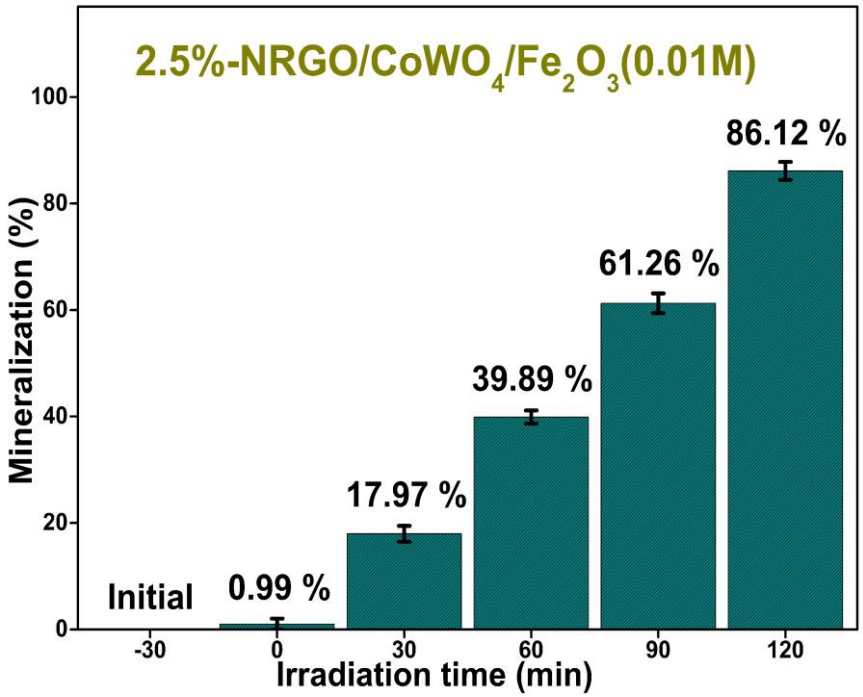


**Figure 4.13** Mineralization test bar diagram.

To find out the active species involved in photocatalytic degradation, reactions were carried out via the trapping experiments. A series of quenchers consisting of BQ (1 mM) as a scavenger for $O_2^{\cdot -}$, KI (10 mM) as a scavenger for $h^+$, $AgNO_3$ (10 mM) as a scavenger for $e^-$ and TBA (10 mM) as a scavenger for $OH^{\cdot}$ were added to the MB solution before the addition of nanocomposite to determine the dominant active species. For the ternary nanocomposites, the addition of TBA causes a small decrease in photocatalytic degradation efficiency and hence it can be assumed that it is not the main active species (Figure 4.12c). On the contrary the addition of KI, $AgNO_3$ and the BQ led to extreme decrease in the efficiency in that order. Hence it can be concluded that holes are the major species in this catalyst system influencing the photo degradation.

To assess the usefulness of the catalyst, catalytic stability and reusability of the NRGO/$CoWO_4$/$Fe_2O_3$ nanocomposite has been studied. The catalyst was recovered from the previous reaction mixture, washed with 10 % ethanol, then dried in a vacuum oven for 6 hours at 60 °C. The reused catalyst exhibited excellent catalytic activity even

after 5 successive cycles (Figure 4.12d), with small loss of activity which is 2.5 % which is acceptable for practical applications.

For the ternary nanocomposites, the improved photocatalytic degradation performance may be well ascribed to the synergetic contribution of $Fe_2O_3$, $CoWO_4$ and NRGO. The photocatalytic degradation mechanism follows equations (4.1) to (4.4).

$$Fe_2O_3 + h\upsilon \rightarrow Fe_2O_3 (e^-_{CB} + h^+_{VB}) \quad \text{----------} \quad (4.1)$$

$$Fe_2O_3 (e^-_{CB}) + CoWO_4 \rightarrow Fe_2O_3 + CoWO_4 (e^-_{CB}) \quad \text{----------} \quad (4.2)$$

$$CoWO_4 (e^-_{CB}) + O_2 \rightarrow CoWO_4 + O_2^{\cdot -} \quad \text{----------} \quad (4.3)$$

$$Fe_2O_3 (h^+_{VB}) + MB \rightarrow CO_2 + H_2O \quad \text{----------} \quad (4.4)$$

where $e^-_{CB}$ is the electron in the CB and $h^+_{VB}$ is the holes in the VB, respectively.

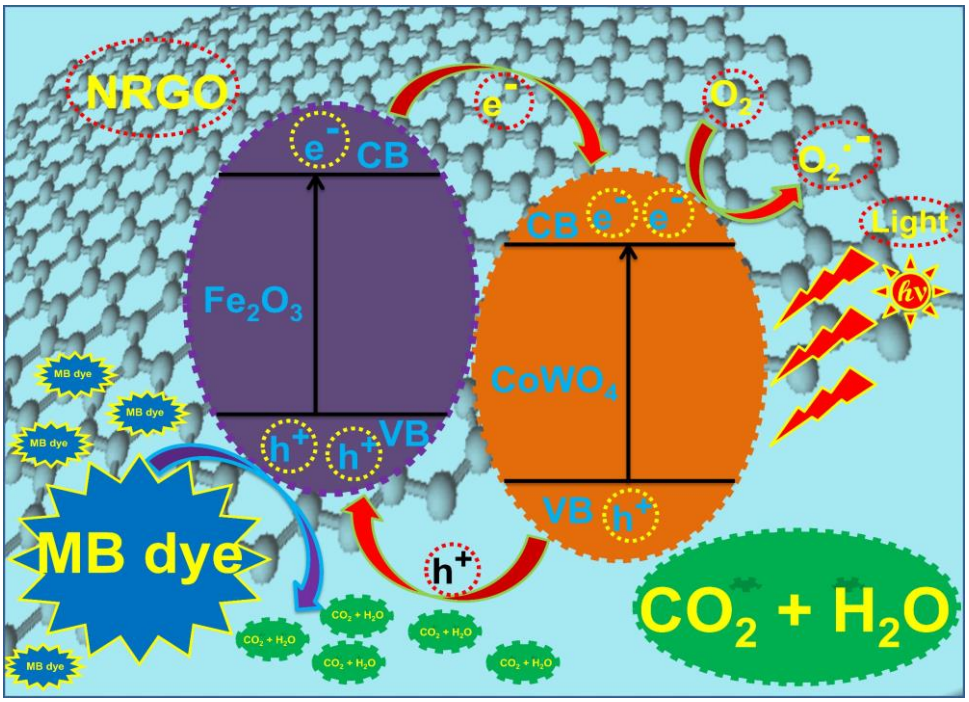


**Figure 4.14** Schematic diagram showing mechanism for photodegradation of MB using NRGO/$CoWO_4$/$Fe_2O_3$.

The schematic diagram depicting the mechanism of photocatalytic degradation in the presence of ternary nanocomposites is shown in Figure 4.14. When NRGO/$CoWO_4$/$Fe_2O_3$ is irradiated with visible light, first the electrons are excited from

the VB to the CB of the $Fe_2O_3$. Then, the electrons from the CB of $Fe_2O_3$ move to the CB of $CoWO_4$ and then get transported through NRGO interlayer for reduction of oxygen. The holes will immediately react with MB to yield harmless products like $CO_2$ and $H_2O$. Thus, the recombination of photogenerated electron-hole pairs prevented and results in improved photocatalytic degradation performance of the synthesized ternary nanocomposites. The results also suggest that the ternary nanocomposites materials could be promising candidates for various environmental applications.

### 4.3.8 Hydrogenation Activity

The catalytic activity of NRGO/$CoWO_4$/$Fe_2O_3$ nanocomposite towards hydrogenation was evaluated by the reduction of 4-NP using $NaBH_4$ in an aqueous solution. Blank test was performed in the absence of the nanocomposite which revealed negligible reduction. However, when NRGO/$CoWO_4$/$Fe_2O_3$ nanocomposite was added to the 4-NP solution, the absorption of 4-NP found at 400 nm peak decreased immediately and the new absorption peak of 4-AP appeared at 300 nm which increased in intensity with time as shown in Figure 4.15a. The catalytic reduction of 4-NP to 4-AP took 30 seconds to undergo completion which could also be seen visually in the form of color change from bright yellow to colorless (inset in Figure 4.15a). The efficiency of the ternary composite is compared with the component materials NRGO, $CoWO_4$, NRGO/$CoWO_4$ and $CoWO_4$/$Fe_2O_3$. The component materials show lower activity than the ternary composite as shown in Figure 4.15b indicating that introduction of NRGO improves the reduction efficiency of $CoWO_4$/$Fe_2O_3$.

The reaction followed first order kinetics with respect to 4-NP concentration (Kumar et al. 2016). The reaction kinetics can be expressed by the relation, $-\ln(C/C_o) = kt$, where k and t are the rate constant at a given temperature and reaction time, respectively. $C_o$ and C are the 4-NP concentration at the beginning and at time t, respectively. The first order rate constants (k) obtained from the slopes of $-\ln(C/C_o)$ vs. time plots for all the materials are shown in Figure 4.15c.

It is obvious that, among all the catalysts, NRGO/$CoWO_4$/$Fe_2O_3$ nanocomposite exhibits the maximum rate constant of 0.08438 $s^{-1}$, which is 2.3 times that of $CoWO_4$/$Fe_2O_3$ (0.03620 $s^{-1}$), 3.5 times that of NRGO/$CoWO_4$ (0.02435 $s^{-1}$) and 4.5

times that of $CoWO_4$ (0.01883 $s^{-1}$), which demonstrates the extremely good catalytic activity of NRGO/$CoWO_4$/$Fe_2O_3$ nanocomposite. The above results clearly indicate that NRGO/$CoWO_4$/$Fe_2O_3$ nanocomposite exhibits a significantly enhanced catalytic activity due to the contribution of NRGO.

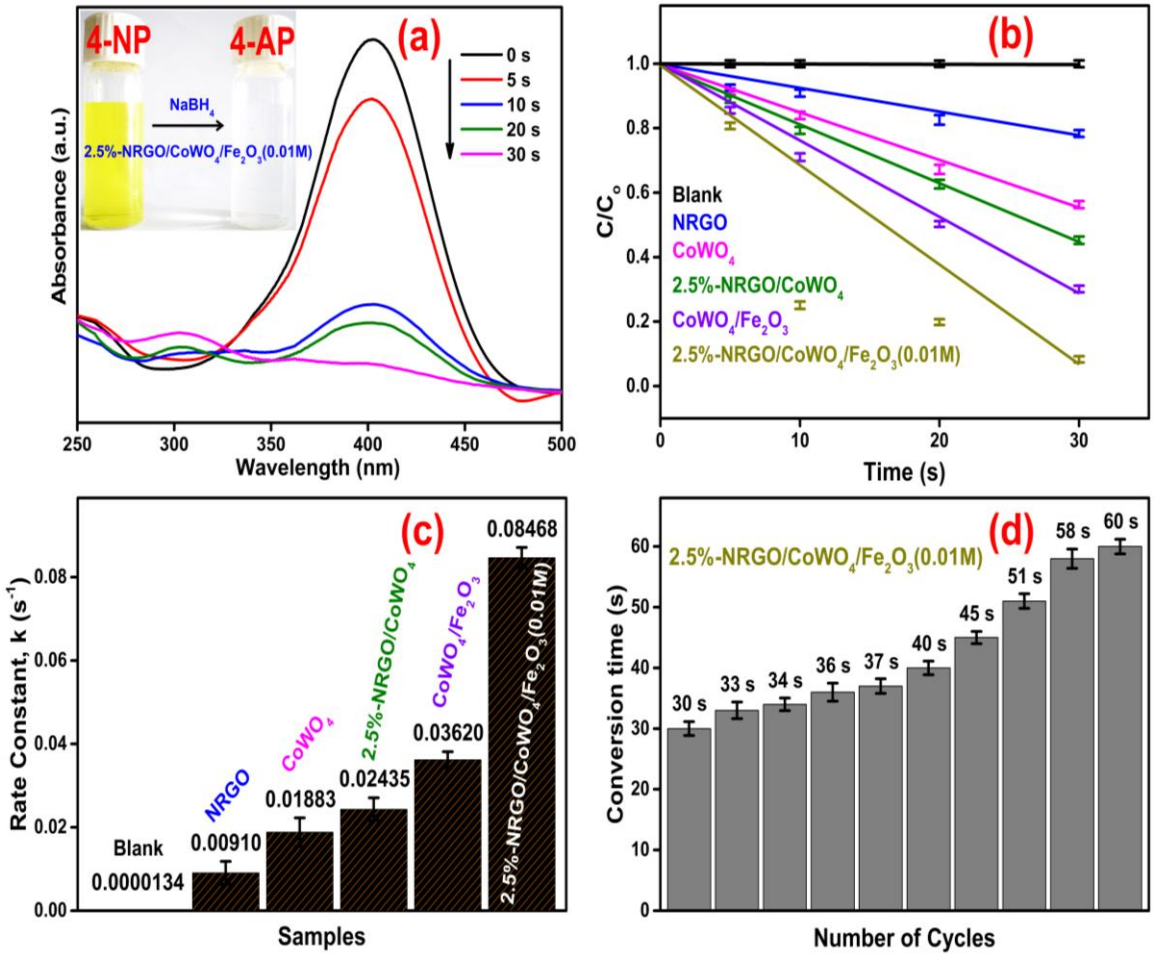


**Figure 4.15** (a) Absorption plot showing reduction of 4-NP to 4-AP using NRGO/$CoWO_4$/$Fe_2O_3$ nanocomposites, (b) Relative concentration plots for reduction of 4-NP to 4-AP using different catalysts, (c) First order rate constants for reduction of 4-NP to 4-AP using different catalysts and (d) Reusability test plots.

The catalytic stability and reusability of the NRGO/$CoWO_4$/$Fe_2O_3$ nanocomposite were carried out by extracting the catalyst from the previous reaction, washing it with 10 % ethanol, later drying it in a vacuum oven for 6 hours at 60 °C. The reused catalyst exhibited excellent catalytic activity even after 10 successive cycles, with nearly 100 % conversion within a time period of 60 seconds (Figure 4.15d).

### 4.3.9 Electrocatalytic Activity

The electrocatalytic performance of the NRGO/$CoWO_4$/$Fe_2O_3$ nanocomposite was investigated in 0.1 M KOH solution using a standard three-electrode system. For the sake of comparison, component materials and 20 wt.% Pt/C were also tested under the same conditions. The polarization curves for the HER on various electrodes are shown in Figure 4.16a. NRGO/$CoWO_4$/$Fe_2O_3$ nanocomposites demonstrated a remarkably high activity with an onset potential of 133 mV vs RHE and a HER current density of 10 mA $cm^{-2}$ at an overpotential of 331 mV. On the other hand, NRGO/$CoWO_4$ and $CoWO_4$/$Fe_2O_3$ had an onset potential of 270 mV and 288 mV and current density of 10 mA $cm^{-2}$ at an overpotential of 439 mV and 484 mV, respectively.

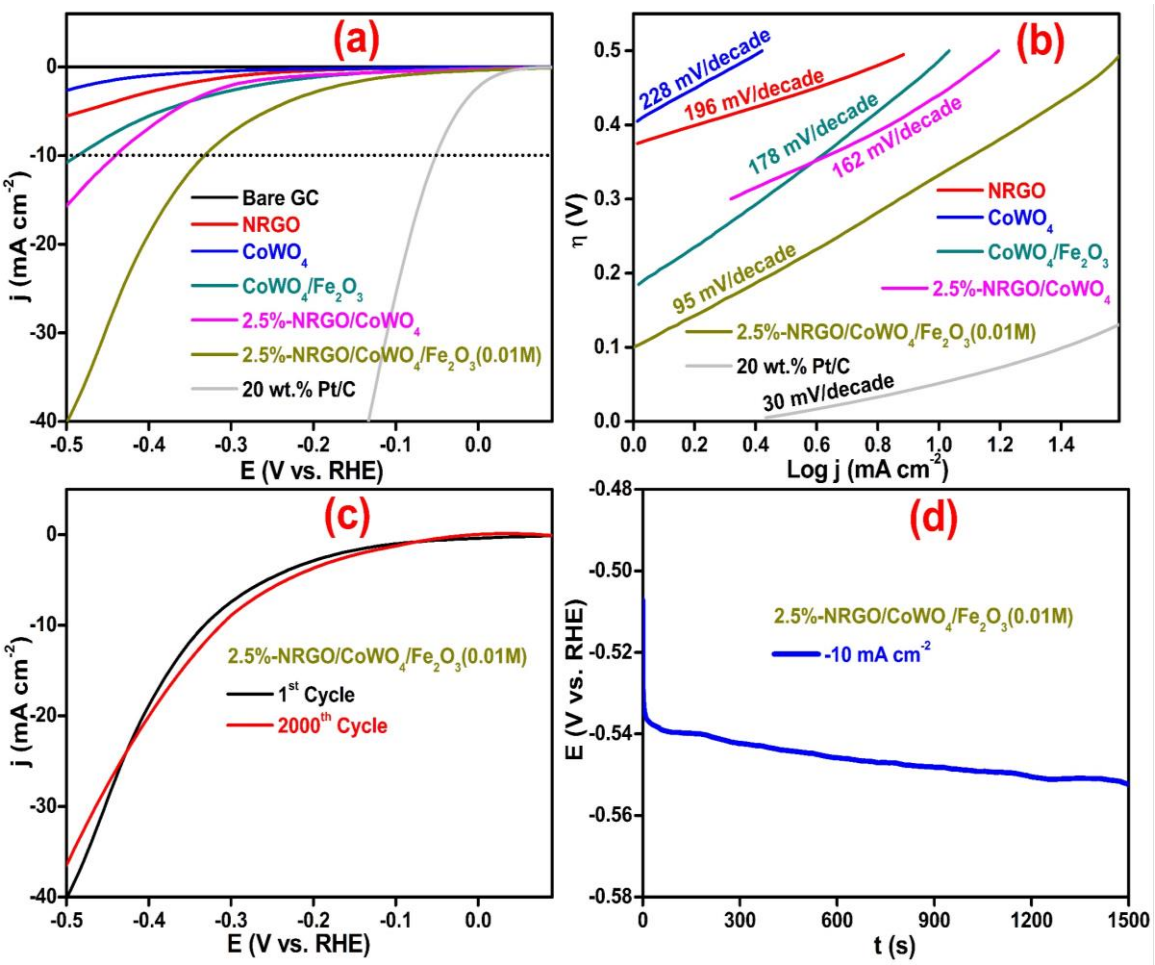


**Figure 4.16** (a) LSV and (b) Tafel curves for different electrode materials. (c) Stability curve of NRGO/$CoWO_4$/$Fe_2O_3$ nanocomposite and (d) Chronopotentiometry curve at -10 mA $cm^{-2}$ recorded using NRGO/$CoWO_4$/$Fe_2O_3$ nanocomposites.

The linear regions of the Tafel plots (Figure 4.16b) were fitted to the Tafel equation ($\eta = a + b \log (j)$, where j is the current density and b is the Tafel slope (Tilak and Chen 1993) yielding 95 mV $dec^{-1}$, 162 mV $dec^{-1}$, 178 mV $dec^{-1}$, 196 mV $dec^{-1}$ and 228 mV $dec^{-1}$ for NRGO/$CoWO_4$/$Fe_2O_3$, NRGO/$CoWO_4$, $CoWO_4$/$Fe_2O_3$, NRGO, and $CoWO_4$, respectively. This indicates that the NRGO/$CoWO_4$/$Fe_2O_3$ nanocomposites electrode has much higher activity than the component materials electrode. Although its activity is still lower than the 20 wt.% Pt/C electrodes, it may be considered significant because of the fact that it is a Pt-free catalyst. Thus, the experimentally observed Tafel slope of 95 mV $dec^{-1}$ indicated that the Heyrovsky mechanism is operating in the HER process for NRGO/$CoWO_4$/$Fe_2O_3$ nanocomposites (Bhardwaj and Balasubramaniam 2008). The measured values for important electrocatalytic parameters of the nanocomposites are given in Table 4.3.

**Table 4.3** Comparison of HER electrocatalysis parameter values of different catalysts.

| **Catalysts** | **Onset potential** | **Over potential** | **Tafel slope (mV $dec^{-1}$)** |
|---|---|---|---|
| | **(mV vs. RHE) at -10 mA $cm^{-2}$** | | |
| NRGO | -- | -- | 196 |
| $CoWO_4$ | -- | -- | 228 |
| NRGO/$CoWO_4$ | 270 | 439 | 162 |
| $CoWO_4$/$Fe_2O_3$ | 288 | 484 | 178 |
| NRGO/$CoWO_4$/$Fe_2O_3$ | 133 | 331 | 95 |

The stability test for the NRGO/$CoWO_4$/$Fe_2O_3$ catalyst has been carried out via CV measurements (2000 cycles) in 0.1 M KOH. As can be observed from Figure 4.16c, the current loss even after 2000 cycles is negligible. Thus, the test confirms that the NRGO/$CoWO_4$/$Fe_2O_3$ catalyst has good electrochemical stability for HER in 0.1 M KOH solution.

Further, the commercial application of the electrocatalyst was studied by chronopotentiometry technique at a constant current density of -10 mA/$cm^2$ applied for

a duration of 1500 seconds (Figure 4.16d). The observed result shows that the initially high potential decreases slowly and then reach to a stabilized state of HER. This phenomenon is attributed to the development of $H_2$ bubbles on the electrode surfaces. Overall, the results demonstrate that the NRGO/$CoWO_4$/$Fe_2O_3$ nanocomposite is indeed a highly efficient electrocatalyst for HER in alkaline medium.

## 4.4 CONCLUSIONS

In this work, the preparation of NRGO/$CoWO_4$/$Fe_2O_3$ ternary nanocomposite by microwave irradiation method and its characterization by XRD, TEM, HRTEM, XPS, BET, Raman, PL and UV-Vis spectroscopy is reported. The composite is studied for its photocatalytic activity on MB dye under visible light irradiation, for reduction of 4-NP to 4-AP using $NaBH_4$ and also for electrocatalytic HER. The catalytic efficiency of NRGO/$CoWO_4$/$Fe_2O_3$ is better in comparison to other composites generally used for the purpose. Based on the experimental results, possible mechanism for photodegradation is also proposed.

# CHAPTER - 5

# SYNTHESIS, CHARACTERIZATION AND STUDIES OF CATALYTIC PERFORMANCE OF NRGO/$FeWO_4$/$Fe_3O_4$ TERNARY NANOCOMPOSITE IN ENVIRONMENTAL AND ENERGY APPLICATIONS

***Chapter 5*** *describes the synthesis, characterization and studies on catalytic performance of NRGO/$FeWO_4$/$Fe_3O_4$ ternary nanocomposite in environmental and energy applications.*

## 5.1 INTRODUCTION

Iron tungstate, a Scheelite member of metal tungstate family has attracted attention due to its wide range of applications like optoelectronics, humidity sensors, solid-state laser, water splitting, scintillator, photocatalysis, photoluminescence, Li-ion batteries and energy storage materials (Zhou et al. 2009, Ma et al. 2015). But its meager adsorptive performance and high recombination rate of photogenerated electron-hole pair makes it less efficient in the field of photocatalysis (Cao et al. 2014). In order to overcome this, strategies such as doping of metal ion, coupling with semiconductor and carbonaceous materials have been made (He et al. 2015). In order to get photoresponse of the larger band gap semiconductor into the visible region, it has been coupled with semiconductor of smaller band gap. The size tunable optical and electrical properties and excellent compatibility with ZnO, $Fe_3O_4$, $TiO_2$, $Co_3O_4$ and NiO has made hybrid structures of these materials possible (Bhat 2008, Bhatt et al. 2011, Bhatt and Bhat 2012, Selvakumar and Bhat 2012, Hisatomi et al. 2014). Cao et al. synthesized $Fe_3O_4$/$FeWO_4$ composite photocatalysts via one-step hydrothermal process and examined the MB degradation (Cao et al. 2014). But it was found that the electron hole pair recombination rate was faster than the reaction rate between the $Fe_3O_4$/$FeWO_4$ composite and adsorbed pollutants. Although, different strategies have been developed to produce $FeWO_4$ based nanocomposites to inhibit the electron-hole pair recombination, the research community has not reached the goal quite yet.

N-doped graphene seems to be a perfect material to act as a support for semiconductor photocatalyst, to enhance the adsorption capacity and to reduce the recombination rate of photogenerated electron hole pairs (Li et al. 2009, Zhang et al. 2016). A good material for photocatalysis has two requirements: one-efficient charge separation and reduction in the rate of recombination of electron hole pairs; two-faster electron transfer. $FeWO_4$ coupled semiconductor with N-doped graphene may assist the

electron transfer and charge separation between the hybrid semiconductor and N-doped graphene.

A facile, scalable and low-cost synthesis of NRGO/$FeWO_4$/$Fe_3O_4$ ternary nanocomposite via microwave irradiation method is reported here. The prepared materials were thoroughly characterized and tested for their catalytic efficiency. The synergistic interactions of NRGO nanosheets, $FeWO_4$/$Fe_3O_4$ coupled semiconductor is found to increase the adsorptive property and reduce the recombination rate of photogenerated electron hole pairs. This in turn increases the efficiency of photodegradation of MB dye, reduction of 4-NP to 4-AP and electrocatalytic HER.

## 5.2 EXPERIMENTAL

### 5.2.1 Preparation of NRGO/$FeWO_4$/$Fe_3O_4$

NRGO/$FeWO_4$/$Fe_3O_4$ ternary nanocomposites were synthesized using a facile microwave irradiation method. GO was synthesized by following procedure given in section 2.2.2. Iron acetate (0.01 M), ammonium tungstate (0.005 M), ammonia (10 mL) and urea (1 %) was mixed with the calculated amount of dispersed GO solution under constant magnetic stirring for 2 hours. Later, the above reaction mixture was irradiated with microwave radiation at 350 W for 10 minutes. The black precipitate obtained was allowed to cool and washed with dilute ethanol several times and vacuum dried at 80 °C for 12 hours. For the control experiments, similar procedures were carried out with required precursors to obtain $FeWO_4$, $Fe_3O_4$ and $FeWO_4$/$Fe_3O_4$. The detailed scheme is shown in Figure 5.1.

### 5.2.2 Characterization and Catalytic Studies

The characterization of the synthesized samples was carried out as given in section 2.2.9 and section 3.2.3. The catalytic studies were performed as described in section 2.2.10 -2.2.12.

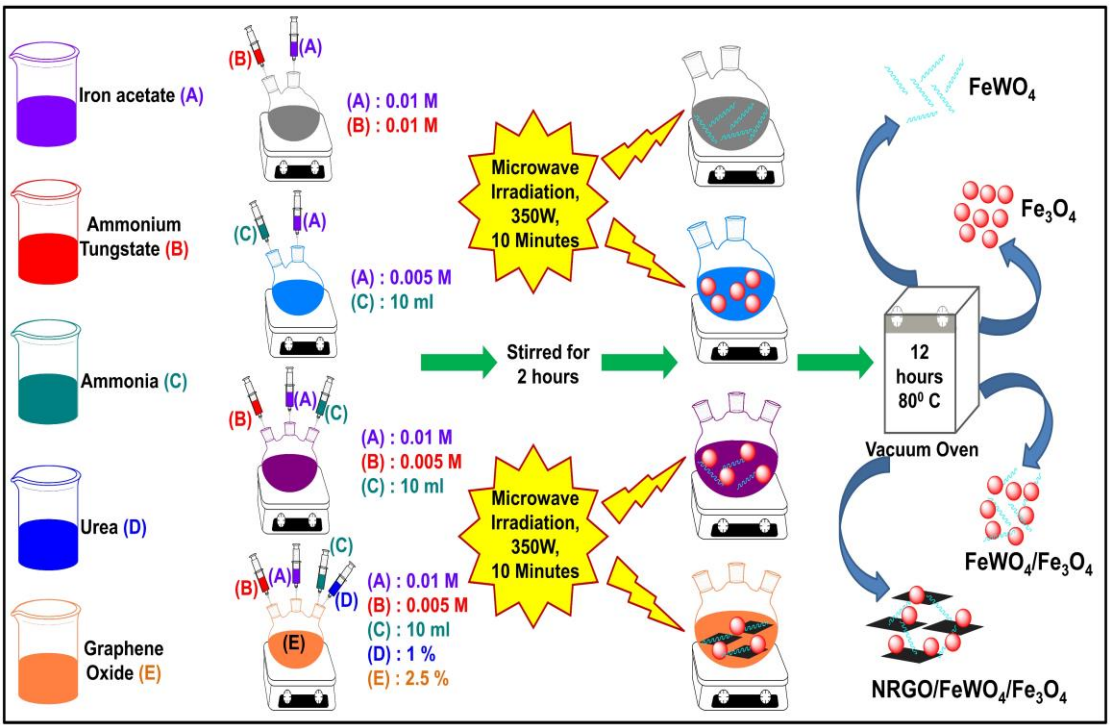


**Figure 5.1** Scheme for the synthesis of various catalytic materials.

## 5.3 RESULTS AND DISCUSSION

### 5.3.1 XRD Studies

The crystal structure of GO and NRGO/$FeWO_4$/$Fe_3O_4$ nanocomposites was determined by XRD (Figure 5.2). The XRD pattern of NRGO/$FeWO_4$/$Fe_3O_4$ nanocomposites clearly shows that no other impurity peaks are present. Only the characteristic diffraction patterns of $FeWO_4$ crystals in monoclinic ferberite structure (JCPDS No. 46-1446, space group P2/c, space group number 13, lattice constant a = 0.4739 nm, b = 0.5718 nm, c = 0.4965 nm, $\alpha = \gamma = 90°$ and $\beta = 90.12°$) and $Fe_3O_4$ crystals in cubic phase (JCPDS No. 19-0629, space group Fd-3m, space group number 227, lattice constant a = 0.8396 nm, $\alpha = \beta = \gamma = 90°$) are seen. For GO (Figure 5.2a), the diffraction peak appears at $2\theta = 10.5°$. But, in the case of NRGO/$FeWO_4$/$Fe_3O_4$ nanocomposite, no diffraction peak corresponding to GO is seen which indicates the reduction of GO during the preparation, eliminating the oxygen containing functional groups and exfoliation (Sudhakar et al. 2014). It is clear that NRGO coupling had negligible effect on the crystal structure of $FeWO_4$ and $Fe_3O_4$.

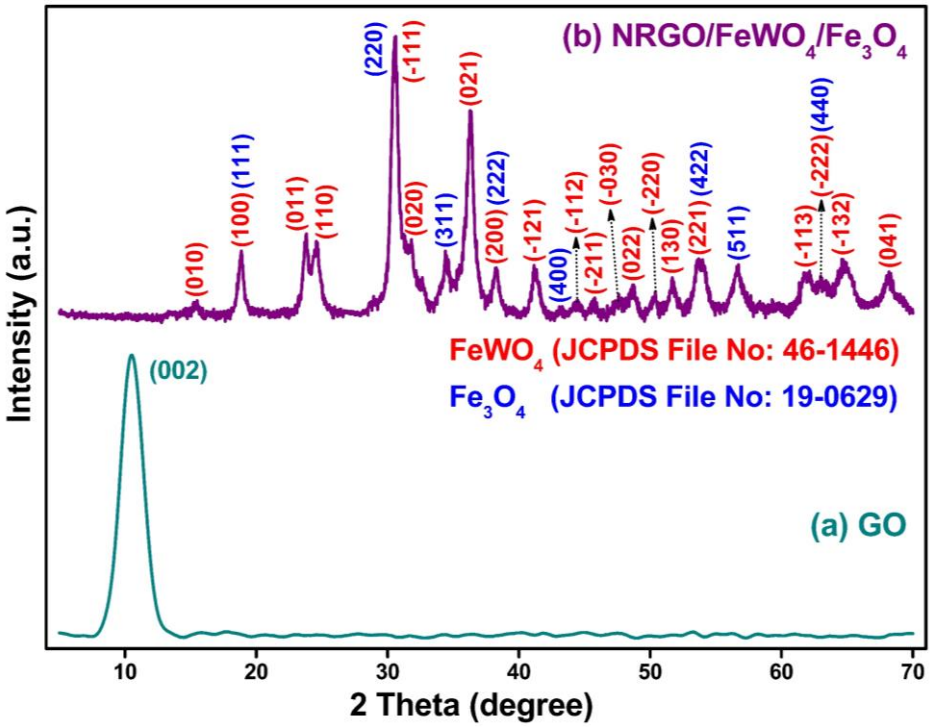


**Figure 5.2** XRD spectra of (a) GO and (b) NRGO/$FeWO_4$/$Fe_3O_4$ nanocomposites.

### 5.3.2 Raman Studies

The Raman spectrum of NRGO/$FeWO_4$/$Fe_3O_4$ nanocomposite (Figure 5.3) shows bands at 113 $cm^{-1}$, 185 $cm^{-1}$, 263 $cm^{-1}$, 340 $cm^{-1}$, 774 $cm^{-1}$ and 894 $cm^{-1}$ corresponding to the $FeWO_4$, in agreement with the previous report (Zhou et al. 2009). The strong band at 894 $cm^{-1}$ is attributed to $\nu_1$ symmetric $A_g$ mode of terminal $WO_2$. The ν3 antisymmetric stretching mode at 774 $cm^{-1}$, $\nu_2$ bending mode at 340 $cm^{-1}$ and ν4 bending mode at 263 $cm^{-1}$ are related to the bands associated with tungstate anion. The bands at 185 $cm^{-1}$ and 113 $cm^{-1}$ that are below 200 $cm^{-1}$ are related to the lattice vibration (Cao et al. 2014). The Raman peaks at 406 $cm^{-1}$, 532 $cm^{-1}$ and 697 $cm^{-1}$ corresponds to $Fe_3O_4$ (Cao et al. 2014). The peak at 697 $cm^{-1}$ is assigned to the $A_{1g}$ symmetric stretch mode of Fe-O bonds. The two bands at 406 $cm^{-1}$ and 532 $cm^{-1}$ are ascribed to $T_{2g}^3$ and $T_{2g}^2$ vibration modes of $Fe_3O_4$, respectively.

In general, graphene exhibits Raman modes at 1600 $cm^{-1}$ and 1350 $cm^{-1}$, referred to as the G and D bands, respectively (Graf et al. 2007). In the Raman spectrum of GO, the D peak at 1355 $cm^{-1}$ arises from the $sp^3$ defective carbon structures, while the G peak at 1599 $cm^{-1}$ occurs due to $E_{2g}$ graphite mode, reflecting the graphitization

of $sp^2$ carbon material. After microwave reduction, NRGO exhibits the D and G band peak being downshifted to lower wavenumber region from 1355 $cm^{-1}$-1346 $cm^{-1}$ and from 1599 $cm^{-1}$-1598 $cm^{-1}$ respectively, owing to the self-healing characteristics of the NRGO that recovers the hexagonal network of carbon atoms with defects. This suggests the successful reduction of GO to NRGO. During the reduction of GO to NRGO, the defects on the surface of the NRGO can increase, leading to an increase in the D band intensity compared to that of GO. NRGO/$FeWO_4$/$Fe_3O_4$ nanocomposite also exhibits two peaks at 1368 $cm^{-1}$ and 1642 $cm^{-1}$ which are the D and G bands, respectively. When $FeWO_4$/$Fe_3O_4$ is incorporated with NRGO, a notable shift in the D and G band is observed towards higher wavenumber from 1346 $cm^{-1}$ and 1598 $cm^{-1}$ of NRGO to 1368 $cm^{-1}$ and 1642 $cm^{-1}$ respectively indicating strong interaction between NRGO sheet and $FeWO_4$/$Fe_3O_4$.

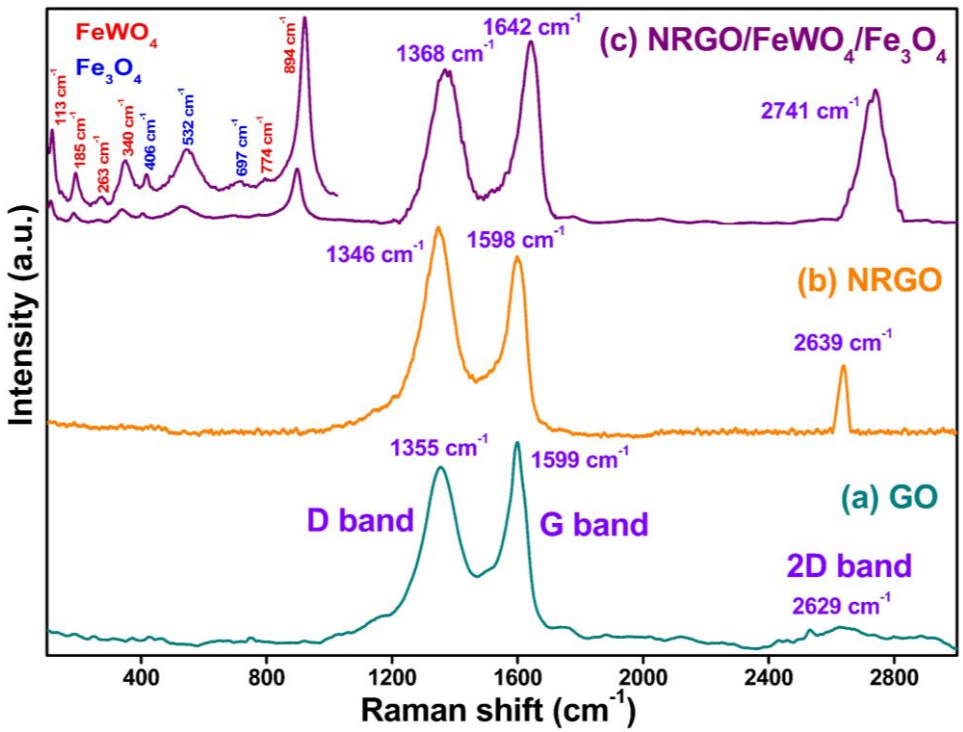


**Figure 5.3** Raman spectra of (a) GO, (b) NRGO and (c) NRGO/$FeWO_4$/$Fe_3O_4$ nanocomposites.

The GO intensity ratio of D to G peaks ($I_D/I_G$ is 0.87) displays the extent of defects in graphitic structure. Thus, more the $I_D/I_G$ ratio, lesser is the graphite carbon structures (Graf et al. 2007). The $I_D/I_G$ intensity ratio of NRGO and

NRGO/$FeWO_4$/$Fe_3O_4$ nanocomposites are higher than that of the GO. This modification indicates an increase in the defective domains after the microwave reduction of GO. More interestingly, the $I_D/I_G$ value of NRGO/$FeWO_4$/$Fe_3O_4$ is decreased to 0.88, which is less in comparison with the calculated $I_D/I_G$ value of NRGO (1.15). This clearly suggests that the incorporation of $FeWO_4$/$Fe_3O_4$ has taken place on the defective sites of the NRGO and has contributed to the reduction of defects and restoration of the basal plane conjugation on the surface of NRGO. This phenomenon can also be associated with the charge transfer between the NRGO and $FeWO_4$/$Fe_3O_4$ nanoparticles. In this work, the presence of the 2D band at 2629 $cm^{-1}$ (GO), 2639 $cm^{-1}$ (NRGO) and 2741 $cm^{-1}$ (NRGO/$FeWO_4$/$Fe_3O_4$) originates from a double resonance process. The calculated intensity ratio values of $I_{2D}/I_G$ show that it changed from 0.06 to 0.66 and 0.74 after reduction with microwave irradiation, demonstrating the increase in exfoliation extent of multilayer structured graphene sheets and reduction in the size of graphene domains. These studies show that surface defects are present in NRGO/$FeWO_4$/$Fe_3O_4$ nanocomposites which may also contribute to the catalytic efficiency of the nanocomposite.

### 5.3.3 Morphology Studies

The BET specific surface area of as-synthesized NRGO/$FeWO_4$/$Fe_3O_4$ nanocomposites is found to be 48.98 $m^2g^{-1}$. This value is lower than the theoretical surface area of graphene (2630 $m^2g^{-1}$) and more than the surface area of $FeWO_4$/$Fe_3O_4$ (24.20 $m^2/g$). This increase in surface area is due to the introduction of N-doped graphene nanosheets into hybrid semiconductor. In addition to this, morphology was studied using FESEM and HRTEM (Figure 5.4). FESEM image (Figure 5.4a) shows that the NRGO/$FeWO_4$/$Fe_3O_4$ nanocomposite is composed of $Fe_3O_4$ nanospheres with $FeWO_4$ nanowire like structures along with the NRGO sheets. The nanowires of $FeWO_4$ have a length of 1.13 μm and a width of about 150 nm. The particle size distribution of the $Fe_3O_4$ nanospheres shows that the average particle size is around 11.4 nm. The HRTEM lattice fringes of $FeWO_4$ and $Fe_3O_4$ nanoparticles in the nanocomposite are shown in Figure 5.4b. The lattice fringes of 0.37 nm and 0.26 nm match the (002) planes of monoclinic $FeWO_4$ and (311) planes of cubic $Fe_3O_4$, respectively. The HRTEM image also reveals the formation of a smooth heterojunction interface between $FeWO_4$

and $Fe_3O_4$ nanoparticles in the nanocomposite. To get more detailed information on the distribution of particles in NRGO/$FeWO_4$/$Fe_3O_4$ nanocomposite elemental mapping analysis was carried out, which showed uniform distribution of N, C, Fe, W and O (Figure 5.5).

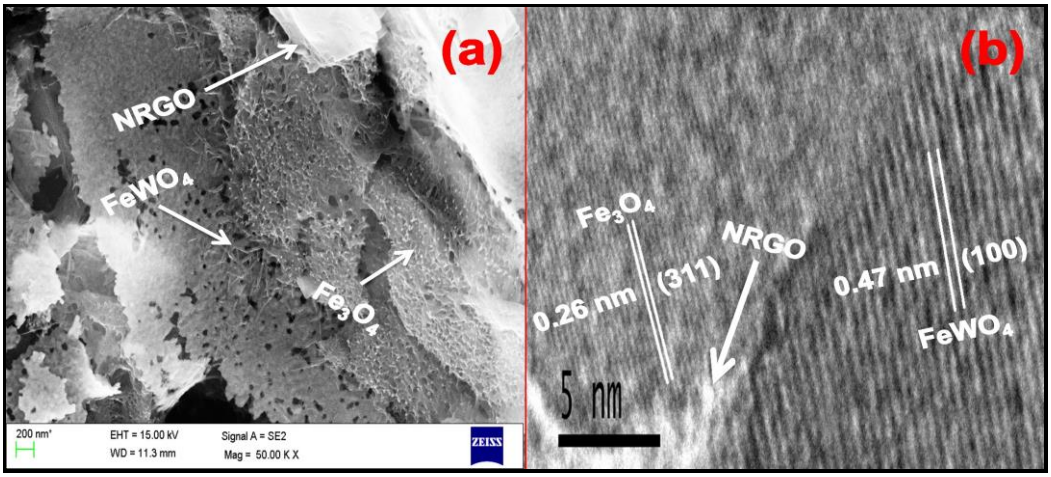


**Figure 5.4** Electron microscopy images of NRGO/$FeWO_4$/$Fe_3O_4$ nanocomposites (a) FESEM image showing NRGO decorated with $FeWO_4$ nanowires and $Fe_3O_4$ nanospheres, (b) HRTEM image**.**

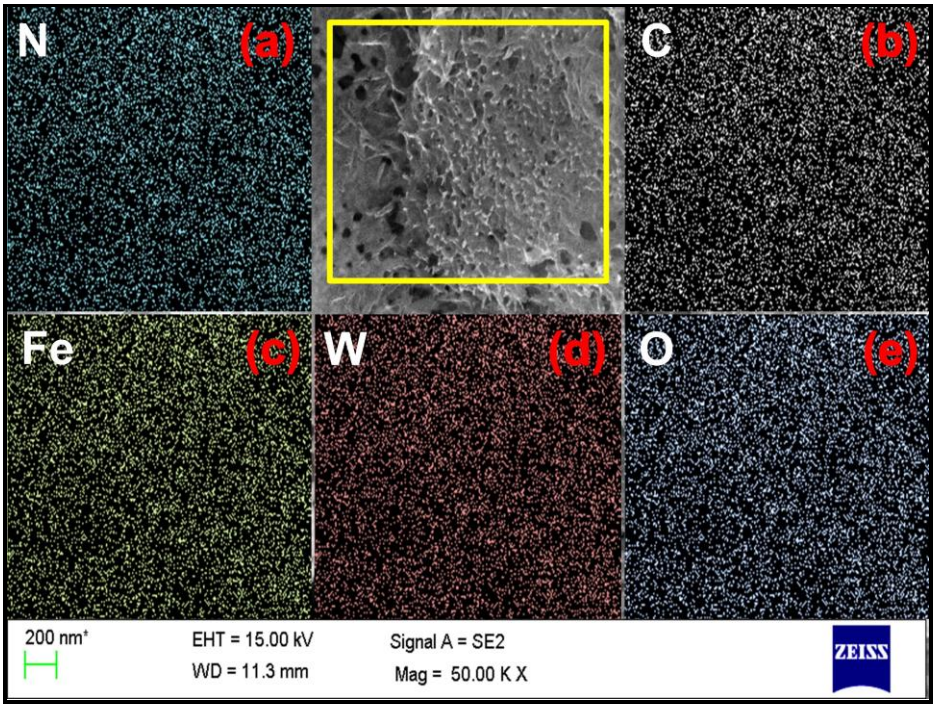


**Figure 5.5** Elemental mapping of NRGO/$FeWO_4$/$Fe_3O_4$ nanocomposites (a) N, (b) C, (c) Fe, (d) W and (e) O.

### 5.3.4 XPS Studies

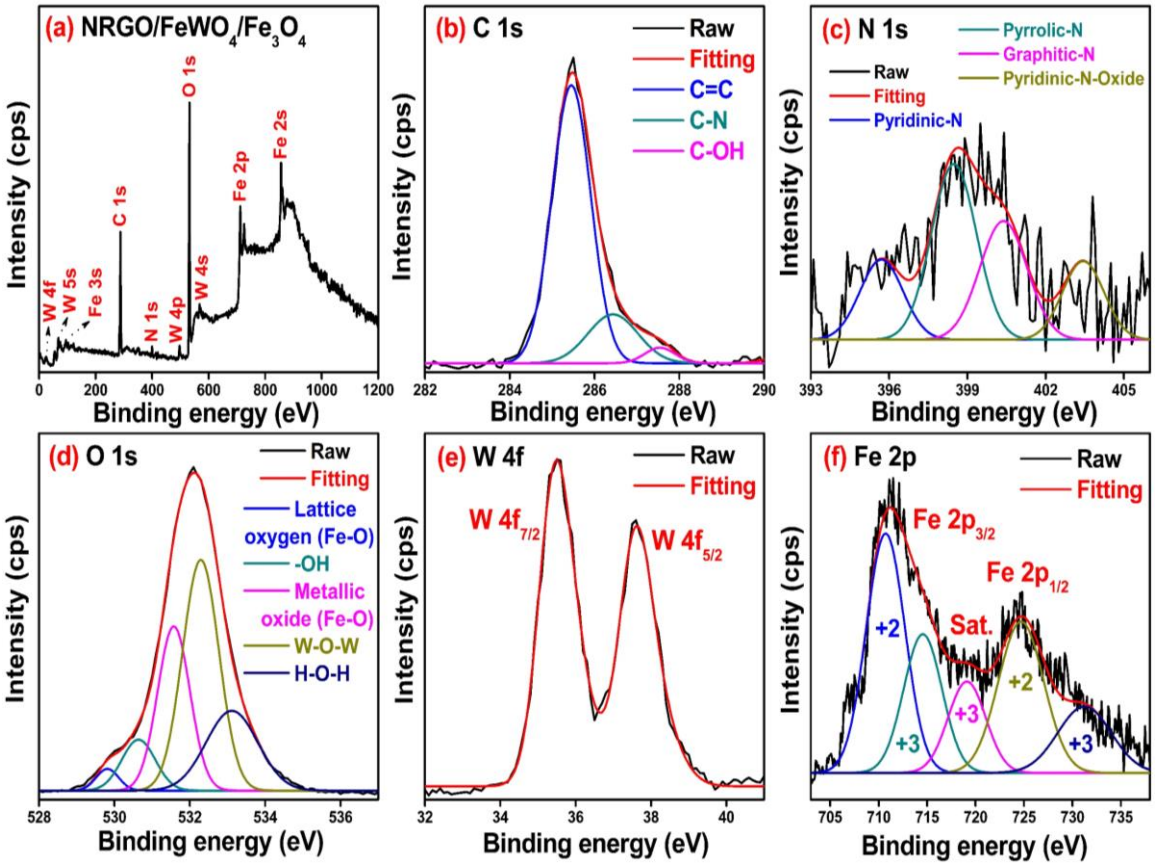


**Figure 5.6** XPS spectra of NRGO/$FeWO_4$/$Fe_3O_4$ nanocomposites (a) survey and high resolution XPS of (b) C 1s, (c) N 1s, (d) O 1s, (e) W 4f, (f) Fe 2p.

The XPS survey spectrum (Figure 5.6a) of NRGO/$FeWO_4$/$Fe_3O_4$ nanocomposite reveals peaks corresponding to C 1s (284.8 eV), N 1s (399.8 eV), Fe 2p (710.6 eV), O 1s (530.8 eV) and W 4f (35.5 eV). The detailed elemental compositions are summarized in Table 5.1. The C 1s XPS (Figure 5.6b) spectrum was deconvoluted into three peaks of C-C (284.8 eV), C-N (286.5 eV) and C-OH (288.0 eV). The peak corresponding to C-OH is very small, demonstrating that GO has been reduced to RGO (Zhang et al. 2016). The N 1s XPS (Figure 5.6c) was deconvoluted into four peaks of pyridinic-N (398.4 eV), pyrrolic-N (399.4 eV), graphitic-N (400.8 eV) and pyridine-N-oxide (402.4 eV), respectively (Li et al. 2009; Zhang et al. 2016). The deconvoluted Fe 2p XPS (Figure 5.6f) consists of two peaks located at 710.6 eV and 723.6 eV which corresponds to the binding energies of Fe $2p_{3/2}$ and Fe $2p_{1/2}$. A satellite peak was

observed at 719 eV, which conforms to the Fe ions in $FeWO_4/Fe_3O_4$. The Fe $2p_{3/2}$ and Fe $2p_{1/2}$ peaks are deconvoluted into $Fe^{2+}$ and $Fe^{3+}$ peaks, and a satellite peak at $Fe^{3+}$. In W 4f XPS (Figure 5.6e), two peaks appearing at 35.5 eV and 37.6 eV corresponds to the binding energies of W $4f_{7/2}$ and W $4f_{5/2}$ corresponding to the +6 valence state of W in $FeWO_4$ (Cao et al. 2014). The O 1s XPS (Figure 5.6d) region was deconvoluted into five peaks corresponding to lattice oxygen of Fe-O (529.8 eV), –OH bonds (530.3 eV), metallic oxides of Fe-O (531.5 eV), W-O-W (532.5 eV) and water molecules (H-O-H) adsorbed on the surface (533.3 eV), respectively. The obtained data agrees well with the results from XRD and Raman analysis and confirms the formation of ternary composite.

**Table 5.1** Surface elemental composition and C, N, Fe, W, O contents with relative intensities of C 1s, N 1s, Fe 2p, W 4f, O 1s peaks from XPS analysis of the NRGO/$FeWO_4/Fe_3O_4$ nanocomposites.

| | | | | | |
|---|---|---|---|---|---|
| **At %** | **Contents** | | | | |
| | **N** | **C** | **Fe** | **W** | **O** |
| | 0.31 % | 13.24 % | 50.87 % | 6.92 % | 28.66 % |
| **C 1s** | **C=C** | | **C-N** | **C-OH** | |
| | 80.04 % | | 14.20 % | 5.76 % | |
| **N 1s** | **Pyridinic N** | **Pyrrolic N** | **Graphitic N** | **Pyridinic N Oxide** | |
| | 15.23 % | 43.77 % | 26.70 % | 14.30 % | |
| **O 1s** | **Lattice oxygen Fe-O** | **–OH bonds** | **Metallic oxides Fe-O** | **W-O-W** | **H-O-H** |
| | 5.27 % | 10.82 % | 28.27 % | 41.94 % | 13.7 % |
| **W 4f** | **W $4f_{7/2}$** | | **W $4f_{5/2}$** | | |
| | 52.17 % | | 47.83 % | | |
| **Fe 2p** | **Fe $2p_{3/2}$** | | **Sat.** | **Fe $2p_{1/2}$** | |
| | **+2** | **+3** | **+3** | **+2** | **+3** |
| | 30.71 % | 21.84 % | 14.67 % | 22.98 % | 9.80 % |

### 5.3.5 DRS Analysis

The DRS analysis used to explore the electronic structural properties of the $FeWO_4$, $Fe_3O_4$, $FeWO_4/Fe_3O_4$ and $NRGO/FeWO_4/Fe_3O_4$ nanocomposites. It is observed that the optical absorption of all the samples at wavelength higher than 400 nm, which corresponds to the excitation of electrons from the VB to the CB in the visible light region. The absorption edge of the ternary composite displayed extreme red-shift in comparison with component materials (Figure 5.7a). The band gap energy was estimated from plot of $(\alpha h\upsilon)^2$ versus photon energy ($h\upsilon$) for $FeWO_4$, $Fe_3O_4$, $FeWO_4/Fe_3O_4$ and $NRGO/FeWO_4/Fe_3O_4$ nanocomposites (Figure 5.8). The band gaps were evaluated using Tauc approach as explained in previous chapters. The direct band gap energies for $FeWO_4$, $Fe_3O_4$, $FeWO_4/Fe_3O_4$ and $NRGO/FeWO_4/Fe_3O_4$ nanocomposite are 2.73 eV, 2.61 eV, 2.12 eV, and 1.94 eV, respectively. The decrease in the band gap of ternary composite makes it more efficient in photocatalysis compared to other component materials.

Based on the DRS results, the band edge positions of the nanocomposites were also calculated theoretically using the Mulliken electronegativity theory as described in previous chapters. The calculated band edge energy of CB and VB of $FeWO_4$ and $Fe_3O_4$ are listed in Table 5.2. For $Fe_3O_4$, the band edge values of $E_{CB}$ and $E_{VB}$ are slightly lesser than those for $FeWO_4$. The comparison of UV-Vis absorption spectra and bandgap energies of the composite and components of the composite considered separately show distinct differences in their values. Such variation in the results is attributed to the delocalization of surface charges resulting due to the interactions of NRGO in the composite. It is believed that such interactions lead to the formation of new molecular orbitals of lower energy which in turn facilitates the reduction in the bandgap and hence variations in the photo physical properties (Wang et al. 2012, Jo and Selvam 2015).

**Table 5.2** Band gap parameters of the $FeWO_4$ and $Fe_3O_4$.

| **Samples** | **χ (eV)** | **$E_g$ (eV)** | **$E_{VB}$ (eV)** | **$E_{CB}$ (eV)** |
|---|---|---|---|---|
| **$FeWO_4$** | 6.301 | 2.73 | 3.082 | 0.352 |
| **$Fe_3O_4$** | 5.792 | 2.61 | 2.588 | -0.022 |

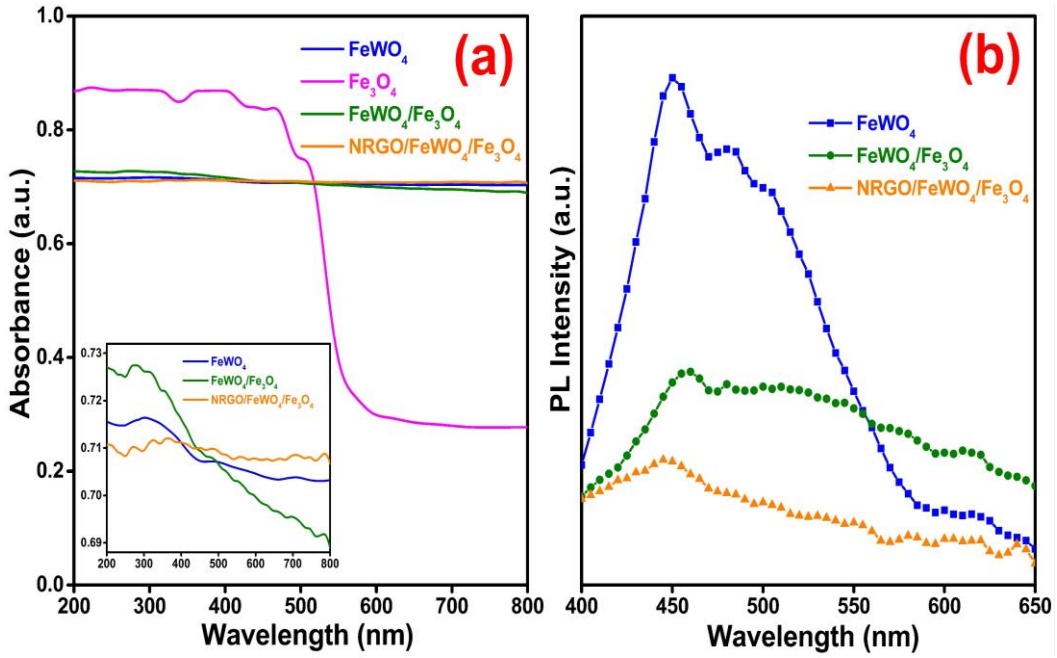


**Figure 5.7** (a) DRS of $FeWO_4$, $Fe_3O_4$, $FeWO_4/Fe_3O_4$ and $NRGO/FeWO_4/Fe_3O_4$ nanocomposites, (b) PL spectra of $FeWO_4$, $FeWO_4/Fe_3O_4$ and $NRGO/FeWO_4/Fe_3O_4$ nanocomposites.

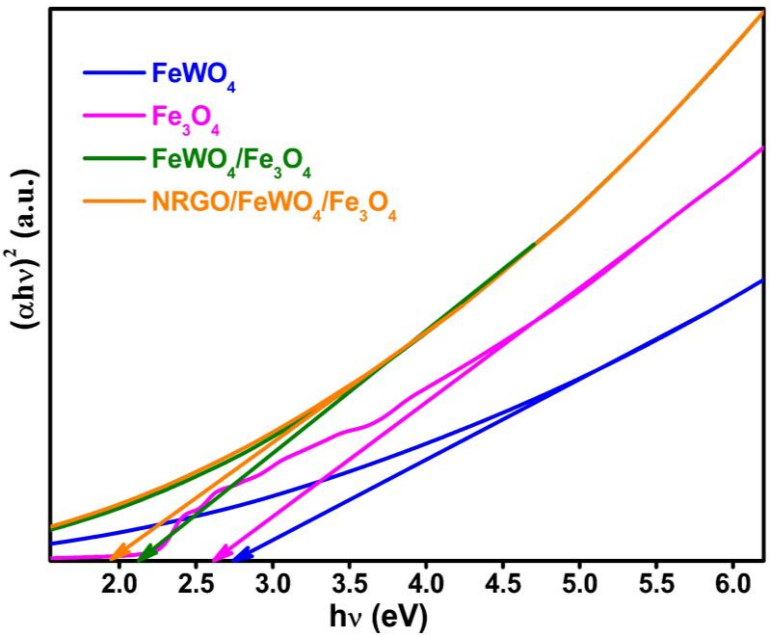


**Figure 5.8** Tauc plots of $FeWO_4$, $Fe_3O_4$, $FeWO_4/Fe_3O_4$ and $NRGO/FeWO_4/Fe_3O_4$ nanocomposites.

### 5.3.6 Photoluminescence Analysis

PL spectra can be used to study the recombination rate of the photogenerated electron hole pairs. If the recombination rate is lower, then the intensity of PL peak will be lower (Wang et al. 2015). The PL spectrum of the nanocomposite was recorded using an excitation wavelength of 380 nm and compared with that of the component materials (Figure 5.7b). A highly intense peak at 450 $cm^{-1}$ was observed for $FeWO_4$. The intensity of this peak decreased for the $FeWO_4/Fe_3O_4$ hybrid semiconductor indicating the decrease in the recombination rate in $FeWO_4$. In the case of the ternary composite the intensity of the peak was very less suggesting that NRGO contributes effectively to decrease the recombination rate to a bare minimum.

### 5.3.7 Photocatalytic Activity

The photocatalytic activity of the ternary nanocomposite and the individual components were determined by studying the degradation of MB dye using visible light source. The blank test conducted in absence of the catalyst revealed negligible degradation of the dye. The photocatalytic dye degradation efficiency under visible light irradiation in the presence of the NRGO, $FeWO_4$, $Fe_3O_4$, NRGO/$FeWO_4$, NRGO/$Fe_3O_4$, $FeWO_4/Fe_3O_4$ and mechanically mixed NRGO/$FeWO_4/Fe_3O_4$ (NRGO mix $FeWO_4/Fe_3O_4$) are 17.34 %, 54.20 %, 36.96 %, 79.47 %, 62.05 %, 86.66 % and 92.43 % respectively (Figure 5.9a). The total reaction time considered was 120 minutes. However, in the case of the ternary nanocomposite the degradation was over within 100 min. The results suggest that compositing of NRGO with the $FeWO_4/Fe_3O_4$ hybrid semiconductor improves the photodegradation efficiency vastly which is further confirmed by the rate constants obtained.

The reaction kinetics for the degradation of MB under visible light was determined using the equation $-\ln(C/C_o) = kt$, where k, t, $C_o$ and C are the rate constant at temperature T, irradiation time, MB concentration at the beginning and at time t, respectively (Kumar et al. 2016). The first order kinetic plots of $-\ln(C/C_o)$ vs. irradiation time for all the catalysts are shown in Figure 5.9b. The comparison of the reaction rate constants (k) are shown in Figure 5.9c, obtained from the slope of the plot in Figure

5.9b. NRGO/$FeWO_4$/$Fe_3O_4$ nanocomposite had the highest rate constant among all amounting up to 0.02668 $min^{-1}$ showing incredible photocatalytic activity.

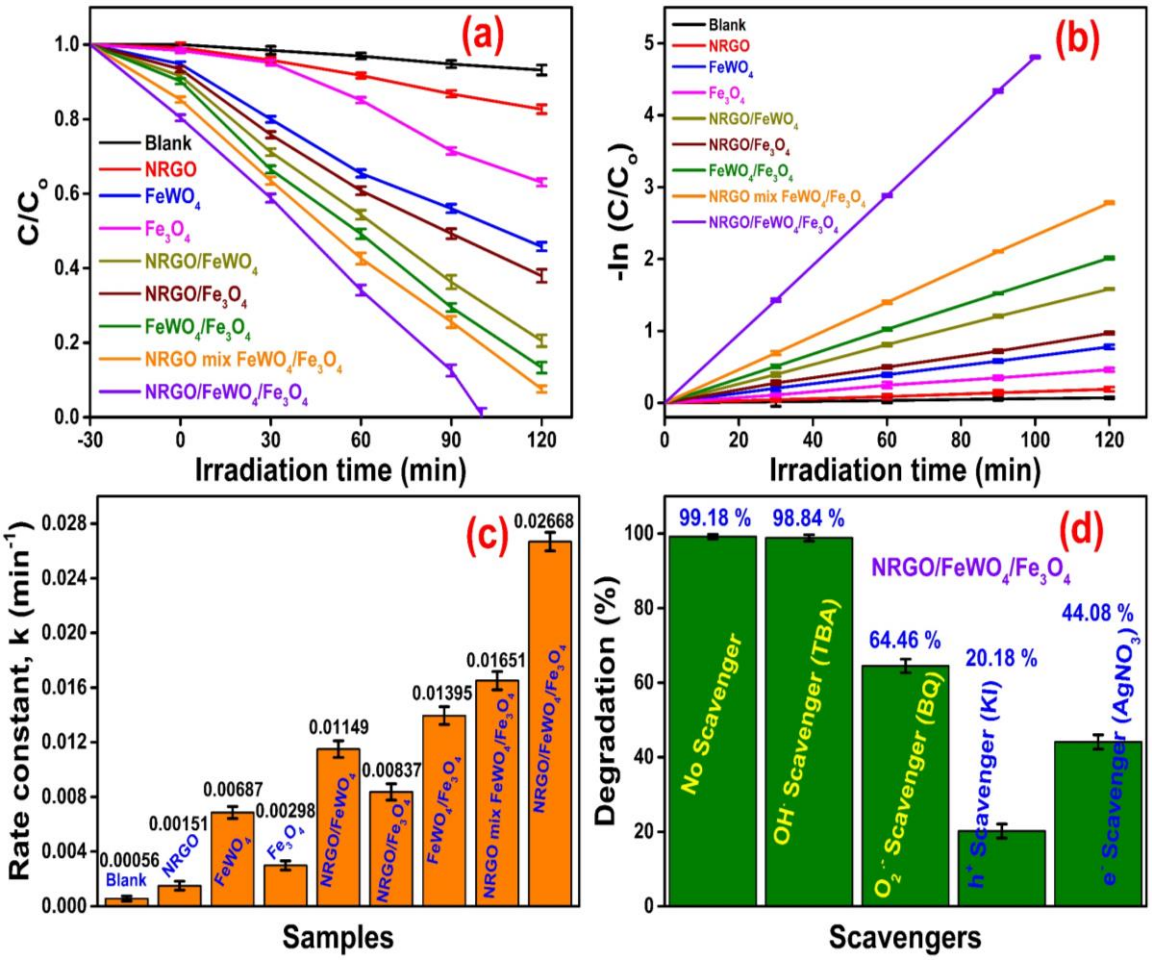


**Figure 5.9** (a) Degradation rates for MB dye, (b) First order kinetic plots of -ln($C/C_o$) against the irradiation time, (c) Rate constant k ($min^{-1}$) for the photodegradation of MB over various catalytic materials, (d) Effects of the different scavengers on the photodegradation efficiency of NRGO/$FeWO_4$/$Fe_3O_4$ nanocomposites.

To determine the degree of mineralization of MB, during its photodegradation catalyzed by NRGO/$FeWO_4$/$Fe_3O_4$ nanocomposite, TOC analysis was performed (Cui et al. 2013). Figure 5.10 shows the TOC values for the MB solution at different intervals of time. As can be observed from the figure, it is evident that the mineralization value increased to 89.22 % in 120 minutes or TOC content decreased to 10.78 % indicating that the organic carbon is mostly converted to $CO_2$ during the process. In view of this, it can be concluded that the nanocomposite is an eco-friendly photocatalyst.

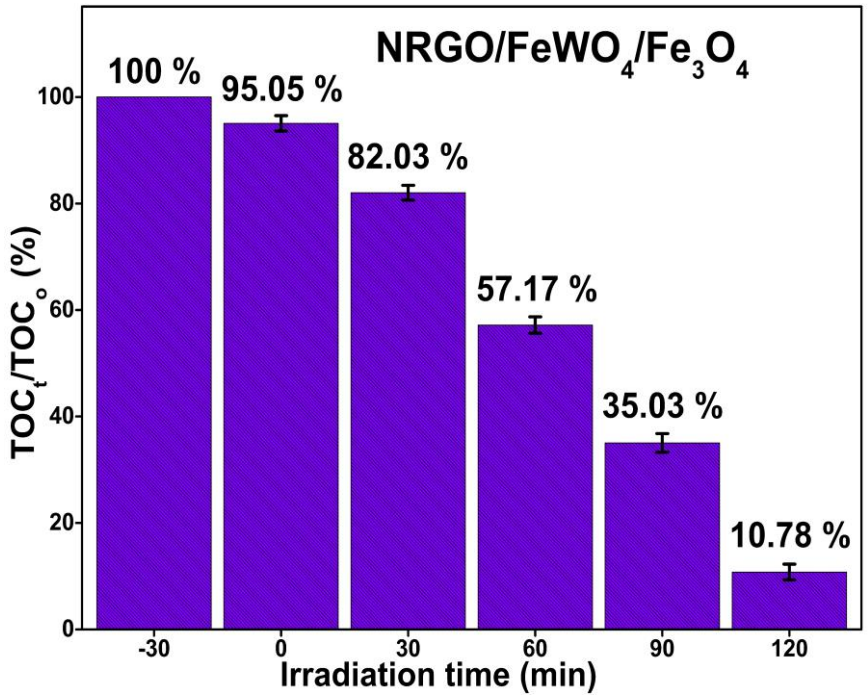


**Figure 5.10** TOC values for the degradation of MB at different intervals of time.

The commercial application of a catalyst would require it to be highly stable and reusable. NRGO/$FeWO_4$/$Fe_3O_4$ nanocomposite catalyst was recovered from the reaction, washed with ethanol and dried in vacuum oven for 6 hours at 60 °C and it was reused. The percentage degradation for next 10 consecutive cycles is shown in Figure 5.11. The degradation efficiency decreased from 99.18 % to 93.44 % after 10 cycles indicating high stability and reusability of the catalyst.

In order to figure out the mechanism of photodegradation of MB dye, experiments were carried out using radical scavengers (Figure 5.9d). The control experiments were done to analyze the role of $O_2^{\cdot -}$, OH, $e^-$ and $h^+$ in the photocatalysis process by using BQ, TBA, $AgNO_3$ and KI for $O_2^{\cdot -}$, ·OH, photogenerated $e^-$ and $h^+$, respectively. Addition of TBA caused slight decrease in the photodegradation efficiency due to the removal of hydroxyl radicals, indicating that they play a minor role in the mechanism. BQ, silver nitrate and KI caused decrease in the efficiency in the increasing order suggesting that holes play a major role in the overall degradation pathway.

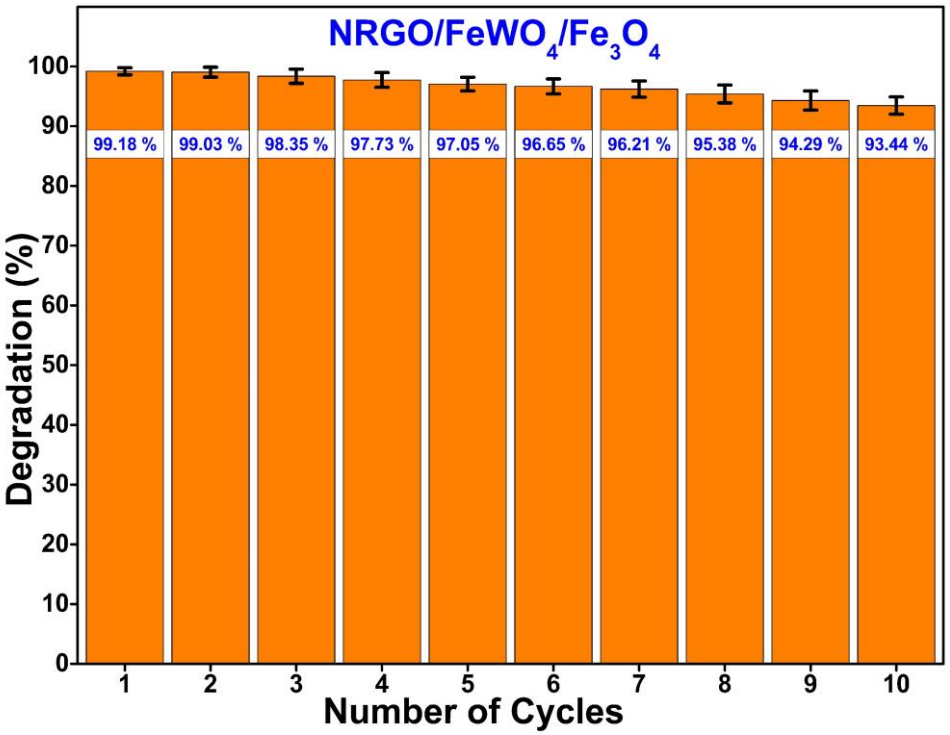


**Figure 5.11** Stability of NRGO/$FeWO_4$/$Fe_3O_4$ nanocomposites during the photodegradation of MB.

The possible mechanism is schematically shown in Figure 5.12. The MB molecules get partially adsorbed on the surface of the ternary nanocomposite. When light is irradiated on the solution, electrons get excited from the VB to the CB of $Fe_3O_4$ leaving a hole in the VB. This photogenerated electron is quickly transferred to $FeWO_4$ and then to NRGO decreasing the recombination rate of electron and hole. The transferred $e^-$ then reacts with the dissolved $O_2$ to yield $O_2^{\cdot -}$. The holes in the VB would get transported through the NRGO matrix to react with $H_2O$ to form ·OH. Finally, all the formed active species, ·OH, $e^-$, $h^+$ and $O_2^{\cdot -}$ react with the dye molecules to give harmless products such as $CO_2$ and $H_2O$. Thus, NRGO/$FeWO_4$/$Fe_3O_4$ ternary nanocomposite can effectively optimize the charge transfer, reduce the recombination rate and hence improves the photodegradation rate immensely.

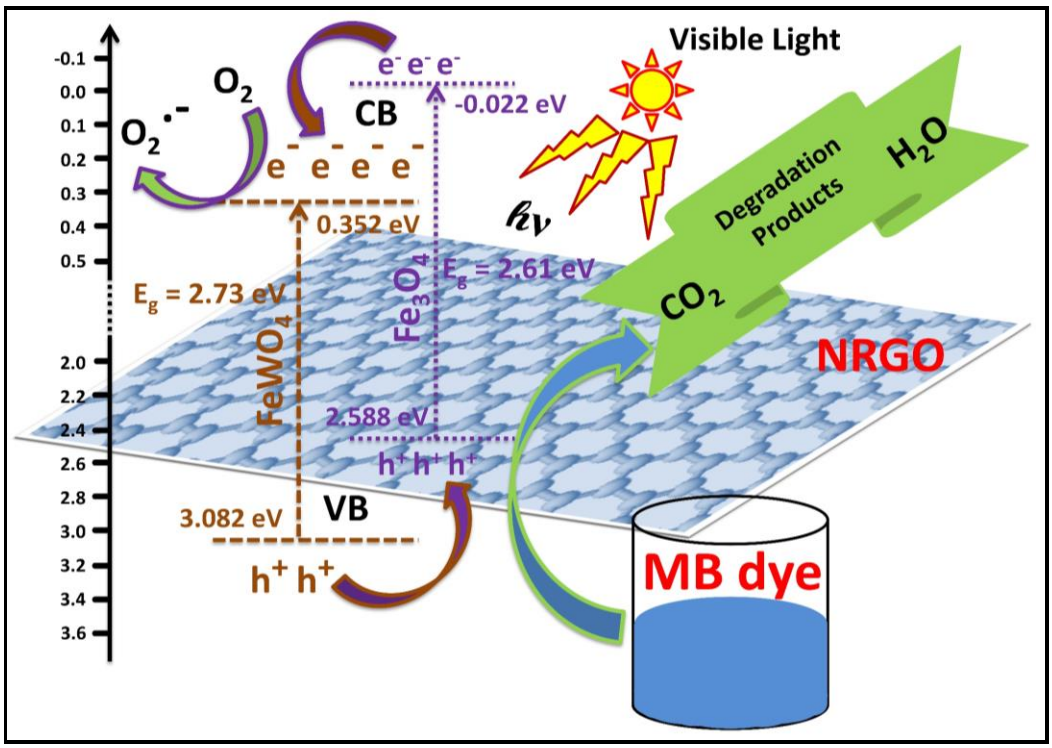


**Figure 5.12** Schematic diagram of the possible photocatalytic mechanism for degradation of MB over NRGO/$FeWO_4$/$Fe_3O_4$ nanocomposites under visible light irradiation.

### 5.3.8 Hydrogenation Studies

The catalytic activity of NRGO/$FeWO_4$/$Fe_3O_4$ nanocomposites was also estimated in the reduction reaction of 4-NP using $NaBH_4$ in an aqueous solution, the results of which are compared with NRGO, $FeWO_4$, $Fe_3O_4$, NRGO/$FeWO_4$, NRGO/$Fe_3O_4$, $FeWO_4$/$Fe_3O_4$ and mechanically mixed NRGO/$FeWO_4$/$Fe_3O_4$. The control experiment carried out in the absence of catalyst did not lead to the reduction of 4-NP. But in the presence of NRGO/$FeWO_4$/$Fe_3O_4$ nanocomposite, the intensity of absorption peak at 400 nm which is due to the presence of 4-NP, reduced immediately. A new peak at 300 nm was observed and it increased in its intensity with time (Figure 5.13a). The peak at 300 nm resulted due to presence of 4-AP which reached its saturation within 45 seconds indicating the complete reduction of 4-NP to 4-AP. The changes in the color of solution from yellow to colorless indicated the completion of the reaction. The component materials showed lower catalytic activity than the ternary composite (Figure 5.13b). The reaction rate constant was also determined in this case

similar to the case of photodegradation reaction of MB (Figure 5.13c) and it revealed a rate constant value of 0.04338 $s^{-1}$ which is much higher than that for the individual components (Figure 5.13d).

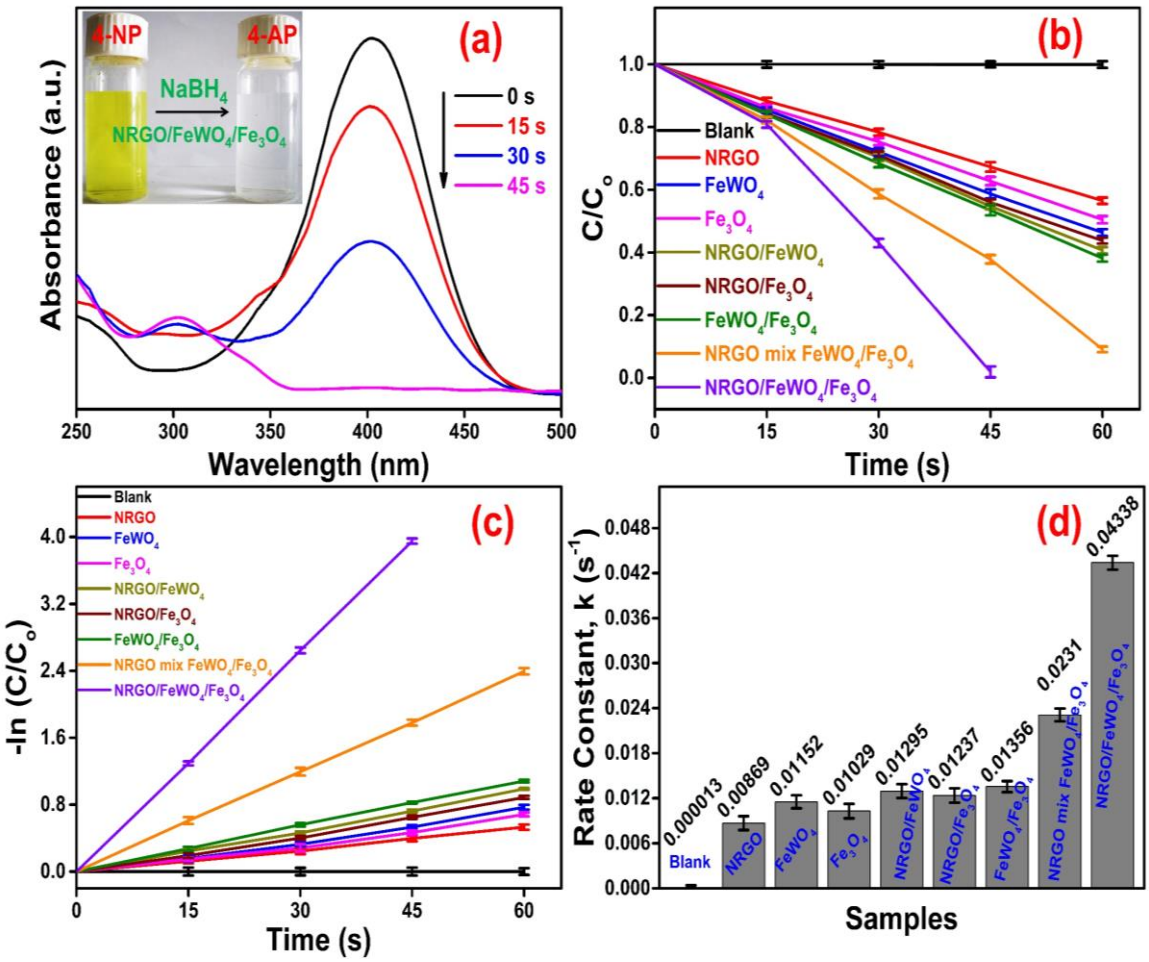


**Figure 5.13** (a) UV-Vis absorption spectra for the reduction of 4-NP to 4-AP by $NaBH_4$ in the presence of $NRGO/FeWO_4/Fe_3O_4$ nanocomposite (inset shows the visible color change during the process), (b) Catalytic reduction of 4-NP to 4-AP over various catalysts using $NaBH_4$, (c) First order kinetic plots of $-\ln(C/C_o)$ against the reduction time of 4-NP to 4-AP, (d) Rate constant values of 4-NP obtained using various catalytic materials.

The catalyst was recovered from the reaction, washed with 10 % ethanol, dried in vacuum for 6 hours at 60 °C and then tested for its stability and reusability. Even after 20 successive cycles it exhibited 100 % conversion within 100 seconds (Figure 5.14). Therefore, $NRGO/FeWO_4/Fe_3O_4$ nanocomposite can be regarded as a stable high

performance visible light photocatalyst for photodegradation of organic pollutants and reduction of 4-NP to 4-AP, possessing great prospects in environmental protection.

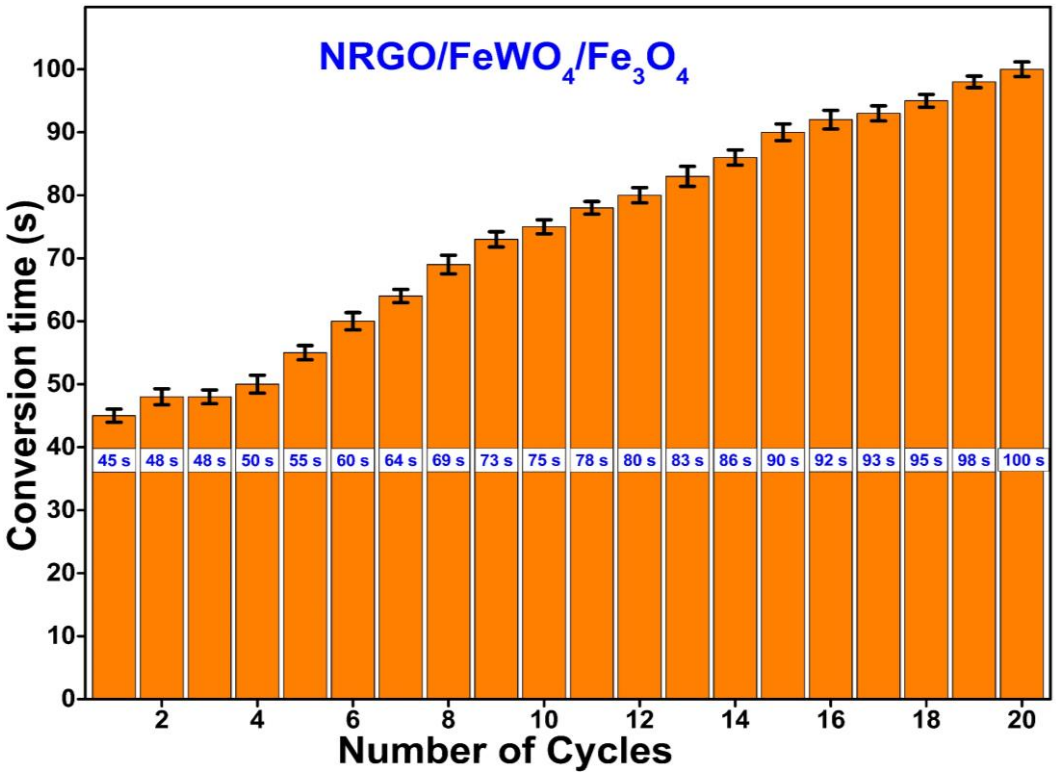


**Figure 5.14** Stability of NRGO/$FeWO_4$/$Fe_3O_4$ nanocomposites during 20 successive cycles of reduction reaction.

It is known that reduction of 4-NP to 4-AP does not take place in the absence of catalyst due to the repulsion between the groups of 4-NP and $BH_4^-$, which introduces a kinetic barrier. When the ternary catalyst is added, it efficiently transfers the electron donated by the $BH_4^-$ to the nitro group of 4-NP. The rate of reduction depends on the adsorption of 4-NP on the surface of the catalyst and the transfer of the electron from $BH_4^-$ to the nitro group of 4-NP through the NRGO/$FeWO_4$/$Fe_3O_4$ nanocomposite. NRGO can improve the transfer of electron due to N-doping species like pyridine-N, graphitic-N and pyrrole-N which can also offer electrons for conjugation with the π-conjugated rings. This can facilitate effective electron transfer in the active sites for catalytic reactions (Liu et al. 2016). Thus, $FeWO_4$/$Fe_3O_4$ hybrid semiconductor supported by NRGO shows enhanced catalytic efficiency in conversion of 4-NP to 4-AP.

### 5.3.9 Electrocatalytic Activity

The electrocatalytic performance of the NRGO/$FeWO_4$/$Fe_3O_4$ nanocomposite was investigated in 0.1 M KOH solution using a standard three-electrode system. For the sake of comparison, component materials and 20 wt.% Pt/C were also tested under the same conditions. The polarization curves for the HER on various electrodes are shown in Figure 5.15a. NRGO/$FeWO_4$/$Fe_3O_4$ nanocomposites demonstrated a remarkably high activity with an onset potential of ~59 mV vs RHE and a HER current density of 10 mA $cm^{-2}$ at an overpotential of 292 mV. On the other hand, $FeWO_4$/$Fe_3O_4$ had an onset potential of ~187 mV and current density of 10 mA $cm^{-2}$ at an overpotential of 421 mV, respectively.

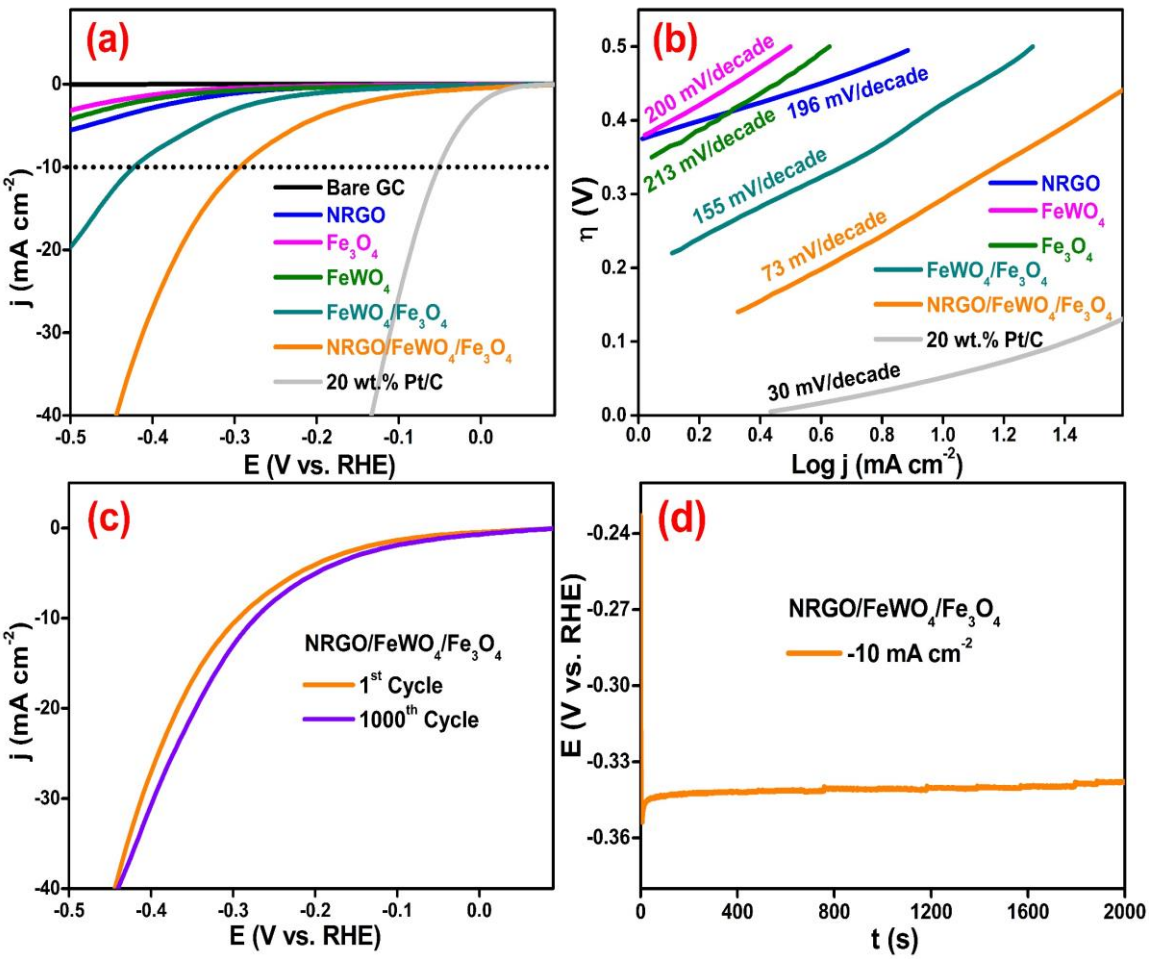


**Figure 5.15** (a) LSV curves and (b) Tafel curves for different catalysts. (c) Stability curve of NRGO/$FeWO_4$/$Fe_3O_4$ and (d) Chronopotentiometric curves at -10 mA $cm^{-2}$ recorded using NRGO/$FeWO_4$/$Fe_3O_4$.

The linear regions of the Tafel plots (Figure 5.15b) were fitted to the Tafel equation ($\eta = a + b \log (j)$, where j is the current density and b is the Tafel slope (Tilak and Chen 1993) yielding 73 mV $dec^{-1}$, 155 mV $dec^{-1}$, 196 mV $dec^{-1}$, 200 mV $dec^{-1}$ and 213 mV $dec^{-1}$ for NRGO/$FeWO_4$/$Fe_3O_4$, $FeWO_4$/$Fe_3O_4$, NRGO, $FeWO_4$, and $Fe_3O_4$, respectively. This indicates that the NRGO/$FeWO_4$/$Fe_3O_4$ nanocomposite electrode has much higher activity than the component materials electrode. Although its activity is still lower than the 20 wt.% Pt/C electrode, it may be considered significant because of the fact that it is a Pt-free catalyst. Thus, the experimentally observed Tafel slope of 73 mV $dec^{-1}$ indicated that the Heyrovsky mechanism is operating in the HER process for NRGO/$FeWO_4$/$Fe_3O_4$ nanocomposites (Bhardwaj and Balasubramaniam 2008). The measured values for important electrocatalytic parameters of the nanocomposites are given in Table 5.3.

**Table 5.3** Comparison of the HER parameters of the NRGO/$FeWO_4$/$Fe_3O_4$ with its component materials.

| **Catalysts** | **Onset potential (mV)** | **Overpotential (mV)** | **Tafel slope (mV $dec^{-1}$)** |
|---|---|---|---|
| | **at -10 mA $cm^{-2}$ (vs. RHE)** | | |
| NRGO | -- | -- | 196 |
| $FeWO_4$ | -- | -- | 200 |
| $Fe_3O_4$ | -- | -- | 213 |
| $FeWO_4$/$Fe_3O_4$ | - 187 | 421 | 155 |
| NRGO/$FeWO_4$/$Fe_3O_4$ | - 59 | 292 | 73 |

Stability test for the NRGO/$FeWO_4$/$Fe_3O_4$ catalysts was also carried out via CV measurements of 1000 cycles in 0.1 M KOH. As can be observed from Figure 5.15c, the current loss even after 1000 cycles is negligible. Thus, the test confirms that the NRGO/$FeWO_4$/$Fe_3O_4$ catalyst has good electrochemical stability for HER in 0.1 M KOH solution.

Further, the commercial application of the electrocatalyst was studied by chronopotentiometry technique at a constant current density of -10 mA $cm^{-2}$ applied for a duration of 2000 seconds (Figure 5.15d). The observed result shows that the initially high potential decreases slowly and then reaches a stabilized state of HER. This phenomenon is attributed to the development of $H_2$ bubbles on the electrode surfaces. Overall, the results demonstrate that the NRGO/$FeWO_4$/$Fe_3O_4$ nanocomposite is indeed a highly efficient electrocatalyst for HER in alkaline medium.

## 5.4 CONCLUSIONS

In conclusion, this study presents a facile synthesis of NRGO/$FeWO_4$/$Fe_3O_4$ ternary nanocomposite by a one-step microwave method and studies on its multifunctional catalytic properties. The synthesized materials are characterized by various techniques. The material has excellent catalytic efficiency towards the photodegradation of MB dye and reduction of 4-NP. The nanocomposite catalyst has high stability and reusability even after 10 and 20 cycles in the case of photodegradation and reduction reactions, respectively. The mechanism of catalytic action is also proposed. Further, NRGO/$FeWO_4$/$Fe_3O_4$ nanocomposites exhibited outstanding HER activity and stability requiring as low as 292 mV overpotential to deliver a current density of -10 mA $cm^{-2}$. The Tafel slope is 73 mV $dec^{-1}$ indicating that the mechanism follows Volmer-Heyrovsky pathway. Therefore, NRGO/$FeWO_4$/$Fe_3O_4$ nanocomposites showed higher catalytic activities for photodegradation, reduction and HER than $FeWO_4$/$Fe_3O_4$ or NRGO alone, suggesting a synergic role of NRGO and $FeWO_4$/$Fe_3O_4$ in the catalytic process.

# CHAPTER - 6

# SYNTHESIS, CHARACTERIZATION AND MULTIFUNCTIONAL CATALYTIC PERFORMANCE OF NOVEL NRGO/$BaWO_4$/g-$C_3N_4$ NANOCOMPOSITE

***Chapter 6*** *gives a descriptive report on the synthesis, characterization and multifunctional catalytic performance of novel NRGO/$BaWO_4$/g-$C_3N_4$ nanocomposite.*

## 6.1 INTRODUCTION

The abundance of existing major sources of energy such as coal, natural gas and other fossil fuels is limited and they are non-renewable too. With increase in the population, the global energy demand has increased and society is not able to cope with the demand. The quest for renewable clean energy sources has turned our attention towards hydrogen (Acar et al. 2016). Hydrogen can be produced by water splitting through electrocatalysis. But most of the materials currently used for electrocatalytic water splitting are noble and expensive. Development of low cost and environmental friendly electrocatalyst is the need of the day now to commercialize hydrogen production (Roger et al. 2017). Semiconductor photocatalysis has attracted interest of research community as it can solve both environmental and energy problems (Li et al. 2017). A good photocatalyst should have an extended excitation wavelength, low recombination rate of charge carriers and active sites on the surface to facilitate adsorption and reaction. Several strategies have been developed to achieve the above said properties like doping, coupling with semiconductors and compositing with layered materials to improve the surface area (Li et al. 2017). Despite these efforts commercialization of these materials is yet to be realized. Hence designing of materials with multifaceted catalytical activity such as, high performance towards electrolysis, photodegradation and reduction which would help in solving the energy and environmental problems must be looked into. Such multifunctional catalysts will provide an economic way to serve several applications.

Graphene based architectures not only provide support to other materials but also have a potential to harness the electrical and redox properties (Chang and Wu 2013, Sudhakar et al. 2014, Subramanya and Bhat 2014, 2015). The electronic property and the chemical reactivity of graphene can be tailored by doping nitrogen (Li et al. 2009, Zhang et al. 2016). In N doped graphene ~0.5 electron per N atom is provided to carbon $\pi$ conjugated system thus enhancing the photocatalytic efficiency. When composited

with semiconductors, NRGO increases the rate of transfer of electrons from the conduction band of semiconductors in comparison with graphene.

g-$C_3N_4$, a metal-free polymeric semiconductor, with higher nitrogen content and porous structure has attracted significant attentions in the field of photocatalysis due to its good thermal-chemical stability, electronic and optical characteristics, low cost and non-toxicity. The g-$C_3N_4$ possesses a band gap of 2.7 eV with the CB position at -1.1 eV and VB position at +1.6 eV. As the CB potential of g-$C_3N_4$ is sufficiently negative, the strong reducing capability of the electrons in the CB of g-$C_3N_4$ surface can have great potential for photocatalytic studies. Combining g-$C_3N_4$ with other appropriate semiconductors to form semiconductor heterostructure is considered as an effective method to enhance photocatalytic activity (Pawar et al. 2015).

Semiconducting materials which possess narrow band gap have been used as photocatalysts, as their band gap energy lies in the energy range of the UV or visible light (Hisatomi et al. 2014). Tungsten oxides, hydrates and metal tungstates have been studied for their photocatalytic capabilities (Montini et al. 2010). In particular, $ZnWO_4$, $CoWO_4$, $FeWO_4$, $NiWO_4$ have been extensively used for preparation of composites for water splitting (Zheng et al. 2015). On the other hand, $BaWO_4$ which has a wide variety of applications has been studied meagerly in the field of photocatalysis due to its instability and slow electron transfer rate. To extend the absorption of $BaWO_4$ from UV region to visible region of solar spectrum the band gap has to be decreased. Since smaller band gap leads to higher recombination rate, the transport property is tuned by doping carbon based material to improve the photocatalytic efficiency (Wang et al. 2015).

Based on the above facts, the synthesis of NRGO/$BaWO_4$/g-$C_3N_4$ nanocomposites via a facile, simple one-pot microwave method is reported here. The as synthesized material is thoroughly characterized using various advanced techniques. The reported material is highly efficient in catalyzing HER, photodegradation of MB dye and reduction of 4-NP to 4-AP.

## 6.2 EXPERIMENTAL

### 6.2.1 Synthesis of g-$C_3N_4$

g-$C_3N_4$ was prepared according to the previously reported technique (Yan et al. 2009). Typically, 2 g of melamine was put into a semi-closed alumina crucible which was calcined at 550 °C with a heating rate of 10 °C/min for 4 hours in the air atmosphere in a muffle furnace. The obtained light-yellow g-$C_3N_4$ product was collected and ground into powder form, then thoroughly washed with deionized water and dried at 60 °C overnight for further use.

### 6.2.2 Synthesis of $BaWO_4$

The $BaWO_4$ nanoparticles were prepared by simple microwave route. In a typical synthesis, solutions of barium chloride, ammonium tungstate and CTAB in $H_2O$/ethanol were prepared with desired molar ratio and mixed together using ultrasonication for about 30 minutes. The resulting mixture was treated with microwave irradiation at 350 W for 10 minutes and then allowed to cool to room temperature. The obtained precipitate of $BaWO_4$ was filtered and washed thoroughly with 10 % ethanol several times to remove the impurities. Finally, the precipitate was dried at 60 °C overnight.

### 6.2.3 Synthesis of NRGO/$BaWO_4$/g-$C_3N_4$ Nanocomposites

The NRGO/$BaWO_4$/g-$C_3N_4$ nanocomposites were prepared using a simple microwave route. GO was synthesized as given in section 4.2.1. In a typical synthesis, a calculated amount of g-$C_3N_4$ and GO was dispersed in the water. Then solutions of barium chloride, ammonium tungstate, CTAB and urea in $H_2O$/ethanol with desired molar ratios were added. The pH of the reaction mixture was maintained at 9 using ammonia. After 30 minutes of ultrasonication, the resulting mixture was treated with microwave irradiation at 350 W for 10 minutes and then allowed to cool to room temperature. The obtained precipitate of NRGO/$BaWO_4$/g-$C_3N_4$ nanocomposite was filtered and washed thoroughly with 10 % ethanol several times and finally dried at 60 °C overnight.

Similarly, g-$C_3N_4$/$BaWO_4$ and NRGO/$BaWO_4$ nanocomposites were prepared using appropriate starting materials. NRGO/$BaWO_4$ nanocomposites with NRGO content varying from 0.5 % to 5 % were prepared and their catalytic efficiency for photodegradation of MB dye was tested. The nanocomposite with 2.5 % NRGO showed highest activity and hence 2.5 % NRGO was taken as the optimized composition for NRGO/$BaWO_4$ nanocomposites. Similarly, in the case of NRGO/$BaWO_4$/g-$C_3N_4$ ternary nanocomposites, keeping NRGO content fixed at 2.5 %, g-$C_3N_4$ content was varied from 5% to 20 %. The nanocomposite with 10 % g-$C_3N_4$ showed maximum catalytic activity and hence it was taken as the optimized composition of g-$C_3N_4$ in the ternary nanocomposite (Figure 6.1). Schematic representation of the synthesis of NRGO/$BaWO_4$/g-$C_3N_4$ nanocomposites is shown in Figure 6.2.

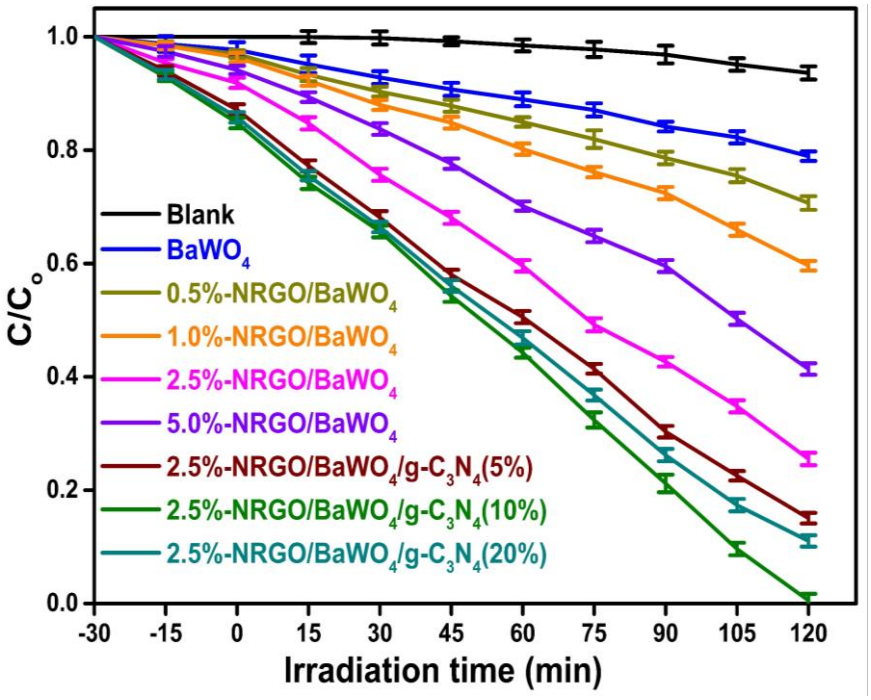


**Figure 6.1** Catalytic activities of various compositions of NRGO/$BaWO_4$/g-$C_3N_4$ nanocomposite.

### 6.2.4 Characterization and Catalytic Studies

The characterization of the synthesized samples was carried out as given in section 2.2.9 and section 3.2.3. The catalytic studies were performed as described in section 2.2.10 - 2.2.12.

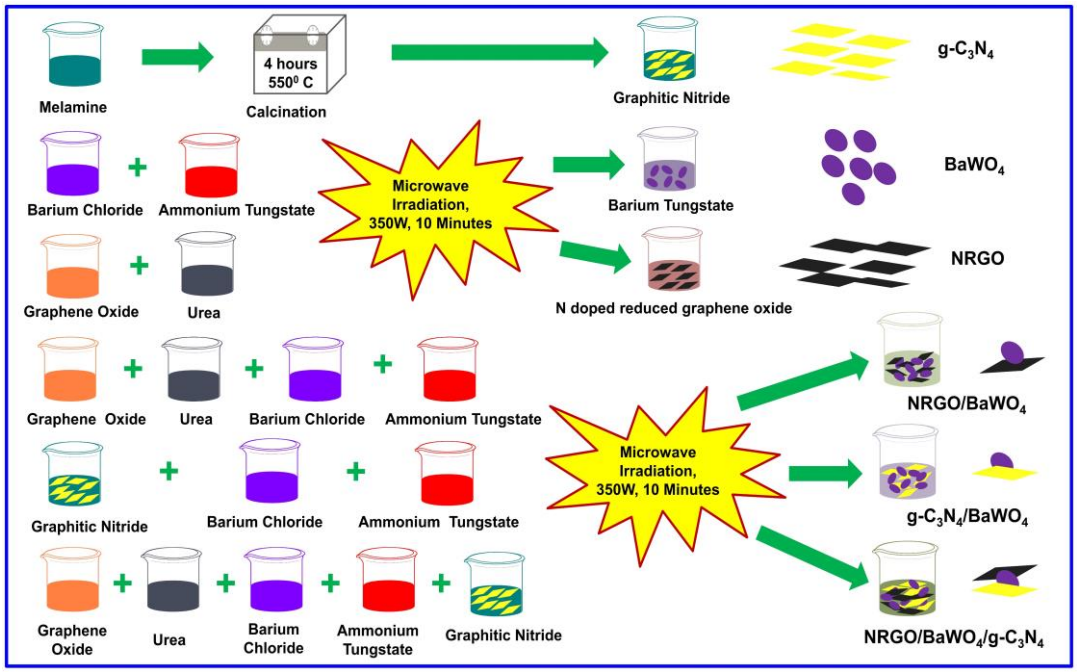


**Figure 6.2** Schematic representation of the synthesis of NRGO/$BaWO_4$/g-$C_3N_4$ ternary nanocomposite and its constituents.

## 6.3 RESULTS AND DISCUSSION

### 6.3.1 X-ray Diffraction Studies

The XRD patterns of NRGO, g-$C_3N_4$, $BaWO_4$, NRGO/$BaWO_4$ and NRGO/$BaWO_4$/g-$C_3N_4$ nanocomposites are shown in Figure 6.3. The diffraction peak at $2\theta = 24.4°$ corresponds to the (002) reflection plane of reduced phase of NRGO. The peaks at $2\theta = 12.8°$ and 27.5° seen in pure g-$C_3N_4$, can be indexed to the (100) and (002) diffraction planes conforming to the JCPDS No. 87-1526 of the graphitic carbon nitride. The diffraction pattern of $BaWO_4$ matches well with JCPDS No. 43-0646 suggesting that the material has the scheelite-type tetragonal crystal structure with space group of I41/a symmetry (Cavalcante et al. 2008). The peaks found at $2\theta$ values 17.3°, 26.5°, 28.1°, 31.9°, 43.0°, 45.7°, 48.7°, 53.6°, 54.5°, 66.6°, 67.7°, 69.4°, 73.0°, 73.8°, 75.8° and 76.8° can be ascribed to the (101), (112), (004), (200), (204), (220), (116), (312), (224), (400), (208), (411), (332), (404), (420) and (228) planes of $BaWO_4$. NRGO/$BaWO_4$ and NRGO/$BaWO_4$/g-$C_3N_4$ nanocomposite have similar diffraction peaks corresponding to $BaWO_4$. These results specify that the introduction of NRGO and NRGO/g-$C_3N_4$ do not disturb the orientation and structure of scheelite $BaWO_4$.

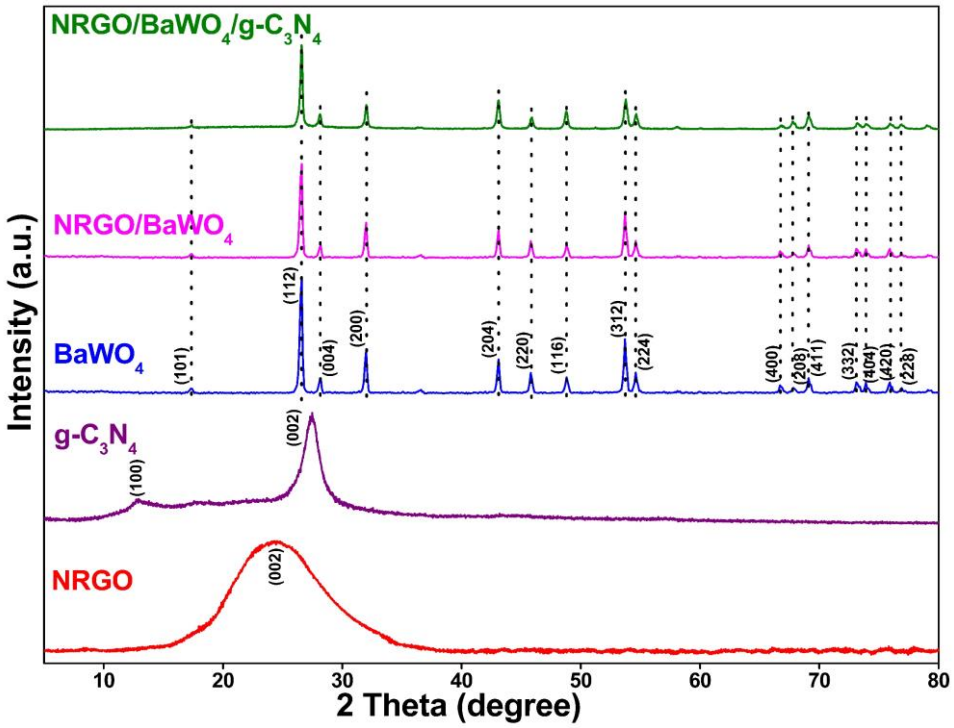


**Figure 6.3** XRD patterns of the NRGO, g-$C_3N_4$, $BaWO_4$, NRGO/$BaWO_4$ and NRGO/$BaWO_4$/g-$C_3N_4$ nanocomposite.

### 6.3.2 Raman Studies

The as-synthesized nanocomposites are further characterized by using Raman spectroscopy. As shown in Figure 6.4, five peaks are observed at 334 $cm^{-1}$, 478 $cm^{-1}$, 794 $cm^{-1}$, 830 $cm^{-1}$ and 927 $cm^{-1}$ in the pure $BaWO_4$ sample. The bands positioned around 334 $cm^{-1}$ is indexed to the stretching vibration of the $BaO_6$ octahedra. The bands located at 478 $cm^{-1}$, 794 $cm^{-1}$, 830 $cm^{-1}$ are assigned to the W-O stretching vibration of the $WO_4$ tetrahedra. The band at 927 $cm^{-1}$ is associated with the $WO_6$ symmetric stretching vibration of the crystalline $BaWO_4$ (Zawawi et al. 2013). The Raman spectrum of the pure NRGO reveals two prominent peaks D band and G band at 1356 $cm^{-1}$ and 1598 $cm^{-1}$, respectively (Li et al. 2009, Zhang et al. 2016). The Raman spectrum of the NRGO/$BaWO_4$/g-$C_3N_4$ nanocomposites contains all the bands corresponding to $BaWO_4$ and NRGO. The ratios of $I_D/I_G$ in pure NRGO and NRGO/$BaWO_4$/g-$C_3N_4$ nanocomposites are 1.09 and 1.13, respectively. The higher value for ternary composite may be due to the interaction of NRGO, g-$C_3N_4$, and $BaWO_4$ leading to more defects and disorders in the NRGO/$BaWO_4$/g-$C_3N_4$

nanocomposite. The typical bands of g-$C_3N_4$ appear at 421 $cm^{-1}$, 605 $cm^{-1}$, 897 $cm^{-1}$, 1087 $cm^{-1}$, 1219 $cm^{-1}$ and 1339 $cm^{-1}$ (Pawar et al. 2015). However, these bands of g-$C_3N_4$ are difficult to identify in the Raman spectrum of the NRGO/$BaWO_4$/g-$C_3N_4$ nanocomposite. This may be due to the weak scattering ability of g-$C_3N_4$ on the surface of the nanocomposite (Pawar et al. 2015).

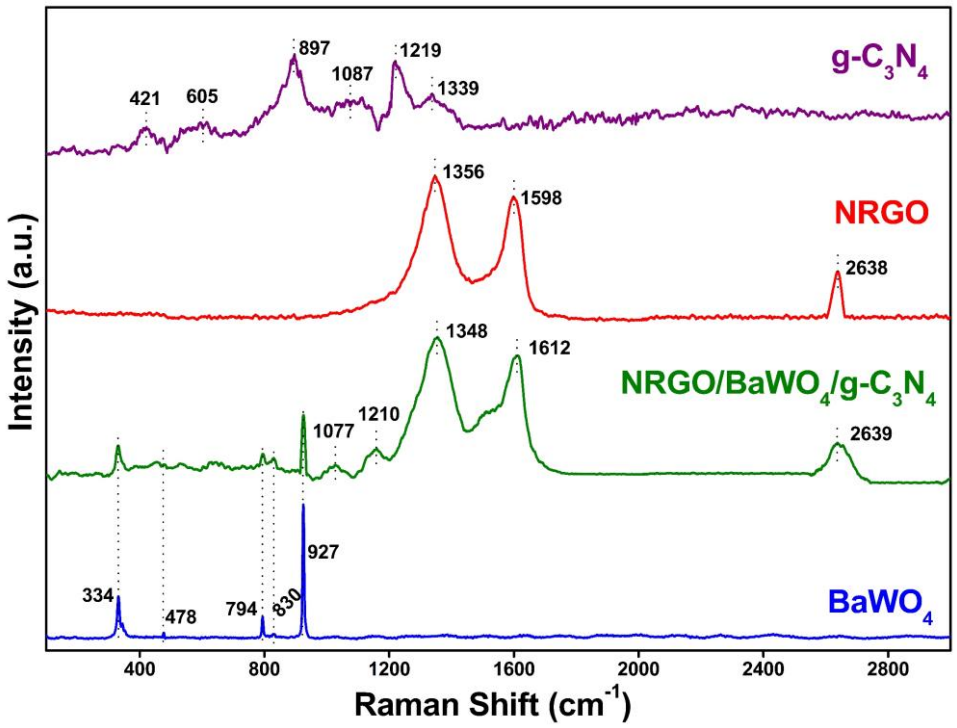


**Figure 6.4** Raman spectra of the NRGO, g-$C_3N_4$, $BaWO_4$ and NRGO/$BaWO_4$/g-$C_3N_4$ nanocomposite.

### 6.3.3 FTIR Studies

The presence of $BaWO_4$, NRGO, and g-$C_3N_4$ in the as-synthesized nanocomposite can be identified using FT-IR spectra. As shown in Figure 6.5, the main peak at 819 $cm^{-1}$ assigned to the stretching vibration of Ba-O, W-O, and W-O-W, is seen in the spectrum of the pure $BaWO_4$ and NRGO/$BaWO_4$/g-$C_3N_4$ nanocomposites (Clark and Doyle 1966). As shown in the inset of Figure 6.5, the peaks at 3406 $cm^{-1}$, 2969 $cm^{-1}$, 2884 $cm^{-1}$, 1633 $cm^{-1}$, 1465 $cm^{-1}$ and 1248 $cm^{-1}$ in the FT-IR spectra of NRGO and NRGO/$BaWO_4$/g-$C_3N_4$ nanocomposites can be ascribed to the asymmetric and symmetric vibrations of O-H and C-H, respectively (Appavu et al. 2016). The spectrum of g-$C_3N_4$ shows peaks at 1248 $cm^{-1}$, 1326 $cm^{-1}$, 1415 $cm^{-1}$, 1465 $cm^{-1}$, 1575

$cm^{-1}$ and 1633 $cm^{-1}$ which are characteristic stretching modes of C-N heterocycles. The peaks at 808 $cm^{-1}$ and 3184 $cm^{-1}$ are attributed to the typical breathing mode of triazine units and the stretching mode of N-H in g-$C_3N_4$, respectively (Xu et al. 2014). The FT-IR spectrum of NRGO/$BaWO_4$/g-$C_3N_4$ nanocomposites reveals similar peaks as that of g-$C_3N_4$. All the peaks corresponding to the $BaWO_4$, NRGO, and g-$C_3N_4$ are present in the spectrum of NRGO/$BaWO_4$/g-$C_3N_4$ nanocomposites.

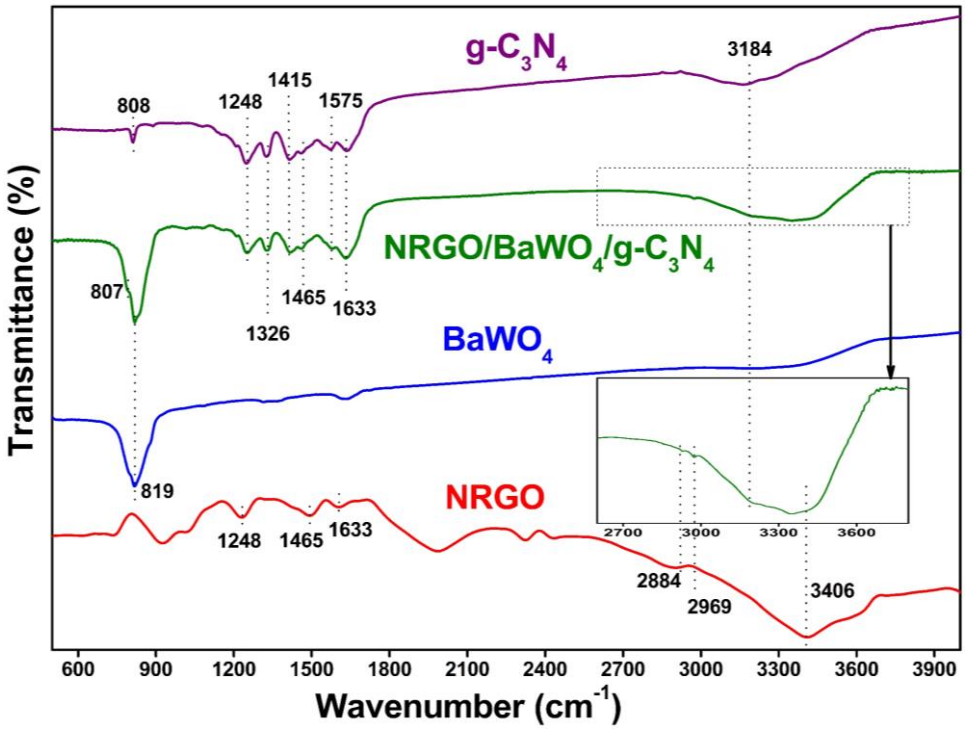


**Figure 6.5** FTIR spectra of the NRGO, g-$C_3N_4$, $BaWO_4$ and NRGO/$BaWO_4$/g-$C_3N_4$ nanocomposite.

### 6.3.4 Surface Morphology Studies

The specific surface area of the as-synthesized nanocomposites was measured by BET analysis. The specific surface areas of $BaWO_4$ and NRGO/$BaWO_4$/g-$C_3N_4$ nanocomposites are 3.51 and 25.02 $m^2g^{-1}$, respectively. It is very clear that the specific surface area increases due to the introduction of the NRGO and g-$C_3N_4$ on the $BaWO_4$ substrate. This increase in surface area facilitates the surface adsorption and creates more number of active sites resulting in enhanced catalytic activities (Subramanya and Bhat 2014).

The HRTEM image (Figure 6.6a) reveals that $BaWO_4$ particles are successfully deposited on the surface of the g-$C_3N_4$ and NRGO nanosheets. The spacing of the lattice fringes in the $BaWO_4$ is about 0.51 nm which corresponds to the (101) plane of scheelite-type tetragonal crystal phase (JCPDS No. 43-0646). In addition, the lattice spacing of about 0.34 nm corresponds to the (002) plane of the graphitic carbon nitride (JCPDS No. 87-1526) and lattice spacing of 0.36 nm corresponds to the (002) planes of the NRGO nanosheets. The SAED pattern of the nanocomposite (inset of Figure 6.6a) shows ring pattern indicating the polycrystalline nature of the sample. The particle size distribution of the $BaWO_4$ (Figure 6.6b) shows that the average particle sizes is around 12 nm.

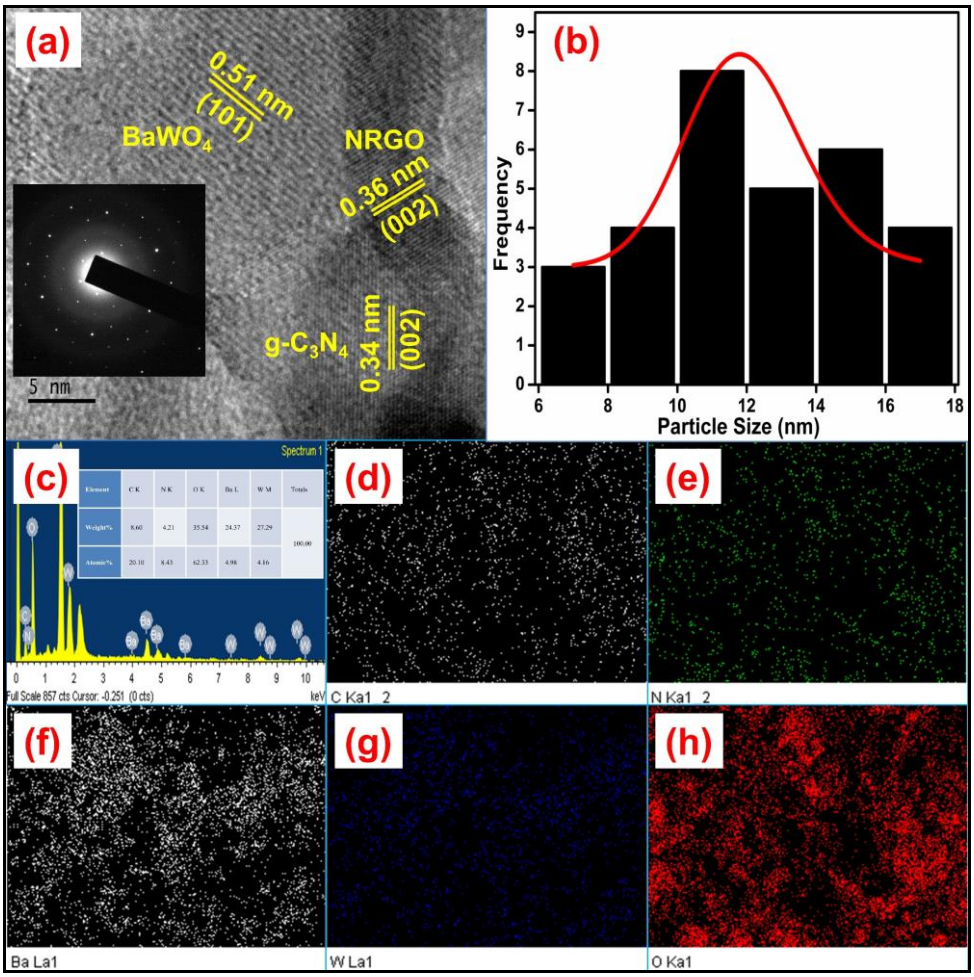


**Figure 6.6** (a) HRTEM (inset showing SAED pattern), (b) particle size distribution, (c) EDX spectrum and Elemental mapping (d) C, (e) N, (f) Ba, (g) W and (h) O of the NRGO/$BaWO_4$/g-$C_3N_4$ nanocomposite.

The EDX analysis (Figure 6.6c) of NRGO/$BaWO_4$/g-$C_3N_4$ nanocomposite further confirms the formation of the ternary composite. In addition to that, the distribution of elements in NRGO/$BaWO_4$/g-$C_3N_4$ nanocomposites was determined by elemental mapping analysis (Figure 6.6d-h). The analysis infers the uniform distribution of the particles in the composite.

### 6.3.5 XPS Studies

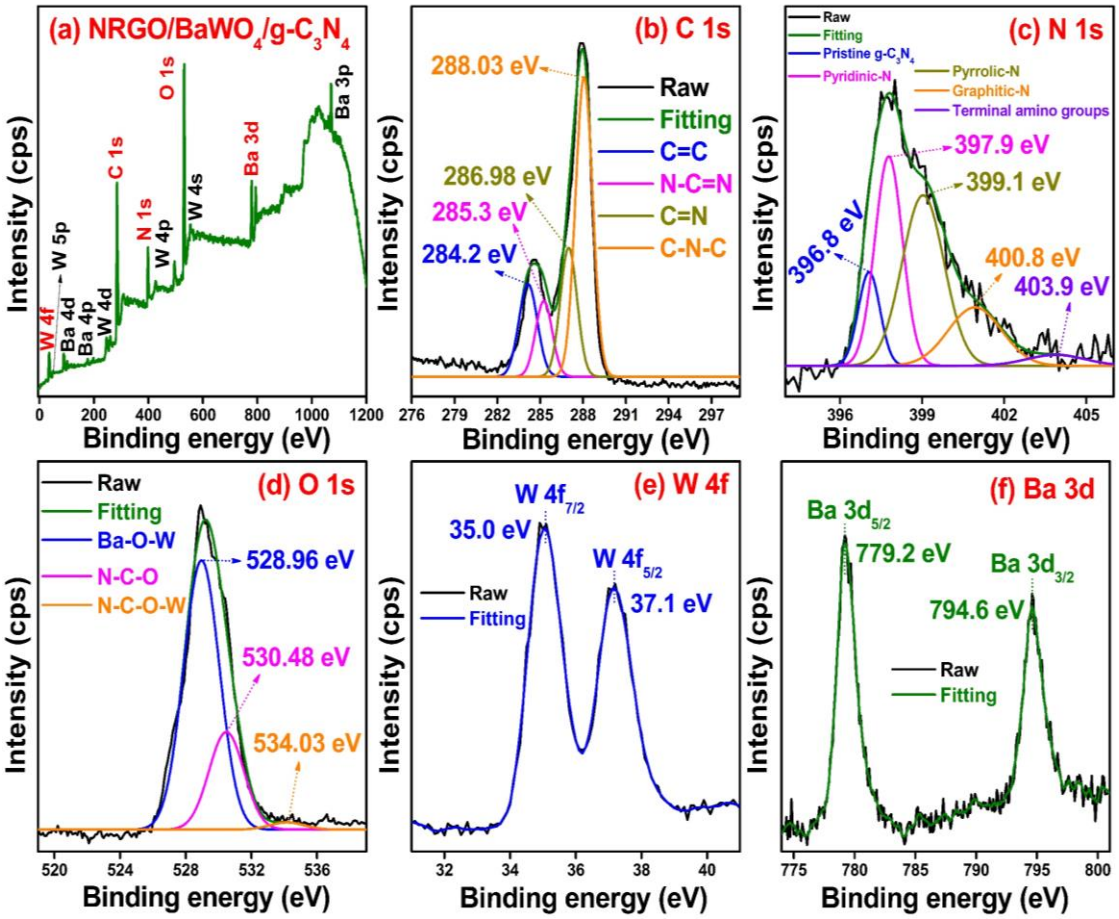


**Figure 6.7** XPS spectrum (a) survey, high-resolution spectra (b) C1s, (c) N 1s, (d) O 1s, (e) W 4f and (f) Ba 3d of NRGO/$BaWO_4$/g-$C_3N_4$ nanocomposite.

XPS is used to investigate the elemental composition as well as the chemical environment on the surface of the as-prepared nanocomposites. XPS survey spectrum of NRGO/$BaWO_4$/g-$C_3N_4$ nanocomposite is shown in Figure 6.7a. The elemental peaks of C, N, O, Ba and W are found in the NRGO/$BaWO_4$/g-$C_3N_4$ nanocomposites, which confirm the presence of NRGO, g-$C_3N_4$, and $BaWO_4$ in the nanocomposite. High

resolution C 1s spectra (Figure 6.7b) can be deconvoluted into four peaks. Peaks at 284.2 eV and 285.3 eV can be allocated to carbon (C=C) and typical $sp^2$ carbon atoms bonded to N atoms in an aromatic ring (N-C=N), peak at 286.98 eV can be ascribed to C=N originated from NRGO and the formation of C-O-C bond between NRGO and g-$C_3N_4$ during microwave treatment. The peak at 288.03 eV can be ascribed to the interaction of C-N-C between g-$C_3N_4$ and NRGO. As shown in Figure 6.7c, five deconvoluted peaks in the high-resolution N 1s spectrum of NRGO/$BaWO_4$/g-$C_3N_4$ nanocomposites are assigned to pristine g-$C_3N_4$ (396.8 eV), pyridinic N (397.9 eV), pyrrolic N (399.1 eV), graphitic N (400.8 eV) and terminal amino groups (403.9 eV), which is in agreement with the reported data (Pawar et al. 2015). The O 1s peaks in Figure 6.7d at 528.96 eV, 530.48 eV and 534.03 eV corresponds to Ba-O-W, N-C-O and N-C-O-W of the NRGO/$BaWO_4$/g-$C_3N_4$ nanocomposites, revealing the chemical interaction between the NRGO, g-$C_3N_4$, and $BaWO_4$ in the nanocomposites. As shown in Figure 6.7e, the doublet peaks at 37.1 eV and 35.0 eV belong to W $4f_{5/2}$ and W $4f_{7/2}$, which are the features of $W^{6+}$ in pure $BaWO_4$. The peaks at 794.6 eV and 779.2 eV correspond to Ba $3d_{3/2}$ and Ba $3d_{5/2}$ (Figure 6.7f), which can be assigned to $Ba^{2+}$ of pure $BaWO_4$.

### 6.3.6 Optical Studies

The optical properties of NRGO, g-$C_3N_4$, $BaWO_4$, NRGO/$BaWO_4$ and NRGO/$BaWO_4$/g-$C_3N_4$ nanocomposite are determined via the UV-Visible DRS technique (Figure 6.8a). As shown in Figure 6.8a, the NRGO absorbs in the whole visible region. The NRGO/$BaWO_4$ and NRGO/$BaWO_4$/g-$C_3N_4$ nanocomposites show higher absorption as well as wider wavelength window of absorption in the visible-light region compared with the pure g-$C_3N_4$ and $BaWO_4$. Thus, the observation suggests that the NRGO/$BaWO_4$/g-$C_3N_4$ nanocomposite can efficiently utilize visible-light and generate more electron–hole pairs under visible-light irradiation.

For a given semiconductor, its band gap energy ($E_g$) can be measured from the intercept of the tangents in the Tauc plot of $(ah\upsilon)^{2/n}$ vs photon energy ($h\upsilon$) (equation, (2.3)) as shown in Figure 6.8b. The band gaps of pure g-$C_3N_4$, $BaWO_4$, NRGO/$BaWO_4$, and NRGO/$BaWO_4$/g-$C_3N_4$ nanocomposite are 2.69 eV, 4.43 eV, 3.04 eV and 2.41 eV,

respectively (Figure 6.8b). The band gaps of NRGO/$BaWO_4$/g-$C_3N_4$ nanocomposite are reduced compared to its components. The reduction in the band gap may be attributed to the delocalization of surface charges resulted by the interactions of the components in the composite. It is believed that interactions lead to the formation of new molecular orbitals of lower energy which in turn facilitates the reduction in the bandgap. Such observations for semiconductor composites are reported in the literature (Wang et al. 2012, Jo and Selvam 2015). Such reduction in the band gap of the materials is beneficial for enhancing both visible-light absorption and photocatalytic activity.

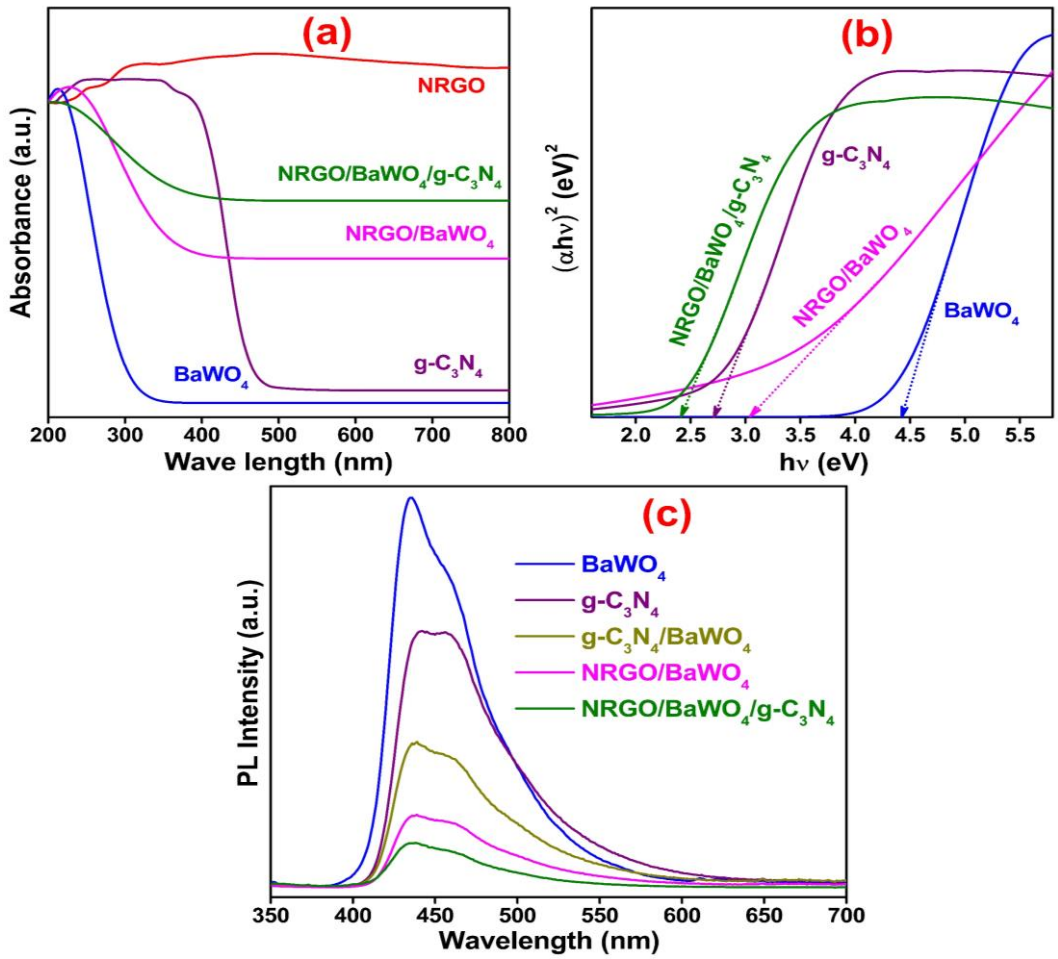


**Figure 6.8** (a) DRS spectrum, (b) Band gap plots and (c) PL spectrum of the NRGO/$BaWO_4$/g-$C_3N_4$ nanocomposites.

### 6.3.7 PL Studies

PL analysis represents the recombination performance of photogenerated charge carriers in a semiconductor. Higher rate of recombination results in higher

intensity of the PL spectrum. The enhanced photocatalytic efficiency of NRGO/$BaWO_4$/g-$C_3N_4$ nanocomposite is attributed to the effective separation of photogenerated charge carriers (Wang et al. 2015). The nature of charge carrier recombination in $BaWO_4$, NRGO/$BaWO_4$, g-$C_3N_4$/$BaWO_4$ and NRGO/$BaWO_4$/g-$C_3N_4$ nanocomposite was investigated by PL analysis (Figure 6.8c). $BaWO_4$ exhibits strong emission peak around 445 nm, which is due to the recombination of the photogenerated electron-hole pairs. After NRGO or g-$C_3N_4$ was introduced, the heterostructure samples show lower PL emission intensity compared with that of pure $BaWO_4$, suggesting lower recombination of the photogenerated electron-hole pairs. The PL peak of NRGO/$BaWO_4$/g-$C_3N_4$ nanocomposite shows the lowest intensity, which reveals higher separation between the photogenerated electron-hole pairs in the NRGO/$BaWO_4$/g-$C_3N_4$ nanocomposite surface.

### 6.3.8 Photocatalytic Studies

The nanocomposite and its components were tested for their photocatalytic activities in degradation of MB dye. In the absence of the catalyst the degradation was negligible. As shown in Figure 6.9a, the efficiencies of pure NRGO, $BaWO_4$, g-$C_3N_4$, g-$C_3N_4$/$BaWO_4$, NRGO/$BaWO_4$, NRGO/g-$C_3N_4$ and NRGO/$BaWO_4$/g-$C_3N_4$ nanocomposite are 13.10 %, 21.06 %, 46.99 %, 65.47 %, 74.49 %, 79.63 % and 99.44 % under 120 minutes visible-light irradiation, respectively. Clearly, the photocatalytic degradation efficiency of these samples decreases in the following order: NRGO/$BaWO_4$/g-$C_3N_4$ > NRGO/g-$C_3N_4$ > NRGO/$BaWO_4$ > g-$C_3N_4$/$BaWO_4$ > g-$C_3N_4$ > $BaWO_4$ > NRGO. These results demonstrate that the NRGO/$BaWO_4$/g-$C_3N_4$ nanocomposite shows higher photocatalytic activity for MB degradation than the pure NRGO, g-$C_3N_4$, $BaWO_4$, g-$C_3N_4$/$BaWO_4$, NRGO/$BaWO_4$ and NRGO/g-$C_3N_4$.

It is observed that the kinetics of photocatalytic degradation of MB follows Langmuir-Hinshelwood first-order kinetics model, which can be described by the equation (2.4). The rate constants can be obtained from the slope of the plot of -ln($C/C_o$) vs. irradiation time (Figure 6.9b).

The rate constant of NRGO/$BaWO_4$/g-$C_3N_4$ (0.01767 $min^{-1}$) is about 11.70, 9.11, 4.09, 2.67, 2.04 and 1.63 times greater than those of the pure NRGO (0.00151

$min^{-1}$), $BaWO_4$ (0.00194 $min^{-1}$), g-$C_3N_4$ (0.00432 $min^{-1}$), g-$C_3N_4$/$BaWO_4$ (0.00663 $min^{-1}$), NRGO/$BaWO_4$ (0.00865 $min^{-1}$) and NRGO/g-$C_3N_4$ (0.01087 $min^{-1}$), respectively (Figure 6.9c). The enhanced performance of the ternary nanocomposite may be attributed to the factors such as narrow band gap, higher extent of energy absorption in the visible light region and efficient separation of charge carriers, contributing significantly towards improved photodegradation of MB in comparison to that of component materials.

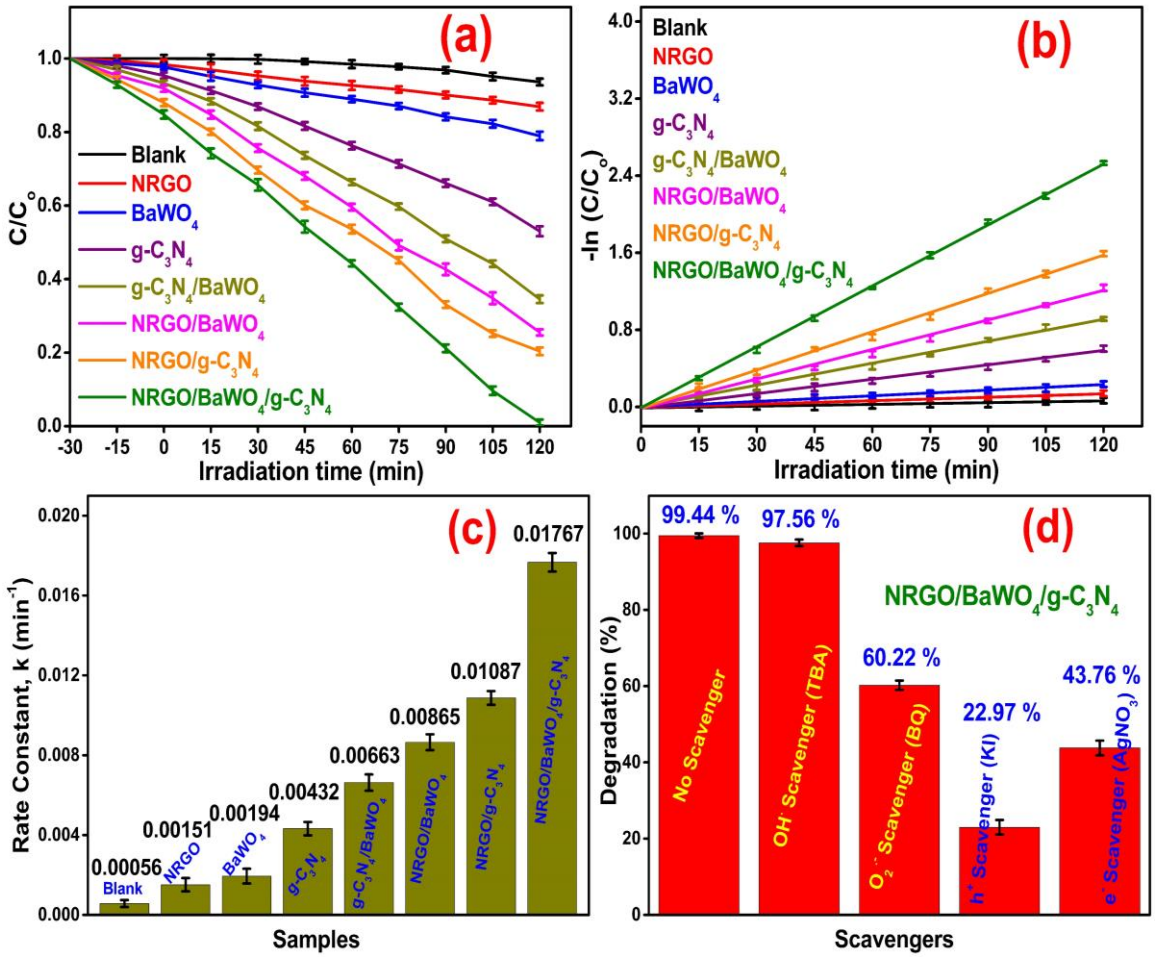


**Figure 6.9** (a) Degradation plots of MB over various catalysts, (b) First order kinetics plots of MB over various catalysts, (c) Rate constant of MB over various catalysts, (d) Plot depicting effects of different scavengers on degradation efficiency of NRGO/$BaWO_4$/g-$C_3N_4$ nanocomposite under visible light irradiation.

The durability and stability of the photocatalysts are significantly important for their practical applications. The catalytic stability was determined by recycling the

nanocomposite. The degradation extent changed from 99.44 % to 97.44 % from 1st to 5th cycle, respectively (Figure 6.10). These results indicate that the NRGO/$BaWO_4$/g-$C_3N_4$ nanocomposite is relatively stable during the photocatalytic process.

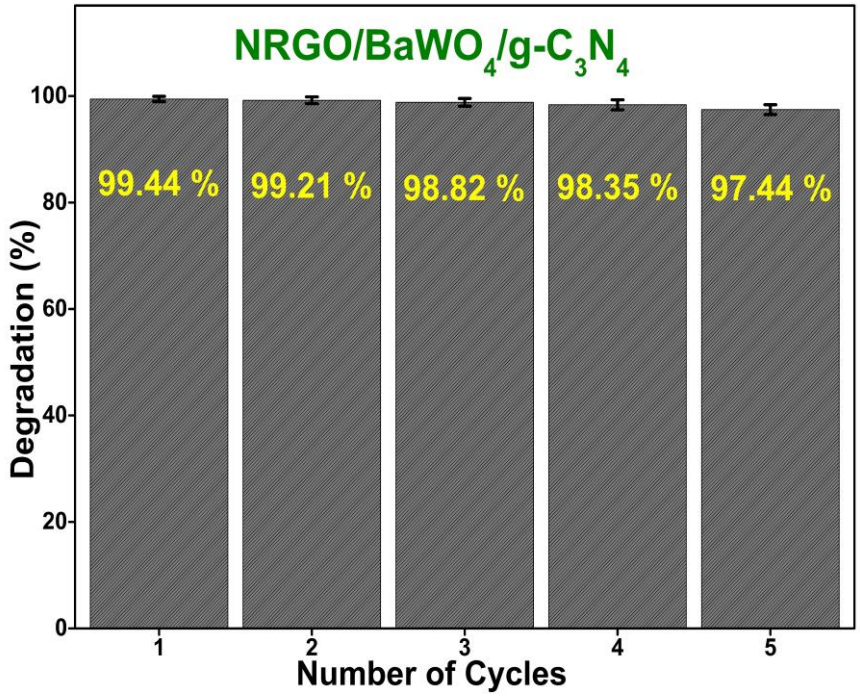


**Figure 6.10** Photocatalytic stability of NRGO/$BaWO_4$/g-$C_3N_4$ nanocomposites.

In order to understand the photocatalysis mechanism of the NRGO/$BaWO_4$/g-$C_3N_4$ nanocomposite, the active species generated during the photocatalytic degradation process are identified through radical and hole trapping experiments. 10 mM TBA, 10 mM KI, 1 mM BQ and 10 mM $AgNO_3$ acted as the scavengers for $^{\bullet}OH$, $h^+$, $^{\bullet}O_2^-$ and $e^-$, respectively.

Figure 6.9d displays the influence of different quenchers on the visible light photocatalytic activity of NRGO/$BaWO_4$/g-$C_3N_4$ nanocomposite for the degradation of MB. With the addition of TBA, the photodegradation efficiency of MB did not change much indicating that the $^{\bullet}OH$ is the not the active species generated in the NRGO/$BaWO_4$/g-$C_3N_4$ photocatalytic reaction system. The degradation efficiency of MB changed slightly with the addition of BQ and $AgNO_3$, implying that $^{\bullet}O_2^-$ and $e^-$ was formed in the photocatalytic reaction system of NRGO/$BaWO_4$/g-$C_3N_4$ under visible light irradiation. However, after addition of KI, the photodegradation efficiency of MB

decreased significantly as a result of quenching of $h^+$ in a reaction system, which indicated that $h^+$ is the main active species generated in the NRGO/$BaWO_4$/g-$C_3N_4$ photocatalytic degradation of MB. The proposed reactions are shown in equations (6.1-6.4),

$$g\text{-}C_3N_4 + h\upsilon \rightarrow g\text{-}C_3N_4\ (e^- + h^+) \quad \text{----------} \quad (6.1)$$

$$g\text{-}C_3N_4\ (e^-) + BaWO_4 \rightarrow g\text{-}C_3N_4 + BaWO_4\ (e^-) \quad \text{----------} \quad (6.2)$$

$$BaWO_4\ (e^-) + O_2 \rightarrow BaWO_4 + {}^{\bullet}O_2^- \quad \text{----------} \quad (6.3)$$

$$g\text{-}C_3N_4(h^+) + Dye \rightarrow CO_2 + H_2O + \text{Other species} \quad \text{----------} \quad (6.4)$$

where $e^-$ is the electron in the conduction band edge and $h^+$ is the hole in the valence band edge, respectively.

The visible light photocatalytic efficiency of the NRGO/$BaWO_4$/g-$C_3N_4$ nanocomposite can be elucidated by the band edge positions of the respective semiconductor materials. Therefore, the VB and CB energy levels of $BaWO_4$ and g-$C_3N_4$ were measured using the Mulliken electronegativity formula (equations 2.5 and 2.6). The $\chi$ values of $BaWO_4$ and g-$C_3N_4$ are 5.6954 eV and 4.73 eV, respectively. The calculated VB potentials of $BaWO_4$ and g-$C_3N_4$ were 3.4104 eV and 1.575 eV. The CB potentials were -1.0196 eV and -1.115 eV, respectively for $BaWO_4$ and g-$C_3N_4$.

Based on the above discussions and analysis, a possible charge transfer mechanism for the NRGO/$BaWO_4$/g-$C_3N_4$ nanocomposite is proposed, as shown in Figure 6.11. When the system is under visible irradiation, the VB electrons of g-$C_3N_4$ semiconductors are excited to the CB, leaving holes in the VB, thereby forming photoinduced electron-hole pairs. Because the CB potential of $BaWO_4$ is slightly lower than that of the CB of g-$C_3N_4$, the CB electrons of g-$C_3N_4$ would easily jump to the CB of $BaWO_4$ and from there to the highly conducting NRGO sheets, resulting in effective charge separation and transport. These electrons would then react with the oxygen to form superoxide radical anion. The holes will immediately get transported with the support of conductive NRGO matrix to react with MB to form products such as $CO_2$, $H_2O$ and other species. Thus, the entire process leads to efficient separation of the

photogenerated electron-hole pairs, which in turn results in the enhancement of the photocatalytic activity of NRGO/$BaWO_4$/g-$C_3N_4$ nanocomposite for the degradation of MB.

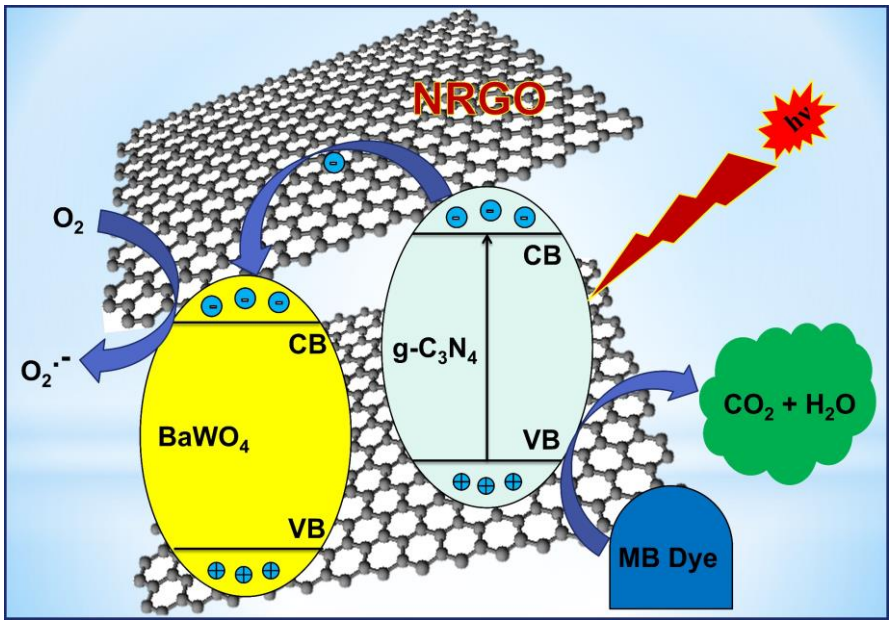


**Figure 6.11** Proposed mechanism for the photocatalytic degradation of dye by NRGO/$BaWO_4$/g-$C_3N_4$ nanocomposite under visible light irradiation.

In order to understand the nature of products formed during photocatalytic degradation of MB, the TOC of the reaction medium during the photo catalysis process was determined (Cui et al. 2013). Using the TOC values, percentage mineralization of the dye was calculated employing the equation (2.2) given earlier. For comparison, the decrease in concentration of MB in terms of % decolorization was determined during catalytic photodegradation. The concentrations of solutions were calculated from absorbance at 664 nm. Figure 6.12a shows absorbance versus wavelength plot at different intervals of time and Figure 6.12b shows variation of % mineralization and % decolorization with time in the form of a bar diagram. As can be observed from the plot, the absorbance at 664 nm decreased with time and reached 0.56 % during scan at 120 minutes under visible light irradiation. The TOC value decreased to 14.36 % or mineralization extent increased to 85.74 % under visible light irradiation for 120 minutes of visible light irradiation. Thus, the results suggest that, the organic carbon is

mostly converted to $CO_2$ during the process. In view of this, it can be concluded that the nanocomposite is an eco-friendly photocatalyst.

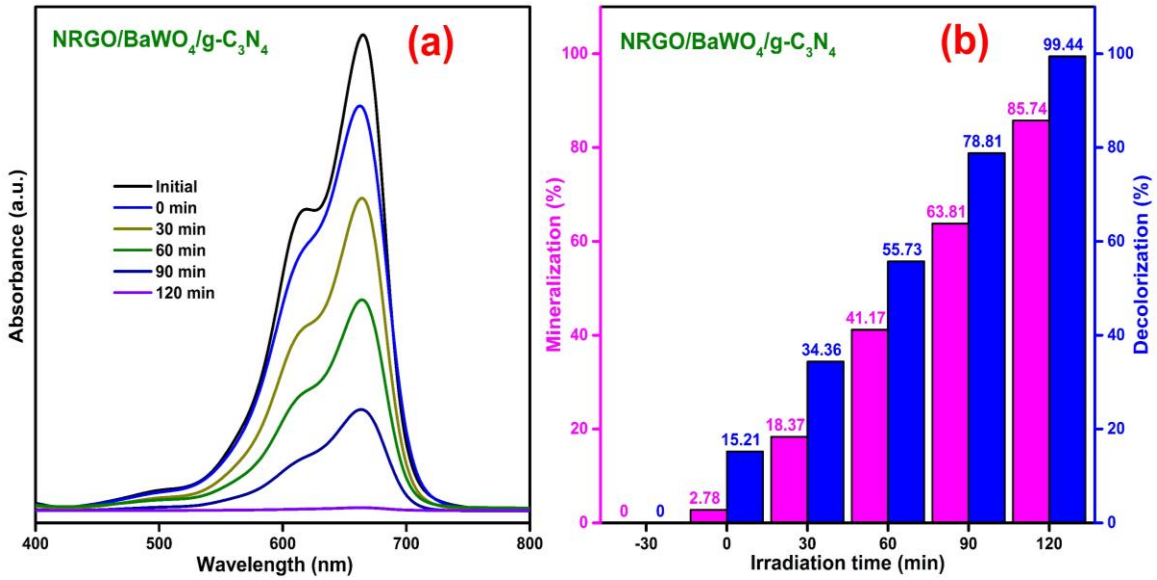


**Figure 6.12** (a) Absorbance versus wavelength and (b) Mineralization/Decolorization test bar diagram for photodegradation of MB catalyzed by NRGO/$BaWO_4$/g-$C_3N_4$ nanocomposite at different intervals of time.

### 6.3.9 Hydrogenation Studies

The catalytic activity of NRGO/$BaWO_4$/g-$C_3N_4$ nanocomposites was evaluated in the reduction of 4-NP using $NaBH_4$ in an aqueous solution. In the absence of the catalyst the reduction was negligible. However, when NRGO/$BaWO_4$/g-$C_3N_4$ nanocomposites were added into the 4-NP solution, the absorption of 4-NP found at 400 nm peak decreased immediately and the new absorption peak of 4-AP found at 300 nm was obtained, and it increased with time as shown in Figure 6.13a. The catalytic reduction of 4-NP into 4-AP was completed in 60 seconds. The complete change of 4-NP can be visually seen (inset in Figure 6.13a) as the solution color changes from bright yellow to colorless. The observed results indicated that the NRGO/$BaWO_4$/g-$C_3N_4$ nanocomposites are excellent catalyst in the reduction of 4-NP to 4-AP than that of pure NRGO, $BaWO_4$, g-$C_3N_4$, g-$C_3N_4$/$BaWO_4$ and NRGO/$BaWO_4$ materials (Figure 6.13b).

The reaction rate for the reduction process followed pseudo-first order kinetics with respect to 4-NP concentration similar to the one described for photodegradation

previously. The first order kinetic plots of -ln(C/C$_o$) vs. conversion time for all the catalyst materials are shown in Figure 6.13c. The reaction rate constant (k) is calculated from the slope of these plots and the same is given in the form of a bar diagram for comparison as shown in the Figure 6.13d. The above results clearly indicate that NRGO/BaWO$_4$/g-C$_3$N$_4$ nanocomposites exhibit a significantly enhanced catalytic activity for the reduction of 4-NP to 4-AP than that of component materials.

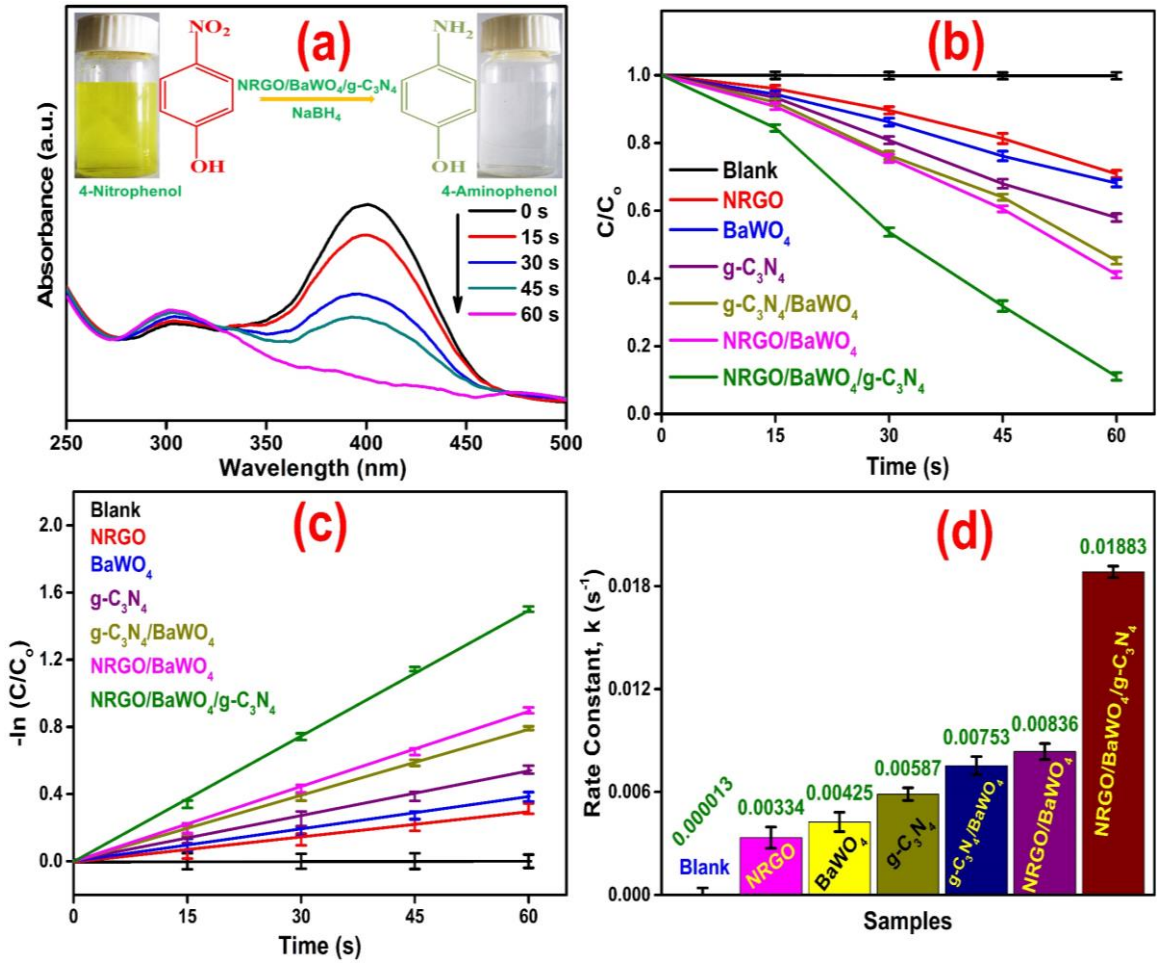


**Figure 6.13** (a) UV-Vis absorption spectra for the reduction of 4-NP to 4-AP by NaBH$_4$ in the presence of NRGO/BaWO$_4$/g-C$_3$N$_4$ nanocomposite. (b) Catalytic reduction of 4-NP to 4-AP over various catalysts using NaBH$_4$. (c) First order kinetic plots of -ln(C/C$_o$) against the reduction time of 4-NP to 4-AP and (d) Rate constant values of 4-NP over various catalytic materials.

The catalytic stability and reusability of the NRGO/BaWO$_4$/g-C$_3$N$_4$ nanocomposites were tested after recovery from the previous reaction mixture (Figure

6.14). The recycled catalyst exhibited excellent catalytic activity even after 10 successive cycles, with nearly 100 % conversion within a time period of 92 seconds.

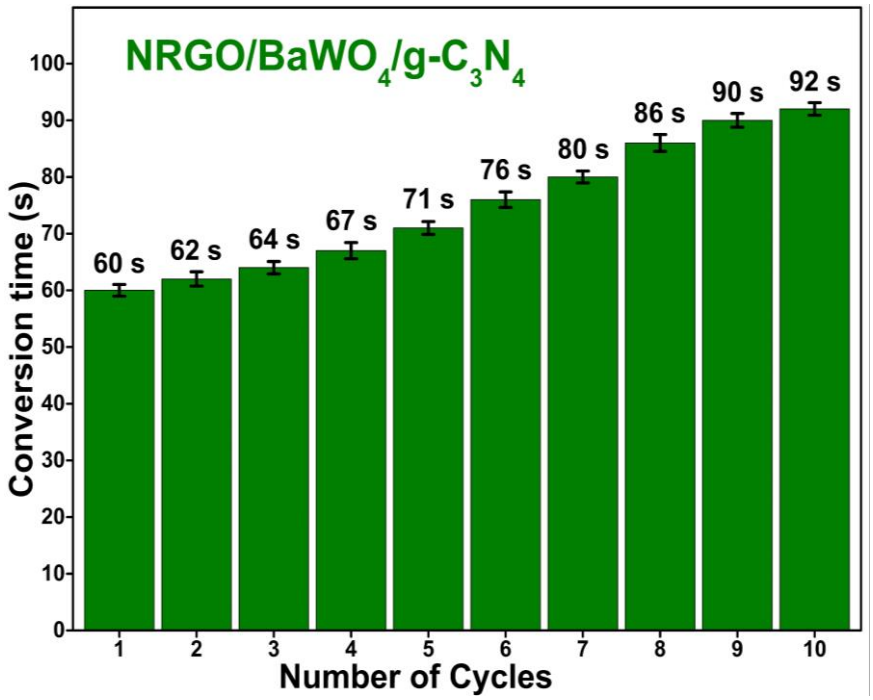


**Figure 6.14** Catalytic efficiency of NRGO/$BaWO_4$/g-$C_3N_4$ nanocomposite for successive 10 cycles.

### 6.3.10 Electrocatalytic Studies

The electrocatalytic performance of the NRGO/$BaWO_4$/g-$C_3N_4$ nanocomposite was investigated in 0.1 M KOH solution using a standard three-electrode system. For the sake of comparison, component materials and 20 wt.% Pt/C were also tested under the same conditions. The polarization curves for the HER on various electrodes are shown in Figure 6.15a. NRGO/$BaWO_4$/g-$C_3N_4$ nanocomposites demonstrated a remarkably high activity with an onset potential of ~83 mV vs RHE and a HER current density of 10 mA $cm^{-2}$ at an overpotential of 211 mV. On the other hand, NRGO/$BaWO_4$ and g-$C_3N_4$/$BaWO_4$ had an onset potential of ~186 mV and ~205 mV and current density of -10 mA $cm^{-2}$ at an overpotential of 320 mV and 347 mV, respectively.

The linear regions of the Tafel plots (Figure 6.15b) were fitted into the Tafel equation ($\eta = b\log(j) + a$, where b is the Tafel slope) (Subramanya et al. 2015) yielding

30 mV $dec^{-1}$, 62 mV $dec^{-1}$, 103 mV $dec^{-1}$, 112 mV $dec^{-1}$, 160 mV $dec^{-1}$, 196 mV $dec^{-1}$ and 227 mV $dec^{-1}$ for 20 wt.% Pt/C, NRGO/$BaWO_4$/g-$C_3N_4$, NRGO/$BaWO_4$, g-$C_3N_4$/$BaWO_4$, $BaWO_4$, NRGO and g-$C_3N_4$ electrode, respectively. This indicates that the NRGO/$BaWO_4$/g-$C_3N_4$ nanocomposites electrode has much higher activity than the component materials electrode. Although its activity is still lower than the 20 wt.% Pt/C electrode, it may be considered significant because of the fact that it is a Pt-free catalyst. Thus, the experimentally observed Tafel slope of 62 mV $dec^{-1}$ indicated that the Heyrovsky process is the rate determining step for NRGO/$BaWO_4$/g-$C_3N_4$ nanocomposites.

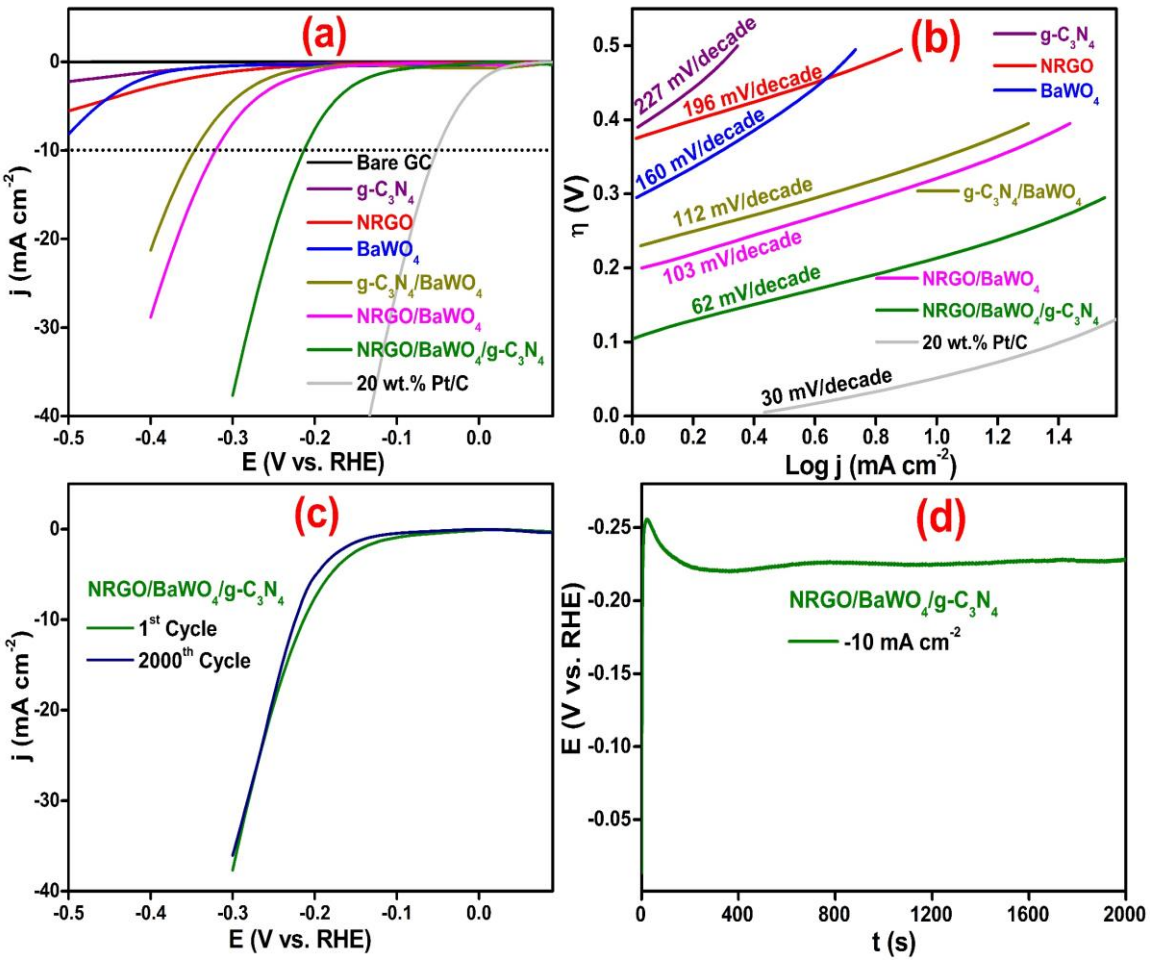


**Figure 6.15** (a) LSV and (b) Tafel slope curve for different electrode materials. (c) Stability curve and (d) Chronopotentiometry curves at -10 mA $cm^{-2}$ recorded using NRGO/$BaWO_4$/g-$C_3N_4$ nanocomposites.

Stability is one of the key factors in evaluating catalyst performance. In view of this, to assess the stability of NRGO/$BaWO_4$/g-$C_3N_4$ nanocomposites during HER, continuous cyclic voltammograms up to 2000 cycles and galvanostatic polarization curves at a current density of -10 mA $cm^{-2}$ were recorded. Figure 6.15c displays LSV curves recorded at a scan rate of 10 mV $s^{-1}$ for NRGO/$BaWO_4$/g-$C_3N_4$ nanocomposites before and after performing 2000 continuous cyclic voltammograms between 0.0 V and -0.5 V. Notably, no appreciable activity change was observed after 2000 cycles indicating excellent stability of the NRGO/$BaWO_4$/g-$C_3N_4$ nanocomposites during HER. This observation further suggests that the NRGO/$BaWO_4$/g-$C_3N_4$ nanocomposite structure and composition remain unchanged during the catalytic process. The potential required to deliver a current density of -10 mA $cm^{-2}$ is an important figure of merit for the viability of a HER catalyst because it corresponds to the current density required to attain 10 % efficiency in a solar-to-fuel conversion device (Subramanya et al. 2015). Galvanostatic measurements also demonstrated the outstanding stability of the NRGO/$BaWO_4$/g-$C_3N_4$ nanocomposites in basic media (Figure 6.15d), confirming that the ternary nanocomposite can be a very useful, efficient and promising candidate as catalyst for HER.

## 6.4 CONCLUSIONS

In this work, NRGO/$BaWO_4$/g-$C_3N_4$ nanocomposite is successfully synthesized by microwave irradiation method and characterized by different techniques such as XRD, SEM, HRTEM, BET, XPS, DRS, Raman, PL and UV-Vis spectroscopy. The synthesized composite exhibited enhanced catalytic efficiency towards HER, photodegradation of MB dye and reduction of 4-NP to 4-AP, suggesting that the material can be a very promising multifunctional catalyst.

# CHAPTER - 7

## SUMMARY AND CONCLUSIONS

***Chapter 7*** *outlines the summary of the work presented in the thesis along with the important conclusions drawn from the study. Scope for further research has also been included here.*

## 7.1 SUMMARY

The thesis reports the successful synthesis of five different kinds of novel graphene-metal tungstate based nanocomposites namely, NRGO/$ZnWO_4$/$Fe_3O_4$, NRGO/$NiWO_4$/ZnO, NRGO/$CoWO_4$/$Fe_2O_3$, NRGO/$FeWO_4$/$Fe_3O_4$, and NRGO/$BaWO_4$/g-$C_3N_4$ using facile microwave irradiation method. All the synthesized nanocomposites were carefully characterized for their structures, morphologies, elemental and optical properties by employing appropriate techniques such as XRD, SEM, FESEM, TEM, HRTEM, BET, XPS, DRS, Raman, FTIR, UV-Vis and PL spectroscopy. Thereafter, each nanocomposite has been investigated for its catalytic efficiency towards, (i) The photodegradation of MB dye under the visible light irradiation, (ii) The reduction of 4-NP to 4-AP in the presence of $NaBH_4$ in aqueous media and (iii) The electrolytic HER in alkaline media.

A brief summary of the overall work presented in the thesis is given here.

**Chapter 1** gives a brief introduction to the basic aspects of the study undertaken. It also gives a brief overview of the relevant works in the literature which focus upon graphene, metal tungstate, metal tungstate-based nanocomposites, graphene-based nanocomposites, their synthesis methods and catalytic applications. Scope and objectives of the present research work have been given at the end.

**Chapter 2** presents and discusses the synthesis of novel NRGO/$ZnWO_4$/$Fe_3O_4$ nanocomposite as an efficient catalytic material for energy and environmental applications.

The visible light photocatalytic activities of the as-prepared nanocomposites are evaluated using MB solution. It is observed that 3 wt.% NRGO/$ZnWO_4$/$Fe_3O_4$ (0.01 M) is the optimum concentration for efficient catalysis of MB decomposition. The decomposition process is completed in 120 minutes. It is shown that the synergistic effects of the components of the catalyst are responsible for the enhanced photocatalytic activity. The nanocomposites showed high activity and high stability,

even after 5 cycles of photocatalytic processes. Also, the resulting nanocomposite possess outstanding catalytic activity in the reduction of 4-NP to 4-AP in the presence of $NaBH_4$ which is completed in 30 seconds. The catalyst showed good stability, recyclability (10 cycles) and high catalytic performance due to its synergistic chemical adsorption and electron transfer effects. Additionally, the electrocatalytic activity of HER in 0.1M KOH solution is investigated. It showed a lesser onset potential and overpotential of -113 mV and -218.55 mV at a current density of -10 mA $cm^{-2}$. The observed Tafel slope of 75 mV $dec^{-1}$ suggests that the Volmer-Heyrovsky mechanism is operating in the HER process. Further, the nanocomposite exhibited good durability and high activity for HER even after 1000 cycles.

**Chapter 3** deals with the microwave synthesis of NRGO/$NiWO_4$/ZnO ternary nanocomposite as an efficient catalyst for photodegradation of MB, reduction of 4-NP and electrolytic HER.

The optimized concentration of efficient catalyst is found to be 2.5%-NRGO/$NiWO_4$/ZnO (0.01 M). The photodegradation efficiency of 2.5%-NRGO/$NiWO_4$/ZnO (0.01 M) is approximately 9 times higher than that of $NiWO_4$ and it showed high stability even after 5 cycles. The trapping experiments suggested that the photogenerated holes are the active species involved in the photocatalytic reactions. On the basis of the experimental results, the possible photodegradation mechanism is proposed. The composite also showed excellent catalytic activity in the reduction of 4-NP to 4-AP in the presence of $NaBH_4$. The reaction completed in 80 seconds. Additionally, it exhibited outstanding HER activity and stability requiring a low onset potential of 101 mV delivering a current density of -10 mA $cm^{-2}$ at a low overpotential of 257 mV. The Tafel slope of the HER is 93 mV $dec^{-1}$, indicating that the kinetics of the reaction follows Volmer-Heyrovsky mechanism.

**Chapter 4** provides details of synthesis, characterization and catalytic applications of novel NRGO/$CoWO_4$/$Fe_2O_3$ nanocomposite.

The photodegradation efficiency of NRGO/$CoWO_4$/$Fe_2O_3$ is approximately 99.05 % for 120 minutes and it showed high stability even after 5 cycles. Based on the experimental results, possible mechanism for photodegradation is also proposed. The composite also showed excellent catalytic activity in the reduction of 4-NP to 4-AP in

the presence of $NaBH_4$. The reaction completed in 30 seconds and it showed high stability even after 10 cycles. The nanocomposite has outstanding HER activity and stability requiring only a low onset potential of 133 mV at a current density of -10 mA $cm^{-2}$ and at a low overpotential of 331 mV. The Tafel slope is 95 mV $dec^{-1}$ indicating that the mechanism follows Volmer-Heyrovsky pathway. Further, the material also exhibits good durability and high activity for HER even after 2000 cycles. The catalytic efficiency of NRGO/$CoWO_4$/$Fe_2O_3$ is better in comparison to other composites.

**Chapter 5** describes the synthesis, characterization and studies on catalytic performance of NRGO/$FeWO_4$/$Fe_3O_4$ ternary nanocomposite in environmental and energy applications.

The material showed excellent catalytic efficiency towards the photodegradation of MB dye, reduction of 4-NP and electrolytic HER. The photodegradation efficiency is approximately 99.18 % for 100 minutes and reduction reaction is completed in 45 seconds. The nanocomposite catalyst has high stability and reusability even after 10 and 20 cycles in the case of photodegradation and reduction reactions, respectively. The mechanism of catalytic action is also proposed. The nanocomposite as a catalyst exhibited outstanding HER activity and stability requiring a low onset potential of 59 mV to deliver a current density of -10 mA $cm^{-2}$ at a low overpotential of 292 mV. The Tafel slope is 73 mV $dec^{-1}$ indicating that the process follows Volmer-Heyrovsky mechanism. The durability and activity for HER even after 1000 cycles is quite good.

**Chapter 6** gives a descriptive report on the synthesis, characterization and multifunctional catalytic performance of novel NRGO/$BaWO_4$/g-$C_3N_4$ nanocomposite.

The synthesized composite exhibited high catalytic efficiency towards HER, photodegradation of MB dye and catalytic reduction of 4-NP to 4-AP suggesting that the material can be a very promising multifunctional catalyst. The photodegradation efficiency of NRGO/$BaWO_4$/g-$C_3N_4$ is approximately 9.11 times higher than $BaWO_4$ and it showed high stability even after 5 cycles. On the basis of the experimental results, the possible photodegradation mechanism is proposed. The composite also

showed excellent catalytic activity in the reduction of 4-NP to 4-AP in the presence of $NaBH_4$. The reaction completed in 60 seconds and it showed high stability even after 10 cycles. The nanocomposite needed onset potential of 83 mV and a current density of -10 mA $cm^{-2}$ at a low overpotential of 211 mV, indicating its high efficiency for HER. The Tafel slope of the HER is 62 mV $dec^{-1}$, indicating that the kinetics of the reaction follows Volmer-Heyrovsky mechanism. Also, the material delivered good durability and high activity for HER even after 2000 cycles.

**Chapter 7** outlines the summary of the work presented in the thesis along with important conclusions drawn from the study. The results of experimental investigation presented in the thesis are compared with reported literatures. Scope for further research has also been included in this chapter.

References used have been listed at the end followed by the Bio-data.

## 7.2 CONCLUSIONS

The major conclusions drawn from the present research work are listed below:

- Graphene - transition metal tungstate based nanocomposites can be efficiently synthesized employing microwave irradiation approach.
- The synthesized nanocomposites can be used as effective catalysts for photodegradation of dyes, reduction of 4-NP to 4-AP and electrolytic HER.
- The synthesized nanocomposites exhibit high catalytic activity due to the synergistic effects of the components of the catalyst.
- The synthesized nanocomposite catalysts are highly stable and reusable.
- The observed results suggest that novel graphene-transition metal tungstate based ternary nanocomposites are potential candidates as multifunctional catalysts in the field of clean energy and environmental applications.

The summarized results of the present research work are given in Table 7.1.

Further, the results obtained pertaining to the catalysts discussed in this work have also been compared with those of other catalysts reported in the literature in Table 7.2, 7.3 and 7.4.

**Table 7.1** Summarized results from this work.

| **Catalysts** | **NRGO/$ZnWO_4$/$Fe_3O_4$** | **NRGO/$NiWO_4$/ZnO** | **NRGO/$CoWO_4$/$Fe_2O_3$** | **NRGO/$FeWO_4$/$Fe_3O_4$** | **NRGO/$BaWO_4$/g-$C_3N_4$** |
|---|---|---|---|---|---|
| **Photocatalytic activity towards MB under visible light irradiation<br>MB: 200 mL (20 mg/L), Catalyst: 20 mg, Visible light source: 250 W Mercury lamp (cutoff filter, 400 nm)** | | | | | |
| **Efficiency and time required** | 99.49 %,<br>120 min | 99.27 %,<br>120 min | 99.05 %,<br>120 min | 99.18 %,<br>100 min | 99.44 %,<br>120 min |
| **Active species** | $h^+$ | $h^+$ | $h^+$ | $h^+$ | $h^+$ |
| **Reusability** | 5 cycles (99.49 % to 97.51 %) | 5 cycles (99.27 % to 96.72 %) | 5 cycles (99.05 % to 96.58 %) | 5 cycles (99.18 % to 97.05 %) | 5 cycles (99.44 % to 97.44 %) |
| **Catalytic activity towards reduction of 4-NP to 4-AP using $NaBH_4$ in aqueous solutions<br>4-NP: 2.7 mL (0.1 mM), $NaBH_4$: 0.3 mL (0.1 M) and Catalyst: 0.1 mg** | | | | | |
| **Time required for complete reduction** | 30 s | 80 s | 30 s | 45 s | 60 s |
| **Reusability and time** | 10 cycles,<br>30 s to 48 s | 10 cycles,<br>80 s to 108 s | 10 cycles,<br>30 s to 60 s | 10 cycles,<br>45 s to 75 s | 10 cycles,<br>60 s to 92 s |
| **Electrocatalytic activity towards HER in alkaline medium<br>Catalyst: 0.142 mg/$cm^2$, Medium: 0.1 M KOH and Scan rate: 10 mV/s** | | | | | |
| **Onset** | 113 | 101 | 133 | 59 | 83 |
| **Over potential** | 218.55 | 257 | 331 | 292 | 211 |
| **Tafel slope** | 75 | 93 | 95 | 73 | 62 |
| **Stability** | 1000 cycles | 1000 cycles | 1000 cycles | 1000 cycles | 1000 cycles |

**Table 7.2** Comparison of the photocatalytic degradation process parameters of reported catalysts.

| Photocatalysts | Light Source | Concentration | Degradation extent and Time | Reference |
|---|---|---|---|---|
| g-$C_3N_4$-NS/$CuCr_2O_4$ (10%) | Visible light (50 W LED lamp) | Catalyst: 0.1 g, RhB: 250 mL (2.5 x $10^{-5}$ M) | 98.8 %, 210 min | Akhundi and Habibi 2017 |
| g-$C_3N_4$/$TiO_2$ | Visible-light (350 W Xe arc lamp, cutoff filter, 420 nm) | Catalyst: 0.04 g (20 mL), RhB: 30 mL (1 x $10^{-5}$ M) | 95.2 %, 90 min | Hao et al. 2017 |
| H-m$SiO_2$-BiOCl@PANI@Pd (HBPP) | Visible light irradiation (500 W Xe lamp) | Catalyst: 0.1 g, MO: 100 mL (50 mg/L) | Completely degraded in 230 min | Tian et al. 2017 |
| rGO-$TiO_2$-0.55CdS | Visible light (300 W Xe lamp, cutoff filter, 400 nm) | Catalyst: 5 mg, MB: 80 mL (5 mg/L) or 4-CP: 25 mL (1 mg/L) | MB: 90.3 % and 4-CP: 65.3 % in 60 min | Tian et al. 2017 |
| AgCl@Ag/N-rGO | Light source (150 W Xe arc lamp, cutoff filter, 400 nm) | Catalyst: 1.6 g/L, 2-CP: 60 mL (10 mg/L) | 97 %, 150 min | Wang et al. 2017 |
| (NGQDs)-BiOI/$MnNb_2O_6$ | Visible light (250 W Xe lamp, cutoff filter, 420 nm) | Catalyst: 50 mg, Antibiotics (tetracycline, oxytetracyline, ciprofloxacin and doxycycline): 100 mL, (10 mg/L) | Ciprofloxacin: 57.4 %, doxycycline: 64.7 %, oxytetracyline: 72.1 % in 120 min and tetracycline: 87.2 %, 60 min | Yan et al. 2017 |
| RGO/Ag/$TiO_2$-nanotubes/Ti plates | UV resource (125 W Mercury lamp) | MB: 100 mL (10 ppm) | 89 %, 120 min | Faraji and Mohaghegh 2016 |
| Cu-doped$TiO_2$/RGO | UV light source (UV-A light 300 W, λ=315-400 nm) | MB: 35 mL (10 ppm) | 63 %, 180 min | Thanh-Truc et al. 2015 |

| | | | | |
|---|---|---|---|---|
| Graphene-ZnO-CoPC | Exposure to natural sunlight (700–800 W/$m^2$) | Catalysts: 10 mg, RhB: 100 mL (10 mg/L) | Completely degraded in 140 min | Gururaj et al. 2014 |
| Graphene-$Bi_2MoO_6$ | Visible light (250 W halogen lamp, cutoff filter, 400 nm) | Brilliant red X-3B (25 mg/L), 0.1 g of photocatalyst (200 mL) | 90.4 %, 90 min | Wang et al. 2012 |
| NRGO/$ZnWO_4$/$Fe_3O_4$ | Visible light source (250 W Mercury lamp, cutoff filter, 400 nm) | Catalyst: 20 mg, MB: 200 mL (20 mg/L) | 99.49 %, 120 min | Present work |
| NRGO/$NiWO_4$/ZnO | | | 99.27 %, 120 min | Present work |
| NRGO/$CoWO_4$/$Fe_2O_3$ | | | 99.05 %, 120 min | Present work |
| NRGO/$FeWO_4$/$Fe_3O_4$ | | | 99.18 %, 100 min | Present work |
| NRGO/$BaWO_4$/g-$C_3N_4$ | | | 99.44 %, 120 min | Present work |

**Table 7.3** Comparison of 4-NP to 4-AP reduction parameters of reported catalysts.

| **Catalysts** | **Time (min or s)** | **Rate Constant ($min^{-1}$ or $s^{-1}$)** | **Reference** |
|---|---|---|---|
| Pd-GA/RGO | 5 min | 0.1199 $min^{-1}$ | Ezhil Vilian et al. 2017 |
| [Pt(ppy)Cl(3-ampy)]/GO | 840 s | 2.04 x $10^{-3}$ $s^{-1}$ | Fath et al. 2017 |
| 5 wt.% Ag-$Fe_2O_3$ xerogel | 90 s | 2.08 x $10^{-2}$ $s^{-1}$ | Feng et al. 2017 |
| NiFe/AC | 2.5 min | 1.936 $min^{-1}$ | Gao et al. 2017 |
| Ag NPs/PD/PANFP | 30 min | 0.1370 $min^{-1}$ | Lu et al. 2017 |
| POT/$Fe_3O_4$/Au | 15 min | 2.28 x $10^{-3}$ $s^{-1}$ | Sun and Chen 2017 |
| AgNPs@MWCNTs-polymer composite | 5 min | 0.473 $min^{-1}$ | Alshehri et al. 2016 |

| | | | |
|---|---|---|---|
| $Pd/RGO/Fe_3O_4$ | 60 min | 3.06 $min^{-1}$ | Atarod et al. 2016 |
| 1 wt % $Au_{25}/Al_2O_3$ | 90 s | ---- | Farrag 2016 |
| $Ni\text{-}Ca\text{-}Al_2O_3$ | 18 min | 2.85 x $10^{-3}$ $s^{-1}$ | Feng et al. 2016 |
| Ni-RGO | 480 s | 1.8 x $10^{-3}$ $s^{-1}$ | Tian et al. 2015 |
| Guar gum-PtNPs | 240 min | 0.42 $min^{-1}$ | Pandey and Mishra 2014 |
| XG/Ag NPs | 24 h | 0.90 $min^{-1}$ | Xu et al. 2014 |
| GO/Ag | 0.5 min | 14.5 x $10^{-3}$ $s^{-1}$ | Mao et al. 2012 |
| $NRGO/ZnWO_4/Fe_3O_4$ | 30 s | 0.13344 $s^{-1}$ | Present work |
| $NRGO/NiWO_4/ZnO$ | 80 s | 0.02355 $s^{-1}$ | Present work |
| $NRGO/CoWO_4/Fe_2O_3$ | 30 s | 0.08468 $s^{-1}$ | Present work |
| $NRGO/FeWO_4/Fe_3O_4$ | 45 s | 0.04338 $s^{-1}$ | Present work |
| $NRGO/BaWO_4/g\text{-}C_3N_4$ | 60 s | 0.1883 $s^{-1}$ | Present work |

**Table 7.4** Comparison of HER parameters using alkaline medium of reported catalysts.

| **Catalysts** | **Onset potential** | **Over potential** | **Tafel slope (mV $dec^{-1}$)** | **References** |
|---|---|---|---|---|
| | **(mV vs. RHE) at -10 mA $cm^{-2}$** | | | |
| $Mo_2C$@NPC | -137 | -- | 126.4 | Li et al. 2016 |
| $Zn_{0.76}Co_{0.24}S/CoS_2$ | -- | 238 | 164 | Liang et al. 2016 |

| | | | | |
|---|---|---|---|---|
| $MoS_2$ CNTs aerogel | -210 | -- | 135 | Reddy et al. 2016 |
| $Ag_2S$/CuS | -323 | -- | 104 | Ren et al. 2016 |
| Carbon paper/carbon tubes/cobalt-sulfide | -- | 190 | 138 | Wang et al. 2016 |
| Co-NRCNTs | -- | 380 | -- | Wu et al. 2016 |
| AuNPs@NCNRs/CNFs-8 | -190 | 386 | 110 | Zhang et al. 2016 |
| $CoO_X$@N-doped carbon | -- | 232 | 115 | Jin et al. 2015 |
| $NiCo_2S_4$ nanowires | -- | 228 | 141 | Liu et al. 2015 |
| Co-PCPTF | -- | 370 | -- | Yang et al. 2015 |
| CoP/CC | -- | 550 | 129 | Tian et al. 2014 |
| Fe@N–C | -- | 330 | 158 | Wang et al. 2014 |
| N,P-graphene | 389 | 585 | 145 | Zheng et al. 2014 |
| Co-NRCNTs | -- | 370 | -- | Zou et al. 2014 |
| $Ni_xCo_{10-x}$/C nanoflakes | 200 | -- | 64 | Baranton and Coutanceau 2013 |
| NRGO/$ZnWO_4$/$Fe_3O_4$ | 113 | 218.55 | 75 | Present work |
| NRGO/$NiWO_4$/ZnO | 101 | 257 | 93 | Present work |
| NRGO/$CoWO_4$/$Fe_2O_3$ | 133 | 331 | 95 | Present work |
| NRGO/$FeWO_4$/$Fe_3O_4$ | 59 | 292 | 73 | Present work |
| NRGO/$BaWO_4$/g-$C_3N_4$ | 83 | 211 | 62 | Present work |

## 7.3 SCOPE FOR FUTURE WORK

As a continuation of the investigations carried out in this thesis, there is ample scope for further studies. The following work is suggested for the future research.

- In this thesis, the MB is selected as a model pollutant to evaluate the photocatalytic activities of the catalysts. A host of other dyes can be taken as substrates for photocatalytic degradation studies.
- The techniques such as HPLC and LC/MS can be utilized to further study the intermediate products and monitor the temporal course of the reaction in detail during the photocatalytic degradation.
- Morphology and components of the graphene based composite can be varied and its effect on catalytic efficiency can be studied.
- Graphene based nanocomposites can be studied as cathode materials in fuel cells for electrocatalysis of oxygen reduction reactions in both acidic and basic medium.

# REFERENCES

Acar, C., Dincer, I. and Naterer, G.F. (2016). "Review of photocatalytic water-splitting methods for sustainable hydrogen production." *Int. J. Energy Res.,* 40, 1449-1473.

Ahmad, M., Ahmed, E., Hong, Z.L., Xu, J.F., Khalid, N.R., Elhissi, A. and Ahmed, W. (2013). "A facile one-step approach to synthesizing ZnO/graphene composites for enhanced degradation of methylene blue under visible light." *Appl. Surf. Sci.,* 274, 273-281.

Ahmed, S., Rasul, M.G., Martens, W.N., Brown, R. and Hashib, M.A. (2010). "Heterogeneous photocatalytic degradation of phenols in wastewater: A review on current status and developments." *Desalination,* 261, 3-18.

Akhundi, A. and Habibi, Y.A. (2017). "Graphitic carbon nitride nanosheets decorated with $CuCr_2O_4$ nanoparticles: Novel photocatalysts with high performances in visible light degradation of water pollutants." *J. Colloid Interface Sci.,* 504, 697-710.

Alborzi, A. and Abedini, A. (2016). "Synthesis, characterization and investigation of magnetic and photocatalytic property of cobalt tungstate nanoparticles." *J. Mater. Sci. Mater. Electron.,* 27, 4057-4061.

Allen, M.J., Tung, V.C. and Kaner, R.B. (2009). "Honeycomb carbon: a review of graphene." *Chem. Rev.,* 110, 132-145.

Alshehri, S.M., Almuqati, T., Almuqati, N., Al-Farraj, E., Alhokbany, N. and Ahamad, T. (2016). "Chitosan based polymer matrix with silver nanoparticles decorated multiwalled carbon nanotubes for catalytic reduction of 4-nitrophenol." *Carbohydr. Polym.,* 151, 135-143.

An, C., Tang, K., Shen, G., Wang, C. and Qian, Y. (2002). "Hydrothermal preparation of luminescent $PbWO_4$ nanocrystallites." *Mater. Lett.,* 57, 565-568.

Appavu, B., Kannan, K. and Thiripuranthagan, S. (2016). "Enhanced visible light photocatalytic activities of template free mesoporous nitrogen doped reduced graphene oxide/titania composite catalysts." *J. Ind. Eng. Chem.,* 36, 184-193.

Areerob, Y., Cho, K. and Oh, W. (2017). "Microwave assisted synthesis of graphene-$Bi_8La_{10}O_{27}$-Zeolite nanocomposite with efficient photocatalytic activity towards organic dye degradation." *J. Photochem. Photobiol. A Chem.,* 340, 157-169.

Atarod, M., Nasrollahzadeh, M. and Sajadi, S.M. (2016). "Green synthesis of Pd/RGO/$Fe_3O_4$ nanocomposite using Withania coagulans leaf extract and its application as magnetically separable and reusable catalyst for the reduction of 4-nitrophenol." *J. Colloid Interface Sci.,* 465, 249-258.

Banerjee, S., Pillai, S.C., Falaras, P., Oshea, K.E., Byrne, J.A. and Dionysiou, D.D. (2014). "New insights into the mechanism of visible light photocatalysis." *J. Phys. Chem. Lett.,* 5, 2543-2554.

Baranton, S. and Coutanceau, C. (2013). "Nickel cobalt hydroxide nanoflakes as catalysts for the hydrogen evolution reaction." *Appl. Catal. B Environ.,* 136-137, 1-8.

Berzelius, J.J. (1835). "Årsberättelsen om framsteg i fysik och kemi." *Royal Swedish Academy of Sciences,* Stockholm.

Bhardwaj, M. and Balasubramaniam, R. (2008). "Uncoupled non-linear equations method for determining kinetic parameters in case of hydrogen evolution reaction following Volmer-Heyrovsky-Tafel mechanism and Volmer-Heyrovsky mechanism." *Int. J. Hydrogen Energy,* 33, 2178-2188.

Bhat, D.K. (2008). "Facile synthesis of ZnO nanorods by microwave irradiation of zinc-hydrazine hydrate complex." *Nanoscale Res. Lett.,* 3, 31-35.

Bhatt, A.S. and Bhat, D.K. (2012). "Crystallinity, magnetic and electrochemical studies of PVDF/$Co_3O_4$ polymer electrolyte." *Mater. Sci. Eng. B,* 177, 127-131.

Bhatt, A.S., Bhat, D.K. and Santosh, M.S. (2011). "Crystallinity, conductivity and magnetic properties of PVDF-$Fe_3O_4$ composite films." *J. Appl. Polym. Sci.,* 119, 968-972.

Bhatt, A.S., Bhat, D.K., Tai, C. and Santosh, M.S. (2011). "Microwave-assisted synthesis and magnetic studies of cobalt oxide nanoparticles." *Mater. Chem. Phys.,* 125, 347-350.

Bhattacharjee, A. and Ahmaruzzaman, M. (2015). "Photocatalytic-degradation and reduction of organic compounds using $SnO_2$ quantum dots (via a green route) under direct sunlight." *RSC Adv.,* 5, 66122-66133.

Bokris, J.O., Conway, B.E., Yeager, E. and White, R.E. (1981). "Comprehensive treatise of electrochemistry." Plenum press, New York.

Brindha, A. and Sivakumar, T. (2017). "Visible active N, S co-doped $TiO_2$/graphene photocatalysts for the degradation of hazardous dyes." *J. Photochem. Photobiol. A Chem.,* 340, 146-156.

Bruno, F.M. and Philippe, S. (2012). "Graphene-based materials for catalysis." *Catal. Sci. Technol.,* 2, 54-75

Butler, S.Z., Hollen, S.M., Cao, L., Cui, Y., Gupta, J.A., Gutierrez, H.R., Heinz, T.F., Hong, S.S, Huang, J. and Ismach, A.F. (2013). "Progress, challenges, and opportunities in two-dimensional materials beyond graphene." *ACS Nano,* 7, 2898-2926.

Cao, X., Chen, Y., Jiao, S., Fang, Z., Xu, M., Liu, X., Li, L., Pang, G. and Feng, S. (2014). "Magnetic photocatalysts with a p-n junction: $Fe_3O_4$ nanoparticle and $FeWO_4$ nanowire heterostructures." *Nanoscale,* 6, 12366-12370.

Cavalcante, L., Sczancoski, J., Lima Jr, L., Espinosa, J., Pizani, P., Varela, J.A. and Longo, E. (2008). "Synthesis, characterization, anisotropic growth and photoluminescence of $BaWO_4$." *Cryst. Growth Des.,* 9, 1002-1012.

Cavalli, E., Belletti, A. and Brik, M. (2008). "Optical spectra and energy levels of the $Cr^{3+}$ ions in $MWO_4$ (M= Mg, Zn, Cd) and $MgMoO_4$ crystals." *J. Phys. Chem. Solids,* 69, 29-34.

Chang, D.W. and Baek, J.B. (2016). "Nitrogen-Doped Graphene for Photocatalytic Hydrogen Generation." *Chem. Asian J.,* 11, 1125-1137.

Chang, H. and Wu, H. (2013). "Graphene-based nanocomposites: preparation, functionalization and energy and environmental applications." *Energy Environ. Sci.,* 6, 3483-3507.

Chang, Y.C. and Chen, D.H. (2009). "Catalytic reduction of 4-nitrophenol by magnetically recoverable Au nanocatalyst." *J. Hazard. Mater.,* 165, 664-669.

Chen, C., Ma, W. and Zhao, J. (2010). "Semiconductor-mediated photodegradation of pollutants under visible-light irradiation." *Chem. Soc. Rev.,* 39, 4206-4219.

Chen, D., Zhu, H., Yang, S., Li, N., Xu, Q., Li, H., He, J. and Lu, J. (2016). "Micro-nanocomposites in environmental management." *Adv. Mater.,* 28, 10443-10458.

Chen, G., Guan, H., Dong, C., Xiao, X. and Wang, Y. (2016). "Effect of calcination temperatures on the electrochemical performances of nickel oxide/reduction graphene oxide (NiO/RGO) composites synthesized by hydrothermal method." *J. Phys. Chem. Solids,* 98, 209-219.

Chen, P., Xing, X., Xie, H., Sheng, Q. and Hongxia, Q. (2016). "High catalytic activity of magnetic $CuFe_2O_4$/graphene oxide composite for the degradation of organic dyes under visible light irradiation." *Chem. Phy. Lett.,* 660, 176-181.

Chen, S.J., Li, J., Chen, X.T., Hong, J.M., Xue, Z. and You, X.Z. (2003). "Solvothermal synthesis and characterization of crystalline $CaWO_4$ nanoparticles." *J. Cryst. Growth,* 253, 361-365.

Chen, S.J., Zhou, J.H., Chen, X.T., Li, J., Li, L.H., Hong, J.M., Xue, Z. and You, X.Z. (2003). "Fabrication of nanocrytalline $ZnWO_4$ with different morphologies and sizes via hydrothermal route." *Chem. Phys. Lett.,* 375, 185-190.

Chen, T., Zeng, B., Liu, J.L., Dong, J.H., Liu, X.Q., Wu, Z., Yang, X.Z. and Li Z.M. (2009). "High throughput exfoliation of graphene oxide from expanded graphite with

assistance of strong oxidant in modified Hummers method." *J. Phys. Conf. Ser.,* 188, 012051-012055.

Chen, W.F., Muckerman, J.T. and Fujita, E. (2013). "Recent developments in transition metal carbides and nitrides as hydrogen evolution electrocatalysts." *Chem. Commun.,* 49, 8896-8909.

Cheng, L., Zhang, S., Wang, Y., Ding, G. and Jiao, Z. (2016). "Ternary P25-graphene-$Fe_3O_4$ nanocomposite as a magnetically recyclable hybrid for photodegradation of dyes." *Mater. Res. Bull.,* 73, 77-83.

Chiou, J.R., Lai, B.H., Hsu, K.C. and Chen, D.H. (2013). "One-pot green synthesis of silver/iron oxide composite nanoparticles for 4-nitrophenol reduction." *J. Hazard. Mater.,* 248, 394-400.

Chowdhury, S. and Balasubramanian, R. (2014). "Graphene/semiconductor nanocomposites (GSNs) for heterogeneous photocatalytic decolorization of wastewaters contaminated with synthetic dyes: a review." *Appl. Catal. B Environ.,* 160, 307-324.

Clark, G. and Doyle, W. (1966). "Infra-red spectra of anhydrous molybdates and tungstates." *Spectrochim. Acta,* 22, 1441-1447.

Conway, B.E. and Tilak, B.V. (2002). "Interfacial processes involving electrocatalytic evolution and oxidation of $H_2$, and the role of chemisorbed H." *Electrochim. Acta,* 47, 3571-3594.

Cooper, P. (1993). "Removing colour from dyehouse waste waters-a critical review of technology available." *J. Soc. Dyers Colour.,* 109, 97-100.

Cui, Y., Li, H., Hong, W., Fan, S. and Zhu, L. (2013). "The effect of carbon content on the structure and photocatalytic activity of nano-$Bi_2WO_6$ powder." *Powder Technol.,* 247, 151-160.

Dai, H., Gao, X., Liu, E., Yang, Y.H., Hou, W.Q., Kang, L.M., Fan, J. and Hu, X. (2013). "Synthesis and characterization of graphitic carbon nitride sub-microspheres using microwave method under mild condition." *Diam. Relat. Mater.,* 38, 109-117.

Dai, K., Zhang, X., Fan, K., Peng, T. and Wei, B. (2013). "Hydrothermal synthesis of single-walled carbon nantube-$TiO_2$ hybrid and its photocatalytic activity." *Appl. Surf. Sci.,* 270, 238-244.

Daneshvar, N., Salari, D. and Khataee, A. (2004). "Photocatalytic degradation of azo dye acid red 14 in water on ZnO as an alternative catalyst to $TiO_2$." *J. Photochem. Photobiol. A,* 162, 317-322.

Das, R.K., Kar, J.P. and Mohapatra, S. (2016). "Enhanced photodegradation of organic pollutants by carbon quantum dot (CQD) deposited $Fe_3O_4$@m-$TiO_2$ nano kooshballs." *Ind. Eng. Chem. Res.,* 55, 5902-5910.

Debe, M.K. (2012). "Electrocatalyst approaches and challenges for automotive fuel cells." *Nature,* 486, 43-51.

Deng, Z., Wang, J., Nie, Y. and Wei, Z. (2017). "Tuning the interface of Ni@$Ni(OH)_2$/Pd/rGO catalyst to enhance hydrogen evolution activity and stability." *J. Power Sources,* 352, 26-33.

Dhilip, R.K. and Karuppuchamy, S. (2014). "Microwave-assisted synthesis of copper tungstate nanopowder for supercapacitor applications." *Ceram. Int.,* 40, 12397-13402.

Dinesh, K., Karamjit, S., Veena V. and Bhatti, H.S. (2016). "Microwave assisted synthesis and characterization of graphene nanoplatelets." *Appl. Nanosci.,* 6, 97-103.

Dong, F., Wu, L., Sun, Y., Min, F., Wu, Z. and Lee, S.C. (2011). "Efficient synthesis of polymeric g-$C_3N_4$ layered materials as novel efficient visible light driven photocatalysts." *J. Mater. Chem.,* 21, 15171-15174.

Dong, F., Zhao, Z., Ting, X., Zilin, N., Wendong, Z., Yanjuan, S. and Ho, W. (2013). "In Situ Construction of g-$C_3N_4$/g-$C_3N_4$ Metal-Free Heterojunction for Enhanced Visible-Light Photocatalysis." *ACS Appl. Mater. Interfaces,* 5, 11392-11401.

Du, X.Y., He, J., Zhu, J., Sun, L.J. and An, S.S. (2012). "Ag-deposited silica-coated $Fe_3O_4$ magnetic nanoparticles catalyzed reduction of p-nitrophenol." *Appl. Surf. Sci.,* 258, 2717-2723

Dutta, S.K., Mehetor, S.K. and Pradhan, N. (2015). "Metal semiconductor heterostructures for photocatalytic conversion of light energy." *J. Phys. Chem. Lett.,* 6, 936-944.

El-Bahy, Z.M. (2013). "Preparation and characterization of Pt-promoted NiY and CoY catalysts employed for 4-nitrophenol reduction." *Appl. Catal. A,* 468 175-183

Fang, W., Deng, Y., Tang, L., Zeng, G., Zhou, Y., Xie, X., Wang, J., Wang, Y. and Wang, J. (2017). "Synthesis of Pd/Au bimetallic nanoparticle-loaded ultrathin graphitic carbon nitride nanosheets for highly efficient catalytic reduction of p-nitrophenol." *J. Colloid Interface Sci.,* 490, 834-843.

Faraji, M. and Mohaghegh, N. (2016). "Ag/$TiO_2$-nanotube plates coated with reduced graphene oxide as photocatalysts." *Surf. Coat. Technol.,* 288, 144-150.

Farhadian, M., Sangpour, P. and Hosseinzadeh, G. (2016). "Preparation and photocatalytic activity of $WO_3$-MWCNT nanocomposite for degradation of naphthalene under visible light irradiation." *RSC Adv.,* 6, 39063-39073.

Farrag, M. (2016). "Microwave-assisted synthesis of ultrasmall bare gold clusters supported over $Al_2O_3$ and $TiO_2$ as catalysts in reduction of 4-nitrophenol to 4-aminophenol." *Microporous Mesoporous Mater.,* 232, 248-255.

Farsi, H. and Zahra, B. (2014). "Synthesis, characterization and electrochemical studies of nanostructured $CaWO_4$ as platinum support for oxygen reduction reaction." *Mater. Res. Bull.,* 59, 261-266.

Fath, R.H., Hoseini, S.J. and Khozestan, H.G. (2017). "A nanohybrid of organoplatinum(II) complex and graphene oxide as catalyst for reduction of p-nitrophenol." *J. Organometal. Chem..,* 842, 1-8.

Feng, J., Fan, D., Wang, Q., Ma, L., Wei, W., Xie, J. and Zhu, J. (2017). "Facile synthesis silver nanoparticles on different xerogel supports as highly efficient catalysts for the reduction of p-nitrophenol." *Colloids Surf. A*, 520, 743-756.

Feng, J., Wang, Q., Fan, D., Ma, L., Jiang, D., Xie, J. and Zhu, J. (2016). "Nickel-based xerogel catalysts: Synthesis via fast sol-gel method and application in catalytic hydrogenation of p-nitrophenol top-aminophenol." *Appl. Surf. Sci.,* 382, 135-143

Ferrari, A.C. and Basko, D.M. (2013). "Raman spectroscopy as a versatile tool for studying the properties of graphene." *Nat. Nanotechnol.,* 8, 235-246.

Fu, C., Song, C., Liu, L., Xie, X. and Zhao, W. (2016). "Synthesis and properties of nitrogen-doped graphene as anode materials for lithium-ion batteries." *Int. J. Electrochem. Sci.,* 11, 3876-3886.

Galindo, C. and Jacques, P.K. (2001). "Photooxidation of the phenyl azo naphthol AO on $TiO_2$: kinetic and mechanistic investigations." *Chemosphere,* 45, 997-1005.

Gao, S., Tang, Y., Wang, L., Liu, L., Jia, D. and Zhao, Z. (2017). "NiFe nanoalloys in-situ immobilized on coal based activated carbons through one-step pyrolysis as magnetically recoverable catalysts for reduction of 4-nitrophenol.' *J. Alloys Compd.,* 702, 531-537.

Gao, W., Alemany, L.B., Ci, L. and Ajayan, P.M. (2009). "New insights into the structure and reduction of graphite oxide." *Nat. Chem.,* 1, 403-408.

Garadkar, K.M., Ghule, L.A., Sapnar, K.B. and Dhole, S.D. (2013). "A facile synthesis of $ZnWO_4$ nanoparticles by microwave assisted technique and its application in photocatalysis." *Mater. Res. Bull.,* 48, 1105-1109.

Garg, V.K., Amita, M., Kumar, R. and Gupta, R. (2004). "Basic dye (methylene blue) removal from simulated wastewater by adsorption using Indian Rosewood sawdust: a timber industry waste." *Dyes Pigm.,* 63 (3), 243-250.

Ge, C., Jiang, P., Cui, W., Pu, Z., Xing, Z., Asiri, A.M., Obaid, A.Y., Sun, X. and Tian, J. (2014). "Shape-controllable synthesis of $Mo_2C$ nanostructures as hydrogen

evolution reaction electrocatalysts with high activity." *Electrochim. Acta,* 134, 182-186.

Gedye, R., Smith, F., Westaway, K., Ali, H., Baldisera, L., Laberge, L. and Rousell, J. (1986). "The use of microwave ovens for rapid organic synthesis." *Tetrahedron Lett.,* 27, 279-282.

Geng, J., Zhu, J.J., Lu, D.J. and Chen, H.Y. (2006). "Hollow $PbWO_4$ nanospindles via a facile sonochemical route." *Inorg. Chem.,* 45, 8403-8407.

Ghosh, S.K., Mandal, M., Kundu, S., Nath, S. and Pal, T. (2004). "Bimetallic Pt-Ni nanoparticles can catalyze reduction of aromatic nitro compounds by sodium borohydride in aqueous solution." *Appl. Catal. A,* 268, 61-66.

Gohari, M.S. and Yangieh, A.H. (2017). "$Fe_3O_4$/ZnO/$CoWO_4$ nanocomposites: Novel magnetically separable visible-light-driven photocatalysts with enhanced activity in degradation of different dye pollutants." *Ceram. Int.,* 43, 3063-3071.

Graf, D., Molitor, F., Ensslin, K., Stampfer, C., Jungen, A., Hierold, C. and Wirtz, L. (2007). "Spatially resolved Raman spectroscopy of single-and few-layer graphene." *Nano Lett.,* 7, 238-242.

Guo, J., Sun, G., Wang, Q., Wang, G., Zhou, Z., Tang, S., Jiang, L., Zhou, B. and Xin, Q. (2006). "Carbon nanofibers supported Pt-Ru electrocatalysts for direct methanol fuel cells." *Carbon,* 44 152-157.

Guo, J., Zhu, S., Chen, Z., Li, Y., Yu, Z., Liu, Q., Li, J., Feng, C. and Zhang, D. (2011). "Sonochemical synthesis of $TiO_2$ nanoparticles on graphene for use as photocatalyst." *Ultrason. Sonochem.,* 18, 1082-1090.

Gururaj, M.N., Oki, A. and Luo, Z. (2014). "ZnO and cobalt phthalocyanine hybridized graphene: Efficient photocatalysts for degradation of rhodamine B." *J. Colloid Interface Sci.,* 430, 257-264.

Hao, R., Wang, G., Jiang, C., Tang, H. and Xu, Q. (2017). "In situ hydrothermal synthesis of g-$C_3N_4$/$TiO_2$ heterojunction photocatalysts with high specific surface area for Rhodamine B degradation." *Appl. Surf. Sci.,* 411, 400-410.

He, D., Zhang, X., Xie, T., Zhai, J., Li, H., Chen, L., Peng, L., Zhang, Y. and Jiang, T. (2011). "Studies of photo-induced charge transfer properties of $ZnWO_4$ photocatalyst." *Appl. Surf. Sci.,* 257, 2327-2331.

He, G.L., Chen, M.J., Liu, Y.Q., Li, X., Liu, Y.J. and Xu, Y.H. (2015). "Hydrothermal synthesis of $FeWO_4$-graphene composites and their photocatalytic activities under visible light." *Appl. Surf. Sci.,* 351, 474-479.

Herrmann, J.M. (1999). "Heterogeneous photocatalysis: fundamentals and applications to the removal of various types of aqueous pollutants." *Catal. Today,* 53, 115-129.

Hisatomi, T., Kubota, J. and Domen, K. (2014). "Recent advances in semiconductors for photocatalytic and photoelectrochemical water splitting." *Chem. Soc. Rev.,* 43, 7520-7535.

Hojamberdiev, M., Zhu, G. and Xu, Y. (2010). "Template-free synthesis of $ZnWO_4$ powders via hydrothermal process in a wide pH range." *Mater. Res. Bull.,* 45, 1934-1940.

Hu, D., Peng, D., Di, X., Mengyang, X., Yue, G., Qingyong, W., Chao, L. and Shubin, Y. (2016). "Copper (II) tungstate nanoflake array films: Sacrificial template synthesis, hydrogen treatment, and their application as photoanodes in solar water splitting." *Nanoscale,* 8, 5892-5901.

Huang, C., Li, C. and Shi, G. (2012). "Graphene based catalysts." *Energy Environ. Sci.,* 5, 8848-8868.

Huang, R., Ge, H., Lin, X., Guo, Y., Yuan, R., Fu, X. and Li, Z. (2013). "Facile one-pot preparation of α-$SnWO_4$/reduced graphene oxide (RGO) nanocomposite with

improved visible light photocatalytic activity and anode performance for Li-ion batteries." *RSC Adv.,* 3, 1235-1242.

Huang, X., Qi, X., Boey, F. and Zhang, H. (2012). "Graphene-based composites." *Chem. Soc. Rev.,* 41, 666-686.

Hummers Jr, W.S. and Offeman, R.E. (1958). "Preparation of graphitic oxide." *J. Am. Chem. Soc.,* 80, 1339-1339.

Imran, M., Yousaf, A.B., Zaidi, S.J. and Fernandez, C. (2017). "Tungsten-molybdenum oxide nanowires/reduced graphene oxide nanocomposite with enhanced and durable performance for electrocatalytic hydrogen evolution reaction." *Int. J. Hydrogen Energy,* 42, 8130-8138.

Islam, D. and Acharya, H. (2015). "Magnetically separable palladium nanocluster supported iron based metal-organic framework (MIL-88B) catalyst in efficient hydrogenation reactions." *RSC Adv.,* 5, 46583-46588.

Jacob, R.M., Machhi, R., Wroblewski, J., Taylor, B., Anne, L.G. and Arnold, M.S. (2015). "Simple graphene synthesis via Chemical Vapor Deposition." *J. Chem. Educ.,* 92, 1903-1907.

Jafari, Z., Mokhtarian, N., Hosseinzadeh, G., Farhadian, M., Faghihi, A. and Shojaie, F. (2016). "Ag/$TiO_2$/freeze-dried graphene nanocomposite as a high performance photocatalyst under visible light irradiation." *J. Energy Chem.,* 25, 393-402.

Jiang, H.L., Akita, T., Ishida, T., Haruta, M. and Xu, Q. (2011). "Synergistic catalysis of Au@Ag core-shell nanoparticles stabilized on metal-organic framework." *J. Am. Chem. Soc.,* 133, 1304-1306.

Jin, H., Wang, J., Su, D., Wei, Z., Pang, Z. and Wang, Y. (2015). "In situ cobalt-cobalt oxide/N-doped carbon hybrids as superior bifunctional electrocatalysts for hydrogen and oxygen evolution." *J. Am. Chem. Soc.,* 137, 2688-2694

Jo, W.K. and Selvam, N.C. (2015). "Synthesis of GO supported $Fe_2O_3$-$TiO_2$ nanocomposites for enhanced visible-light photocatalytic applications." *Dalton Trans.,* 44, 16024-16035.

Ju, K.S. and Parales, R.E. (2010). "Nitroaromatic compounds, from synthesis to biodegradation." *Microbiol. Mol. Biol. Rev.,* 74, 250-272.

Kalinko, A. and Kuzmin, A. (2011). "Static and dynamic structure of $ZnWO_4$ nanoparticles." *J. Non-Cryst. Solids,* 357, 2595-2599.

Kasinath, O., Soumen, S., Hristo, K., Bharat, K. and Ashok, K.G. (2016). "Composites of graphene-$Mo_2C$ rods: highly active and stable electrocatalyst for hydrogen evolution reaction." *Electrochim. Acta,* 193, 268-274.

Keihan, A.H., Hosseinzadeh, R., Farhadian, M., Kooshki, H. and Hosseinzadeh, G. (2016). "Solvothermal preparation of Ag nanoparticle and graphene co-loaded $TiO_2$ for Photocatalytic degradation of paraoxon pesticide under visible light irradiation." *RSC Adv.,* 6, 83673-83687.

Khademolhosein, S. and Zarkar, S.A. (2016). "Preparation and characterization of barium tungstate nanoparticles via a new simple surfactant-free route." *J. Mater. Sci. Mater. Electron.,* 27, 9605-9609.

Khaksar, M., Davar, M.B. and Amini, M. (2015). "Synthesis, structural characterization and reactivity of manganese tungstate nanoparticles in the oxidative degradation of methylene blue." *C.R. Chimie,* 18, 199-203.

Khandelwal, M. and Kumar, A. (2015). "One-step chemically controlled wet synthesis of graphene nanoribbons from graphene oxide for high performance supercapacitor applications." *J. Mater. Chem. A,* 3, 22975-22988.

Khodja, A., Sehili, T., Pilichowski, J. and Boule, P. (2001). "Photocatalytic degradation of 2-phenylphenol on $TiO_2$ and ZnO in aqueous suspensions." *J. Photochem. Photobiol. A,* 141, 231-239.

Kloprogge, J.T., Weier, M.L., Duong, L.V. and Frost, R.L. (2004). "Microwave-assisted synthesis and characterisation of divalent metal tungstate nanocrystalline minerals: ferberite, hübnerite, sanmartinite, scheelite and stolzite." *Mater. Chem. Phys.,* 88, 438-443.

Kochuveedu, S.T., Jang, Y.H. and Kim, D.H. (2013). "A study on the mechanism for the interaction of light with noble metal-metal oxide semiconductor nanostructures for various photophysical applications." *Chem. Soc. Rev.,* 42, 8467-8493.

Kumar, A., Guo, C., Sharma, G., Pathania, D., Naushad, M., Kaliab, S. and Dhimane, P. (2016). "Magnetically recoverable $ZrO_2/Fe_3O_4$/chitosan nanomaterials for enhanced sunlight driven photoreduction of carcinogenic Cr(VI) and dechlorination & mineralization of 4-chlorophenol from simulated waste water." *RSC Adv.,* 6, 13251-13263.

Kumar, D.R. and Karuppuchamy, S. (2016). "Microwave mediated synthesis of nanostructures $CoWO_3$ and $CoWO_4$ for supercapacitor applications." *J. Alloys Compd.,* 674, 384-391.

Kumar, G.B., Sivaiah, K. and Buddhudu, S. (2010). "Synthesis and characterization of $ZnWO_4$ ceramic powder." *Ceram. Int.,* 36, 199-202.

Kuo, W. (1992). "Decolorizing dye wastewater with Fenton's reagent." *Water Res.,* 26, 881-886.

Lai, C., Wang, M., Zeng, G., Liu, Y., Huang, D., Chen, Z., Wang, R., Piao, X., Min, C., Chao, H., Wu, H. and Qin, L. (2016). "Synthesis of surface molecular imprinted $TiO_2$/graphene photocatalyst and its highly efficient photocatalytic degradation of target pollutant under visible light irradiation." *Appl. Surf. Sci.,* 390, 368-376.

Lang, B. and Yu, H.K. (2017). "Novel $Ag_2S$ nanoparticles on reduced graphene oxide sheets as a super-efficient catalyst for the reduction of 4-nitrophenol." *Chinese Chem. Lett.,* 28, 417-421.

Li, C., Xu, Y., Tu, W., Chen, G. and Xu, R. (2017). "Metal free photocatalysts for various applications in energy conversion and environmental purification." *Green Chem.,* 19, 882-899.

Li, D., Mueller, M.B., Gilje, S., Kaner, R.B. and Wallace, G.G. (2008). "Processable aqueous dispersions of graphene nanosheets." *Nat. Nanotechnol.,* 3, 101-105.

Li, J., Liu, C.Y. and Liu, Y. (2012). "Au/graphene hydrogel: synthesis, characterization and its use for catalytic reduction of 4-nitrophenol." *J. Mater. Chem.,* 22, 8426-8430.

Li, J.S., Wang, Y., Liu, C.H., Li, S.L., Wang, Y.G., Dong, L.Z., Dai, Z.H., Li, Y.F. and Lan, Y.Q. (2016). "Coupled molybdenum carbide and reduced graphene oxide electrocatalysts for efficient hydrogen evolution." *Nat. Commun.,* 7, 1-8.

Li, P., Zhao, X., Jia, C.J., Sun, H., Sun, L., Cheng, X., Liu, L. and Fan, W. (2013). "$ZnWO_4$/BiOI heterostructures with highly efficient visible light photocatalytic activity: the case of interface lattice and energy level match." *J. Mater. Chem. A,* 1, 3421-3429.

Li, Q., Shen, Y. and Li, T. (2013). "Fast Microwave Assisted Synthesis and Photoluminescence of $CaWO_4$ Nanocrystals." *J. Chem.,* 2013, 1-5.

Li, X., Ma, Y., Yang, Z., Huang, D., Xu, S., Wang, T., Su, Y., Hu, N. and Zhang, Y. (2017). "In situ preparation of magnetic Ni-Au/graphene nanocomposites with electron-enhanced catalytic performance." *J. Alloys Compd.,* 706, 377-386.

Li, X., Wang, H., Robinson, J.T., Sanchez, H., Diankov, G. and Dai, H. (2009). "Simultaneous nitrogen doping and reduction of graphene oxide." *J. Am. Chem. Soc.,* 131, 15939-15944.

Li, Y.Z., Li, Y.F., Su, F.Y., Xie, L.J., Kong, Q.Q., Li, X.M., Gao, J.G. and Chen, C.M. (2016). "Easy one-step synthesis of N-doped graphene for supercapacitors." *Energy Storage Mater.,* 2, 69-75.

Lianbo, M., Xiaoping, S., Hu, Z., Guoxing, Z., Zhenyuan, J. and Kangmin, C. (2015). "CoP nanoparticles deposited on reduced graphene oxide sheets as an active electrocatalyst for the hydrogen evolution reaction." *J. Mater. Chem.,* 10, 5337-5343.

Liang, Y., Liu, Q., Luo, Y., Sun, X., He, Y. and Asiri, A.M. (2016). "$Zn_{0.76}Co_{0.24}S/CoS_2$ nanowires array for efficient electrochemical splitting of water." *Electrochim. Acta,* 190, 360-364.

Liao, H.W., Wang, Y.F., Liu, X.M., Li, Y.D. and Qian, Y.T. (2002). "Hydrothermal preparation and characterization of luminescent $CdWO_4$ nanorods." *Chem. Mater.,* 12, 2819-2821.

Lin, X.X., Zhang, X.F., Wang, A.J., Fang, K.M., Yuan, J. and Feng, J.J. (2017). "Simple one-pot aqueous synthesis of AuPd alloy nanocrystals/reduced graphene oxide as highly efficient and stable electrocatalyst for oxygen reduction and hydrogen evolution reactions." *J. Colloid Interface Sci.,* 499, 128-137.

Lingpu, J., Xiao, S., Yimin, J., Shenjiao, Y. and Chunming W. (2015). "A novel $MoSe_2$-reduced graphene oxide/polyimide composite film for applications in electrocatalysis and photoelectrocatalysis hydrogen evolution." *Adv. Funct. Mater.,* 12, 1814-1820.

Liu, D., Lu, Q., Luo, Y., Sun, X. and Asiri, A.M. (2015). "$NiCo_2S_4$ nanowires array as an efficient bifunctional electrocatalyst for full water splitting with superior activity." *Nanoscale,* 7, 15122-15126.

Liu, L., Chen, R., Liu, W., Wu, J. and Gao, D. (2016). "Catalytic reduction of 4-nitrophenol over Ni-Pd nanodimers supported on nitrogen-doped reduced graphene oxide." *J. Hazard. Mater.,* 320, 96-104.

Liu, Y., Pei, F., Lu, R., Xu, S. and Cao, S. (2014). "$TiO_2$/N-graphene nanocomposite via a facile In-situ hydrothermal sol-gel strategy for visible light photodegradation of eosin Y." *Mater. Res. Bull.,* 60, 188-194.

Liu, Y., Zhu, Y., Fan, X., Wang, S., Li, Y., Zhang, F., Zhang, G. and Peng, W. (2017). "(0D/3D) $MoS_2$ on porous graphene as catalysts for enhanced electrochemical hydrogen evolution." *Carbon,* 121, 163-169.

Liu, Y.R., Shang, X., Gao, W.K., Dong, B., Chi, J.Q., Li, X., Yan, K.L., Chai, Y.M., Liu, Y.Q. and Liu, C.G. (2017). "Ternary $CoS_2/MoS_2$/RGO electrocatalyst with CoMoS phase for efficient hydrogen evolution." *Appl. Surf. Sci.,* 412 138-145

Liu, Y.Z., Li, Y.F., Su, F., Xie, L., Kong, Q., Li, X., Gao, J. and Chen, C. (2016). "Easy one-step synthesis of N-doped graphene for supercapacitors." *Energy Storage Mater.,* 2, 69-75.

Liu, Z., Lee, J.Y., Chen, W., Han, M. and Gan, L.M. (2004). "Physical and electrochemical characterizations of microwave-assisted polyol preparation of carbon-supported PtRu nanoparticles." *Langmuir,* 20, 181-187.

Long, J., Yu-Xiao, Z. and Hai-Long, J. (2016). "Metal-organic framework-based CoP/reduced graphene oxide: high-performance bifunctional electrocatalyst for overall water splitting." *RSC Adv.,* 7, 1690-1695.

Lu, S., Yu, J., Cheng, Y., Wang, Q., Barras, A., Xu, W., Szunerits, S., Cornu, D. and Boukherroub, R. (2017). "Preparation of silver nanoparticles/polydopamine functionalized polyacrylonitrile fiber paper and its catalytic activity for the reduction 4-nitrophenol." *Appl. Surf. Sci.,* 411, 163-169.

Ma, R., Song, E., Zhou, Y., Zhou, Z., Liu, G., Liu, Q., Liu, J., Zhu, Y. and Wang, J. (2017). "Ultrafine WC nanoparticles anchored on co-encased, N-doped carbon nanotubes for efficient hydrogen evolution." *Energy Storage Mater.,* 6, 104-111.

Ma, Y., Guo, Y., Jiang, H., Qu, D., Liu, J., Kang, W., Yi, Y., Zhang, W., Shi, J. and Han, Z. (2015). "Preparation of network-like ZnO-$FeWO_4$ mesoporous heterojunctions with tunable band gaps and their enhanced visible light photocatalytic performance." *New J. Chem.,* 39, 5612-5620.

Madhavan, J., Kumar, P.S.S., Anandan, S., Grieser, F. and Ashokkumar, M. (2010). "Sonophotocatalytic degradation of monocrotophos using $TiO_2$ and $Fe^{3+}$." *J. Hazard. Mater.,* 177, 944-949.

Maham, M., Nasrollahzadeh, M., Sajadi, S.M. and Nekoei, M. (2017). "Biosynthesis of Ag/reduced graphene oxide/$Fe_3O_4$ using Lotus garcinii leaf extract and its application as a recyclable nanocatalyst for the reduction of 4-nitrophenol and organic dyes." *J. Colloid Interface Sci.,* 497, 33-42.

Mao, A., Zhang, D., Jin, X., Gu, X., Wei, X., Yang, G. and Liu, X. (2012). "Synthesis of graphene oxide sheets decorated by silver nanoparticles in organic phase and their catalytic activity." *J. Phys. Chem. Solids,* 73, 982-986.

Marcano, D.C., Dmitry, V.K., Jacob, M.B., Sinitskii, A., Sun, Z., Slesarev, A., Lawrence, B. A., Lu, W. and James, M.T. (2010). "Improved Synthesis of Graphene Oxide." *ACS Nano,* 4, 4806-4814

Markovic, N. and Ross, P.N. (2002). "Surface science studies of model fuel cell electrocatalysts." *Surf. Sci. Rep.,* 45, 117-229.

Meng, A., Shao, J., Fan, X., Wang, J. and Li, Z. (2014). "Rapid synthesis of a flower-like ZnO/rGO/Ag micro/nano-composite with enhanced photocatalytic performance by a one-step microwave method." *RSC Adv.,* 4, 60300-60305.

Meng, N., Cheng, J., Zhou, Y., Nie. W. and Chen, P. (2017). "Green synthesis of layered 1T-$MoS_2$/reduced graphene oxide nanocomposite with excellent catalytic performances for 4-nitrophenol reduction." *Appl. Surf. Sci.,* 396, 310-318.

Meng, N., Zhang, S., Zhou, Y., Nie, W. and Chen, P. (2015). "Novel synthesis of silver/reduced graphene oxide nanocomposite and its high catalytic activity towards hydrogenation of 4-nitrophenol." *RSC Adv.,* 5, 70968-70971.

Mills, A. and Le Hunte, S. (1997). "An overview of semiconductor photocatalysis." *J. Photochem. Photobiol. A Chem.,* 108, 1-35.

Min, Z., Wang, X., Li, Y., Jiang, J., Li, J., Qian, D. and Li, J. (2017). "A highly efficient visible-light responding $Cu_2O$-$TiO_2$/g-$C_3N_4$ photocatalyst for instantaneous discolorations of organic dyes." *Mater. Lett.,* 193, 18-21.

Momirlan, M. (2002). "Current status of hydrogen energy." *Renew. Sust. Energy Rev.,* 6, 141-179.

Montini, T., Gombac, V., Hameed, A., Felisari, L., Adami, G. and Fornasiero, P. (2010). "Synthesis, characterization and photocatalytic performance of transition metal tungstates." *Chem. Phys. Lett.,* 498, 113-119.

Mostafa, S.H.M. and Ali, S.N. (2016). "Simple synthesis and characterization of copper tungstate nanoparticles: investigation of surfactant effect and its photocatalyst application." *J. Mater. Sci. Mater. Electron.,* 27, 7548-7553.

Nasrollahzadeh, M., Atarod, M., Jaleh, B. and Gandomirouzbahani, M. (2016). "In situ green synthesis of Ag nanoparticles on graphene oxide/$TiO_2$ nanocomposite and their catalytic activity for the reduction of 4-nitrophenol, congo red and methylene blue." *Ceram. Int.,* 42, 8587-8596.

Nguyen, T.V., Kim, K.J. and Yang, O.B. (2005). "Photocatalytic water decomposition for hydrogen production over silicotungstic acid-silica photocatalyst." *J. Photochem. Photobiol. A Chem.,* 173, 56-63.

Norskov, J.K., Bligaard, T., Logadottir, A., Kitchin, J.R., Chen, J.G., Pandelov, S. and Stimming. U. (2005). "Trends in the exchange current for hydrogen evolution." *J. Electrochem. Soc.,* 152, J23-J26.

Ou, M., Qin, Z., Yanxiao, Z., Xue, Y. and Song, F. (2016). "Graphene-decorated 3D $BiVO_4$ photocatalyst with controlled size and shape for efficient visible-light-induced photocatalytic performance." *Mater. Lett.,* 184, 227-231.

Pal, M., Garcia Serrano, J., Santiago, P. and Pal, U. (2007). "Size-controlled synthesis of spherical $TiO_2$ nanoparticles: morphology, crystallization, and phase transition." *J. Phys. Chem. C,* 111, 96-102.

Pandey, S. and Mishra, S.B. (2014). "Catalytic reduction of p-nitrophenol by using platinum nanoparticles stabilised by guar gum." *Carbohydr. Polym.,* 113, 52-531.

Paola, A.D., Lopez, E.G., Marci, G. and Palmisano, L. (2012). "A survey of photocatalytic materials for environmental remediation." *J. Hazard. Mater.,* 211-212, 3-29.

Patel, N., Jaiswal, R., Warang, T., Scarduelli, G., Dashora, A., Ahuja, B., Kothari, D. and Miotello, A. (2014). "Efficient photocatalytic degradation of organic water pollutants using V-N-codoped $TiO_2$ thin films." *Appl. Catal. B Environ.,* 150, 74-81.

Pawar, R.C., Kang, S., Ahn, S.H. and Lee, C.S. (2015). "Gold nanoparticle modified graphitic carbon nitride/multi-walled carbon nanotube (g-$C_3N_4$/CNTs/Au) hybrid photocatalysts for effective water splitting and degradation." *RSC Adv.,* 5, 24281-24292.

Pearson, R.G. (1988). "Absolute electronegativity and hardness: application to inorganic chemistry." *Inorg. Chem.,* 27, 734-740.

Pera-Titus, M., García-Molina, V., Baños, M.A., Giménez, J. and Esplugas, S. (2004). "Degradation of chlorophenols by means of advanced oxidation processes: a general review." *Appl. Catal. B Environ.,* 47, 219-256.

Phani, A., Passacantando, M., Lozzi, L. and Santucci, S. (2000). "Structural characterization of bulk $ZnWO_4$ prepared by solid state method." *J. Mater. Sci.,* 35, 4879-4883.

Philippe, S. and Bruno, F.M. (2015). "Nanostructured carbon materials for photocatalysis." *RSC Catal. Series,* 23, 419- 438.

Pirhashemi, M. and Yangjeh, A.H. (2017). "Ultrasonic-assisted preparation of plasmonic ZnO/Ag/$Ag_2WO_4$ nanocomposites with high visible light photocatalytic performance for degradation of organic pollutants." *J. Colloid Interface Sci.,* 491, 216-229.

Pourmortazavi, S.M., Mehdi, R.N., Morteza, K.S., Ghaeni, H.R. and Hajimirsadeghi, S.S. (2014). "Facile chemical synthesis and characterization of copper tungstate nanoparticles." *J. Inorg. Organometal. Polym. Mater.,* 24, 333-339.

Pradhan, D., Mohapatra, S.K., Tymen, S., Misra, M. and Leung, K.T. (2011). "Morphology-controlled ZnO nanomaterials for enhanced photoelectrochemical performance." *Mater. Express,* 1, 59-67.

Pradhan, N., Pal, A. and Pal, T. (2001). "Catalytic reduction of aromatic nitro compounds by coinage metal nanoparticles." *Langmuir,* 17, 1800-1802.

Qi, F., Li, P., Chen, Y., Zheng, B., Liu, J., Zhou, J., He, J., Hao, X. and Zhang, W. (2017). "Three-dimensional structure of $WS_2$/graphene/Ni as a binder-free electrocatalytic electrode for highly effective and stable hydrogen evolution reaction." *Int. J. Hydrogen Energy,* 42, 7811-7819.

Qiu, J., Lai, C., Wang, Y., Li, S. and Zhang, S. (2014). "Resilient mesoporous $TiO_2$/graphene nanocomposite for high rate performance lithium-ion batteries." *Chem. Eng. J.,* 256, 247-254.

Reddy, S., Du, R., Kang, L., Mao, N. and Zhang, J. (2016). "Three dimensional CNTs aerogel/MoSx as an electrocatalyst for hydrogen evolution reaction." *Appl. Catal. B Environ.,* 194, 16-21.

Ren, H., Xu, W., Zhu, S., Cui, Z., Yang, X. and Inoue, A. (2016). "Synthesis and properties of nanoporous $Ag_2S$/CuS catalyst for hydrogen evolution reaction." *Electrochim. Acta,* 190, 221-228.

Renkun, H., Hao, G., Xiujuan, L., Yonglang, G., Rusheng, Y., Xianzhi, F. and Zhaohui, L. (2013). "Facile one-pot preparation of α-$SnWO_4$/reduced graphene oxide (RGO) nanocomposite with improved visible light photocatalytic activity and anode performance for Li-ion batteries." *RSC Adv.,* 3, 1235-1242.

Roberto, C.D., Martin-Ramos, P., Correa-Guimaraes, A. and Martin-Gil, J. (2011). "Synthesis of graphitic carbon nitride by reaction of melamine and uric acid." *Mater. Chem. Phys.,* 130, 1094-1102.

Robinson, T., McMullan, G., Marchant, R. and Nigam, P. (2001). "Remediation of dyes in textile effluent: a critical review on current treatment technologies with a proposed alternative." *Bioresour. Technol.,* 77, 247-255.

Rode, C., Vaidya, M. and Chaudhari, R. (1999). "Synthesis of p-aminophenol by catalytic hydrogenation of nitrobenzene." *Org. Process Res. Dev.,* 3, 465-470.

Roger, I., Shipman, M.A. and Symes, M.D. (2017). "Earth-abundant catalysts for electrochemical and photoelectrochemical water splitting." *Nature Rev. Chem.,* 1, 0003-1-14.

Ryu, J.H., Yoon, J.W., Lim, C.S., Oh, W.C. and Shim, K.B. (2005). "Microwave assisted synthesis of nanocrystalline $MWO_4$ (M: Ca, Ni) via water-based citrate complex precursor." *Ceram. Int.,* 31, 883-888.

Saad, M.A., Turki, A., Naif, A., Eida, A.F., Norah, A. and Tansir, A. (2017). "Chitosan based polymer matrix with silver nanoparticles decorated multiwalled carbon nanotubes for catalytic reduction of 4-nitrophenol." *Carbohyd. Polym.,* 151, 135-143.

Sakthivel, T., Gunasekaran, V. and Kim, S.J. (2014). "Enhanced photocatalytic efficiency of organic dyes using β-tin tungstate reduced graphene oxide nanocomposites." *Mater. Chem. Phys.,* 145, 108-115.

Sakthivel, T., Manikandan, E. and Gunasekaran, V. (2012). "Synthesis and properties of tungsten oxide and reduced graphene oxide nanocomposites." *Mater. Express,* 2, 327-334.

Sato, S., Lin, S.Y., Suzuki, Y. and Hatano, H. (2003). "Hydrogen production from heavy oil in the presence of calcium hydroxide." *J. Fuel,* 82, 561-567.

Selvakumar, M. and Bhat, D.K. (2012). "Microwave-assisted synthesis of $TiO_2$ nano particles and its electrochemical properties with activated carbon." *Appl. Surf. Sci.,* 263, 236-241.

Shao, Y., Liu, J., Wang, Y. and Lin, Y. (2008). "Novel catalyst support materials for PEM fuel cells: current status and future prospects." *J. Mater. Chem.,* 19, 46-59.

Shen, Y., Li, W. and Li, T. (2011). "Microwave-assisted synthesis of $BaWO_4$ nanoparticles and its photoluminescence properties." *Mater. Lett.,* 165, 2956- 958.

Sheng, Z., Lin, S., Chen, J., Bao, W., Wang, F. and Xia, X. (2011). "Catalyst-free synthesis of nitrogen- doped graphene via thermal annealing graphite oxide with melamine and its excellent electrocatalysis." *ACS Nano,* 5, 4350-4358.

Shi, R., Wang, Y., Li, D., Xu, J. and Zhu, Y. (2010). "Synthesis of $ZnWO_4$ nanorods with [100] orientation and enhanced photocatalytic properties." *Appl. Catal. B Environ.,* 100, 173-178.

Somchai, T., Surangkana, W., Anukorn, P. and Titipun, T. (2008). "Cyclic microwave-assisted spray synthesis of nanostructured $MnWO_4$." *Mater. Lett.,* 63, 833-836.

Soofivand, F. and Masoud, S.N. (2017). "Step synthesis and photocatalytic activity of NiO/graphene nanocomposite under UV and visible light as an effective photocatalyst." *J. Photochem. Photobiol. A Chem.,* 337, 44-53

Stankovich, S., Dikin, D.A., Dommett, G.H., Kohlhaas, K.M., Zimney, E.J., Stach, E.A., Piner, R.D., Nguyen, S.T. and Ruoff, R.S. (2006). "Graphene-based composite materials." *Nature,* 442, 282-286.

Subramanya, B. and Bhat, D.K. (2014). "Novel one-pot green synthesis of graphene in aqueous medium under microwave irradiation using regenerative catalyst and study of its electrochemical properties." *New J. Chem.,* 39, 420-430.

Subramanya, B. and Bhat, D.K. (2015). "Novel eco-friendly synthesis of graphene directly from graphite using TEMPO and study of its electrochemical properties." *J. Power Sources,* 275, 90-98.

Subramanya, B., Bhat, D.K., Shenoy, U.S., Ullal, Y. and Hegde, A.C. (2015). "Novel Fe-Ni-Graphene composite electrode for hydrogen production." *Int. J. Hydrogen Energy,* 40, 10453-10462.

Sudhakar, Y.N., Selvakumar, M., Bhat, D.K. and Senthilkumar, S. (2014). "Reduced graphene oxide derived from used cell graphite, and its green fabrication as eco-friendly supercapacitor." *RSC Adv.,* 4, 60039-60051.

Sun, B., Jia, X. J., Wu J.H. and Chen P. (2015). "Controlled synthesis and room-temperature ferromagnetism of $CaWO_4$ nanostructures." *J. Alloys Compd.,* 653, 12-25.

Sun, H., Cao, L. and Lu, L. (2011). "Magnetite/reduced graphene oxide nanocomposites: one step solvothermal synthesis and use as a novel platform for removal of dye pollutants." *Nano Res.,* 4, 550-562.

Sun, J. and Chen, L. (2017). "Superparamagnetic POT/$Fe_3O_4$ nanoparticle composites with supported Au nanoparticles as recyclable high-performance nanocatalysts." *Mater. Today Chem.,* 5, 43-51.

Sun, M., Fang, Y., Wang, Y., Sun, S., He, J. and Yan, Z. (2015). "Synthesis of $Cu_2O$/graphene/rutile $TiO_2$ nanorod ternary composites with enhanced photocatalytic activity." *J. Alloys Compd.,* 650, 520-527.

Sun, T., Zhang, Z., Xiao, J., Chen, C., Xiao, F., Wang, S. and Liu, Y. (2013). "Facile and green synthesis of palladium nanoparticles-graphene-carbon nanotube material with high catalytic activity." *Sci. Rep.,* 3, 1-6.

Sun, Y., Wu, Q. and Shi, G. (2011). "Graphene based new energy materials." *Energy Environ. Sci.,* 4, 1113-1132.

Suresh, S., Pandikumar, A., Murugesan, S., Ramaraj, R. and Paul Raj, S. (2011). "Metal-free low-cost organic dye-sensitized ZnO-nanorod photoanode for solid-state solar cell." *Mater. Express,* 1, 307-314.

Suslick, K.S. (1989). "The chemical effects of ultrasound." *Sci. Am.,* 260, 80-86.

Szabo, T., Berkesi, O., Forgo, P., Josepovits, K., Sanakis, Y., Petridis, D. and Dékány, I. (2006). "Evolution of surface functional groups in a series of progressively oxidized graphite oxides." *Chem. Mater.,* 18, 2740-2749.

Tang, W.Z. and Huren. A. (1995). "UV/$TiO_2$ photocatalytic oxidation of commercial dyes in aqueous solutions." *Chemoshpere,* 31, 9-16.

Tauc, J., Grigorovici, R. and Vancu, A. (1966). "Optical Properties and Electronic Structure of Amorphous Germanium." *Phys. Status Solidi B,* 15, 627-637.

Thanh-Truc, P., ChinhNguyen, H., Hyun-Jun, L., Thuy-Duong, N.P., Tae, H.S., Chang-Koo, K. and EunWoo, S. (2015). "Cu-doped $TiO_2$/reduced graphene oxide thin-film photocatalysts: Effect of Cu content upon methylene blue removal in water." *Ceram. Int.,* 41, 11184-11193.

Tian, J., Liu, Q., Asiri, A.M. and Sun, X. (2014). "Self-supported nanoporous cobalt phosphide nanowire arrays: an efficient 3D hydrogen-evolving cathode over the wide range of pH 0-14." *J. Am. Chem. Soc.,* 136, 7587-7590.

Tian, Y., Li, W., Zhao, C., Wang, Y., Zhang, B. and Zhang, Q. (2017). "Fabrication of hollow mesoporous $SiO_2$-BiOCl@PANI@Pd photocatalysts to improve the photocatalytic performance under visible light." *Appl. Catal. B Environ.,* 213, 136-146.

Tian, Y., Liu, Y., Pang, F., Wang, F. and Zhang, X. (2015). "Green synthesis of nanostructed Ni-reduced graphene oxide hybrids and their application for catalytic reduction of 4-nitrophenol." *Colloids Surf. A,* 464, 96-103.

Tian, Z., Yu, N., Cheng, Y., Wang, Z., Chen, Z. and Zhang, L. (2017). "Hydrothermal synthesis of graphene/$TiO_2$/CdS nanocomposites as efficient visible-light driven photocatalysts." *Mater. Lett.,* 194, 172-175.

Tilak, B. and Chen, C.P. (1993). "Generalized analytical expressions for Tafel slope, reaction order and ac impedance for the hydrogen evolution reaction (HER): mechanism of HER on platinum in alkaline media." *J. Appl. Electrochem.,* 23, 631-640.

Ullah, K., Meng, Z.D., Ye, S., Zhu, L. and Oh, W.C. (2014). "Synthesis and characterization of novel PbS-graphene/$TiO_2$ composite with enhanced photocatalytic activity." *J. Ind. Eng. Chem.,* 20, 1035-1042.

Vaidya, M.J., Kulkarni, S.M. and Chaudhari, R.V. (2003). "Synthesis of p-aminophenol by catalytic hydrogenation of p-nitrophenol." *Org. Process Res. Dev.,* 7, 202-208.

Vilian, A.T.E, Choe, S.R., Giribabu, K., Jang, S.C., Roh, C., Huh, Y.S. and Han, Y.K. (2017). "Pd nanospheres decorated reduced graphene oxide with multi-functions: Highly efficient catalytic reduction and ultrasensitive sensing of hazardous 4-nitrophenol pollutant." *J. Hazard. Mater.,* 333, 54-62.

Viswanathan, B. (2009). "Catalysis: Principles and Applications." *Narosa Publishing Pvt. Ltd.,* Delhi.

Wan, Q., Wang, T.H. and Zhao, J.C. (2005). "Enhanced photocatalytic activity of ZnO nanotetrapods." *Appl. Phys. Lett.,* 87, 8-16.

Wang, D., Pan, Z., Wu, Z., Wang, Z. and Liu, Z. (2014). "Hydrothermal synthesis of $MoS_2$ nanoflowers as highly efficient hydrogen evolution reaction catalysts." *J. Power Sources,* 264, 229-234.

Wang, J., Gao, D., Wang, G., Miao, S., Wu, H., Li, J. and Bao, X. (2014). "Cobalt nanoparticles encapsulated in nitrogen-doped carbon as a bifunctional catalyst for water electrolysis." *J. Mater. Chem. A,* 2, 20067-20074.

Wang, J., Zhong, H., Wang, Z., Meng, F. and Zhang, X. (2016). "Integrated three-dimensional carbon paper/carbon tubes/cobalt-sulfide sheets as an efficient electrode for overall water splitting." *ACS Nano,* 10, 2342-2348.

Wang, L., Ding, J., Chai, Y., Liu, Q., Ren, J., Liu, X. and Dai, W.L. (2015). "$CeO_2$ nanorods/g-$C_3N_4$/N-rGO composite: Enhanced visible-light driven photocatalytic performance and the role of N-rGO as electronic transfer media." *Dalton Trans.,* 44, 11223-11234.

Wang, L., Shi, Y., Wang, T. and Zhang, L. (2017). "Silver chloride enwrapped silver grafted on nitrogen-doped reduced graphene oxide as a highly efficient visible-light-driven photocatalyst." *J. Colloid Interface Sci.,* 505, 421-429.

Wang, M., Chen, L. and Sun, L. (2012). "Recent progress in electrochemical hydrogen production with earth-abundant metal complexes as catalysts." *Energy Environ. Sci.,* 5, 6763-6778.

Wang, P., Ao, Y., Wang, C., Hou, J. and Qian, J. (2012). "A one-pot method for the preparation of graphene–$Bi_2MoO_6$ hybrid photocatalysts that are responsive to visible-light and have excellent photocatalytic activity in the degradation of organic pollutants." *Carbon,* 50, 5256-5264.

Wang, T., Li, X., Jiang, Y., Zhou, Y., Jia, L. and Wang, C. (2017). "Reduced graphene oxide-polyimide/carbon nanotube film decorated with NiSe nanoparticles for electrocatalytic hydrogen evolution reactions." *Electrochim. Acta,* 243, 291-298.

Wang, X. Xu, H. Wang H. and Yan, H. (2006). "Morphology-controlled $BaWO_4$ powders via a template-free precipitation technique." *J. Cryst. Growth,* 130, 277-281.

Wang, Y., Shi, Z. and Yin, J. (2011). "Facile synthesis of soluble graphene via a green reduction of graphene oxide in tea solution and its biocomposites." *ACS Appl. Mater. Interfaces,* 3, 1127-1133.

Wang, Y., Wang, Z., Muhammad, S. and He, J. (2012). "Graphite-like $C_3N_4$ hybridized $ZnWO_4$ nanorods: Synthesis and its enhanced photocatalysis in visible light." *Cryst. Eng. Comm.,* 14, 5065-5070.

Wei, Q., Zhang, Z., Li, Z., Zhou, Q. and Zhu, Y. (2008). "Enhanced photocatalytic activity of porous α-$Fe_2O_3$ films prepared by rapid thermal oxidation." *J. Phys. D Appl. Phys.,* 41, 202002(1-4).

Williams, G. and Kamat, P.V. (2009). "Graphene-semiconductor nanocomposites: Excited state interactions between ZnO nanoparticles and graphene oxide." *Langmuir,* 25, 13869-13873.

Woo, H., Kim, J.W., Kim, M., Park, S. and Park, K.H. (2015). "Au nanoparticles supported on magnetically separable $Fe_2O_3$-graphene oxide hybrid nanosheets for the catalytic reduction of 4-nitrophenol." *RSC Adv.,* 5, 7554-7558.

Woo, M.K. (2012). "Electrocatalyst approaches and challenges for automotive fuel cells." *Nature,* 486, 43-51.

Wu, L., Bi, J., Li, Z., Wang, X. and Fu, X. (2008). "Rapid preparation of $Bi_2WO_6$ photocatalyst with nanosheet morphology via microwave-assisted solvothermal synthesis." *Catal. Today,* 131, 15-20.

Wu, S., Shen, X., Zhu, G., Zhou, H., Ji, Z., Ma, L., Xu, K., Yang, J. and Yuan, A. (2017). "Metal organic framework derived NiFe@N-doped graphene microtube composites for hydrogen evolution catalyst." *Carbon,* 116, 68-76.

Wu, Y.G., Wen, M., Wu, Q.S. and Fang, H. (2014). "Ni/graphene nanostructure and its electron-enhanced catalytic action for hydrogenation reaction of nitrophenol." *J. Phys. Chem. C,* 118, 6307-6313.

Wu, Z., Hu, B., Wu, P., Liang, H., Yu, Z., Lin, Y., Zheng, Y., Li, Z. and Yu, S. (2016). "$Mo_2C$ nanoparticles embedded within bacterial cellulose-derived 3D N-doped carbon nanofiber networks for efficient hydrogen evolution." *NPG Asia Mater.,* 8, e288(1-8).

Wu, Z., Wang, J., Zhu, J., Guo, J., Xiao, W., Xuan, C., Lei, W. and Wang, D. (2017). "Highly efficient and stable MoP-RGO nanoparticles as electrocatalysts for hydrogen evolution." *Electrochim. Acta,* 232, 254-261.

Xiang, Q. and Yu, J. (2013). "Graphene-based photocatalysts for hydrogen generation." *J. Phys. Chem. Lett.,* 4, 753-759.

Xiang, Q., Lang, D., Shen, T. and Liu, F. (2015). "Graphene-modified nanosized $Ag_3PO_4$ photocatalysts for enhanced visible-light photocatalytic activity and stability." *Appl. Cat. B Environ.,* 162, 196-203.

Xiaobing, X., Yuan, S., Wen, Q., Xing, Z., Xing, C., Xueyin, S., Liqian, W., Wei, Z. and Youwei, D. (2017). "3D $MoS_2$-graphene hybrid aerogels as catalyst for enhanced efficient hydrogen evolution." *Appl. Surf. Sci.,* 396, 1520-1527.

Xie, B., Wu, Y., Jiang, Y., Li, F., Wu, J., Yuan, S., Yu. W. and Qian, Y.T. (2002). "Shape-controlled synthesis of $BaWO_4$ crystals under different surfactants." *J. Cryst. Growth,* 235, 283-286.

Xu, H., Yan, J., She, X., Xu, L., Xia, J., Xu, Y., Song, Y., Huang, L. and Li, H. (2014). "Graphene-analogue carbon nitride: novel exfoliation synthesis and its application in photocatalysis and photoelectrochemical selective detection of trace amount of $Cu^{2+}$." *Nanoscale,* 6, 1406-1415.

Xu, J., Cui, Y., Han, Y., Hao, M. and Zhang, X. (2016). "ZnO-graphene composites with high photocatalytic activities under visible light." *RSC Adv.,* 6, 96778-96784.

Xu, J.W., Gao, Z.D., Han, K., Liu, Y. and Song, Y.Y. (2014). "Synthesis of magnetically separable $Ag_3PO_4/TiO_2/Fe_3O_4$ heterostructure with enhanced photocatalytic performance under visible light for photoinactivation of bacteria." *ACS Appl. Mater. Interfaces,* 6, 15122-15131.

Xu, L., Wang, Y., Liu, J., Han, S., Pan, Z. and Gan, L. (2017). "High-efficient visible-light photocatalyst based on graphene incorporated $Ag_3PO_4$ nanocomposite applicable

for the degradation of a wide variety of dyes." *J. Photochem. Photobiol. A Chem.,* 340, 70-79.

Xu, W., Jin, W., Lin, L., Zhang, C., Li, Z., Li, Y., Song, R. and Li, B. (2014). "Green synthesis of xanthan conformation-based silver nanoparticles: antibacterial and catalytic application." *Carbohydr. Polym.,* 101, 961-967.

Xu, X., Shen, J., Li, N. and Ye, M. (2014). "Facile synthesis of reduced graphene oxide/$CoWO_4$ nanocomposites with enhanced electrochemical performances for supercapacitors." *Electrochim. Acta,* 150, 23-34.

Yan, M., Hua, Y., Zhu, F., Gu, W., Jiang, J., Shen, H. and Shi, W. (2017). "Fabrication of nitrogen doped graphene quantum dots-BiOI/$MnNb_2O_6$ p-n junction photocatalyts with enhanced visible light efficiency in photocatalytic degradation of antibiotics." *Appl. Catal. B Environ.,* 202, 518-527.

Yan, S., Li, Z. and Zou, Z. (2009). "Photodegradation Performance of g-$C_3N_4$ fabricated by directly heating melamine." *Langmuir,* 25, 10397-10401.

Yang, F., Tu, C., Wang, H., Wei, Y., You, Z., Jia, G., Li, J., Zhu, Z., Lu, X. and Wang, Y. (2008). "Growth and spectroscopy of $ZnWO_4$: $Ho^{3+}$ crystal." *J. Alloys Compd.,* 455, 269-273.

Yang, J., Voiry, D., Ahn, S.J. and Shin, H.S. (2013). "Two-dimensional hybrid nanosheets of tungsten disulfide and reduced graphene oxide as catalysts for enhanced hydrogen evolution." *Angew. Chem. Int. Ed.,* 52, 13751-13754.

Yang, T., Shen, C., Li, Z., Zhang, H., Xiao, C., Chen, S., Xu, Z., Shi, D., Li, J. and Gao, H. (2005). "Highly ordered self-assembly with large area of $Fe_3O_4$ nanoparticles and the magnetic properties." *J. Phys. Chem. B,* 109, 23233-23236.

Yang, Y., Fei, H., Ruan, G. and Tour, J.M. (2015). "Porous cobalt-based thin film as a bifunctional catalyst for hydrogen generation and oxygen generation." *Adv. Mater.,* 27, 3175-3180.

Yang, Y., Ren, Y., Sun, C. and Hao, S. (2014). "Facile route fabrication of nickel based mesoporous carbons with high catalytic performance towards 4-nitrophenol reduction." *Green Chem.,* 16, 2273-2280.

Yu, C. and Jimmy, C.Y. (2009). "Sonochemical fabrication, characterization and photocatalytic properties of Ag/$ZnWO_4$ nanorod catalyst." *Mater. Sci. Eng. B,* 164, 16-22.

Yu, J.G., Liu, S.W. and Yu, H.G. (2007). "Microstructures and photoactivity of mesoporous anatase hollow microspheres fabricated by fluoride-mediated self-transformation." *J. Catal.,* 249, 59-66.

Yusran, Y., Xu, D., Fang, Q., Zhang, D. and Qiu, S. (2017). "MOF-derived Co@N-C nanocatalyst for catalytic reduction of 4-nitrophenol to 4-aminophenol." *Microporous Mesoporous Mater.,* 241, 346-354.

Zawawi, S.M.M., Yahya, R., Hassan, A., Mahmud, H.E. and Daud, M.N. (2013). "Structural and optical characterization of metal tungstates ($MWO_4$; M= Ni, Ba, Bi) synthesized by a sucrose-templated method." *Chem. Cent. J.,* 7, 1-10.

Zeng, K. and Zhang, D. (2010). "Recent progress in alkaline water electrolysis for hydrogen production and applications." *Prog. Energy Combust. Sci.,* 36, 307-326.

Zhang, H., Fan, X., Quan, X., Chen, S. and Yu, H. (2011). "Graphene sheets grafted Ag@AgCl hybrid with enhanced plasmonic photocatalytic activity under visible light." *Environ. Sci. Technol.,* 45, 5731-5736.

Zhang, H., Jiang, M., Wang, Z. and Wu, F. (2007). "Decolorisation of CI Reactive Black 8 by zero-valent iron powder with/without ultrasonic irradiation." *Color. Technol.,* 123, 203-208.

Zhang, L., Ji, B.C., Wang, K. and Song, J. (2014). "Synthesis of nitrogen-doped graphene via solid microwave method." *Mater. Sci. Eng. B,* 185, 129-133.

Zhang, L., Mohamed, H.H., Dillert, R. and Bahnemann, D. (2012). "Kinetics and mechanisms of charge transfer processes in photocatalytic systems: A review." *J. Photochem. Photobiol. C Photochem. Rev.,* 13, 263-276.

Zhang, M., Li, Y., Pan, D., Yan, Z., Meng, S. and Xie, J. (2016). "Nickel core-palladium shell nanoparticles grown on nitrogen-doped graphene with enhanced electrocatalytic performance for ethanol oxidation." *RSC Adv.,* 6, 33231-33239.

Zhang, M., Wang, S., Li, T., Chen, J., Zhu, H. and Du, M. (2016). "Nitrogen and gold nanoparticles co-doped carbon nanofiber hierarchical structures for efficient hydrogen evolution reactions." *Electrochim. Acta,* 208, 1-9.

Zhang, N., Zhang, Y. and Xu, Y.J. (2012). "Recent progress on graphene-based photocatalysts: current status and future perspectives." *Nanoscale,* 4, 5792-5813.

Zhang, Y., Tang, Z.R, Fu, X. and Xu, Y.J. (2010). "$TiO_2$-graphene nanocomposites for gas-phase photocatalytic degradation of volatile aromatic pollutant: is $TiO_2$-graphene truly different from other $TiO_2$-carbon composite materials?." *ACS Nano,* 4, 7303-7314.

Zhao, Z., Sun, Y. and Dong, F. (2015). "Graphitic carbon nitride based nanocomposites: A review." *Nanoscale,* 7, 15-37.

Zheng, J., Dong, Y., Wang, W., Ma, Y., Hu, J., Chen, X. and Chen, X. (2013). "In situ loading of gold nanoparticles on $Fe_3O_4$@$SiO_2$ magnetic nanocomposites and their high catalytic activity." *Nanoscale,* 5, 4894-4901.

Zheng, J.Y., Haider, Z., Van, T.K., Pawar, A.U., Kang, M.J., Kim, C.W. and Kang, Y.S. (2015). "Tuning of the crystal engineering and photoelectrochemical properties of crystalline tungsten oxide for optoelectronic device applications." *Cryst. Eng. Comm.,* 17, 6070-6093.

Zheng, X., Xu, J., Yan, K., Wang, H., Wang, Z. and Yang, S. (2014). "Space-confined growth of $MoS_2$ nanosheets within graphite: The layered hybrid of $MoS_2$ and

graphene as an active catalyst for hydrogen evolution reaction." *Chem. Mater.,* 26, 2344-2353.

Zheng, Y., Jiao, Y., Li, L.H., Xing, T., Chen, Y., Jaroniec, M. and Qiao, S.Z. (2014). "Toward design of synergistically active carbon-based catalysts for electrocatalytic hydrogen evolution." *ACS Nano,* 8, 5290-5296.

Zhou, B., Hermans, S. and Somorjai, G.A. (2004). "Nanotechnology in Catalysis." *Springer,* 1.

Zhou, J., Ga, J., Xu, X., Hong, W., Song, Y., Xue, R., Zhao, H., Liu, Y. and Qiu, H. (2017). "Synthesis of porous Bi@Cs networks by a one-step hydrothermal method and their superior catalytic activity for the reduction of 4-nitrophenol." *J. Alloys Compd.,* 709, 206-212

Zhou, Y.X., Yao, H.B., Zhang, Q., Gong, J.Y., Liu, S.J. and Yu, S.H. (2009). "Hierarchical $FeWO_4$ microcrystals: Solvothermal synthesis and their photocatalytic and magnetic properties." *Inorg. Chem.,* 48, 1082-1090.

Zhu, C., Zheng, J., Fang, L., Hu, P., Liu, Y., Cao, X. and Wu, M. (2016). "Advanced visible-light driven photocatalyst with enhanced charge separation fabricated by facile deposition of $Ag_3PO_4$ nanoparticles on graphene-like h-BN nanosheets." *J. Mol. Catal.,* 424, 135-144.

Zhu, J., Xiaoz, P., Li, H. and Sonia, A.C.C. (2014). "Graphitic carbon nitride: Synthesis, properties, and applications in catalysis." *ACS Appl. Mater. Interfaces,* 6, 16449-16465.

Zhu, S., Dong, Y., Xia, X., Liu, X. and Li, H. (2016). "Synthesis of Mo-doped $TiO_2$ nanowires/reduced graphene oxide composites with enhanced photodegradation performance under visible light irradiation." *RSC Adv.,* 6, 23809-23815.

Zhu, Y., Murali, S., Cai, W., Li, X., Suk, J.W., Potts, J.R. and Ruoff, R.S. (2010). "Graphene and graphene oxide: synthesis, properties, and applications." *Adv. Mater.,* 22, 3906-3924.

Zou, C., Liu, S., Shen, Z., Zhang, Y., Jiang, N. and Ji, W. (2017). "Efficient removal of ammonia with a novel graphene supported $BiFeO_3$ as a reusable photocatalyst under visible light." *Chin. J. Catal.,* 38, 20-28.

Zou, X., Huang, X., Goswami, A., Silva, R., Sathe, B.R., Mikmeková, E. and Asefa, T. (2014). "Cobalt-embedded nitrogen-rich carbon nanotubes efficiently catalyze hydrogen evolution reaction at all pH values." *Angew. Chem. Int. Ed.,* 53, 4372-4376.

Zubair, H., Yong, S.K., Rinklebe, J., Tsang, Y.F., Cho, D.W. and Song, H. (2017). "N doped cobalt-carbon composite for reduction of p-nitrophenol and pendimethaline." *J. Alloys Compd.,* 703, 118-124.

# RESEARCH PUBLICATIONS

**Research Papers Published/being Published in International Journals**

1. **Mohamed Jaffer Sadiq, M.,** Sandhya Shenoy U. and Krishna Bhat, D. (2017). "$NiWO_4$-ZnO-NRGO ternary nanocomposite as an efficient photocatalyst for degradation of methylene blue and reduction of 4-nitro phenol." *J. Phys. Chem. Solids,* 109, 124-133.
2. **Mohamed Jaffer Sadiq, M.,** Sandhya Shenoy, U. and Krishna Bhat, D. (2017). "Enhanced photocatalytic performance of N-doped RGO-$FeWO_4/Fe_3O_4$ ternary nanocomposite in environmental applications." *Mater. Today Chem.,* 04, 133-141.
3. **Mohamed Jaffer Sadiq, M.** and Krishna Bhat, D. (2017). "A facile microwave approach to synthesis of RGO-$BaWO_4$ composites for photocatalytic degradation of various dyes." *AIMS Mater. Sci.,* 04, 487-502.
4. **Mohamed Jaffer Sadiq, M.,** Sandhya Shenoy, U. and Krishna Bhat, D. (2017). "High performance dual catalytic activity of novel zinc tungstate-reduced graphene oxide nanocomposites." *Adv. Sci. Eng. Med.,* 09, 115-121.
5. **Mohamed Jaffer Sadiq, M.** and Krishna Bhat, D. (2017). "Novel $ZnWO_4$/RGO nanocomposite as high performance photocatalyst." *AIMS Mater. Sci.,* 04, 158-171.
6. **Mohamed Jaffer Sadiq, M.,** Sandhya Shenoy, U. and Krishna Bhat, D. (2016). "Novel RGO-$ZnWO_4$-$Fe_3O_4$ nanocomposite as high performance visible light photocatalyst." *RSC Adv.*, 06, 61821-61829.
7. **Mohamed Jaffer Sadiq, M.** and Krishna Bhat, D. (2016). "Novel RGO-$ZnWO_4$-$Fe_3O_4$ nanocomposite as an efficient catalyst for rapid reduction of 4-nitrophenol to 4-aminophenol." *Ind. Eng. Chem. Res.,* 55, 7267-7272.
8. **Mohamed Jaffer Sadiq, M.,** Sandhya Shenoy, U. and Krishna Bhat, D. (2017). "Novel NRGO-$CoWO_4$-$Fe_2O_3$ nanocomposite as an efficient catalyst for dye degradation and reduction of 4-nitrophenol." (Under Review).
9. **Mohamed Jaffer Sadiq, M.,** Sandhya Shenoy, U. and Krishna Bhat, D. (2017). "Synthesis of NRGO/$BaWO_4$/g-$C_3N_4$ nanocomposites with excellent

multifunctional catalytic performance via microwave approach." (Under Review).

10. **Mohamed Jaffer Sadiq, M.,** Sandhya Shenoy, U. and Krishna Bhat, D. (2017). "Novel $ZnWO_4$-RGO-$Fe_3O_4$ nanocomposite as cathode material for hydrogen production." (Under Review).
11. **Mohamed Jaffer Sadiq, M.** and Krishna Bhat, D. (2017). "NRGO@$NiWO_4$/ZnO nanocomposites as an efficient electrocatalyst for the hydrogen evolution reaction." (Under Review).
12. **Mohamed Jaffer Sadiq, M.** and Krishna Bhat, D. (2017). "Novel NRGO/$CoWO_4$/$Fe_2O_3$ nanocomposite as an efficient cathode material for hydrogen production." (Under Review).
13. **Mohamed Jaffer Sadiq, M.** and Krishna Bhat, D. (2017). "N-doped RGO-$FeWO_4$/$Fe_3O_4$ ternary nanocomposite as an efficient electrocatalyst for the hydrogen evolution reaction." (Under Review).

**Research Papers Presented in Conferences**

1. **Mohamed Jaffer Sadiq, M.** and Krishna Bhat, D. (2017). "N-doped RGO@$BaWO_4$ composites as high performance photocatalysts." BRNS and CSIR Sponsored International Conference on Energy, Environment and Advanced Materials for a Sustainable Future (ICEEAMSF-2017), Kongu Engineering College, Perundurai, Erode, Tamilnadu, India, May 23-24$^{th}$ 2017.
2. **Mohamed Jaffer Sadiq, M.** and Krishna Bhat, D. (2017). "Novel $CoWO_4$/NRGO nanocomposite as high performance photocatalysts." International Conference on Advances in Biological Chemical and Physical Sciences (ABCPS-2017), Anna University, BIT Campus, Tiruchirappalli, Tamilnadu, India, March 13-15$^{th}$ 2017.
3. **Mohamed Jaffer Sadiq, M.** and Krishna Bhat, D. (2017). "NRGO-$CoWO_4$-$Fe_2O_3$ nanocomposite as an efficient photocatalyst for environmental applications." International Conference on Green Chemistry and

Nanotechnology Opportunities and Challenges (GCNOC-2017), St Aloysius College (Autonomous), Mangalore, Karnataka, India, February 27-28th 2017.

4. **Mohamed Jaffer Sadiq, M.** and Krishna Bhat, D. (2017). "Novel $NiWO_4$-ZnO-NRGO ternary nanocomposites with enhanced photocatalytic activity." International Conference on Advances in Science and Engineering (ICASE-2017), East West Institute of Technology, Bengaluru, India and Regent's International College, Bangkok, Thailand, January 20-22th 2017.
5. **Mohamed Jaffer Sadiq, M.** and Krishna Bhat, D. (2017). "Novel NRGO-$NiWO_4$ nanocomposites with enhanced photocatalytic activity." International Conference on Advances in Functional Materials (ICAFM-2017), Anna University, Chennai, Tamilnadu, India, January 6-8th 2017.
6. **Mohamed Jaffer Sadiq, M.** and Krishna Bhat, D. (2016). "Ternary NiO/$ZnWO_4$/Graphene nanocomposites with enhanced photocatalytic activity." International Conference on Nanotechnology (ICNANO-2016), Visvesvaraya Technological University, Chikkaballapur, Karnataka, India, April 21-23th 2016.
7. **Mohamed Jaffer Sadiq, M.** and Krishna Bhat, D. (2015). "RGO/$MWO_4$ (M=Zn, Cu, Ba & Co) nanocomposites as a high performance photocatalyst for water treatment." International Conference on Advances in Chemical Engineering (ICACE-2015), NITK Surathkal, Mangalore, Karnataka, India, December 20-22th 2015.
8. **Mohamed Jaffer Sadiq, M.** and Krishna Bhat, D. (2015). "Novel $ZnWO_4$ nanosphere-RGO nanosheets nanocomposites prepared by simple ultrasonic assisted microwave irradiation technique for photocatalytic applications." International Conference on Nanomaterials and Nanotechnology (NANO-2015), K.S.R college of Technology, Tiruchengode, Tamilnadu, India, December 07-10th 2015.

# BIO-DATA

==========

## PERSONAL DETAILS

**Name** : **MOHAMED JAFFER SADIQ M**
**Father Name** : MOHAMED IBRAHIM H (LATE)
**Mother Name**: AMEEN BIVI M
**Address (Permanent)** : 94/2, Jinnah Street, Near Manigundu, Erode - 638001. Tamil Nadu.
**Address (Contact)** : Department of Chemistry, National Institute of Technology Karnataka, Surathkal, Mangalore - 575025. Karnataka.
**Email** : sadiqmsc@gmail.com
**Mobile No** : +91-9964302524

## FIELDS OF COMPETENCE

Development of graphene based nanocomposites for catalytic applications.

## ACADEMIC QUALIFICATIONS

| Qualification | Specialization | Board/University | Year of Passing | Marks CGPA / % |
|---|---|---|---|---|
| Ph.D. | Chemistry | National Institute of Technology Karnataka (NITK), Surathkal, Mangalore | 2017 | 7.0 (CGPA) |
| M.Tech. | Nanotechnology | Karunya University, Coimbatore. | 2014 | 8.51 (CGPA) |
| M.Sc. | Applied Chemistry | National Institute of Technology (NIT), Trichy. | 2008 | 7.21 (CGPA) |
| B.Sc. | Chemistry | Bharathiyar University, Erode. | 2006 | 80.50 % |
| H.S.C | Science + Math's Stream | Tamil Nadu Board of Examinations. | 2003 | 83.08 % |
| S. S. L.C | Science + Math's Stream | Tamil Nadu Board of Examinations. | 2001 | 87.40 % |

## AREA OF INTERESTS

- Nanomaterials
- Nanocomposites

- Photocatalysis
- Water Splitting (HER and OER)
- Energy storage - Supercapacitors
- Fuel cells (ORR)

## AWARDS/CERTIFICATES

- Institute Research Fellowship, National Institute of Technology Karnataka (NITK), Surathkal, 2014-17.
- DST Nano mission Funded Postgraduate Assistantship Program, Karunya University, 2012-14.
- Best Research Poster Award in National Symposium on Nano Science and Nanotechnology at Karunya University, Coimbatore, 2013.
- Second Topper in M.Tech (Nanotechnology) at Karunya University, Coimbatore, 2012-14.
- State Level Science Talent Search Exam - Velammal Educational Trust at Tamil Nadu Science and Technology Centre, Erode, 2002.

## PROFESSIONAL ACTIVITIES

- Board of Studies, Alumni Member in Department of Nanoscience and Technology, Karunya University, Coimbatore, 2016.

## INDUSTRIAL EXPERIENCES

**HINDUSTAN ZINC LIMITED (Vedanta Resources Plc).**

- Worked as Chemist in Hindustan Zinc Limited from June 2008 to July 2012.

## LABORATORY TECHNIQUES / TRAINING

- Trained in a variety of techniques including design of photoreactor set-up, design of HER set-up, electrode fabrication for supercapacitor and electrocatalytic applications, hands on experience in handling microwave reactors, electrochemical workstations, probe sonicator, vibration mill, etc.
- Instruments Handling Training as XRD, SEM, FTIR, DLS, UV-Vis, PL, AAS, ICP, OES etc., 2008-2014.
- Air Monitoring Training Program - SGS Private Ltd, Vizag, 2011.

- ICP testing methods on Pure Zn, Pb, Ag, Cd etc., - Sterlite Ltd, Tuticorin, 2011.
- Dyeing and Printing of Knitted Fabrics from R. P. Colors, Tirupur, 2007.
- Training on 5'S, Six Sigma, Quality circle, ISO 9001, ISO 14001 and OHSAS 18001.
- Training on Presentation skills, Time management, Sampling & Fire Fighting.
- Training on Precious Metal Analysis in concentrates other impurities.

## COMPUTER PROFICIENCY

- Diploma in Computer Application passed with 1st Class Distinction from the FACE Center, Erode.
- Scientific software including Scifinder, Chemsketch, Chemdraw, Origin, EC-Lab, VersaStudio, ZSimpWin, IVIUM, Casa XPS, etc.
- Extensive experience of Microsoft Office and interest in webpage design coupled with sound knowledge of graphics packages.

### Academic Projects

| Project | Topic | Institute | Period |
|---|---|---|---|
| Ph.D | Graphene - Metal tungstate nanocomposites for catalytic applications | National Institute of Technology Karnataka (NITK), Surathkal. | Year 2017 |
| M.Tech Project (Full Semester) | Morphology assisted synthesis and characterization of $BaWO_4$ based semiconductor nanomaterials for photocatalytic applications. | Karunya University, Coimbatore. | Year 2014 |
| M.Tech Project (Half Semester) | Synthesis and Characterization of Novel Nano Crystalline Materials for Potential Applications. | Karunya University, Coimbatore. | Year 2013 |
| M.Sc. Project | Photo induced electron transfer study of Nile Red in the presence of Metal-Semiconductor Nanoparticles. | National Institute of Technology (NIT), Trichy. | Year 2008 |

## JOURNAL PUBLICATIONS

1. **Mohamed Jaffer Sadiq, M.,** Mutyala, S., Mathiyarasu, J. and Krishna Bhat, D. (2017). "RGO/$ZnWO_4$/$Fe_3O_4$ nanocomposite as an efficient electrocatalyst for oxygen reduction reaction." *J. Electroanal. Chem.,* 799, 102-110.
2. **Mohamed Jaffer Sadiq, M.,** Sandhya Shenoy U. and Krishna Bhat, D. (2017). "$NiWO_4$-ZnO-NRGO ternary nanocomposite as an efficient photocatalyst for degradation of methylene blue and reduction of 4-nitro phenol." *J. Phys. Chem. Solids,* 109, 124-133.
3. Sandhya Shetty., **Mohamed Jaffer Sadiq, M.,** Krishna Bhat, D. and Chitharanjan Hegde, A. (2017). "Electrodeposition and Characterization of Ni-Mo alloy as an electrocatalyst for alkaline water electrolysis." *J. Electroanal. Chem.,* 796, 57-65.
4. **Mohamed Jaffer Sadiq, M.,** Sandhya Shenoy, U. and Krishna Bhat, D. (2017). "Enhanced photocatalytic performance of N-doped RGO-$FeWO_4$/$Fe_3O_4$ ternary nanocomposite in environmental applications." *Mater. Today Chem.,* 04, 133-141.
5. **Mohamed Jaffer Sadiq, M.** and Krishna Bhat, D. (2017). "Novel RGO/$ZnWO_4$/$Fe_3O_4$ nanocomposite as high performance electrocatalyst for oxygen evolution reaction in basic medium." *JOJ Mater. Sci.,* 02, 1-5
6. **Mohamed Jaffer Sadiq, M.** and Krishna Bhat, D. (2017). "A facile microwave approach to synthesis of RGO-$BaWO_4$ composites for photocatalytic degradation of various dyes." *AIMS Mater. Sci.,* 04, 487-502.
7. **Mohamed Jaffer Sadiq, M.,** Sandhya Shenoy, U. and Krishna Bhat, D. (2017). "High performance dual catalytic activity of novel zinc tungstate - reduced graphene oxide nanocomposites." *Adv. Sci. Eng. Med.,* 09, 115-121.
8. **Mohamed Jaffer Sadiq, M.** and Krishna Bhat, D. (2017). "Novel $ZnWO_4$/RGO nanocomposite as high performance photocatalyst." *AIMS Mater. Sci.,* 04, 158-171.
9. Sandhya Shetty., **Mohamed Jaffer Sadiq, M.,** Krishna Bhat, D. and Chitharanjan Hegde, A. (2016). "Development of multilayer Sn-Ni alloy

coating by pulsed sonoelectrolysis for enhanced corrosion protection." *RSC Adv.,* 06, 77465-77473.

10. **Mohamed Jaffer Sadiq, M.,** Sandhya Shenoy, U. and Krishna Bhat, D. (2016). "Novel RGO-$ZnWO_4$-$Fe_3O_4$ nanocomposite as high performance visible light photocatalyst." *RSC Adv.*, 06, 61821-61829.
11. **Mohamed Jaffer Sadiq, M.** and Krishna Bhat, D. (2016). "Novel RGO-$ZnWO_4$-$Fe_3O_4$ nanocomposite as an efficient catalyst for rapid reduction of 4-nitrophenol to 4-aminophenol." *Ind. Eng. Chem. Res.,* 55, 7267-7272.
12. **Mohamed Jaffer Sadiq, M.** and Samson Nesaraj, A. (2015). "Soft chemical synthesis and characterization of $BaWO_4$ nanoparticles for photocatalytic removal Rhodamine B present in water sample." *J. Nanostruct. Chem.,* 05, 45-54.
13. **Mohamed Jaffer Sadiq, M.** and Samson Nesaraj, A. (2014). "Reflux condensation synthesis and characterization of $Co_3O_4$ nanoparticles for photocatalytic applications." *Iranian J. Catal.,* 04, 219-226.
14. **Mohamed Jaffer Sadiq, M.** and Samson Nesaraj, A. (2014). "Development of NiO-$Co_3O_4$ nano-ceramic composite materials as novel photocatalysts to degrade organic contaminants present in water." *Int. J. Environ. Res.,* 08, 1171-1184.
15. **Mohamed Jaffer Sadiq, M.** and Samson Nesaraj, A. (2013). "Effect of surfactants in the synthesis of NiO nanoparticles by colloidal thermal assisted reflux condensation method." *J. New Technol. Mater.,* 03, 14-28.
16. **Mohamed Jaffer Sadiq, M.,** Sandhya Shenoy, U. and Krishna Bhat, D. (2017). "Novel NRGO-$CoWO_4$-$Fe_2O_3$ nanocomposite as an efficient catalyst for dye degradation and reduction of 4-nitrophenol." (Under Review).
17. **Mohamed Jaffer Sadiq, M.,** Sandhya Shenoy, U. and Krishna Bhat, D. (2017). "Synthesis of NRGO/$BaWO_4$/g-$C_3N_4$ nanocomposites with excellent multifunctional catalytic performance via microwave approach." (Under Review).

18. **Mohamed Jaffer Sadiq, M.,** Sandhya Shenoy, U. and Krishna Bhat, D. (2017). "Novel $ZnWO_4$-RGO-$Fe_3O_4$ nanocomposite as cathode material for hydrogen production." (Under Review).
19. **Mohamed Jaffer Sadiq, M.** and Krishna Bhat, D. (2017). "NRGO@$NiWO_4$/ZnO nanocomposites as an efficient electrocatalyst for the hydrogen evolution reaction." (Under Review).
20. **Mohamed Jaffer Sadiq, M.** and Krishna Bhat, D. (2017). "Novel NRGO/$CoWO_4$/$Fe_2O_3$ nanocomposite as an efficient cathode material for hydrogen production." (Under Review).
21. **Mohamed Jaffer Sadiq, M.** and Krishna Bhat, D. (2017). "N-doped RGO-$FeWO_4$/$Fe_3O_4$ ternary nanocomposite as an efficient electrocatalyst for the hydrogen evolution reaction." (Under Review).
22. **Mohamed Jaffer Sadiq, M.** and Krishna Bhat, D. (2017). "A synergistic role of nitrogen-doped RGO and CuO/$CuWO_4$ nanocomposite towards the catalytic activity of environmental and energy applications." (Under Review).
23. Sandhya Shetty., **Mohamed Jaffer Sadiq, M.,** Krishna Bhat, D. and Chitharanjan Hegde, A. (2017). "Novel Ni-Mo-RGO composite as an electrode material for hydrogen production." (Under Review).
24. Akshata Shetty., **Mohamed Jaffer Sadiq, M.,** Krishna Bhat, D. and Chitharanjan Hegde, A. (2017). "Novel Co-Ni alloy as an electrocatalyst for alkaline water electrolysis." (Under Review).
25. Mutyala, S., **Mohamed Jaffer Sadiq, M.,** Gurulakshmi, M., Krishna Bhat, D., Shanthi, K., Mathiyarasu, J. and Suresh, C. (2017). "Disintegration of flower like $MoS_2$ to limply allied layer grown on spherical nanoporous $TiO_2$: Enhanced visible light photocatalytic degradation of methylene blue." (Under Review).

**CONFERENCE PAPER PRESENTATIONS**

1. **Mohamed Jaffer Sadiq, M.** and Krishna Bhat, D. (2017). "N-doped RGO@$BaWO_4$ composites as high performance photocatalysts." BRNS and CSIR Sponsored International Conference on Energy, Environment and

Advanced Materials for a Sustainable Future (ICEEAMSF-2017), Kongu Engineering College, Perundurai, Erode, Tamilnadu, India, May 23-24th 2017.

2. **Mohamed Jaffer Sadiq, M.** and Krishna Bhat, D. (2017). "Novel RGO-$ZnWO_4$-$Fe_3O_4$ electrodes materials for future electrochemical energy storage device applications." Indo-Brazil Bilateral International Conference on Advanced Material Processing 2017 (AMP-2017), Kalasalingam University, Krishankoil, Tamilnadu, India, March 27-28th 2017.
3. **Mohamed Jaffer Sadiq, M.** and Krishna Bhat, D. (2017). "Novel $CoWO_4$/NRGO nanocomposite as high performance photocatalysts." International Conference on Advances in Biological Chemical and Physical Sciences (ABCPS-2017), Anna University, BIT Campus, Tiruchirappalli, Tamilnadu, India, March 13-15th 2017.
4. **Mohamed Jaffer Sadiq, M.** and Krishna Bhat, D. (2017). "NRGO-$CoWO_4$-$Fe_2O_3$ nanocomposite as an efficient photocatalyst for environmental applications." International Conference on Green Chemistry and Nanotechnology Opportunities and Challenges (GCNOC-2017), St Aloysius College (Autonomous), Mangalore, Karnataka, India, February 27-28th 2017.
5. Pushyaraga, P.V., **Mohamed Jaffer Sadiq, M.** and Krishna Bhat, D. (2017). "Novel NRGO/$CuWO_4$ nanocomposite as high performance photocatalyst." International Conference on Green Chemistry and Nanotechnology Opportunities and Challenges (GCNOC-2017), St Aloysius College (Autonomous), Mangalore, Karnataka, India, February 27-28th 2017.
6. **Mohamed Jaffer Sadiq, M.** and Krishna Bhat, D. (2017). "Novel $NiWO_4$-ZnO-NRGO ternary nanocomposites with enhanced photocatalytic activity." International Conference on Advances in Science and Engineering (ICASE-2017), East West Institute of Technology, Bengaluru, India and Regent's International College, Bangkok, Thailand, January 19-22th 2017.
7. **Mohamed Jaffer Sadiq, M.** and Krishna Bhat, D. (2017). "Novel NRGO-$NiWO_4$ nanocomposites with enhanced photocatalytic activity." International Conference on Advances in Functional Materials (ICAFM-2017), Anna University, Chennai, Tamilnadu, India, January 6-8th 2017.

8. **Mohamed Jaffer Sadiq, M.** and Krishna Bhat, D. (2016). "Novel RGO-$ZnWO_4$-$Fe_3O_4$ nanocomposite as high performance electrocatalysts for oxygen evolution reaction." International Conference on Science and Technology: Future Chellenges and Solutions (STFCS-2016), University of Mysore, Mysore, Karnataka, India, August 8-9$^{th}$ 2016.
9. **Mohamed Jaffer Sadiq, M.** and Krishna Bhat, D. (2016). "Ternary NiO/$ZnWO_4$/Graphene nanocomposites with enhanced photocatalytic activity." International Conference on Nanotechnology (ICNANO-2016), Visvesvaraya Technological University, Chikkaballapur, Karnataka, India, April 21-23$^{th}$ 2016.
10. Aswini Anilkumar, C.M., **Mohamed Jaffer Sadiq, M.** and Krishna Bhat, D. (2016). "Novel Graphene-NiO nanocomposite as an efficient photocatalyst for the degradation of methylene blue." International Conference on Nanotechnology (ICNANO-2016), Visvesvaraya Technological University, Chikkaballapur, Karnataka, India, April 21-23$^{th}$ 2016.
11. Haritha, A.H., **Mohamed Jaffer Sadiq, M.** and Krishna Bhat, D. (2016). "Novel $Co_3O_4$-RGO nanocomposite as hybrid electrode material for hydrogen evolution reaction." International Conference on Nanotechnology (ICNANO-2016), Visvesvaraya Technological University, Chikkaballapur, Karnataka, India, April 21-23$^{th}$ 2016.
12. Vishwanath G Bekkeri., **Mohamed Jaffer Sadiq, M.** and Krishna Bhat, D. (2016). "Novel Graphene-Manganese oxide nanocomposite as electrode materials for supercapacitor application." International Conference on Nanotechnology (ICNANO-2016), Visvesvaraya Technological University, Chikkaballapur, Karnataka, India, April 21-23$^{th}$ 2016.
13. **Mohamed Jaffer Sadiq, M.** and Krishna Bhat, D. (2015). "RGO/$MWO_4$ (M=Zn, Cu, Ba & Co) nanocomposites as a high performance photocatalyst for water treatment." International Conference on Advances in Chemical Engineering (ICACE-2015), National Institute of Technology Karnataka (NITK), Surathkal, Mangalore, Karnataka, India, December 20-22$^{th}$ 2015.

14. **Mohamed Jaffer Sadiq, M.** and Krishna Bhat, D. (2015). "Novel $ZnWO_4$ nanosphere-RGO nanosheets nanocomposites prepared by simple ultrasonic assisted microwave irradiation technique for photocatalytic applications." International Conference on Nanomaterials and Nanotechnology (NANO-2015), K.S.R college of Technology, Tiruchengode, Tamilnadu, India, December 07-10$^{th}$ 2015.
15. **Mohamed Jaffer Sadiq, M.** and Krishna Bhat, D. (2015). "Sonocatalytic degradation of Rhodamine B by zinc tungstate-reduced graphene oxide nanocomposite prepared using microwave irradiation method." Advanced Materials for Energy and Environmental Applications (AMEEA-2015), Bharathiar University, Coimbatore, Tamilnadu, India, March 18-20$^{th}$ 2015.
16. **Mohamed Jaffer Sadiq, M.,** Samson Nesaraj, A. and Krishna Bhat, D. (2014). "Synthesis and Characterization of Zn doped $BaWO_4$ Nanocrystalline Materials for Photocatalytic Applications." 13$^{th}$ Eurasia Conference on Chemical Science (EuAsC2S-13), Indian Institute of Science (IISc), Bangalore, Karnataka, India, December 14-18$^{th}$ 2014.
17. **Mohamed Jaffer Sadiq, M.** and Samson Nesaraj, A. (2014). "Effect of pH in the Synthesis of $BaWO_4$ Nanocrystals for Photocatalytic Applications." National Conference on Innovations in Chemistry - Health and Energy (iCHEM-HE 2014), Karunya University, Coimbatore, Tamilnadu, India, February 6-8$^{th}$ 2014.
18. **Mohamed Jaffer Sadiq, M.** and Samson Nesaraj, A. (2013). "Synthesis and Characterization of NiO-$Co_3O_4$ Nano composites for Photocatalytic Applications." National Symposium on SCience of NanO (SCiNO 2013), Bharathiar University, Coimbatore, Tamilnadu, India, December 5-6$^{th}$ 2013.
19. **Mohamed Jaffer Sadiq, M.** and Samson Nesaraj, A. (2013). "Synthesis and Characterization of NiO-$Co_3O_4$ Nano composites for Photocatalytic Applications." 6$^{th}$ Bangalore India Nano, Bangalore, Karnataka, India, December 4-6$^{th}$ 2013.
20. **Mohamed Jaffer Sadiq, M.** and Samson Nesaraj, A. (2013). "Synthesis and Characterization of $BaWO_4$ Nanoparticles for Photocatalytic Applications."

National Symposium on Nano Science and Nanotechnology (NSNN-2013), Karunya University, Coimbatore, Tamilnadu, India, September 30th-October 1st 2013. **(Won Best Presentation Award).**

21. **Mohamed Jaffer Sadiq, M.** and Samson Nesaraj, A. (2013). "Synthesis and Characterization of $Co_3O_4$ Nanoparticles for Photocatalytic Applications." Second National Seminar on New Materials Research and Nanotechnology (NSNMRN-2013), Government Arts College, Ooty, Tamilnadu, India, September 25-27th 2013.
22. **Mohamed Jaffer Sadiq, M.** and Samson Nesaraj, A. (2013). "Synthesis and Characterization of CuO as Nano Photocatalysts." Indo-US Workshop on Nano-structured Electronic Materials: Challenges and Relevance to Electronics & Energy Research, Centre for Materials for Electronics Technology (CMET), Thrissur, Kerala, India, March 8-11th 2013.

## CONFERENCE/WORKSHOP/SEMINAR PARTICIPATION

- International conference on 5th Bangalore India Nano, Bangalore, Karnataka, India, 2012.
- International conference on Nanomaterial and its Applications at NIT, Trichy, 2007.
- National Seminar on Nano science and Technology at NIT, Trichy, 2013.
- National Seminar on Nano science and Technology (NSNT 2012) at Karunya University, Coimbatore, 2012.
- Efficient & Smooth Management of Environment "How Best to Perform Air Pollution Monitoring and Analysis" at SGS Ltd, Vizag, 2011.
- National Workshop on Micro Reaction Technology for Process Intensification at NIT, Trichy, 2008.
- National Workshop on Advanced Materials for Optoelectronic Devices at NIT, Trichy, 2008.
- National level Short-Term Course on Advanced Alternative Energy Technologies with Special Emphasis to Fuel Cells at NIT, Trichy, 2008.
- National Seminar on Sensor and its Applications at NIT, Trichy, 2007.

- Dr. Siva Rama Krishnan Naga Rajan Memorial Inter Collegiate Quiz Contest at Bishop Heber College, Trichy, 2007.
- National Workshop on Catalysts in Environmental Applications at NIT, Trichy, 2007.
- National Seminar on Nano science and Technology (NSNT 2007) at Karunya University, Coimbatore, 2007.
- National level Training Programme for PG Students for Clearing NET – National Eligibility Test at NIT, Trichy, 2007.

**SYMPOSIUMS ORGANIZED**

- Horizon 2007 - 15$^{th}$ National Level Students Symposium "Green Chemistry" at NIT, Trichy, 2007.
- Horizon 2006 - 14$^{th}$ National Level Students Symposium "Nanoparticles - The size revolution" at NIT, Trichy, 2006.

**LANGUAGES KNOWN**

Tamil, English and Hindi.

**REFERENCES**

1) Professor. D. Krishna Bhat,
   Department of Chemistry,
   National Institute of Technology Karnataka,
   Surathkal, Mangalore - 575025. Karnataka, INDIA.
   Email: denthajekb@gmail.com
   Mobile No: +91-9481271262

2) Professor. A. Samson Nesaraj,
   Professor & Admissions Officer,
   Karunya University,
   Karunya Nagar, Coimbatore - 641114. Tamil Nadu, INDIA.
   Email: drsamson@karunya.edu
   Mobile No: +91-9894723178

**DECLARATION**

I hereby declare that the information furnished above is true to the best of my knowledge. I like challenges and challenges encourages me to beat them.

Date:

Place: Srinivasnagar MOHAMED JAFFER SADIQ M